Study of non-identical particle ($\pi^{\pm} - K^{\pm}$) femtoscopy in Pb–Pb collisions at $\sqrt{s_{\rm NN}} = 5.02$ TeV with ALICE at the LHC

A Thesis
Submitted in partial fulfillment of
the requirements for the degree of
Doctor of Philosophy
by

Pritam Chakraborty
(Roll No. 174120004)

Supervisor:
Prof. Sadhana Dash

Department of Physics
Indian Institute of Technology Bombay
Mumbai 400076 (India)

20 March 2023

Dedicated to my family, teachers and country. . .

Acceptance Certificate

Department of Physics

Indian Institute of Technology, Bombay

The thesis entitled "Study of non-identical particle ($\pi^{\pm} - K^{\pm}$) femtoscopy in Pb–Pb collisions at $\sqrt{s_{\rm NN}}$ = 5.02 TeV with ALICE at the LHC" submitted by Pritam Chakraborty (Roll No. 174120004) may be accepted for being evaluated.

Sadhana Dash

Prof. Sadhana Dash

Date: 20 March 2023

Approval Sheet

This thesis entitled "Study of non-identical particle ($\pi^{\pm} - K^{\pm}$) femtoscopy in Pb–Pb collisions at $\sqrt{s_{NN}}$ = 5.02 TeV with ALICE at the LHC" by Pritam Chakraborty is approved for the degree of Doctor of Philosophy.

Pradip Sahu 20/3/23
(Prof. P.K. SAHU)

Asmita Khan

Examiners

Sadhana Dash

Supervisor (s)

Ranjan Kumar Pani

Chairman

Date: 20/03/2023

Place: MUMBAI

Declaration

I declare that this written submission represents my ideas in my own words and where others' ideas or words have been included, I have adequately cited and referenced the original sources. I declare that I have properly and accurately acknowledged all sources used in the production of this report. I also declare that I have adhered to all principles of academic honesty and integrity and have not misrepresented or fabricated or falsified any idea/data/fact/source in my submission. I understand that any violation of the above will be a cause for disciplinary action by the Institute and can also evoke penal action from the sources which have thus not been properly cited or from whom proper permission has not been taken when needed.

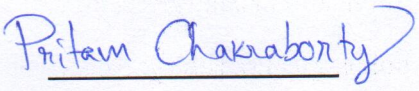

Pritam Chakraborty

(Roll No. 174120004)

Date: 20 March 2023

Abstract

The ALICE (A Large Ion Collider Experiment) detector at the Large Hadron Collider (LHC) experiment at CERN has been developed to study the hot-dense deconfined state of quarks and gluons, named Quark Gluon Plasma (QGP), which is expected to be created due to the collisions of heavy ions in the ultra-relativistic energies. It has not yet been possible to probe the QGP directly due to its extremely short life time and microscopic volume. However, a technique, called "Femtoscopy", has been developed to measure the space–time dimensions of the hot-dense medium using the momentum correlations of two identical or non-identical particles. The femtoscopic analysis of the correlation functions of charged pion-kaon pairs in 0−5% to 70−80% central Pb−Pb collisions at $\sqrt{s_{\mathrm{NN}}}$ = 5.02 TeV in ALICE experiment at the LHC is presented in this thesis. The spherical harmonics representations of the correlation functions (C_0^0 and ReC_1^1) were studied in different centrality bins. The obtained correlation functions were analysed after taking into account a precise treatment of the non-femtoscopic background. The size of particle-emitting source (R_{out}) and the emission asymmetry (μ_{out}) between pions and kaons were extracted from the background-minimised correlation functions. The R_{out} and μ_{out} were observed to increase from peripheral to central events as the number of participants increased. The μ_{out} was observed to be negative in all multiplicity classes, which indicates that pions are emitted closer to the center of the particle-emitting source than kaons, and this result is associated with the hydrodynamic evolution of the source. The results were compared with the predictions from THERMINATOR 2 model calculations where a set of additional delay in kaon-emission time were introduced to mimic the rescattering phase in the system. The values of μ_{out} were observed to lie between the predictions for 0 and 1 fm/c delay in kaon-emission time, indicating the presence of hadronic rescattering phase in the system along with

the collective flow. However, in case of $R_{\rm out}$, the predictions underestimated the results in high-multiplicity events. Moreover, no beam-energy dependence of the femtoscopic parameters was found upon comparing the results with previously performed pion-kaon femtoscopic analysis in Pb–Pb events at $\sqrt{s_{\rm NN}}$ = 2.76 TeV. The femtoscopic parameters were also studied as the function of pair-transverse momentum ($k_{\rm T}$) and pair-transverse mass ($m_{\rm T}$) in different centrality classes. The $R_{\rm out}$ was observed to decrease with increasing $k_{\rm T}$ and $m_{\rm T}$ of the pair, indicating the presence of strong collectivity in the system. This thesis also includes the first ever measurement of $R_{\rm out}$ and $\mu_{\rm out}$ for the charged pion-kaon pairs as a function of pair-transverse velocity ($\beta_{\rm T}$). The $R_{\rm out}$ decreased with increasing $\beta_{\rm T}$ of the pair due to the collective effects. The magnitude of $\mu_{\rm out}$ was observed to decrease with increasing $\beta_{\rm T}$ in the high-multiplicity events due to the possible dominance of collectivity over the thermal velocities of the particles, however, it did not follow the similar trend in low-multiplicity events. The predictions from THERMINATOR model underestimated the measured values of $\mu_{\rm out}$ in the lower $\beta_{\rm T}$ region, opening up the possibility to check for the resonance contribution in the lower $\beta_{\rm T}$ region. The values of $\mu_{\rm out}$ were observed to be more closer to the predictions with no additional delay in kaon emission, compared to an additional delay of 1 fm/c.

This thesis also reports the analysis of two-dimensional $\Delta\eta - \Delta\phi$ correlation functions of the charged-particle pairs in p–p collisions at $\sqrt{s}$ = 7 TeV and 13 TeV using PYTHIA 8.2 Monte Carlo event generator using color reconnection and rope hadronisation mechanisms. A ridge-like structure has earlier been observed in the long-range near-side region of the $\Delta\eta - \Delta\phi$ correlation functions for charged-particle pairs in heavy-ion collisions which is attributed to the presence of collective effects in the system. However, similar ridge-like structures have also been observed in the long-range near-side of $\Delta\eta - \Delta\phi$ correlation functions for charged-hadron pairs in high multiplicity p–p collisions as reported by the CMS and ATLAS experiments, where no QGP-like medium is expected to be formed. It is shown in this thesis that the color reconnection along with the rope hadronisation mechanism can mimic the features of collectivity and may produce the observed ridge-like structure in the long-range near-side region of $\Delta\eta - \Delta\phi$ correlation functions in high multiplicity p–p collisions without forming a hot-dense medium.

Table of Contents

List of Figures

List of Tables

Chapter 1

Introduction

1.1 The Standard Model

The Standard Model of particle physics deals with the elementary particles and interactions between them. It describes three of the four known fundamental interactions present in nature – electromagnetic, strong and weak. The gravitational interaction is still not unified with rest of the interactions. Physicists started developing this theory in the 1950s and the current formulation was established in the mid-1970s after the existence of quarks was experimentally confirmed in a series of deep-inelastic electron-nucleon scattering experiments. The information about the elementary particles along with the mediators of all three interactions is shown in Fig. 1.1.

According to the Standard Model, quarks and leptons are the fundamental particles. There are six flavors of quarks: up (u), down (d), charm (c), strange (s), top (t) and bottom (b). The up and down quarks have relatively lower masses and they are usually stable and abundant in nature. The rest of the heavier quarks can be found only in the cosmic rays and high energy collisions and they rapidly decay to up and down quarks. The quarks have fractional electric charge. The up, charm and top quarks have a charge of $+\frac{2}{3}$e while the down, strange and bottom quarks have a charge of $-\frac{1}{3}$e. Each quark has its antiquark with the opposite charge. The free quarks are not observed in nature (discussed in section 1.2.2), they combine to form composite particles, named "hadrons". The hadrons can be classified by the number of quark

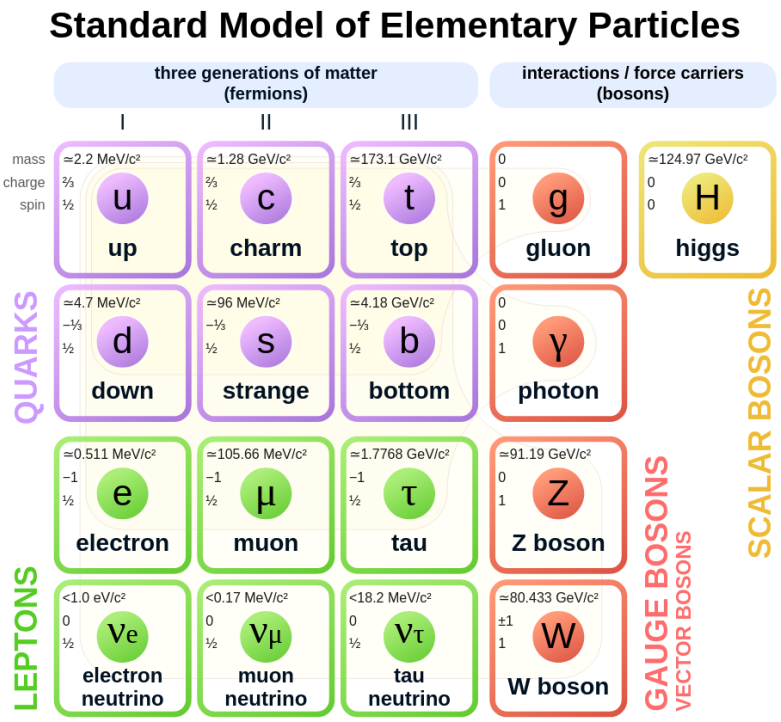

Figure 1.1: The standard model of fundamental particles [1].

content – "mesons" and "baryons". When a quark and antiquark pair up, they form a meson (pion, kaon) whereas three quarks (or antiquarks) combine to form a baryon (proton, neutron) (or antibaryons). The quarks interact with each other via strong, weak and electromagnetic interactions. There are also three types of leptons: electron (e), muon (μ) and tau (τ), and their corresponding neutrinos: ν_{e}, ν_{μ}, ν_{τ} with their anti-particles. Unlike quarks, leptons can exist as free particles. The e, μ and τ are electrically charged and they can interact with each other via both weak and electromagnetic interactions. The neutrinos are neutral particles and can only interact through weak interaction. The quarks and leptons are fermions as they have half-integer spin and obey Fermi-Dirac quantum statistics and Pauli's exclusion principle. However, the mesons have integer spin, hence they are bosons and follow Bose-Einstein statistics.

The Standard Model also consists of Gauge Bosons that mediate the fundamental interactions. The strong interaction is mediated via exchanging gluons, the weak interaction is mediated via $W^{\pm}$ and Z^{0} bosons and the electromagnetic interaction is mediated via photons. All of the gauge bosons are spin-one particles.

The Higgs boson, the latest discovered particle of the Standard Model, which is a scalar boson, is the mediator of interaction of the Higgs field with the massive particles. It was discovered by the CMS and ATLAS experiments at Large Hadron Collider (LHC) in the year 2012 [2, 3] and its mass was estimated to be around 126 GeV. Peter Higgs and François Englert were jointly awarded the Nobel Prize in Physics in 2013, for the theoretical prediction of this particle in 1964.

1.2 Quantum Chromodynamics (QCD)

Quantum Chromodynamics (QCD) is a subclass of the quantum field theory, formulated on the basis of non-abelian gauge theory obeying the SU(3) symmetry. It has been developed to describe the strong interaction between quarks via exchange of gluons and is an integral part of the Standard Model. QCD is analogous to the quantum electrodynamics (QED), which describes the interaction between charged particles via exchanging photons. The quarks consist of three types of color charges – red, green and blue. Here, "color" is a new type of quantum number that has been introduced to distinguish the quarks of same flavors. The total color is always conserved during the strong interaction but the color of individual quark may change which suggests that the gluons are color particles. This property makes QCD more complicated than QED because photons are electrically neutral and they cannot interact with other photons, however, the gluons can interact with other gluons while mediating the strong interaction.

The gauge invariant Lagrangian density for the strong interaction is given in Eq. (1.1) [4].

$$\mathcal{L}_{\mathrm{QCD}} = \overline{\psi}_u \left(i\gamma^\mu (D_\mu)_{uv} - m\delta_{uv} \right) \psi_v - \frac{1}{4} G^a_{\mu\nu} G^{a\mu\nu} \tag{1.1}$$

where, ψ_u is the quark field with color-index u, u and v vary from 1 to 3, γ^μs are the Dirac matrices, D_μ is the gauge covariant derivative, m is the quark mass and $G^a_{\mu\nu}$ is the gauge invariant gluon field strength tensor and it can be expressed as Eq. (1.2):

$$G^a_{\mu\nu} = \partial_\mu A^a_\nu - \partial_\nu A^a_\mu - g f_{abc} A^b_\mu A^c_\nu \tag{1.2}$$

where, A^a_μ is the gluon field and a varies from 1 to 8, f^{abc} denotes the structure constant of SU(3) group. D_μ can be expressed as Eq. (1.3):

$$\left(D_\mu\right)_{uv} = \partial_\mu \delta_{uv} + i g_s (\frac{\lambda_a}{2})_{uv} A^a_\mu \tag{1.3}$$

where, g_s is the strong coupling constant, λ_as are the eight Gell-Mann matrices.

Unlike QED, the coupling constant in QCD is not truly a constant, rather it depends on the momentum transfer (Q^2) during the interaction. The effective strong coupling constant (or referred as "running coupling constant") can be expressed as Eq. (1.4) [5]:

$$\alpha_s(Q^2) = \frac{g_s^2(Q^2)}{4\pi} = \frac{4\pi}{[(11/3)n_c - (2/3)n_f][ln(Q^2/\Lambda^2_{QCD})]}, \tag{1.4}$$

where, n_c is the number of colors, n_f is the number of quark flavors and Λ_{QCD} is the dimensional QCD scale parameter. The estimated value of α_s for the mass of Z^0 boson is 0.118 ± 0.002 and hence, the scale constant $\Lambda_{QCD} = 217^{+25}_{-23}$ MeV [6]. The $\alpha_s(Q^2)$ as the function of Q from various measurements is shown in Fig. 1.2 where, α_s decreases with increasing Q.

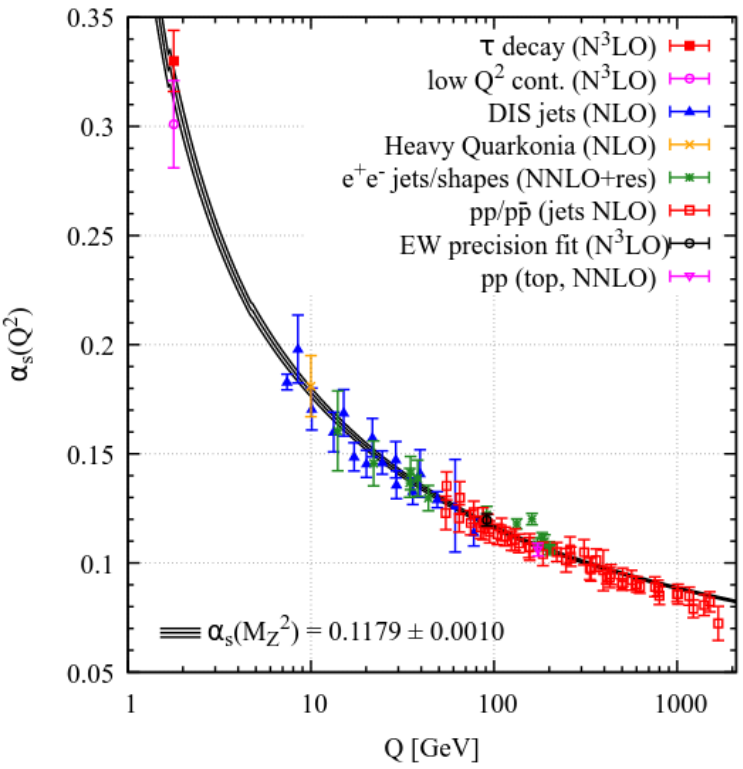

Figure 1.2: The measurement of $\alpha_s(Q^2)$, as a function of momentum transfer Q [6].

The two important properties of QCD are asymptotic freedom and color confinement which are described below:

1.2.1 Asymptotic freedom

It is clear from Fig. 1.2 that the strength of strong interaction becomes weaker at higher energy scale. This property is called asymptotic freedom and it allows the application of perturbative QCD calculations in high energy experiments. David Gross, Frank Wilczek and David Politzer discovered this property in 1974 [7, 8] and won the Nobel Prize in Physics in 2004.

1.2.2 Color confinement

The Color confinement is a property of QCD which suggests that color-charged particles i.e. quarks and gluons cannot be observed independently in nature. They are found as bound objects in nature such as hadrons, which are color-singlet objects. The potential between a quark and antiquark pair is given in Eq. (1.5):

$$V \approx -\frac{\alpha_s}{r} + kr, \tag{1.5}$$

where, r is the separation between the particles and k is the coefficient of the linear term. The $q\bar{q}$ pair inside a hadron can be visualised as two particles attached with a color string. As the separation between those quarks increases, the energy of the string also increases. At a certain point, the energy of the string becomes so high that it breaks and creates a new $q\bar{q}$ pair. Due to this property of QCD, no quarks or gluons can be observed freely in natural conditions. The coupling strength becomes very high at the lower energy scale and the perturbative nature of the QCD breaks down.

1.3 Quark Gluon Plasma (QGP)

When the energy density and temperature in a hadronic system reach ≈ 0.7 GeV/fm^3 and 170 MeV [9], respectively, the Lattice QCD calculations predict a phase transition of quarks and

gluons from the confined hadronic state to a deconfined one. This deconfined state of quarks and gluons is called "Quark Gluon Plasma (QGP)" [10]. The QGP state can be formed by heating and compressing the hadronic matter to an extreme level. It is observed that the QGP is a strongly-coupled hydrodynamic system and behaves almost like a perfect fluid with nearly zero viscosity. It consists of the color-charged particles (quarks and gluons) that can propagate freely inside the nuclear radius.

The cosmological calculations suggest that the universe was created due to the Big Bang, which happened 13 billion years ago. In its early stage, the universe was believed to be in a hot and dense QGP phase of matter [11, 12]. As time passed by, the universe expanded and its temperature gradually decreased. Hence, the energy density became lower, resulting in the confinement of quarks into the hadronic states i.e. protons, neutrons etc. Eventually the nuclei, atoms, molecules etc. were formed upon further expansion of the universe.

The state of Quark-Gluon Plasma, obtained in ultra relativistic collisions carries the signatures of early stages of the universe. Therefore, studying the evolution of QGP and probing its properties can shed more light on the fundamental interactions and tell us more about how our universe has evolved from the primordial state. There are two ways to create a minor version of the Big Bang in laboratory by colliding heavy ions e.g. Lead (Pb), Gold (Au). The first way is to compress the nuclear matter to very high densities, $\rho = 10\rho_0$ ($\rho_0 = 0.17$ nucleons/fm^3) [13] so that the quarks and gluons inside the nucleons get deconfined and QGP phase is produced. This technique has been used in fixed target Super Proton Synchrotron (SPS) experiment at CERN with Pb–Pb events at $\sqrt{s_{\mathrm{NN}}} = 17.3$ GeV, where an indication of QGP has been found [14]. The future fixed-target experiment, CBM at FAIR facility also plans to observe the properties of the QGP. Another way to create the QGP is by heating up the hadronic matter more than the critical temperature. The ALICE experiment at LHC, CERN and RHIC experiment at BNL are executing this technique by colliding heavy ions at the ultra-relativistic energies, which is discussed in section 1.5. However, it is estimated that the QGP state of early universe lasted for ~ 1 ns, whereas lifetime of the one created in laboratory is roughly 10^{-23} seconds [15].

1.4 QCD phase transition

The deconfined state of quarks and gluons cannot be described by the perturbative QCD. The transition from hadronic state to deconfined QGP state can be understood using the Lattice QCD, the most successful non-perturbative approach of QCD, which was developed by considering space-time lattice points. To investigate the phase transition, the QGP is considered to be in a state of thermal and chemical equilibrium. Hence, by assuming the QGP to be a grand-canonical ensemble with baryon-chemical potential (μ_{B}) to be zero (the minimum energy required to add or remove a baryon at fixed temperature and pressure), the hadronic and QGP energy densities are estimated as given in Eq. (1.6) and Eq. (1.7) [14, 16], respectively.

$$\frac{\epsilon_{\mathrm{h}}}{T^4} = \frac{\pi^2}{10} \tag{1.6}$$

$$\frac{\epsilon_{\mathrm{QGP}}}{T^4} = (32 + 21N_{\mathrm{f}})\frac{\pi^2}{60} \tag{1.7}$$

where, N_{f} is the number of flavors. From the above equations, it is evident that energy density of QGP is much higher than the hadronic state. The critical temperature (T_c) of the phase transition for 2-flavor (u, d), 3-flavor (u, d, s are considered as light quarks) and 2+1-flavor (u, d are considered as light quarks and s is considered as heavy quark) QCD have been estimated to be 171±4 MeV, 154±8 MeV and 173±8 MeV, respectively [16]. The energy densities (ϵ/T^4) estimated from lattice QCD calculations are shown as a function of T/T_c in Fig. 1.3, where it is observed that the energy density increases abruptly around T_c and eventually gets saturated at $\sim 2T_c$ for all three considered cases. This observation indicates that the number of degrees of freedom increases as the temperature gets higher than T_c. Since the quarks and gluons remain confined in a hadronic state, the number of degrees of freedom in the hadronic matter is less than the QGP state. Hence, it is evident from Fig. 1.3, that there is a possible phase transition to QGP state around the T_c. Another important observation is that the energy density is always less than the Stefan-Boltzmann limit ($\epsilon_{\mathrm{SB}}/T^4$) irrespective of the flavors of QCD, which suggests that the QGP is not an ideal fluid, rather the quarks and gluons inside the QGP are coupled.

The QCD phase diagram of the strongly interacting matter as the function of temperature and baryon chemical potential is shown in Fig. 1.4. It is observed that the nuclear matter is found

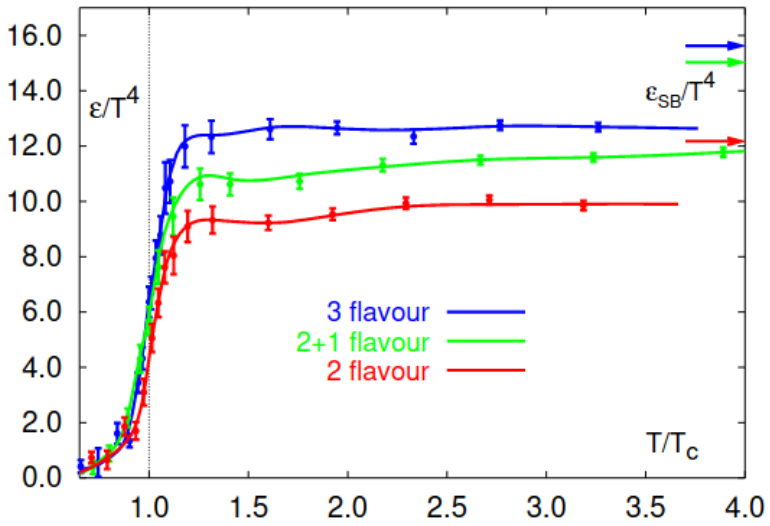

Figure 1.3: The energy density (ϵ/T^4) estimated from the lattice QCD calculations as a function of T/T_c [16].

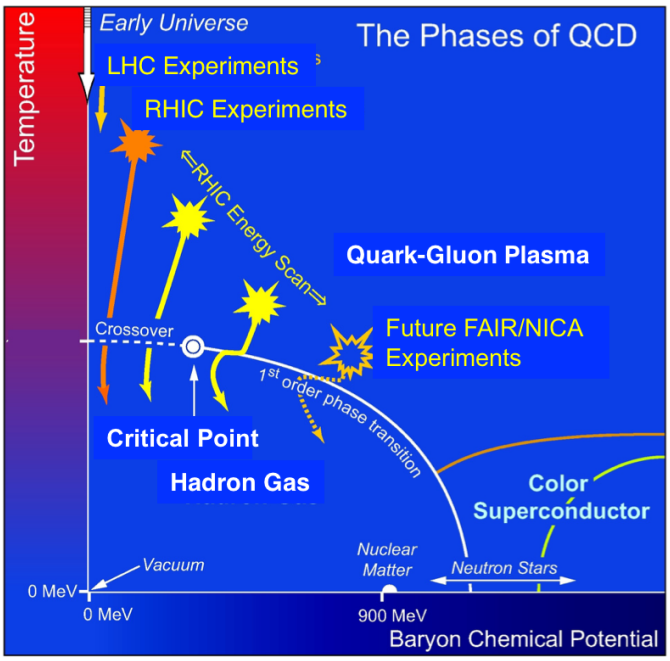

Figure 1.4: The QCD phase diagram of the strongly interacting matter [17].

around $\mu_B \approx 900$ MeV and nearly zero temperature. The neutron stars, which are made of cold dense matter are expected to be found in the higher chemical potential and lower temperature region. At much higher chemical potential and slightly higher temperature region, the quarks form a condensed state, namely "Color Superconductor", where the chiral symmetry breaks

down. The QGP phase is expected to be found at higher temperature and the hadronic state is expected to be found at relatively lower temperature and chemical potential region. The phase transition between the QGP and hadron gas is expected to be of first order. Interestingly, as the chemical potential decreases and temperature increases, the transition between hadron gas and QGP state becomes a smooth crossover (pointed out as dashed-line). The point where the first-order phase transition stops and smooth crossover begins is called the "critical point". The search for the critical point has been one of the major goals of the experiments at LHC and RHIC.

1.5 Relativistic heavy-ion collisions: The Bjorken scenario

The relativistic heavy-ion collisions have been modeled using various hypotheses e.g. Landau model, Fermi statistical model etc. among which the model given by J. D. Bjorken [18] is widely used. In Fig. 1.5, the Bjorken scenario of heavy-ion collision is depicted. The Bjorken model is based on following assumptions:

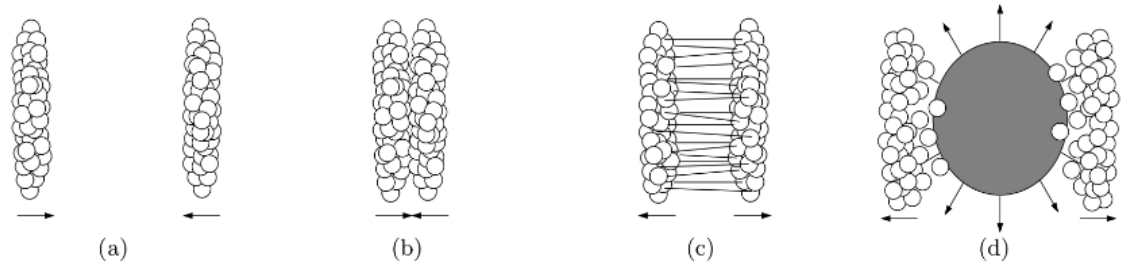

Figure 1.5: The Bjorken scenario of heavy-ion collision [15].

- **Transparency:** The collisions are assumed to be transparent in the mid-rapidity region and the net-baryon density in that region should be zero.
- **Boost invariance:** It is assumed that the number of produced particles in unit rapidity is constant around the mid-rapidity region, which suggests that the fireball created in the collisions is homogeneous and all of its layers expand symmetrically with respect to the rapidity with longitudinal flow velocity, $\beta = z/t$. The proper time of each stage of the space–time evolution of the fire-ball is $\tau = t/\gamma = t\sqrt{1-\beta^2} = \sqrt{t^2 - z^2}$.

- **Hydrodynamic phase:** The expanding fire ball attains the thermal equilibrium at t≈1 fm/c and its dynamics can be described by the relativistic hydrodynamics calculations.

For the central collisions where the nuclei collide with each other head-on, the expansion of the fireball along the transverse direction can be disregarded for a time $t \approx R/c$, where R is the radius of a nucleon. Hence, the evolution of system can be represented as the function of (z,t), as shown in Fig. 1.6. The time axis in Fig. 1.6 corresponds to the proper time as described earlier. This space-time evolution of the system happens in the following stages:

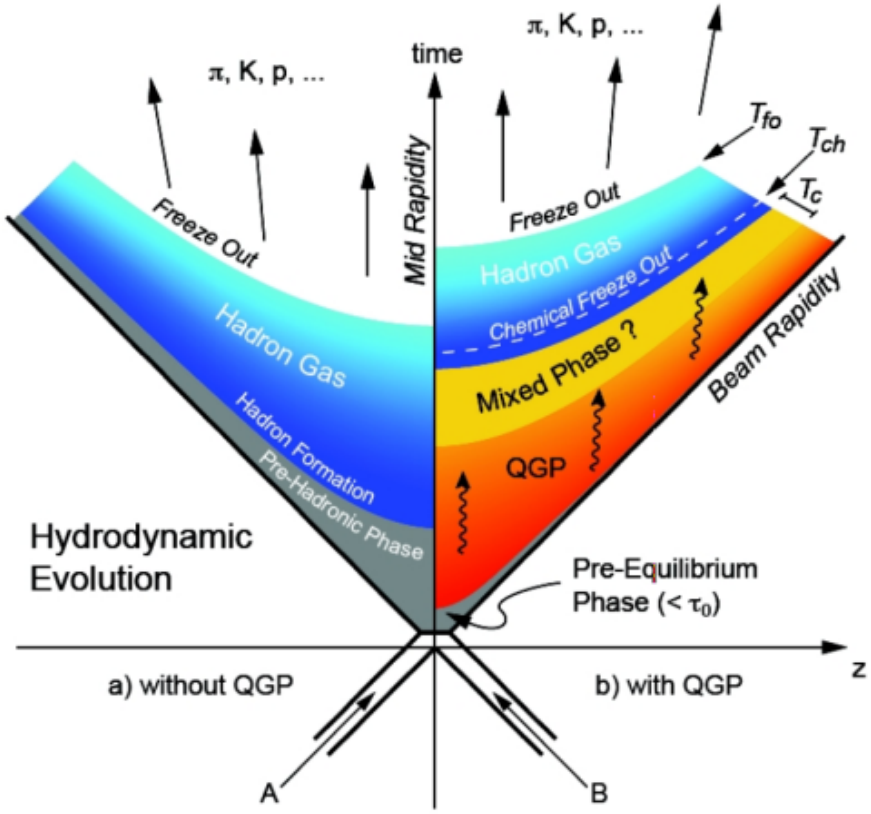

Figure 1.6: The space–time diagram of the system created in heavy-ion collision [19].

1. **Pre-equilibrium**: This stage exists just after the collision i.e. from τ = 0 to 1-2 fm/c. In this stage, the partons interact among themselves multiple times creating more partons. The particles with high momentum (p_{T} >> 1 GeV/c) are also produced in this stage via hard-particle production. Numerous real and virtual photons are also produced, among which the virtual photons produce leptons and antileptons.

2. **Quark-Gluon plasma and thermalisation**: If the energy density of the fireball is very high, i.e. $\epsilon \approx 0.4 - 1.0$ GeV/fm^3, the QGP is formed (Fig. 1.6), where the produced partons scatter among themselves and eventually, the thermal equilibrium is reached. The QGP stage exists roughly from 1-2$< \tau <$ 6 fm/c. Due to the presence of pressure gradient, the thermalised medium starts to expand. The properties of the expanding medium can be described by the hydrodynamical calculations.

3. **Mixed phase - Hadron gas:** As the system expands, its temperature gets lower and the quarks and gluons start to hadronise and the system enters a mixed phase. The time taken by all the quarks and gluons to get hadronised and produce a system of hadron gas is 6$< \tau <$10 fm/c.

4. **Freeze-out:** The temperature of the expanding system gradually decreases. Below a certain temperature, the inelastic collisions among the hadrons stops and the number of hadrons present in the system gets fixed. This is called "chemical freeze out". As the system further expands, the relative separations between the hadrons increase and after a certain time, the elastic collisions among them also stop, which is called "kinetic freeze out" and the hydrodynamic description of the medium breaks down.

However, if the energy density of the produced system is not high enough and the temperature is lower than the critical temperature, the deconfined state of quarks and gluons i.e. the QGP is not formed (Fig. 1.6) and the system goes through the pre-hadronic phase. Eventually the hadrons are produced and detected after the freeze out.

1.6 Signatures of Quark Gluon Plasma

It has not been possible so far to directly probe the QGP state. The detectors can record only the particles that are emitted after the system attains kinetic freeze-out and any information on the early stages of the system after the collision is not directly accessible. Hence, some observables or properties of the detected particles are utilised as the indirect probes to verify the

formation of QGP and examine its properties. These signatures of QGP can be classified into two groups, "hard" and "soft", based on the timeline of particle production at different stages of the collision. The hard probes correspond to the particles created in the initial stages of the collision due to the hard scattering of partons e.g. jets, direct photons, heavy-flavor particles. Some of the hard probes that have been discussed in this section are nuclear modification factor, jet quenching, quarkonium suppression and direct photons. Soft probes correspond to the effects of bulk properties of the thermalised medium e.g. anisotropic flow, strangeness enhancement etc.

1.6.1 Nuclear modification factor

One of the interesting strategies to understand the effect of QGP medium is to study the nuclear modification factor, R_{AA}, which is the ratio between the differential yield of charged particles per event in nucleus-nucleus (A−A) collisions and p–p collisions, scaled over the average number of binary nucleon-nucleon collisions ($<N_{\mathrm{coll}}>$). It can be defined as Eq. (1.8).

$$R_{\mathrm{AA}}(p_{\mathrm{T}}) = \frac{1}{< N_{\mathrm{coll}} >} \frac{N_{\mathrm{evt}}^{\mathrm{pp}}}{N_{\mathrm{evt}}^{\mathrm{AA}}} \frac{\mathrm{d}^2 N_{\mathrm{ch}}^{\mathrm{AA}}/\mathrm{d}\eta \mathrm{d}p_{\mathrm{T}}}{\mathrm{d}^2 N_{\mathrm{ch}}^{\mathrm{pp}}/\mathrm{d}\eta \mathrm{d}p_{\mathrm{T}}} \tag{1.8}$$

Here, p_{T} is the transverse momentum of the particle. The particles produced in a strongly interacting QCD medium go through multiple elastic and inelastic collisions and therefore, their energies gradually decrease and the yields are supposed to be suppressed in the high p_{T} region. The R_{AA} should be less than unity when the QCD medium is formed, whereas it should be close to unity in the absence of a hot dense medium.

The R_{AA} as a function of p_{T} for charged hadrons ($\mathrm{h}^{\pm}$), γ, $\mathrm{W}^{\pm}$ and Z^0 for the central Pb–Pb collisions at $\sqrt{s_{\mathrm{NN}}}$ =2.76 TeV (R_{PbPb}) and $\mathrm{h}^{\pm}$ for p–Pb at $\sqrt{s_{\mathrm{NN}}}$ =5.02 TeV (R_{pPb}) with ALICE and CMS experiments at LHC is shown in the upper panel of Fig. 1.7 [20]. A clear suppression is observed for charged hadrons, produced in Pb–Pb collisions while the yields of W, Z bosons and photons are not suppressed because they interact electromagnetically. The charged hadrons produced in p–Pb collisions are also not suppressed. These two observations can be attributed to the creation of QGP medium in the heavy-ion collisions. In the bottom panel of Fig. 1.7,

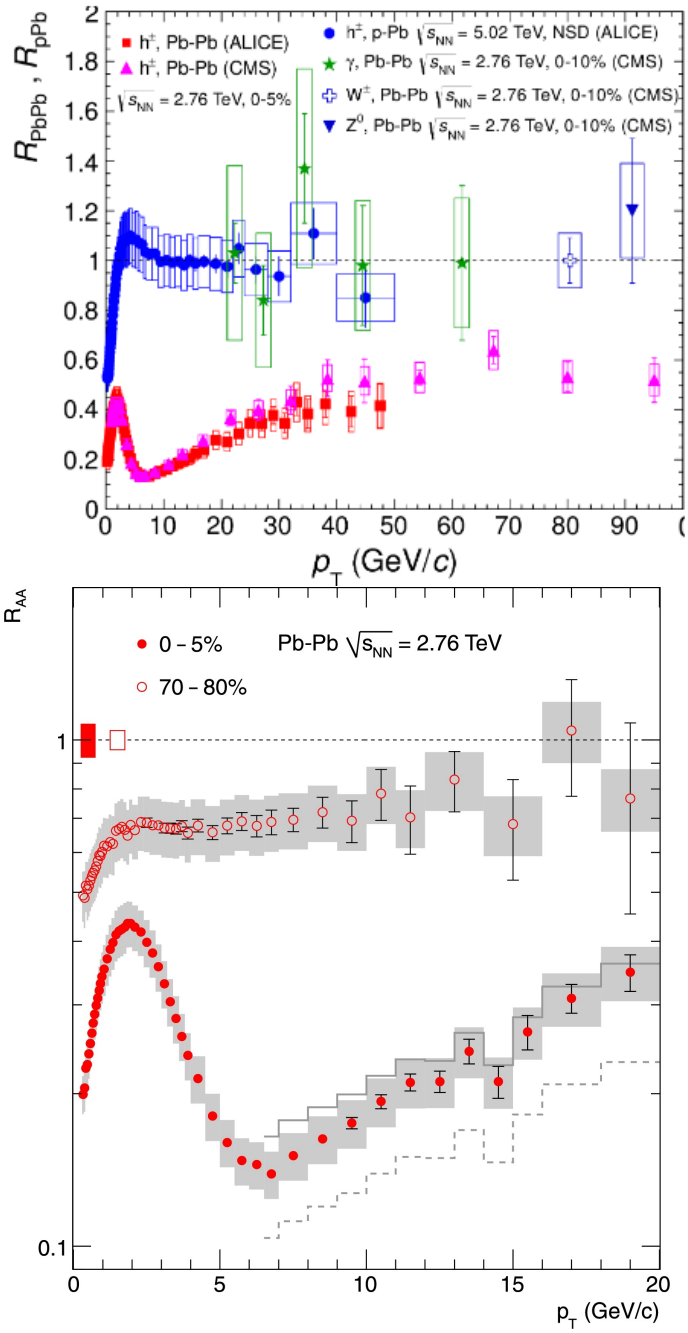

Figure 1.7: Upper panel: The R_{AA} of charged hadrons, γ, $W^{\pm}$ and Z^0 as a function of p_T for the central Pb–Pb collisions at $\sqrt{s_{NN}}$ =2.76 TeV and $h^{\pm}$ for p–Pb at $\sqrt{s_{NN}}$ =5.02 TeV. Bottom panel: The R_{AA} as a function of p_T in the central (0−5%) and peripheral (70−80%) Pb–Pb collisions at $\sqrt{s_{NN}}$ = 2.76 TeV in ALICE [20, 21].

the R_{AA} for charged hadrons produced in the central (0−5%) and peripheral (70−80%) Pb–Pb collisions at $\sqrt{s_{NN}}$ =2.76 TeV [21] is shown as the function of p_T, where it is observed that the

hadrons produced in the central collisions are more suppressed than the ones produced in the peripheral collisions. This suggests that the partons created in the central collisions lose more energy compared to the peripheral ones as they scatter through a more dense and large medium.

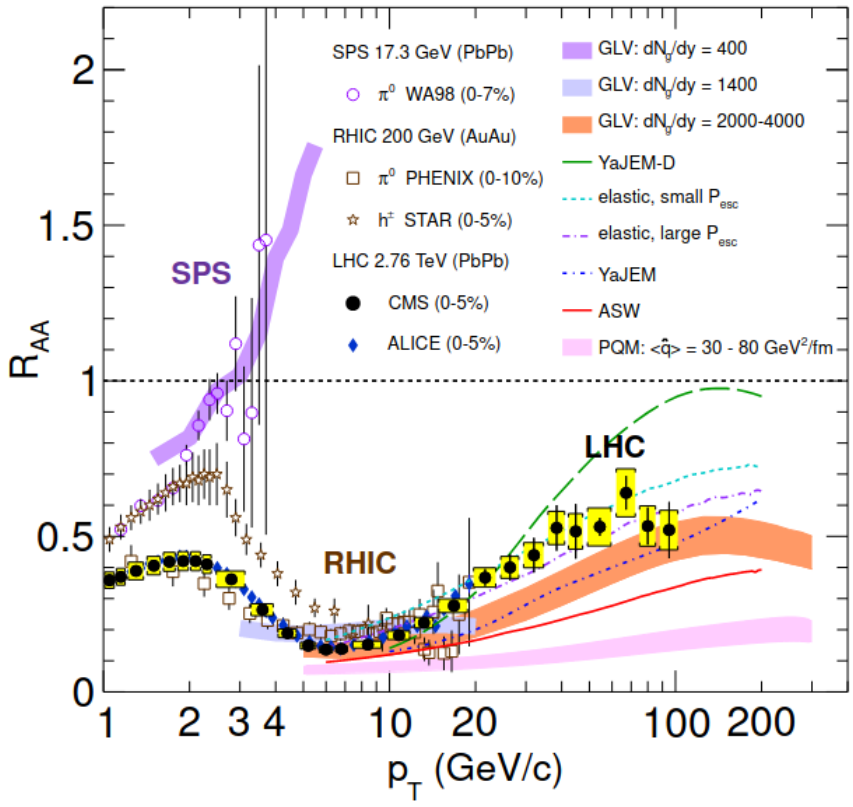

Figure 1.8: The R_{AA} as a function of p_T for the neutral pions (π^0) and charged hadrons ($h^{\pm}$) in the most central heavy-ion collisions at three energies in SPS. RHIC and LHC, compared with various theoretical predictions, such as Parton Quenching Model (PQM), Gyulassy−Levai−Vitev (GLV) approach using pQCD, Armesto-Salgado-Wiedemann (ASW) formalism, Yet another Jet Energy-loss Model (YaJEM), YaJEM-D and Parametrized elastic energy loss [22].

Fig. 1.8 shows the variation of R_{AA} as a function of p_T for the most central Pb–Pb and Au–Au collisions at three different energies at SPS, RHIC and LHC. The uncertainty in R_{AA} corresponding to SPS increases with increasing p_T. At RHIC and LHC energies, the R_{AA} is observed to be suppressed at $p_T > 2$ GeV/c and attains the minimum value around $p_T \sim 6-7$ GeV/c. Moreover, the strength of suppression is higher in the LHC energies than that of RHIC energies. The high-p_T region can be probed utilising the Pb–Pb collisions at LHC energies, which shows that the suppression decreases i.e. R_{AA} gradually increases at $p_T > 8$ GeV/c,

however, it always remains less than one. This suggests that even the particles with very high p_T rescatter through the hot-dense medium and lose energy before finally being detected.

1.6.2 Jet quenching

Jets are the collimated spray of particles which are created by the fragmentation of final state partons, produced from the hard scattering of partons at the initial stage of heavy-ion or hadronic collision. When the jets carrying high momenta traverse through a hot dense QCD matter, they lose energy by radiating gluons. These gluons finally produce hadrons with significantly lower momenta. This process is called "Jet quenching". The jet quenching is studied by two-particle correlation function for charged hadrons as a function of the difference in azimuthal angle ($\Delta\phi$) of a high momentum "trigger" particle and a relatively low momentum "associated" particle. The two-particle azimuthal correlation function for charged hadrons, produced in hadronic collisions is elaborated in chapter 6. $\Delta\phi \sim 0$ corresponds to those jets that move in the same direction and leave the system earlier, whereas $\Delta\phi \sim \pi$ corresponds to back-to-back jets, where the associated particles move in the direction opposite to the leading particle i.e. through the medium and eventually get quenched.

The two-particle azimuthal correlation function for charged hadrons, produced in the minimum bias p–p, 0-20% central and minimum bias d–Au collisions at $\sqrt{s_{NN}} = 200$ GeV at STAR experiment are shown in the upper panel of Fig. 1.9, where the distributions are observed to be similar in the near-side ($\Delta\phi = 0$) and away-side ($\Delta\phi = \pi$) regions for all three collision systems although the correlation functions for d–Au are associated with constant pedestals. The pedestal minimised azimuthal correlation function for charged hadrons produced in the minimum bias p–p, 0-20% central d–Au and central Au–Au collisions are shown in the bottom panel of Fig. 1.9, where the away-side distribution for the central Au–Au collisions is distinctively suppressed. This observation suggests that a hot dense QGP medium of finite volume is created in the central Au–Au collision and is not expected to be produced in the p–p and central d–Au collisions.

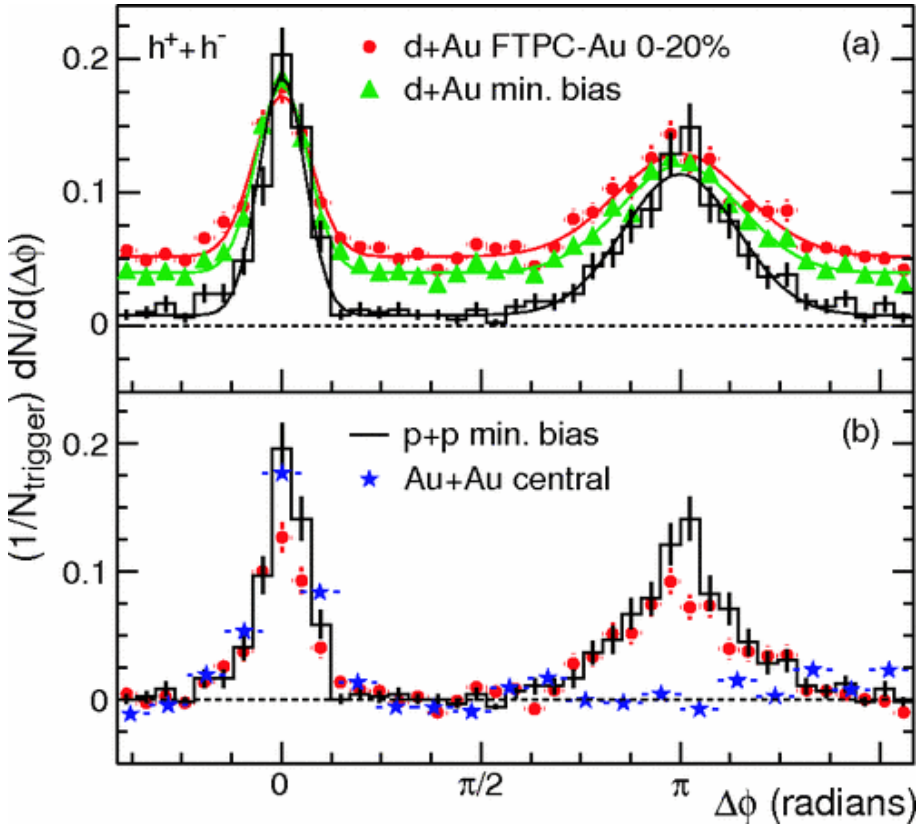

Figure 1.9: The two-particle azimuthal correlation function in p–p, d–Au and Au–Au collision in STAR [23].

1.6.3 Quarkonium suppression

Quarkonium is a mesonic bound state, formed of heavy quark−antiquark pairs. Charmonium, made of $c\bar{c}$ bound state, known as J/ψ and bottomium, made of $b\bar{b}$ bound state, known as Υ are the two available flavors of Quarkonium state. Inside a QGP medium, the color field of a moving color-charge carrier is screened extensively as the matter density inside the medium is very high. This effect is similar to the Debye screening of electric-charge carriers. If the screening length becomes shorter than the binding range of the quark−antiquark pairs, the bound Quarkonium state ceases to exist. Hence, the constituent quarks and antiquarks of a Quarkonium state, pair with other quarks or antiquarks e.g. c and $\bar{c}$, and form open charm mesons such as D($c\bar{u}$ and $c\bar{d}$), $\bar{\text{D}}$($\bar{c}u$ and $\bar{c}d$), D_s($c\bar{s}$) and $\bar{\text{D}}_\text{s}$($\bar{c}s$). Hence, the suppression of yield of the Quarkonium state is a signature of QGP formation. The nuclear modification factor for J/ψ and Υ states in Pb–Pb collisions at $\sqrt{s_{\text{NN}}}$ = 2.76 TeV with ALICE are shown in the left and right

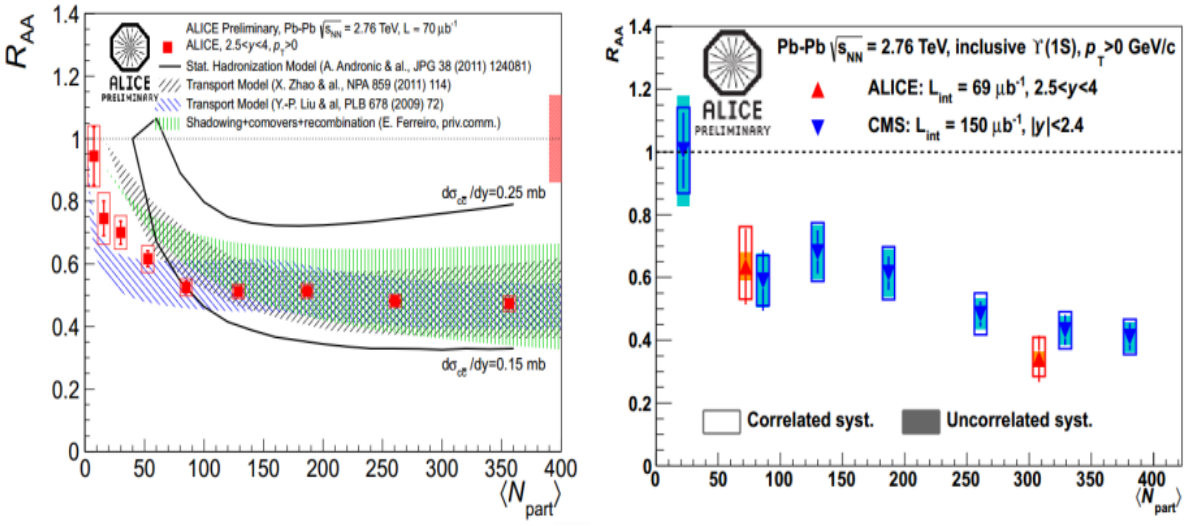

Figure 1.10: The R_{AA} as a function of $<N_{part}>$ of J/ψ (left panel) and Υ (right panel) in Pb–Pb collisions at $\sqrt{s_{NN}}$ = 2.76 TeV in ALICE [24].

panels, respectively of Fig. 1.10. A clear suppression in the R_{AA} of both states can be observed as the $< N_{part} >$ increases, which suggests the production of hot and dense QGP medium due to the heavy-ion collisions.

1.6.4 Direct photons

One of the useful techniques to estimate the properties of QGP is to measure the direct photons produced in heavy-ion collisions. The direct photons can be classified into two groups – prompt and thermal. The prompt photons are produced at the initial stage of the collisions through the hard scattering of partons, quark-antiquark pair annihilation, Compton scattering of quarks and gluons, jet fragmentation etc. The thermal photons are produced from the hard scattering of partons with the thermalised partons. The thermalised partons are also scattered inside the QGP medium and give rise to the thermal photons [25]. The thermalised photons mostly carry lower transverse momenta. The invariant yield of direct photons measured in 0–40% central Pb–Pb collisions at $\sqrt{s_{NN}}$ = 2.76 TeV with ALICE[25] is shown in Fig. 1.11. The NLO-calculation for direct photons produced in p–p collisions at $\sqrt{s}$ = 2.76 TeV, scaled with the average number of binary collisions, is also shown. The yield in lower p_T region is fitted with an exponential function ($e^{(-p_T/T)}$). The temperature of the thermalised medium is

estimated to be $T = 304 \pm 11 \pm 40$ MeV, which is much greater than the estimated critical temperature of QGP formation: T_c ~155−175 MeV.

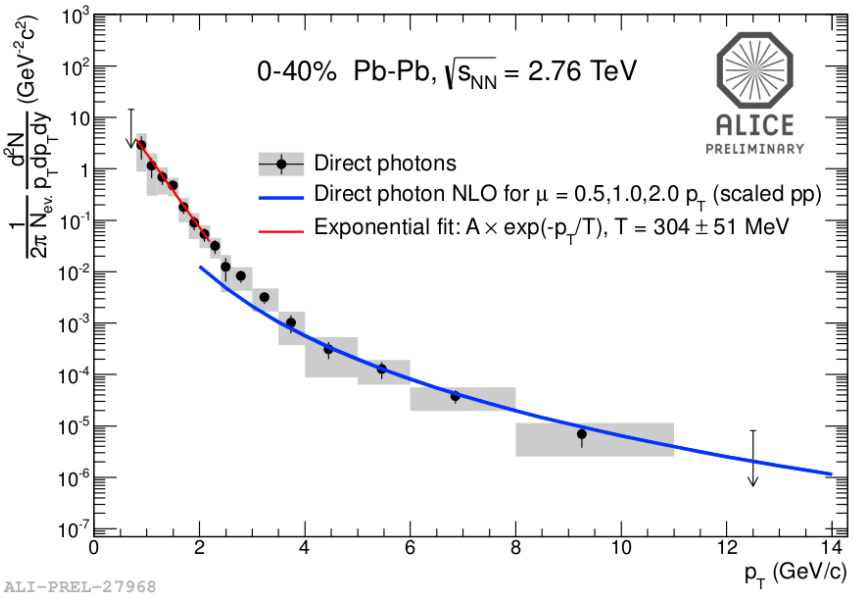

Figure 1.11: The invariant yield of direct photons measured in 0−40% central Pb–Pb collisions at $\sqrt{s_{NN}}$ = 2.76 TeV in ALICE [25].

1.6.5 Anisotropic flow

One of the major experimental evidences towards the creation of QGP as a strongly coupled deconfined state of quarks and gluons in heavy-ion collisions is the observation of anisotropic flow. The medium produced in the relativistic heavy-ion collision expands hydrodynamically due to the presence of high pressure gradient. In case of a non-central collision of two heavy nuclei (when the impact parameter between the nuclei is not zero), the shape of the overlapping region resembles an almond, suggesting a spatial anisotropy. This anisotropy creates a pressure gradient along the transverse direction. The invariant particle distribution can be expressed in terms of the Fourier decomposition of the azimuthal distribution of the particle as given in Eq. (1.9)[26].

$$E\frac{\mathrm{d}^3N}{\mathrm{d}p^3} = \frac{1}{2\pi}\frac{\mathrm{d}^2N}{p_\mathrm{T}\mathrm{d}p_\mathrm{T}\mathrm{d}y}\left(1 + 2\sum_{n=1}^{\infty} v_n \cos[n(\phi - \Psi_n)]\right) \tag{1.9}$$

where, E is the energy, p is the momentum, $p_T = \sqrt{p_x^2 + p_y^2}$ is the transverse momentum, $y = \frac{1}{2} ln \frac{E+p_z}{E-p_z}$ is the rapidity, ϕ is the azimuthal angle of the particle, Ψ is the reaction plane and v_n corresponds to the azimuthal anisotropy of n^{th} order and can be estimated using the following term: $v_n =< \cos(n(\phi - \Psi_n)) >$. The first term in the right hand side of Eq, (1.9) corresponds to the isotropic radial flow, v_1 corresponds to the directed flow, v_2 to the elliptic flow, v_3 to the triangular flow and so on. If the particles are scattered inside the medium multiple times, the system is expected to attain a thermal equilibrium and the pressure gradient inside the spatially anisotropic region eventually creates an anisotropy in the momentum of the final state particles, which pushes more particles towards the low pressure regions. Thus a positive v_2 can be observed for the particles produced in a strongly coupled dense medium. As v_2 is developed during the early stages of the collision due to the spatial anisotropy, it gradually saturates as the system expands and anisotropy decreases. Hence, v_2 can also be utilised to probe the early stages of the collision.

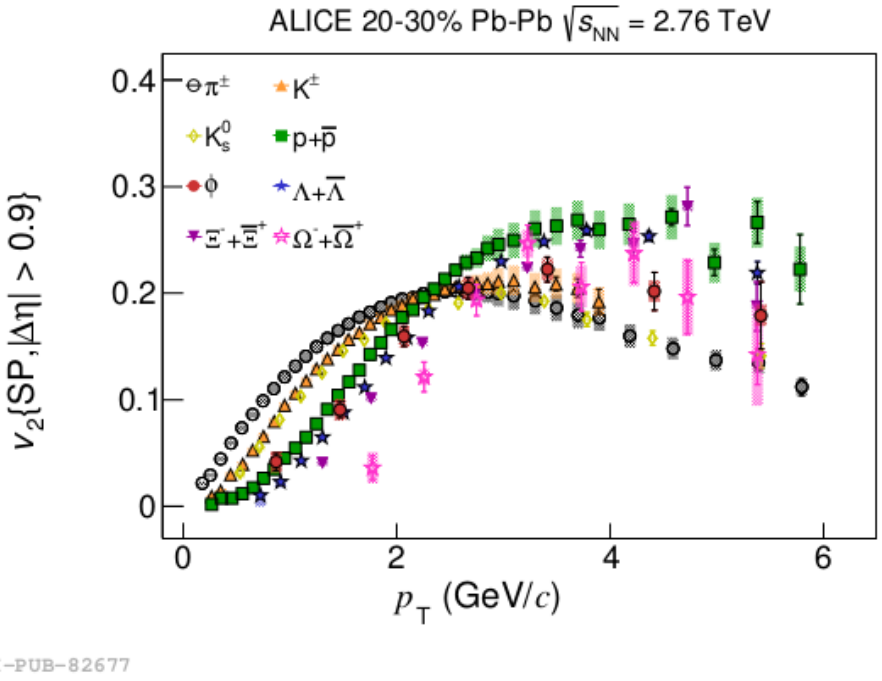

Figure 1.12: The v_2 as a function of p_T for identified particles in 20−30% central Pb–Pb collisions at $\sqrt{s_{NN}}$ =2.76 TeV in ALICE [27, 28].

The v_2 for $\pi^{\pm}$, $K^{\pm}$, K^0_s, p, ϕ, Λ, Ξ and Ω as a function of p_T in 20-30% central Pb–Pb collisions at $\sqrt{s_{NN}}$ =2.76 TeV with ALICE is shown in Fig. 1.12 [27, 28] which indicates the creation of strongly interacting QCD matter. A clear mass ordering in the v_2 can be observed in the lower p_T region. This is due to the fact that the radial flow gives equal velocity boost to all the particles, which moves the heavier particles to higher p_T region. As a result, the lower p_T region lacks heavier particles and hence, the v_2 of heavier particles are much lower in the lower p_T region.

It is observed that v_2 increases with p_T upto ~ 3 GeV/c for all the particles until it saturates and starts decreasing. The suppression in v_2 in the higher p_T region suggests that the thermal equilibrium does not hold anymore and the particles decouple from the QGP medium.

1.6.6 Strangeness enhancement

The phenomenon of strangeness enhancement is one of the important indications of QGP production in heavy-ion collisions [29–31]. Since the strange quarks are absent in the colliding nuclei, it is evident that the strange quarks are produced in the highly dense QCD matter via strong interaction after the thermal equilibrium is achieved. The $s\bar{s}$ pairs are mostly produced by the fusion of gluons. As the density of gluons is very high in the QGP medium, a large number of strange particles are produced in heavy-ion collisions compared to the hadronic collisions. Quark annihilation inside the QGP medium can also produce strange quarks.

Moreover, the strange-particle production is also enhanced by the "Pauli Blocking" of u and d quarks inside the dense QGP state. In the QGP medium, the lower Fermi energy levels get populated with lots of u and d quarks, which eventually makes the Fermi energy higher than the mass of $s\bar{s}$ pair. This leads to the enhancement of the number of $s\bar{s}$ pairs compared to $u\bar{u}$ or $d\bar{d}$ pairs. The $\bar{s}$ then forms a pair with u or d quark and produces $K^+(u\bar{s})$ or $K^0(d\bar{s})$ particle. On the other hand, s quark can unite with u and d to form Λ(uds) baryon.

The strangeness enhancement is studied in terms of the production of $\Xi^{\pm}$ and $\Omega^{\pm}$ as the function of mean number of participants ($< N_{part} >$) for Pb–Pb collisions at $\sqrt{s_{NN}}$ = 2.76 TeV with ALICE. The results from ALICE experiment is compared with the observations from p–Pb

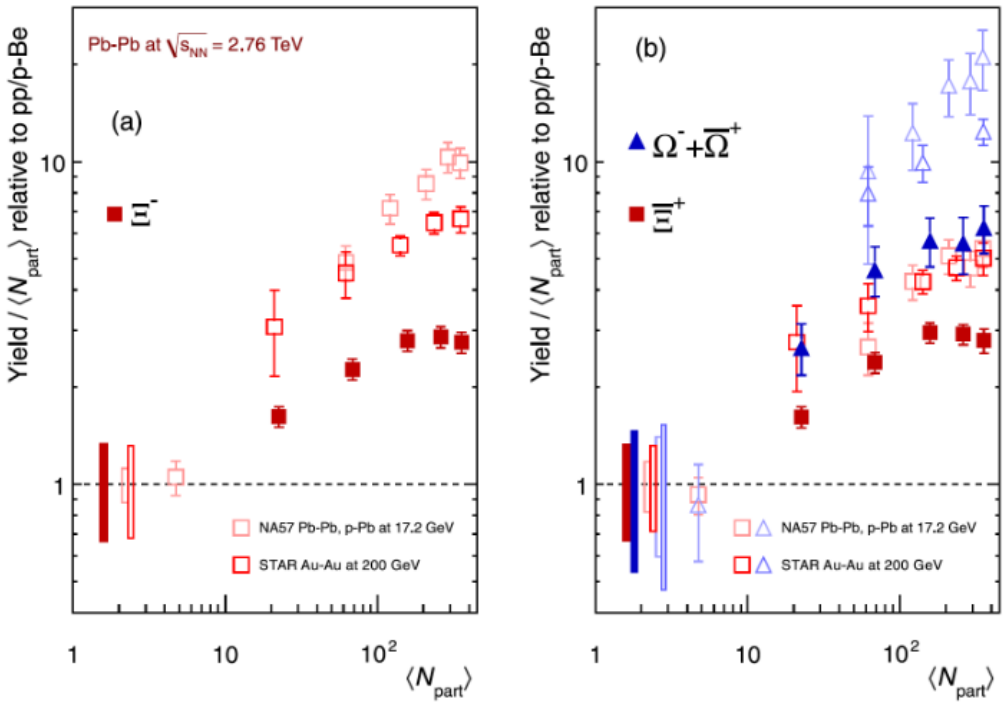

Figure 1.13: The strangeness enhancement as a function of mean number of participants (< N_{part} >) in ALICE at the LHC (solid symbols) with the RHIC and SPS results (open circle) [32].

and Pb–Pb collisions at $\sqrt{s_{\text{NN}}}$ = 17.2 GeV with NA57 and Au–Au collisions at $\sqrt{s_{\text{NN}}}$ = 200 GeV with STAR experiments, as shown in Fig. 1.13. The results from all the three experiments show that the particles containing large number of strange quarks are more enhanced compared to the particles with smaller number of strange quarks which suggests that the QGP contains a large number of $s\bar{s}$ pairs.

1.7 Femtoscopy

The thermalised medium created in heavy-ion collisions has very small size (few units in fm) and exists for a very short period of time ($\sim 10^{-23}$ second). Therefore, it has not yet been possible to directly measure the size of the fireball. However, a technique based on the particle interferometry, called “Femtoscopy”, has been developed to estimate the space-time dimension of the hot-dense medium, created in heavy-ion collisions using the two-particle correlations at low

relative-pair momentum. The relative-momentum distribution of the particle pairs is affected by the Bose-Einstein and Fermi-Dirac statistics for identical particles and by the Coulomb and strong final state interaction for non-identical particles, which eventually produces a finite correlation between the particles. One can probe the spatio-temporal evolution of the system by analysing these correlation functions and investigate various features of QGP e.g. collective flow, lifetime of the system etc. The source radii estimated from the identical-particle femtoscopy for various particle species as a function of average transverse mass (m_{T}) in Pb–Pb collisions at $\sqrt{s_{\mathrm{NN}}}$ = 2.76 TeV in ALICE experiment is shown in Fig. 1.14. The source size is observed to decrease with increasing m_{T} indicating towards the possible presence of collectiveness in the system.

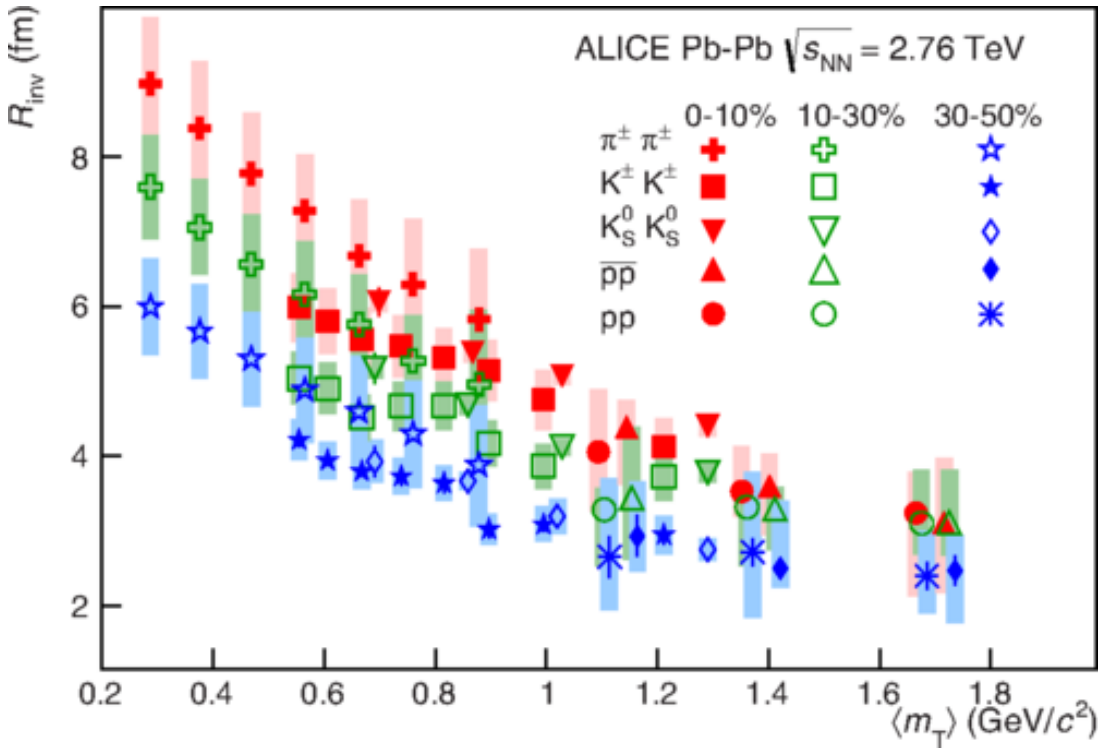

Figure 1.14: The source size (R_{inv}) as a function of average transverse mass (<m_{T}>) for three centrality classes for different pairs of particles in 0−10%, 10−30% and 30−50% central Pb–Pb collisions at $\sqrt{s_{\mathrm{NN}}}$ = 2.76 TeV in ALICE [33].

This thesis reports the femtoscopic analysis of pion-kaon pairs in Pb–Pb collisions at $\sqrt{s_{\mathrm{NN}}}$ = 5.02 TeV in ALICE experiment. A detailed description of the formalism of non-identical particle femtoscopy is discussed in chapter 2.

1.8 Organisation of this thesis

This thesis presents the study of femtoscopic correlation function of all charged-pair combinations of pion and kaon and estimation of the femtoscopic parameters of the system produced in Pb–Pb collisions at $\sqrt{s_{\rm NN}}$ = 5.02 TeV with ALICE detector at the LHC. In Chapter 2, the basic formalism of non-identical particle femtoscopy and spherical harmonic representation of the correlation function is discussed. Chapter 3 contains a brief overview of various sub-detectors in the ALICE experiment and some crucial information regarding selecting the triggers, collision events, particles and centrality determination. The analysis details for constructing the $k_{\rm T}$-(pair-transverse momentum) integrated, $k_{\rm T}$-dependent and $\beta_{\rm T}$- (pair-transverse velocity) dependent correlation functions along with the procedure for fitting them are given in Chapter 4. The results of femtoscopic analysis are discussed in Chapter 5. In Chapter 6, the long-range near-side ridge correlations in high multiplicity p–p collisions in the LHC energies are discussed. Chapter 7 summarises the investigations performed in this thesis.

Chapter 2

Non-identical femtoscopic correlation functions

2.1 Introduction

The heavy-ion collisions in the regime of ultra-relativistic energies at the RHIC and LHC produce a hot-dense QGP [34, 35] like system for a very short period of time. Various properties of the system that depend on the momentum of particles were well understood using the hydrodynamic models [35–39]. However, it was challenging to describe the spatio-temporal dimensions of the system. "Femtoscopy", also known as "Hanbury Brown and Twiss (HBT)" interferometry, is a technique developed to probe the space–time dynamics of the system in femtometer scale using the two-particle correlations [40–42]. The HBT interferometry was originally developed during 1950s to estimate the angular size of stars and other astronomical objects using the intensity-correlation of two photons coming from the stars [43]. A similar technique was developed to estimate the spatial dimensions of the system, created in the proton-antiproton collision using two-pion correlations [42] .

The femtoscopic description of the spatio-temporal dynamics of the QGP-like state produced in heavy-ion collisions was successful only after incorporating the following assumptions in the hydrodynamic models [44–46]:

- The initial profile of the matter was assumed to be a Gaussian function.
- The equation of state was considered to be a cross-over between the deconfined state and hadronic matter instead of a first order phase transition.
- The contribution from the resonances was considered.
- The non-hydrodynamic features of the hadronic state of matter were considered.
- The viscosity and pre-thermal flow were introduced.

In the identical-particle femtoscopic analysis of pions and kaons in Pb–Pb collisions at $\sqrt{s_{\rm NN}}$ = 158 GeV at the Super Proton Synchrotron (SPS)[47–49] by the NA44 and NA49 Collaborations at CERN, it is shown that the source size decreases with increasing transverse mass of the pair, $m_{\rm T} = \sqrt{k_{\rm T}^2 + m^2}$, due to the strong collective flow in the system. Here $k_{\rm T} = (|\boldsymbol{p}_{\rm T_1} + \boldsymbol{p}_{\rm T_2}|)/2$ [50] is the pair-transverse momentum and m is the reduced mass of the pair. Moreover, a $m_{\rm T}$-scaling of the radii along *out*, *side* and *long* directions (explained in detail in section 2.2) [47] for pions and kaons is observed. This leads to the possibility of simultaneous thermal freeze-out for both pions and kaons undergoing similar velocity boost due to the collectivity. However, the scaling along the *long* direction is observed to be broken in Au−Au collision system at $\sqrt{s_{\rm NN}}$ = 200 GeV at RHIC [51–53]. In the identical pion and kaon femtoscopic analyses in Pb–Pb collisions at $\sqrt{s_{\rm NN}}$ = 2.76 TeV with ALICE experiment, the scalings along the *out* and *long* directions are observed to be broken, as shown in Fig. 2.1. However, a $k_{\rm T}$-scaling of the radii ($R_{\rm out}$, $R_{\rm side}$ and $R_{\rm long}$) is observed in all directions as shown in Fig. 2.2) [54–56]. The ratio of $R_{\rm out}$ to $R_{\rm side}$ is observed to be larger for kaons than pions, which indicates towards different space-time correlations between these particle species [56]. The predictions from Hydro-Kinetic Model (HKM) which include the hydrodynamic phase and the hadronic rescattering phase [57] show that the $m_{\rm T}$-scaling is violated due to the rescattering of pions and kaons in the system produced at LHC energies [58].

Recently, physicists have shown a lot of interest in the femtoscopic analysis of non-identical particle pairs. The correlations between two different particles are affected by the

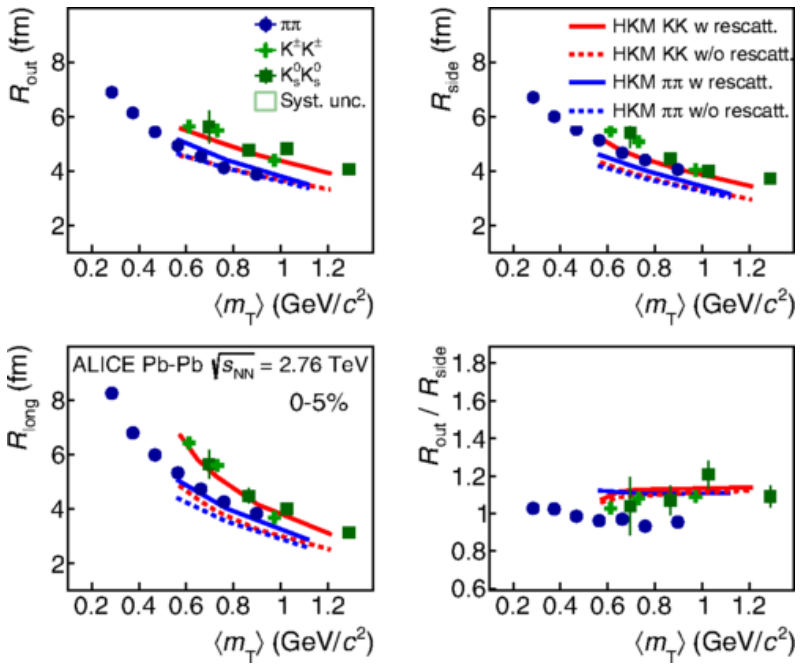

Figure 2.1: The three-dimensional radii as a function of m_{T} for charged pions (blue circles), charged kaons (light green crosses) and neutral kaons (dark green squares) in Pb–Pb collisions at $\sqrt{s_{\mathrm{NN}}}$ = 2.76 TeV in ALICE [56].

difference in average space–time emission points of those particles. It is assumed that the collectivity of the system may lead to a shift in average emission points for different particles. Another theory suggests that the time taken by different particles to leave the system may differ from one another based on their interaction cross sections [59]. Moreover, if a particle is formed mostly through the decay of resonance particles, the average emission time for that particle species may be notably delayed [59]. These effects can be thoroughly investigated by the femtoscopic analysis of non-identical particle pairs. The main objectives of the non-identical particle femtoscopy are to estimate the size of source and also to measure the spatial-emission asymmetry (discussed in section 2.3) between the particles.

In case of non-identical particle femtoscopy, the correlation functions are expressed in terms of two one-dimensional histograms, namely $C_{-}(\boldsymbol{k}^{*})$ and $C_{+}(\boldsymbol{k}^{*})$ [60]. Here, $\boldsymbol{k}^{*}$ is the *reduced*-pair momentum (explained in the section 2.4), the $C_{-}(\boldsymbol{k}^{*})$ corresponds to the phenomenon where the particles move away from each other right after they are produced and the $C_{+}(\boldsymbol{k}^{*})$ corresponds to the case where they move towards each other, and hence, interact for

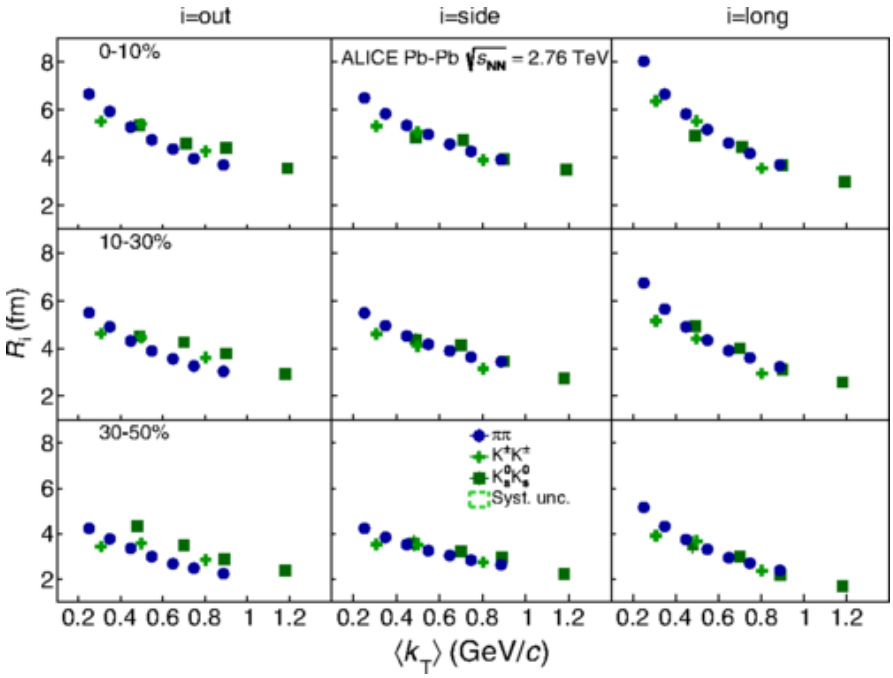

Figure 2.2: The three-dimensional radii as a function of k_{T} for charged pions (blue circles), charged kaons (light green crosses) and neutral kaons (dark green squares) in Pb–Pb collisions at $\sqrt{s_{\mathrm{NN}}}$ = 2.76 TeV in ALICE. The 1$^{\mathrm{st}}$, 2$^{\mathrm{nd}}$ and 3$^{\mathrm{rd}}$ columns correspond to R_{out}, R_{side} and R_{long}, respectively [56].

a longer time than the former case. The $C_+(\boldsymbol{k}^*)$ and $C_-(\boldsymbol{k}^*)$ are constructed in *out* direction and are used to extract the R_{out}. Moreover, the $C_+(\boldsymbol{k}^*)/C_-(\boldsymbol{k}^*)$ i.e. the "Double-ratio"[60] is constructed to extract the pair-emission asymmetry along the *out* direction. The results from pion-kaon femtoscopic analysis in the central Au−Au collisions at $\sqrt{s_{\mathrm{NN}}}$ = 130 GeV at STAR, as shown in Fig. 2.3, shows that the pions and kaons are emitted at different space-time positions. This observation can be attributed to the collective expansion of the system as suggested by the model calculations in Blast Wave Parametrisation (BWP) [59] and Relativistic Quantum Molecular Dynamic (RQMD) [61]. However, the difference in emission points of the particles was not quantified in this measurement by STAR experiment [59].

Recent results from the pion-kaon femtoscopic analysis in Pb–Pb collision system at $\sqrt{s_{\mathrm{NN}}}$ = 2.76 TeV [62] with ALICE experiment (Fig. 2.4) shows that the source size increases from peripheral to most central events, which is expected since the size of the system increases with the increasing number of participants. The pair-emission asymmetry (μ) is also estimated for

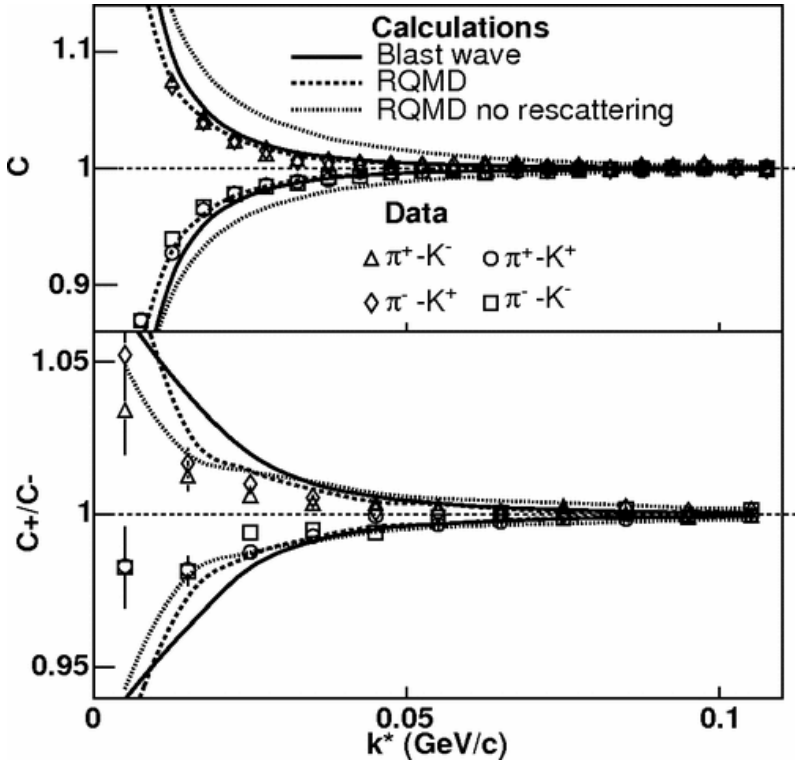

Figure 2.3: The pion-kaon correlation functions in the central Au−Au collisions at $\sqrt{s_{\mathrm{NN}}}$ = 130 GeV as measured by STAR experiment [59]. C is the average of $C_{-}(\boldsymbol{k}^{*})$ and $C_{+}(\boldsymbol{k}^{*})$.

the first time and the results suggest that the average emission-points of kaons are always at a larger distance from the center of source than that of pions. Moreover, its magnitude is observed to increase from peripheral to central events signifying the collective expansion of the system [62]. However, the trend of μ could not be explained by the contribution from radial flow alone. The THERMINATOR 2 model, which incorporates a (3 + 1) dimensional viscous hydrodynamic model with the statistical hadronisation, describes the trend of μ after introducing an additional delay of 1−2 fm/c for the emission of kaons. This suggests the existence of hadronic rescattering phase along with the collective expansion of the system [63].

2.2 Frame of reference

The frames of reference which are used in this analysis are the Longitudinally Co-Moving System (LCMS) and the Pair Rest Frame (PRF). Consider two particles with momentum $\boldsymbol{p}_1$ and $\boldsymbol{p}_2$ being emitted from the system as shown in Fig. 2.5. The LCMS is constructed with

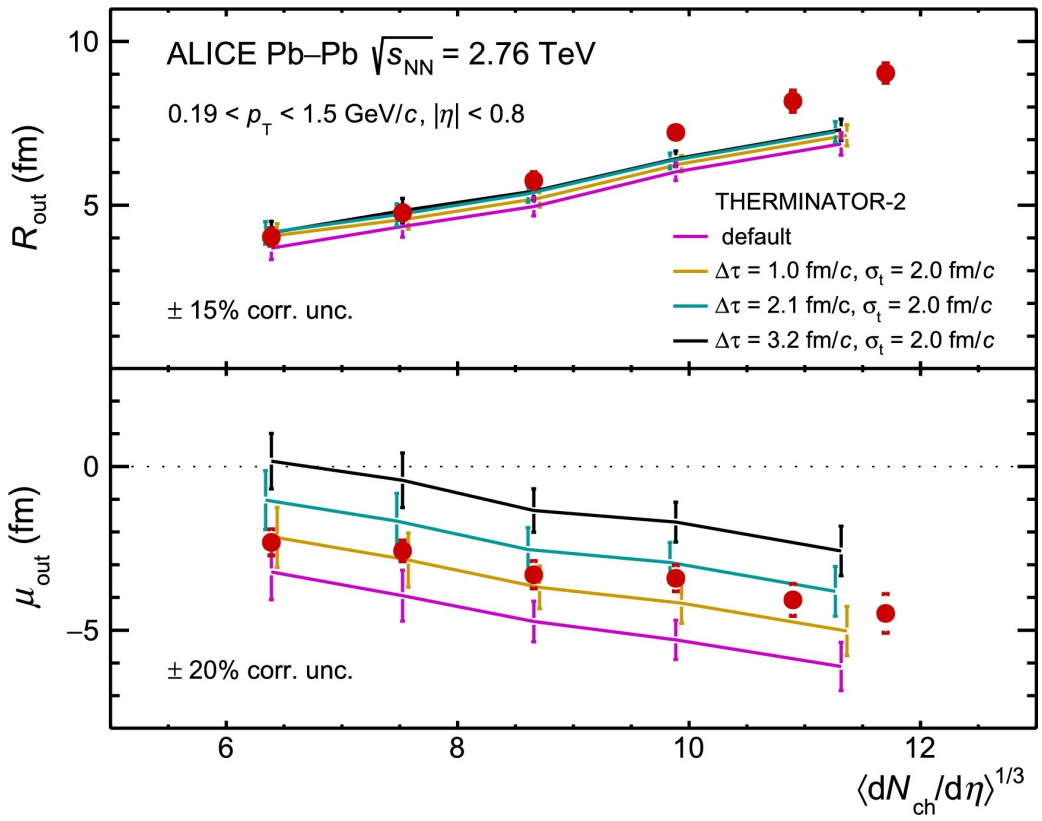

Figure 2.4: The source size (upper panel) and pair-emission asymmetry (lower panel) as a function of $<dN_{ch}/d\eta>^{1/3}$ for pion-kaon pairs in Pb–Pb collisions at $\sqrt{s_{NN}}$ = 2.76 TeV in ALICE [62].

the condition that total pair momentum along the beam axis is zero i.e. $p_{1,z} + p_{2,z} = 0$. The three axes of this frame of reference are "out", "side" and "long". The *out* axis is along the pair-k_T, the *long* is along the beam direction and the *side* axis is orthogonal to both *long* and *out* directions[50]. The equations to express any four-vector (say A) in LCMS are the following:

$$A_{long} = (P_0 A_Z - P_z A_0)/M_T \tag{2.1}$$

$$A_{out} = (P_x A_x + P_y A_y)/P_T \tag{2.2}$$

$$A_{side} = (P_x A_y - P_y A_x)/P_T, \tag{2.3}$$

where, $P = p_1 + p_2$, $P = (P_0, \boldsymbol{P})$, $M_T^2 = P_0^2 - P_z^2$ and $P_T^2 = P_x^2 + P_y^2$.

In the PRF, the total momentum of the pair is conserved i.e. $\boldsymbol{p}_1^* = -\boldsymbol{p}_2^*$. The "*" corresponds to the representation of vectors in the PRF. The transformation equation to boost the

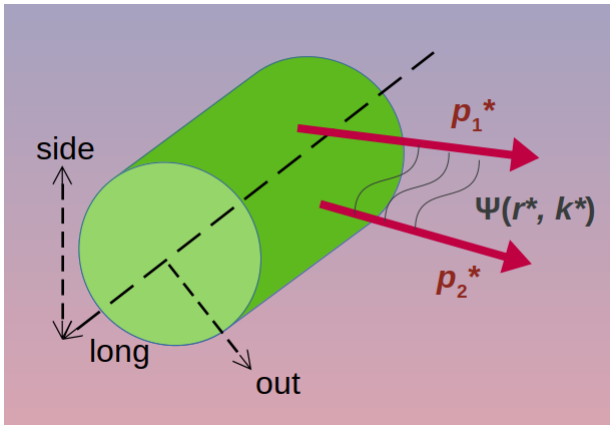

Figure 2.5: The frame of reference constructed with the *out*, *side* and *long* axes.

vectors to the PRF is:

$$A^*_{\rm out} = \frac{M_{\rm inv}}{M_{\rm T}} \frac{(P_{\rm x}A_{\rm x} + P_{\rm y}A_{\rm y})}{P_{\rm T}} - \frac{P_{\rm T}}{M_{\rm T}M_{\rm inv}} P.A. \tag{2.4}$$

If at any instant, the positional co-ordinates of the particles are $\boldsymbol{x}^*_1$ and $\boldsymbol{x}^*_2$, then the separation between them is $\boldsymbol{r}^* = \boldsymbol{x}^*_1 - \boldsymbol{x}^*_2$. Additional information regarding LCMS and PRF can be found in [50].

2.3 Pair-emission asymmetry

The hydrodynamic evolution of the hot-dense matter produced in the collisions of heavy ions suggests that the constituent particles of the system will have a common flow velocity ($\boldsymbol{\beta_{\rm f}}$) in the transverse plane (radial flow) irrespective of their masses. Additionally, the particles will have random thermal velocities as shown in Fig. 2.6 [60]. Hence, the resultant velocity of a particle can be $\boldsymbol{\beta} = \boldsymbol{\beta_{\rm f}} + \boldsymbol{\beta_{\rm t}}$, where $\boldsymbol{\beta_{\rm t}}$ is the thermal velocity of the particle.

The component of emission point (per unit velocity) of a particle along its velocity is [60]:

$$x_{\rm out} = \frac{\boldsymbol{x}.\boldsymbol{\beta}}{\beta} = \frac{r(\beta_{\rm f} + \beta_{\rm t} cos(\phi_{\rm t} - \phi_{\rm f}))}{\beta}. \tag{2.5}$$

Assuming the density of system to be a Gaussian profile with radius r_0 and the flow velocity, $\beta_{\rm f} = \beta_0 r/r_0$, the average of $x_{\rm out}$ is [60],

$$< x_{\rm out} >= \frac{< r\beta_{\rm f} >}{< \sqrt{\beta^2_{\rm t} + \beta^2_{\rm f}} >} = \frac{r_0\beta_0\beta}{\beta^2_0 + T/m_{\rm T}} \tag{2.6}$$

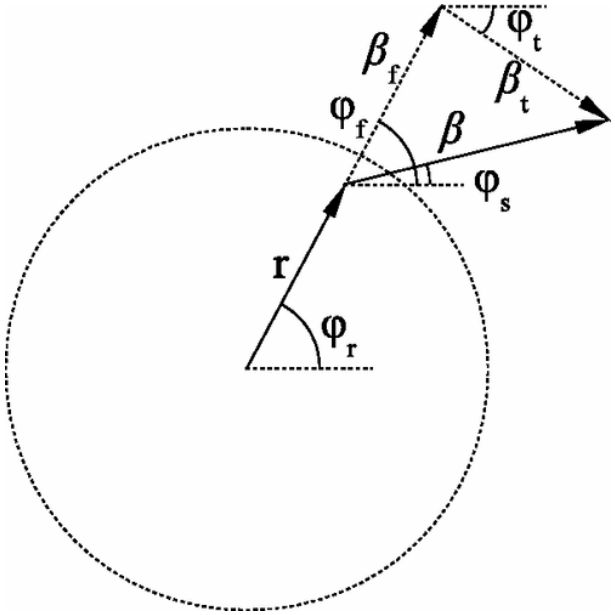

Figure 2.6: The particle velocity ($\boldsymbol{\beta}$) with the flow ($\boldsymbol{\beta}_{\rm f}$) and thermal ($\boldsymbol{\beta}_{\rm t}$) components [60].

where, T is the temperature and $m_{\rm T}$ is the transverse mass of the particle. Assuming similar spatial characteristics for the emissions of both pions (the lighter particle) and kaons (the heavier particle), it is expected that the $<r\beta_{\rm f}>$ will be same for both the particles. However, $T/m_{\rm T}$ will be different for pions and kaons since it depends on the transverse mass of the particles. As $T/m_{\rm T}$ is smaller for the heavier particle, according to Eq. (2.6), the $<x_{\rm out}>$ for kaons are larger than the pions i.e. on average, the kaons are emitted at a larger distance from the center of system than pions [60]. The average pair-emission asymmetry between the particles of a non-identical pair can be expressed as:

$$\mu_{\rm out}^{\rm light,heavy} =< r_{\rm out}^{\rm light,heavy} >=< x_{\rm out}^{\rm light} - x_{\rm out}^{\rm heavy} > . \tag{2.7}$$

There are certain constraints for the pair-emission asymmetry to exist [60], which are the following:

- If there is no radial flow in the system, Eq. (2.6) shows that the $<x_{\rm out}>$ for both heavy and light particles is zero, which means that both of the particles will be emitted from the center of source. Hence, no emission asymmetry would be observed.

- If $\boldsymbol{\beta_t}$ of a particle is very large compared to $\boldsymbol{\beta_f}$, the $<x_{\text{out}}>$ for that particle is zero. If one of the particles in a pair has zero $<x_{\text{out}}>$, a non-zero asymmetry exists. If both the particles have zero $< x_{\text{out}}>$, the asymmetry does not exist.

- If $\boldsymbol{\beta_f} >> \boldsymbol{\beta_t}$, the $<x_{\text{out}}>$ will be dominated by $\boldsymbol{\beta_f}$ and both the particles will have the same $<x_{\text{out}}>$. Hence, the asymmetry will vanish.

Hence, it is clear that the average pair-emission asymmetry exists when both of the $\boldsymbol{\beta_f}$ and $\boldsymbol{\beta_t}$ are comparable in magnitude.

2.4 Femtoscopic correlation function of two non-identical particles

The two-particle femtoscopic correlation function can be expressed as [60]:

$$C(\boldsymbol{p}_1, \boldsymbol{p}_2) = \frac{P_2(\boldsymbol{p}_1, \boldsymbol{p}_2)}{P_1(\boldsymbol{p}_1)P_1(\boldsymbol{p}_2)} \tag{2.8}$$

where, $P_2(\boldsymbol{p}_1, \boldsymbol{p}_2)$ is the probability of detecting two particles having momentum $\boldsymbol{p}_1$ and $\boldsymbol{p}_2$ simultaneously while $P_1(\boldsymbol{p})$ is the probability of detecting the particles having momentum $\boldsymbol{p}$. If there is no correlation between the particles, $P_2(\boldsymbol{p}_1, \boldsymbol{p}_2)$ will be equal to $P_1(\boldsymbol{p}_1)P_1(\boldsymbol{p}_2)$ and hence, $C(\boldsymbol{p}_1, \boldsymbol{p}_2)$ will be unity.

The total and relative momentum of the pair are given in Eq. (2.9)-(2.10):

$$P = p_1 + p_2, \tag{2.9}$$

$$q^\mu = \frac{(p_1 - p_2)^\mu}{2} - \frac{(p_1 - p_2).P}{2P^2} P^\mu. \tag{2.10}$$

The correlation function can be expressed in terms of P and q, as given in Eq. (2.11) [50]:

$$C(P, q) = \frac{\int d^4x_1 d^4x_2 S_1(x_1, p_1) S_2(x_2, p_2) |\Psi(r^*, q^*)|^2}{\int d^4x_1 d^4x_2 S_1(x_1, p_1) S_2(x_2, p_2)} \tag{2.11}$$

where, $S(x, p)$ is the single-particle source function i.e. the probability of emission of a particle with momentum $p = (E, \boldsymbol{p})$ at distance $x = (t, \boldsymbol{x})$, $\Psi(r^*, q^*)$ corresponds to the pair-wave function, $\boldsymbol{r}$ is the relative separation between the particles in a pair. In the PRF, $\boldsymbol{P} = 0$, which

leads $\boldsymbol{q} \rightarrow \boldsymbol{k}^* = (m_2\boldsymbol{p}_1^* - m_1\boldsymbol{p}_2^*)/(m_1 + m_2)$. Here, the $\boldsymbol{k}^*$ is referred as the reduced-pair momentum. The $\Psi(r^*, q^*)$ has an explicit dependence on time, however, in case of PRF, the equal-time approximation can be used, where it is assumed that the particles are emitted simultaneously, i.e. $t_1^* - t_2^* = 0$ [50, 64]. Therefore, the time dependence of $\Psi(r^*, q^*)$ is removed and it is reduced to a stationary state i.e. $\Psi(r^*, q^*) \rightarrow \Psi(\boldsymbol{r}^*, \boldsymbol{q}^*)$. The source function is also modified using the smoothness approximation [50, 64], and Eq. (2.11) can be modified to the Koonin−Pratt equation [65, 66], as given in Eq. (2.13).

$$C(\boldsymbol{k}^*) = \int d^3r^* |\Psi(\boldsymbol{k}^*, \boldsymbol{r}^*)|^2 \int dt^* S(r^*) \tag{2.12}$$

$$= \int d^3r^* S(\boldsymbol{r}^*) |\Psi(\boldsymbol{k}^*, \boldsymbol{r}^*)|^2. \tag{2.13}$$

It is clear from Eq. (2.13) that the correlation function can be calculated using only the source function and pair interaction. In this thesis, however, the experimentally measured correlation function is utilised to estimate the parameters of source function, provided that the interaction between particles in a pair is well estimated (discussed in section 2.4.2).

Generally, two-particle correlation function can be constructed experimentally by taking the ratio of distribution of the particle pairs produced in the same events, to the distribution of particle pairs from the mixed events. The femtoscopic correlation function can be obtained using Eq. (2.14).

$$C(\boldsymbol{k}^*) = N(\boldsymbol{k}^*)\frac{F(\boldsymbol{k}^*)}{G(\boldsymbol{k}^*)}, \tag{2.14}$$

where $F(\boldsymbol{k^*})$ is the distribution of correlated particles coming from the same events ("signal"), $G(\boldsymbol{k^*})$ is the distribution of uncorrelated particles coming from the mixed events ("background") and $N(\boldsymbol{k}^*)$ is the normalising constant.

2.4.1 Source function

Femtoscopy essentially measures the "length of homogeneity" [50]. A thermalised system with no collective expansion is depicted in the left part of Fig. 2.7, where the emission of four particles is shown. Any two particles, emitted from any region of the source with low relative

momentum, can form a pair. Hence, it is possible to probe nearly the whole region of the source. However, if the medium has collective flow along with the thermal interaction, as shown in the middle part of Fig. 2.7, the particles will be boosted radially outward. So, the particles which form a pair and develop correlations, will be constrained in a small region of the medium. Moreover, if the particles with relatively larger k_{T} and similar kinematic properties form a pair, they have to be emitted in the vicinity of each-other. Hence, the region of homogeneity is expected to decrease if the pairs with larger k_{T} are probed for femtoscopic analysis.

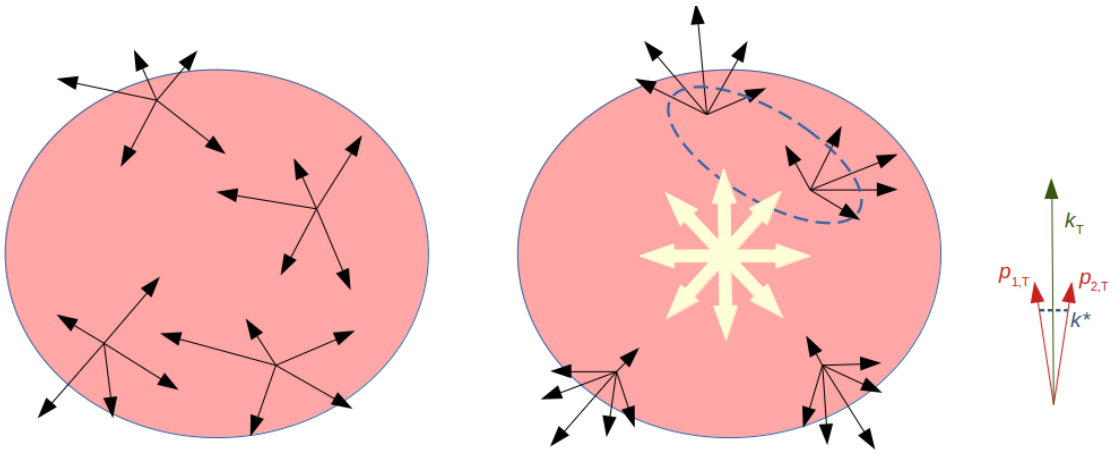

Figure 2.7: The emission of particles with the possible momenta (black arrows) from a static medium (left) and expanding medium with collective velocity (right).

In principle, the source function should contain all the information regarding the emission process and interactions of the particles. However, it is assumed that the source function of each particle is an independent quantity and does not depend on the final-state interaction with other particles [60]. The two-particle emission function, $S(\boldsymbol{r}^*)$, shown in Eq. (2.13), is the convolution of two single-particle source function [60]. Generally, the source function is considered as a three-dimensional Gaussian function with three different radii, R_{out}, R_{side} and R_{long}, along the *out*, *side* and *long* axis, respectively. A pair-emission asymmetry, μ_{out}, along the *out* direction is also assumed and is given in Eq. (2.15) [60].

$$S(\boldsymbol{r}) = exp\left(-\frac{(r_{\mathrm{out}}-\mu_{\mathrm{out}})^2}{2R_{\mathrm{out}}^2} - \frac{r_{\mathrm{side}}^2}{2R_{\mathrm{side}}^2} - \frac{r_{\mathrm{long}}^2}{2R_{\mathrm{long}}^2}\right). \tag{2.15}$$

The three-dimensional source function of the non-identical particle pair can also be approximated to an one-dimensional distribution as given in Eq. (2.16) [60].

$$S(\boldsymbol{r}) \approx r^2 exp\left(-\frac{r^2}{2R_{\mathrm{av}}^2}\right) \tag{2.16}$$

where, R_{av} is the one-dimensional width of the source.

2.4.2 Pair interaction

The pair-wave function $\Psi(\boldsymbol{r}^*, \boldsymbol{k}^*)$ corresponds to the final state interactions (FSI) between the particles in a pair. In case of identical-particle femtoscopy, the $\Psi(\boldsymbol{r}^*, \boldsymbol{k}^*)$ would be symmetric or anti-symmetric, depending on the nature of the particle as given in Eq. (2.17) and Eq. (2.18) [67]. For bosons (e.g pions, kaons),

$$\Psi(\boldsymbol{r}^*, \boldsymbol{k}^*) = 1 + cos(2\boldsymbol{k^*r^*}) \tag{2.17}$$

while for fermions (e.g. protons),

$$\Psi(\boldsymbol{r}^*, \boldsymbol{k}^*) = 1 - \frac{1}{2}cos(2\boldsymbol{k^*r^*}). \tag{2.18}$$

In case of non-identical particles, the $\Psi(\boldsymbol{r}^*, \boldsymbol{k}^*)$ includes Coulomb and/or strong interactions and information about the motion of the pair after freeze out [60]. The $\Psi(\boldsymbol{r}^*, \boldsymbol{k}^*)$, expressed in Eq. (2.19) [60], is an analytical function and its features are well known for all charged-pair combinations of pions and kaons.

$$\Psi(\boldsymbol{r}^*, \boldsymbol{k}^*) = \sqrt{A_C(\eta)}\left[e^{-i\boldsymbol{k}^*\boldsymbol{r}^*}F(-i\eta, 1, i\zeta) + f_C(\boldsymbol{k}^*)\frac{G(\rho, \eta)}{\boldsymbol{r}^*}\right]. \tag{2.19}$$

Here, A_C is the Gamow factor, $\eta = 1/\boldsymbol{k}^* a_C$, a_C is the pair-Bohr radius, which is equal to 248.52 fm for the pion-kaon pairs [60] , F is the confluent hypergeometric function [68], $\zeta = k^* r^*(1 + cos\theta^*)$, θ^* is the angle between $\boldsymbol{k}^*$ and $\boldsymbol{r}^*$ in PRF, f_C is the strong scattering amplitude with modifications from the Coulomb interaction and G is the combination of the regular and singular s-wave Coulomb functions. f_C can be approximated by the following equation [60]:

$$f_C(\boldsymbol{k}^*) = \left[\frac{1}{f_0} + \frac{1}{2}d_0\boldsymbol{k}^{*2} - i\boldsymbol{k^*}A_C(\boldsymbol{k}^*) - \frac{2}{a_C}h(\boldsymbol{k^*}a_C)\right]^{-1} \tag{2.20}$$

where f_0 is -0.071 fm [60] for the unlike-signed pion-kaon pairs and 0.137 fm for the like-signed pion–kaon pairs. In the lower k^* region, the effective radius d_0 can be taken as zero due to the dominance of $\frac{1}{f_0}$.

2.5 Spherical harmonics decomposition of correlation function

Generally, the correlation functions are represented as one-dimensional histograms as a function of $\boldsymbol{k}^*$ or $\boldsymbol{q}^* = 2\boldsymbol{k}^*$ and as three-dimensional histograms of k^*_{out}, k^*_{side} and k^*_{long} or q^*_{out}, q^*_{side} and q^*_{long} [60] components. Recently, a new approach has been developed to construct the correlation functions in terms of Spherical Harmonics (SH). In this analysis, the SH representations of the correlation functions are used to extract the femtoscopic parameters. It has several advantages [60]:

- The correlation functions can be represented as a series of one-dimensional histograms.
- Most of the higher order harmonics (l, m components) vanish due to the intrinsic symmetries of the pair distribution.
- The important femtoscopic information can be extracted from the harmonics with lower order l components.

In order to compute the SH representation of the correlation functions, the components of $\boldsymbol{k}^*$ i.e. k^*_{out}, k^*_{side} and k^*_{long} [50] for each pair are needed to be decomposed into $|\boldsymbol{k}^*|$, $\theta_{\boldsymbol{k}^*}$ and $\phi_{\boldsymbol{k}^*}$ as given in Eq. (2.21)-(2.23).

$$k^*_{\text{out}} = |\boldsymbol{k}^*| sin\theta_{\boldsymbol{k}^*} sin\phi_{\boldsymbol{k}^*} \tag{2.21}$$

$$k^*_{\text{side}} = |\boldsymbol{k}^*| sin\theta_{\boldsymbol{k}^*} cos\phi_{\boldsymbol{k}^*} \tag{2.22}$$

$$k^*_{\text{long}} = |\boldsymbol{k}^*| cos\theta_{\boldsymbol{k}^*}. \tag{2.23}$$

Conventionally, the numerator and denominator of Eq. (2.14) ($F(\boldsymbol{k}^*)$ and $G(\boldsymbol{k}^*)$, respectively) are filled with $|\boldsymbol{k}^*|$, $\theta_{\boldsymbol{k}^*}$ and $\phi_{\boldsymbol{k}^*}$ to form the three-dimensional histograms and their ratio

is taken to estimate the SH representations of the correlation functions. But there is a drawback in this approach. It may happen that some of the $\mathbf{k}^*$ bins do not have enough pairs due to poor statistics of the produced particles or the detector acceptance [60, 69], eventually affecting the correlation functions. Therefore, instead of taking the direct ratio of $F(\boldsymbol{k}^*)$ and $G(\boldsymbol{k}^*)$, the SH components of the correlation functions are calculated in the following way [69]. Eq. (2.14) is expressed as

$$F(\boldsymbol{k}^*) = G(\boldsymbol{k}^*)C(\boldsymbol{k}^*). \tag{2.24}$$

The $F(\boldsymbol{k}^*)$, $G(\boldsymbol{k}^*)$ and $C(\boldsymbol{k}^*)$ of Eq. (2.24) can be decomposed into the respective spherical-harmonics components by the following equations:

$$F(\boldsymbol{k}^*) = \sqrt{4\pi}\sum_{\mathrm{l,m}} F_{\mathrm{lm}}(\boldsymbol{k}^*)Y_{\mathrm{lm}}(\theta_{\boldsymbol{k}^*}, \phi_{\boldsymbol{k}^*}) \tag{2.25}$$

$$G(\boldsymbol{k}^*) = \sqrt{4\pi}\sum_{\mathrm{l,m}} G_{\mathrm{lm}}(\boldsymbol{k}^*)Y_{\mathrm{lm}}(\theta_{\boldsymbol{k}^*}, \phi_{\boldsymbol{k}^*}) \tag{2.26}$$

$$C(\boldsymbol{k}^*) = \sqrt{4\pi}\sum_{\boldsymbol{l},m} C_{\boldsymbol{l}m}(\boldsymbol{k}^*)Y_{\mathrm{lm}}(\theta_{\boldsymbol{k}^*}, \phi_{\boldsymbol{k}^*}) \tag{2.27}$$

where,

$$Y_{\mathrm{lm}}(\theta, \phi) = (-1)^{\mathrm{m}}\sqrt{\frac{(2\mathrm{l}+1)(\mathrm{l}-\mathrm{m})!}{4\pi(\mathrm{l}+\mathrm{m})!}}P_{\mathrm{l}}^{\mathrm{m}}(cos\theta)e^{i\mathrm{m}\phi}, \tag{2.28}$$

Eq. (2.24) can be expressed as:

$$F_{\mathrm{lm}}(\boldsymbol{k}^*) = \sum_{\mathrm{l'm'l"m"}} G_{\mathrm{l'm'}}(\boldsymbol{k}^*)C_{\mathrm{l"m"}}(\boldsymbol{k}^*) \times \int_{4\pi} Y^*_{\mathrm{lm}}(\theta_{\boldsymbol{k}^*}, \phi_{\boldsymbol{k}^*})Y_{\mathrm{l'm'}}(\theta_{\boldsymbol{k}^*}, \phi_{\boldsymbol{k}^*})Y_{\mathrm{l"m"}}(\theta_{\boldsymbol{k}^*}, \phi_{\boldsymbol{k}^*})d\theta_{\boldsymbol{k}^*}d\phi_{\boldsymbol{k}^*} \tag{2.29}$$

$$F_{\mathrm{lm}}(\boldsymbol{k}^*) \equiv \sum \hat{G}_{\mathrm{lml"m"}}(\boldsymbol{k}^*)C_{\mathrm{l"m"}}(\boldsymbol{k}^*). \tag{2.30}$$

The $|\boldsymbol{k}^*|$, $\theta_{\boldsymbol{k}^*}$, $\phi_{\boldsymbol{k}^*}$ and SH are calculated for each pair and each $F_{\mathrm{lm}}(\boldsymbol{k}^*)$ and $G_{\mathrm{lm}}(\boldsymbol{k}^*)$ are stored in the vector $\boldsymbol{F}_{\boldsymbol{k}^*}$ and $\boldsymbol{G}_{\boldsymbol{k}^*}$, respectively according to their weights, which is equal to the values of respective Y_{lm}. The correlation function can be estimated by minimising the χ^2 of Eq. (2.31) [69]:

$$\chi^2 = (\boldsymbol{F}_{\boldsymbol{k}^*} - \hat{\boldsymbol{G}}_{\boldsymbol{k}^*}.\boldsymbol{C}_{\boldsymbol{k}^*})^T.(\Delta^2\boldsymbol{F}_{\boldsymbol{k}^*})^{-1}.(\boldsymbol{F}_{\boldsymbol{k}^*} - \hat{\boldsymbol{G}}_{\boldsymbol{k}^*}.\boldsymbol{C}_{\boldsymbol{k}^*}). \tag{2.31}$$

Hence, the correlation function can be estimated as [69]

$$\boldsymbol{C}_{\boldsymbol{k}^*} = \Delta^2\boldsymbol{C}_{\boldsymbol{k}^*}.\hat{\boldsymbol{G}}^T_{\boldsymbol{k}^*}.(\Delta^2\boldsymbol{F}_{\boldsymbol{k}^*})^{-1}.\boldsymbol{F}_{\boldsymbol{k}^*} \tag{2.32}$$

and the covariance can be calculated as:

$$\Delta^2\boldsymbol{C}_{\boldsymbol{k}^*} = (\hat{\boldsymbol{G}}^T_{\boldsymbol{k}^*}.(\Delta^2\boldsymbol{F}_{\boldsymbol{k}^*})^{-1}.\hat{\boldsymbol{G}}_{\boldsymbol{k}^*})^{-1}. \tag{2.33}$$

Some of the SH components that carry important femtoscopic information are the following:

- C_0^0: corresponds to the system size.
- ReC_1^1 (the real component of C_1^1): indicates the presence of average pair-emission asymmetry along the "out" axis.
- ReC_1^0: indicates the presence of average pair-emission asymmetry along the "long" axis.
- ReC_2^2 and ReC_2^0 (the real components of C_2^2 and C_0^2, respectively): correspond to the unequal size of the system along three axes.

It is shown that the important femtoscopic information of source can be estimated by analysing only C_0^0 and ReC_1^1 instead of all the components [60]. In case of Pb–Pb collisions, the system is expected to be symmetric along the longitudinal direction. So, there should not be any pair-remission asymmetry along the *long* direction and hence, ReC_1^0 is not analysed in this study. The ReC_2^2 and ReC_2^0 can also be analysed to estimate the source parameters in all three dimensions but it requires a lot of statistics. Hence, only C_0^0 and ReC_1^1 are analysed in this study. Ideally all imaginary components (ImC_1^{m}) should vanish due to intrinsic symmetries. However, the deviations of ImC_1^1 from zero might be observed in the experimental data, which may indicate towards the detector effects related to the track reconstruction, splitting or merging effect.

2.6 Extraction of femtoscopic parameters

The femtoscopic parameters of a system are extracted by comparing the experimental correlation functions with the theoretical ones using Eq. (2.13) as mentioned in section 2.4. This process is very straightforward for the identical particles as the theoretical correlation functions can be computed analytically and can be used to fit the experimental correlation functions directly. However, the fitting process is not so trivial for the pion-kaon pairs. The FSI between pions and kaons includes both Coulomb and strong interactions and hence, cannot be averaged out to simplify the integration in Eq. (2.13). Therefore, the estimation of theoretical correlation has to be performed numerically using the following procedure:

- The emission points are generated randomly by assuming the source function to be a three-dimensional Gaussian distribution with the sizes R_{out}, R_{side} and R_{long}, and mean pair-emission asymmetry μ_{out}.
- The momenta of pion-kaon pairs are taken from the experimental data [70].
- The FSI and eventually, the weight for each pair is calculated using the generated pair separation and pair-relative momenta and then, the weight is averaged over all pairs.
- The theoretical correlation function is calculated using the FSI and source function.
- A χ^2 test is performed between the experimental and calculated theoretical correlation functions.
- The input parameters of the source function are varied repeatedly and the values of source parameters, taken from the best-fit result are considered as the femtoscopic parameters.

Chapter 3

The ALICE experiment at the LHC

3.1 The Large Hadron Collider

The Large Hadron Collider (LHC) is world's largest and most powerful particle accelerator, located at 175 m beneath the Switzerland-France border near Geneva with a circumference of 27 km. It is a part of CERN's (European Council for Nuclear Research) accelerator complex. It consists of two parallel beam pipes, kept at ultra-high vacuum, where the bunches of protons and heavy ions are accelerated close to the speed of light in opposite directions. The collisions of accelerated particles and ions happen at four different points, where four experiments i.e. A Large Ion Collider Experiment (ALICE), Compact Muon Solenoid (CMS) experiment, Large Hadron Collider beauty (LHCb) and A Toroidal LHC Apparatus (ATLAS) are located. The beam pipes are guarded by 1232 superconducting dipole magnets [71, 72] to keep the beams in a circular path. The magnets are kept in a cryogenic system with the temperature close to -271.3°C (colder than outer space) to maintain the superconducting state of the magnets. Moreover, various quadruple and higher multipole magnets are used to keep the beams focused.

The various steps involved in particle acceleration (proton and lead (Pb) nucleus) are shown in Fig. 3.1. The protons are produced by removing the electrons from hydrogen atoms and Pb ions are obtained by heating a highly purified Pb sample, which produces a vapour of Pb atoms. The Pb atoms are then ionised by stripping off their electrons. The produced protons and Pb ions are then accelerated sequentially in the Linear Accelerators (LINAC2 and

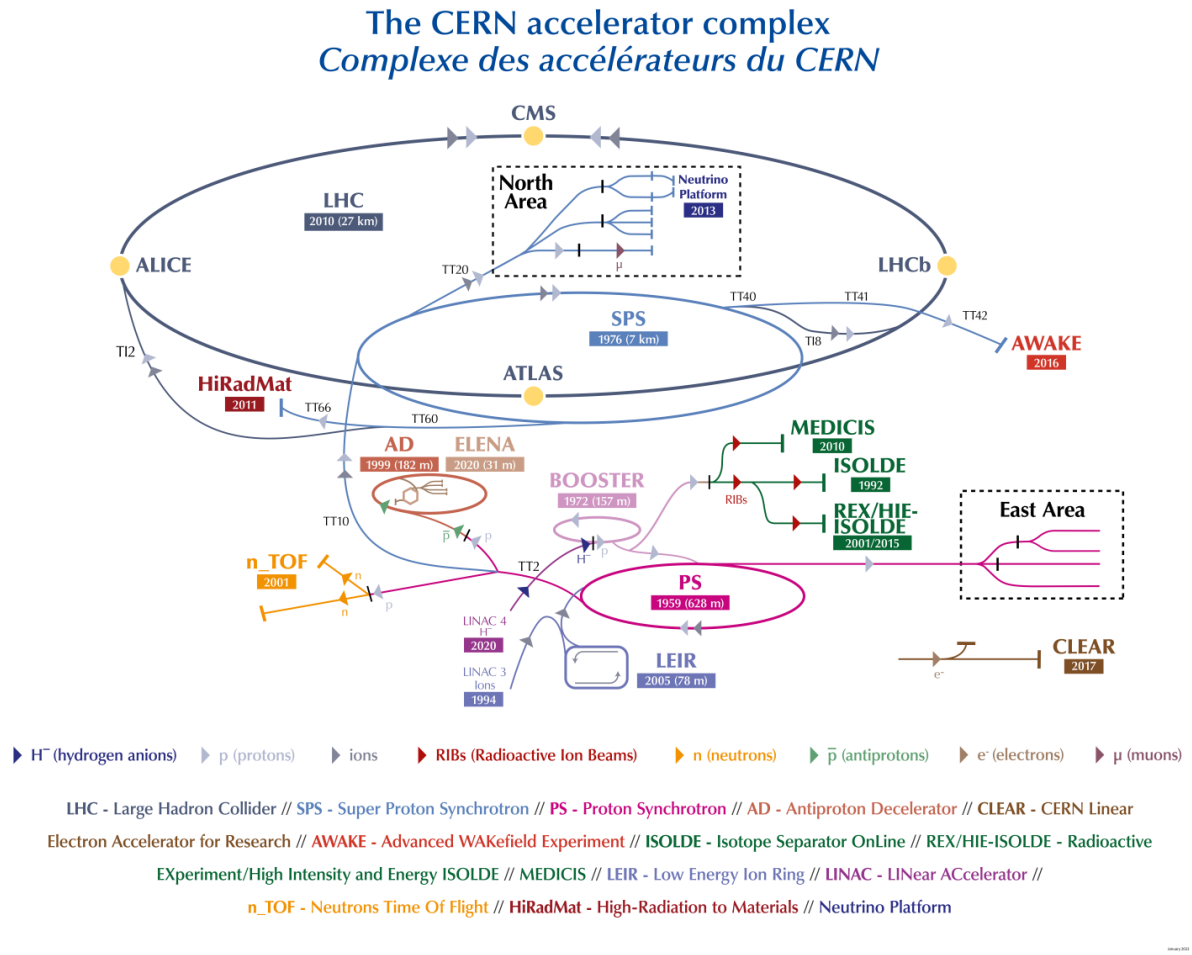

Figure 3.1: The schematic diagram of CERN LHC accelerator complex [73].

LINAC3, respectively), Low Energy Ion Ring (LEIR), Proton Synchrotron (PS) and Super Proton Synchrotron (SPS). The beams from SPS are pushed into the LHC where final acceleration takes place. The maximum center-of-mass energy obtained in Pb–Pb and p–p systems are $\sqrt{s_{\mathrm{NN}}} = 5.02$ TeV and $\sqrt{s} = 13$ TeV, respectively.

3.2 The ALICE experiment

One of the four major experiments at the LHC is ALICE, which is optimised to study the collisions of heavy ions [74, 75]. It is expected that these collisions may create the QGP-like state of matter due to extreme energy densities and temperatures. The main goal of ALICE is to probe various properties of the QGP and to study the physics of strongly interacting matter. Along

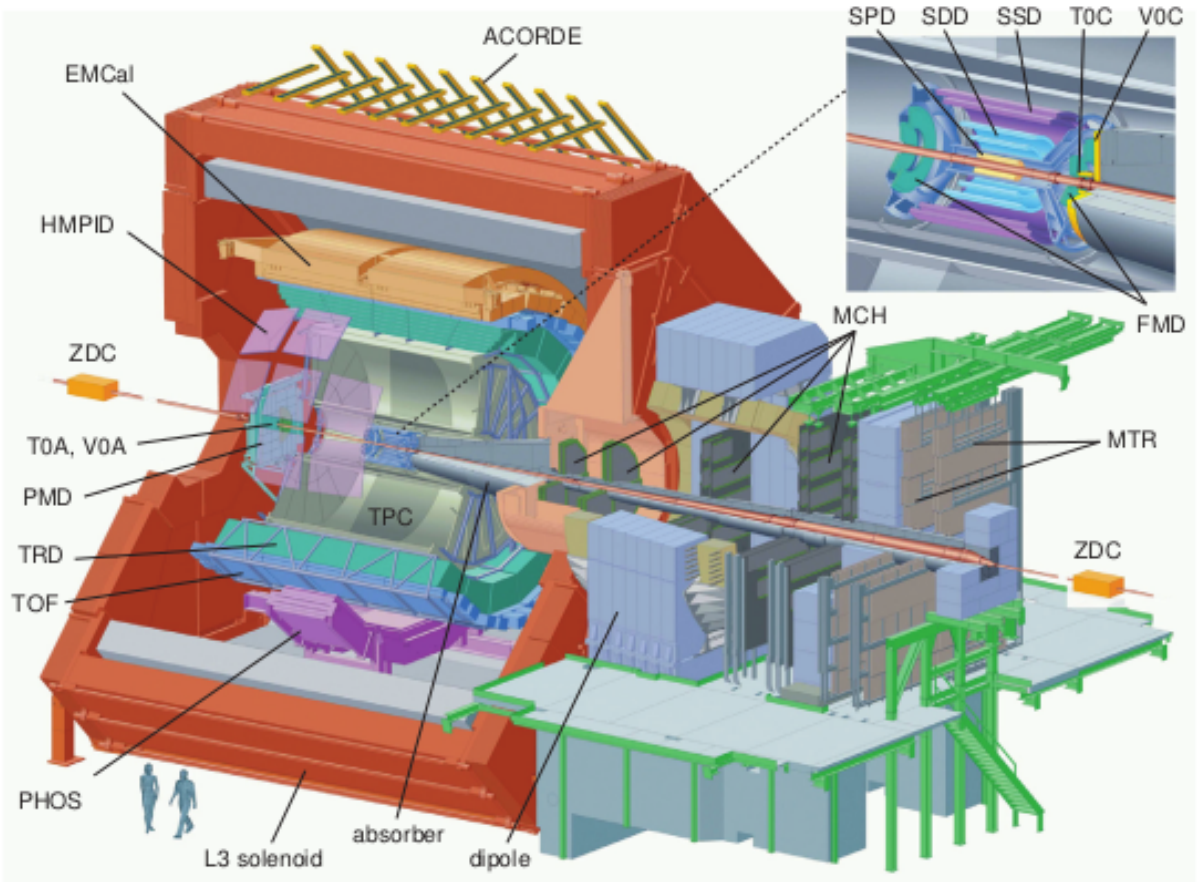

Figure 3.2: The schematic view of ALICE detector [76].

with the heavy-ion collisions, p–p and proton-nucleus (p–Pb) collisions are also investigated, which provides the baseline of the dynamics of heavy-ion collisions[76]. Some of the strengths of ALICE are the following:

- It is optimised to perform in high-multiplicity environment.
- It has high detector granularity.
- It is very efficient in identifying particles with momentum up to 20 GeV/c [76].
- It can measure tracks with very low-transverse momenta (p_T), up to 150 MeV/c [76].

The schematic diagram of ALICE and its sub-detectors is shown in Fig. 3.2. Its total weight is close to 10^4 ton and overall dimensions are $16 \times 16 \times 26$ m^3. It consists of 17 sub-detectors that can be catagorised into three types: central-barrel detectors, forward detectors, and the Muon spectrometer [76]. The central-barrel detectors are the Inner Tracking

System (ITS), Time Projection Chamber (TPC), Transition Radiation Detector (TRD), Time Of Flight detector (TOF), Photon Spectrometer (PHOS), Electromagnetic Calorimeter (EMCal), and High Momentum Particle Identification Detector (HMPID), which are surrounded by the L3 solenoid magnet having a magnetic-field strength of 0.5 T. The ITS, TPC, TRD and TOF cover the full azimuth around the midrapidity region, ($|\eta < 0.9|$). The ITS and TPC are the main charged-particle tracking detectors of ALICE. The forward detectors are the Photon Multiplicity Detector (PMD), Forward Multiplicity Detector (FMD), Cherenkov detector T0, plastic scintillator detector V0 and Zero Degree Calorimeter (ZDC). The muon spectrometer is installed at one side along the beam direction, outside the solenoid.

All the detector systems are described in the following sections. The detectors whose data are primarily used in this analysis, such as ITS, TPC. TOF and V0, are discussed in detail in sections 3.3.1, 3.3.2, 3.3.4 and 3.4.1, respectively.

3.3 Central barrel detectors

3.3.1 Inner Tracking System (ITS)

The ITS [75, 76] is the innermost sub detector of ALICE, installed at the radial distances of $3.9 - 43$ cm from the beam pipe, covering the pseudorapidity range of $|\eta| < 0.9$. It has six cylindrical layers made of silicon detectors. The innermost two layers consist of Silicon Pixel Detectors (SPD), the intermediate two layers consist of Silicon Drift Detectors (SDD) and the outermost two layers consist of Silicon Strip Detectors (SSD). Fig. 3.3 shows the schematic view of the six layers of ITS. The main objectives of the ITS are to construct the primary vertex of the collisions along with the secondary vertices created due to the particle decays, to reconstruct the tracks of charged particles along with the TPC, and to identify the tracks with low-transverse momentum utilising the specific-energy loss (dE/dx) information.

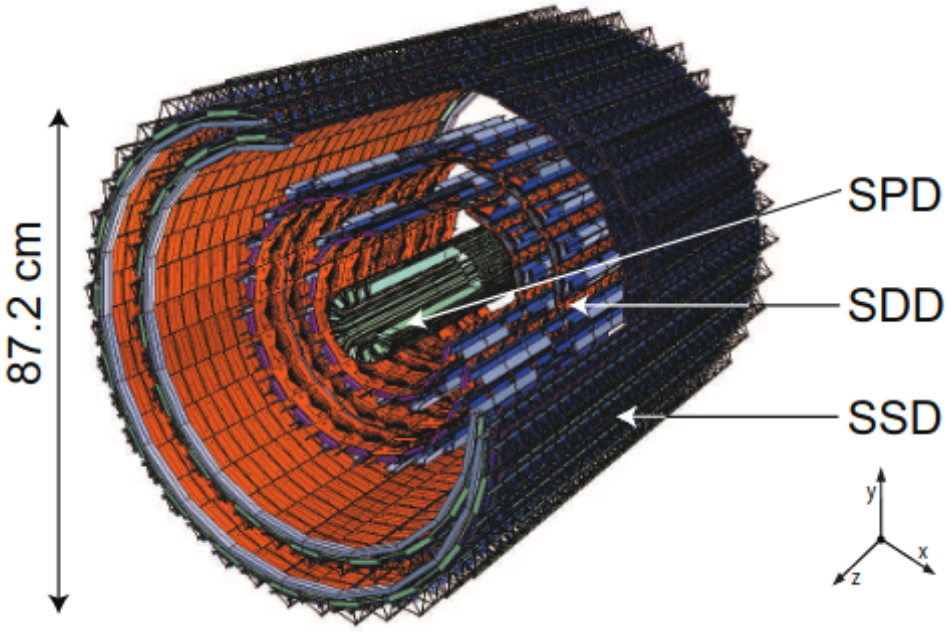

Figure 3.3: The schematic diagram of the ITS detector [77].

Silicon Pixel Detectors (SPD):

The SPD are the innermost layers of ITS (1^{st} and 2^{nd}), installed at the radial distances of 3.9 cm and 7.6 cm from the beam line, covering the pseudorapidity ranges $|\eta| < 2.0$ and $|\eta| < 1.4$, respectively. The layers consist of 9.8×10^6 hybrid silicon pixel detectors. The spatial resolution of SPD is 12 μm ($r\phi$) and 100 μm (z) and the readout time is 300 ns. The primary goal of the SPD is to construct the primary vertex of the collisions and to provide proper triggers to initiate the data-taking process. Additionally, for the tracks with $p_{\mathrm{T}} > 1.3$ GeV/c, the SPD aids in achieving a impact-parameter resolution of greater than 50 μm.

Silicon Drift Detectors (SDD):

The SDD consists of two middle layers (3^{rd} and 4^{th}) of ITS, located at the radial distances of 15.0 cm and 23.9 cm, respectively, covering the pseudorapidity range of $|\eta|<0.9$. Their spatial resolution is 35 μm ($r\phi$) and 25 μm (z) and the readout time is 6.4 μs. It is segmented into two drift regions by the central cathode. When particles hit the detector, they create ionisation electrons that traverse in the opposite direction of the applied drift field. The $r\phi$ position of a

particle is calculated by estimating the drift time, while the z position is calculated by measuring the centroid of the charge deposited in the anodes. The main objectives of this detector are to separate the tracks and identify the low-momentum particles using $\mathrm{d}E/\mathrm{d}x$ measurements.

Silicon Strip Detectors (SSD):

The two outermost layers (5^{th} and 6^{th}) of ITS are made of SSD, placed at the radial distances of 38.0 cm and 43.0 cm, respectively, covering the pseudorapidity range of $|\eta|$<1.0. The SSDs are made of double-sided silicon detectors. Their spatial resolution is 27 μm ($r\phi$) and 830 μm (z) and the readout time is 1 μs. They are used in track reconstruction by connecting the tracks from the TPC to ITS and are also used in particle identification.

3.3.2 Time Projection Chamber (TPC)

The TPC [78] is the main tracking detector in ALICE, installed in the central barrel of the ALICE detector covering the ITS, at the radial distances of 85−247 cm from the beam pipe and covers the pseudorapidity range of $|\eta|<$ 0.9 with the full azimuthal coverage. Its length is 510 cm along the beam direction. A uniform magnetic field of 0.5 T along the z-direction, generated by the L3 magnet is maintained in this detector. The TPC layout is shown in Fig. 3.4. Its objectives are the following:

- To estimate the momenta of particles by measuring their trajectories in the magnetic field of the L3 solenoid.
- To identify the tracks.
- To estimate the primary vertex, together with the ITS, TRD and TOF detectors.

The TPC is a gaseous detector with a cylindrical shape, having a mixture of Argon (Ar) and CO_2 in a proportion of 88:12. The total volume of the gas mixture inside the TPC is 90 m^3. The Central Electrode (CE) positioned at the nominal interaction point divides the volume into two halves. A high voltage of $\sim$ 100 kV is applied to the CE, which produces a drift field of 400 V/cm between the CE and two end-plates. Both of the end-plates are divided into 18

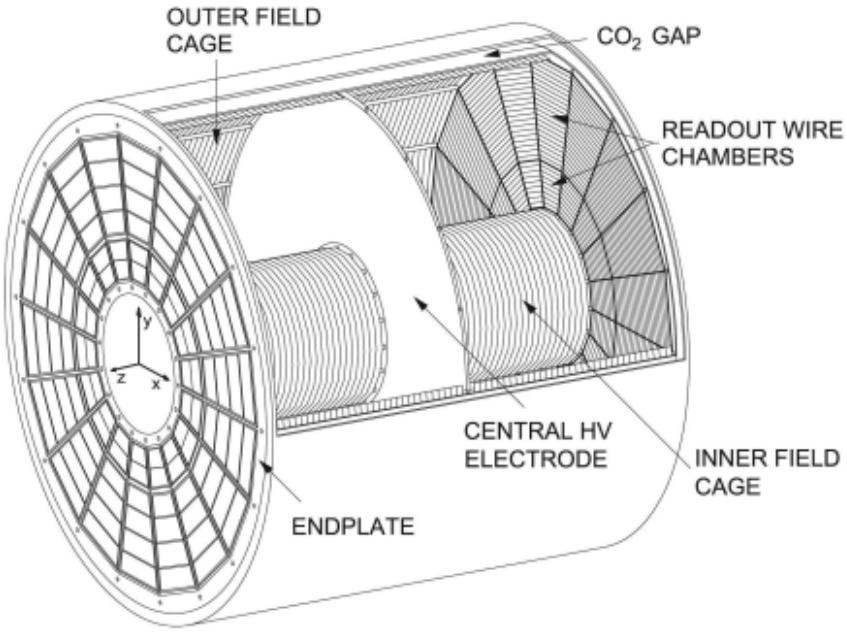

Figure 3.4: The layout of the TPC detector [78].

trapezoidal sectors, where the Multi-Wire-Proportional Counters (MWPC) with cathode-pad readout are installed. Each sector is further subdivided into two chambers, Inner Read-Out Chamber (IROC) covering the radial range of 85 cm $\leq r \leq$ 132 cm and an Outer Read-Out Chamber (OROC) covering the radial range of 135 cm $\leq r \leq$ 247 cm [75, 78]. In the pad planes of IROC and OROC, three different sizes of readout pads are used. There are 557568 pads in TPC readouts and the dimensions of the pads vary from 4×7.5 mm^2 in IROC to 6×15 mm^2 in OROC. Each sector of the TPC has 159 pad-rows [76].

When a charged particle traverses through the TPC, it ionises the gas and produces electrons. These electrons then drift towards the end plate with a constant velocity due to the uniform electric field and produce a signal on a few neighbouring pads in each pad-row. This signal is used to reconstruct one cluster per pad-row, and hence, there can be a maximum of 159 clusters [76] contributing to the trajectory of one particle. The readout chambers present in the end plates estimate the two-dimensional position of the incoming electrons and their arrival times. By measuring the drift velocity, the third spatial dimension of the particle along beam direction is also reconstructed.

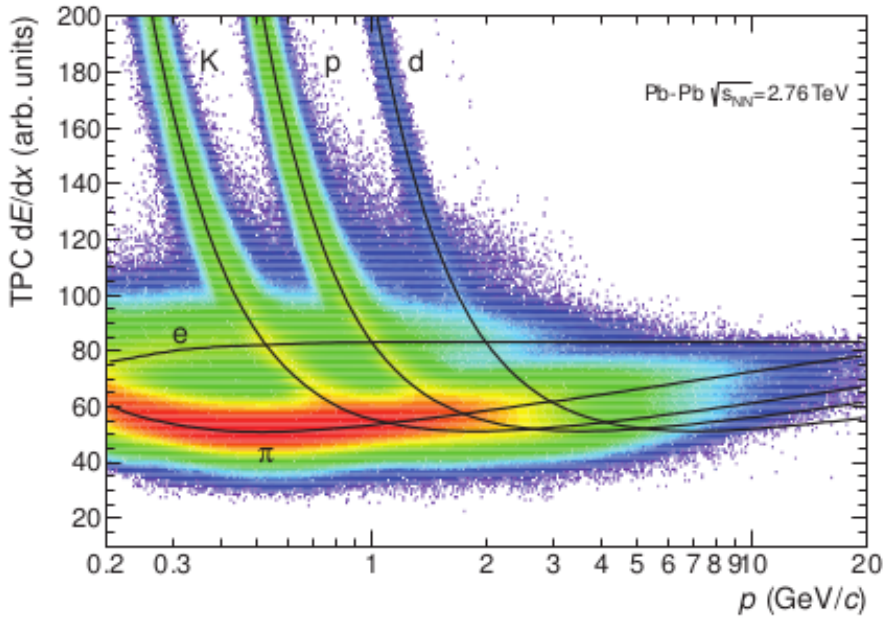

Figure 3.5: The specific-energy loss ($\mathrm{d}E/\mathrm{d}x$) in the TPC as a function of particle momentum in Pb–Pb collisions at $\sqrt{s_{\mathrm{NN}}} = 2.76$ TeV. The solid lines correspond to the parametrisations of the expected mean energy loss [76].

The identification of charged particles using the TPC is carried out by estimating the specific-energy loss ($\mathrm{d}E/\mathrm{d}x$) as a function of momenta of the particles [76]. The total charge in any pad-row is proportional to the energy loss of the particle at that point of its trajectory when it hits that pad. The energy loss of a particle inside the TPC as a function of momenta can be estimated using Bethe-Bloch formula which is given in Eq. (3.1) [79].

$$\frac{\mathrm{d}E}{\mathrm{d}x} = \frac{4\pi N e^4}{m_e c^2}\frac{z^2}{\beta^2}\left(ln\left(\frac{2m_e c^2\beta^2\gamma^2}{I}\right) - \beta^2 - \frac{\delta(\beta)}{2}\right). \tag{3.1}$$

In Eq. (3.1), m_e and e are the mass and charge of the electron, respectively, N is the number density of electrons in the medium, z and β denote the charge and velocity of the projectile, respectively, I is the mean excitation energy of the medium and $\delta(\beta)$ is a material-dependent correction term. In Fig. 3.5, the TPC-$\mathrm{d}E/\mathrm{d}x$ distribution as a function of particle momentum is shown. The distinct bands which are separated over a wide range of momenta correspond to different species of the charged particles e.g. electrons, pions, kaons, protons and deuteriums. The black solid lines are obtained using the Bethe-Bloch parametrisation for

each particle species. The TPC can provide the dE/dx resolution up to 6.5% in the most central collision (0-5%) in Pb–Pb system and 5.2% in pp collisions [76].

3.3.3 Transition Radiation Detector (TRD)

The TRD [76] is placed at the radial distances of 290−368 cm from the nominal interaction point surrounding the TPC with the pseudorapidity coverage of $|\eta| < 0.8$ and full azimuthal coverage. It is made of 18 supermodules. Each of the supermodules has 6 layers of Multi-Wire Proportional Chamber (MWPC), filled with Xe-CO_2, which are arranged in 5 stacks along the direction of beam-line. The main objective of TRD is to separate electrons from the charged particles.

3.3.4 Time Of Flight (TOF)

The TOF detector [76, 80] is the outermost layer of the central-barrel detectors with the barrel length of 745 cm. It is installed at the radial distances of 370−399 cm from the beam line with $|\eta| < 0.9$ and full azimuthal coverage, having an effective area of ∼141 m^2. Its main objectives are to identify the charged particles in the intermediate momentum range, i.e. up to 2.5 GeV/c for pions and kaons and up to 4 GeV/c for protons, and to provide the trigger for cosmic ray events and ultra-peripheral collisions. It consists of 1593 Multigap Resistive Plate Chamber (MRPC) strip detectors, divided into 18 azimuthal sectors in the azimuthal plane. Each MRPC strip is divided into two rows of 48 pickup pads of the size 3.5×2.5 cm^2, for a total of 96 pads for each strip and 152928 readout channels, which guarantees low detector occupancy. The average MRPC time resolution is estimated to be better than 50 ps. The schematic layout of TOF is given in Fig. 3.6.

The velocity of charged particles (v) in terms of $\beta = v/c$, can be measured by calculating the time of flight "t" and the length of trajectory "L". The TOF can perform particle identification using the momentum information obtained from other detectors and measuring the mass of

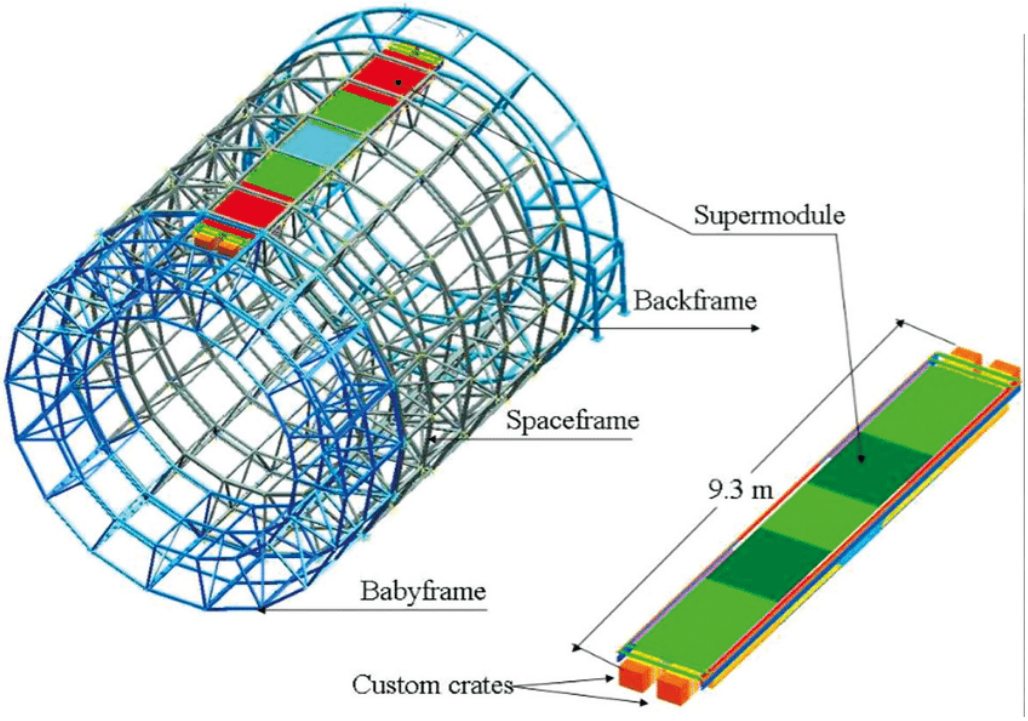

Figure 3.6: The layout of the TOF detector [75].

the particles using Eq. (3.2).

$$m^2 = \frac{p^2}{c^2}\left(\frac{c^2t^2}{L^2} - 1\right). \tag{3.2}$$

If two charged particles have the same momentum (p) and track length (L) but different masses (suppose, m_1 and m_2), they can be identified using the number of standard deviations shown in Eq. (3.3).

$$n_\sigma = \frac{t_1 - t_2}{\delta t} = \frac{\Delta t}{\delta t}, \tag{3.3}$$

where t_1 and t_2 are the time taken by the particles with mass m_1 and m_2, respectively, to traverse through the TOF and δt is the time resolution of the TOF. The Δt can be estimated using Eq. (3.4).

$$\Delta t = \frac{L}{2c}\left(\frac{m_1^2c^2 - m_2^2c^2}{p^2}\right). \tag{3.4}$$

The velocity distribution of charged particles as a function of momentum is shown in Fig. 3.7, where it is observed that the information of pions and kaons are well separated up to 2.5 GeV/c and for protons, up to 4 GeV/c.

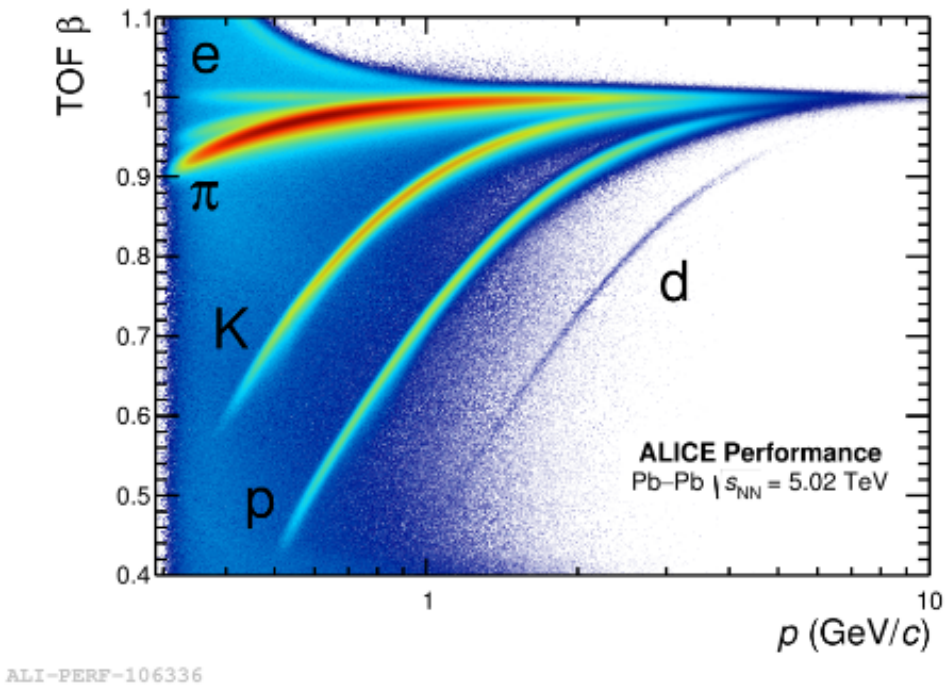

Figure 3.7: The velocities (β) of the particles measured by the TOF detector as a function of charged-track momentum in Pb–Pb collisions at $\sqrt{s_{\mathrm{NN}}}$ = 5.02 TeV [80].

3.3.5 High-Momentum Particle Identification Detector (HMPID)

The HMPID [76, 81] is made of seven identical Ring-Imaging Cherenkov (RICH) modules, installed at 500 cm from the beam line, covering the pseudorapidity range of $|\eta| < 0.6$ and azimuthal range of $1^\circ < \phi < 59^\circ$. It consists of liquid perfluorohexane (C_6F_{14}) radiator and MWPC, together with a pad-segmented, CsI-coated photo cathode, which has an active area of 10.3 m^2 [81]. It covers $\approx 5\%$ of the TPC acceptance. It is used to identify pions and kaons up to $p_{\mathrm{T}} = 3$ GeV/c and protons up to $p_{\mathrm{T}} = 5$ GeV/c with 3σ separation.

3.3.6 Photon Spectrometer (PHOS)

The PHOS [75, 76] is an electromagnetic calorimeter, made of dense scintillating Lead Tungstate ($PbWO_4$), installed outside the TOF, at a distance of 460 cm from the beam line. It covers the pseudorapidity range of $|\eta| < 0.12$ and azimuthal range from 220° to 320°. Its main

goal is to estimate the direct photons coming out of the hot QCD matter as well as the photons produced from the decay of neutral mesons.

3.3.7 Electromagnetic Calorimeter (EMCaL)

The EMCAL [75, 76] is a Pb-scintillator calorimeter, installed at the radial distance of 430 cm from the beam line, opposite to the PHOS, covering the azimuthal range from 80° to 187° and the pseudorapidity range of $|\eta| < 0.7$ (much higher than PHOS). It gives fast and efficient triggers (L0, L1) for electrons, photons and hard jets. It is also used to investigate the jet-quenching effect via probing the jet interactions in the QCD .

3.4 Forward Detectors

3.4.1 V0 scintillator arrays

The V0 detector [75, 82] is one of the forward detectors of ALICE, made up of two arrays of scintillator counters. As shown in Fig. 3.8, they are placed inside the L3 solenoid on both sides of the nominal interaction point of ALICE along the z axis in an asymmetric way. The V0A is installed at $z = 329$ cm on the A (ATLAS) side and V0C is placed at $z = -88$ cm on the C (CMS) side, which is much closer to the nominal interaction point ($z = 0$). The coverage of pseudorapidity for V0A and V0C are $2.8 < \eta < 5.1$ and $-3.7 < \eta < -1.7$, respectively.

The main objectives of the V0 detectors are the following:

- To provide the minimum bias and centrality triggers.
- To measure the charged-particle multiplicity in the forward region.
- To separate the beam-beam interactions from the beam-gas ones.
- To estimate the event plane by measuring the azimuthal distribution of the charged particles.
- To estimate the luminosity of LHC beams.

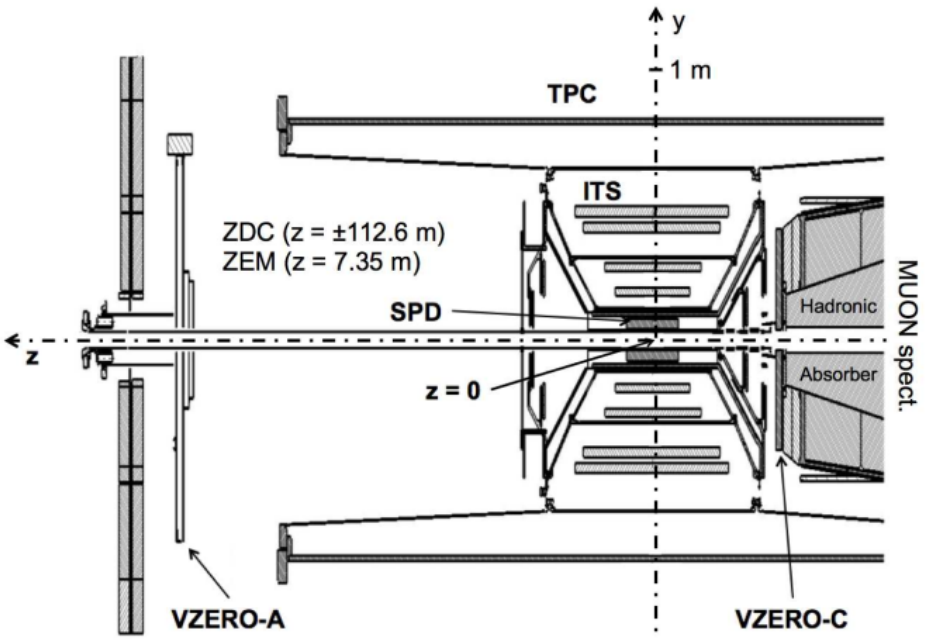

Figure 3.8: The cross-section of inner part of the ALICE along beam direction indicating the positions of two V0 (VZERO) detector arrays [82].

3.4.2 T0 detectors

The T0 [75, 76] detector consists of two arrays of Cherenkov counters (T0A and T0C), placed near the beam pipe on both sides of the nominal interaction point. The T0A is installed at z = 375 cm and covers a pseudorapidity range of $4.6 < \eta < 4.9$ while the T0C is located at z = −72.7 cm, covering a pseudorapidity range of $-3.3 < \eta < -3.0$. The main objectives of T0 are the estimation of "start" time of the interaction as well as to measure its longitudinal position. The T0 also estimates the luminosity of the beam.

3.4.3 Photon Multiplicity Detector (PMD)

The PMD [75] is made of two proportional gas chambers with lead-converter plates between them, placed at z=364 cm on the A side. It has a pseudorapidity range of $2.3 < \eta < 3.7$ with full azimuthal coverage. Its main objectives are to estimate the number of photons in the forward region and measure the reaction plane.

3.4.4 Forward Multiplicity Detector (FMD)

The FMD [75, 76] is made up of three rings of silicon semiconductor detectors, placed at -70 cm, 80 cm and 320 cm along the beam axis, which cover the region $-3.4 < \eta < -1.7$, $1.7 < \eta < 3.7$ and $3.6 < \eta < 5.0$, respectively. Its main objective is to estimate the multiplicity of charged particles.

3.4.5 Zero Degree Calorimeter (ZDC)

The ZDCs [75, 76] consist of two sets of ZDC, namely ZN and ZP, which are made up of two tungsten-quartz neutron and two brass-quartz proton calorimeters, respectively. They are installed near the beam pipe at a distance of 113 m from the nominal interaction point with almost zero azimuthal coverage. The ZDCs are mainly used to select the minimum bias events, estimate the centralities of collisions by counting the numbers of spectator nucleons and calculate the absolute luminosity of the beam. A third set of ZDC, electromagnetic lead-quartz calorimeter (ZEM), made of two modules are placed on both sides of the beam line at the region $4.8 < \eta < 5.7$ to resolve the ambiguity between the most peripheral and most central collisions [76].

3.5 Muon Spectrometer

The Muon spectrometer [75, 76] is used to measure the light vector mesons and quarkonium production as well as high p_{T} muons, which are mainly the decay product of charm and beauty quarks. It is installed at the C side with the pseudorapidity coverage of $-4.0 < \eta < -2.5$. It consists of a hadron absorber of around 10 nuclear-interaction lengths (λ_{int}), a dipole magnet of 3 T−m along with five tracking stations, each having two pad chambers (Muon Chambers, MCH) and two further stations (Muon Trigger, MTR), placed behind an additional $7\lambda_{\mathrm{int}}$ absorber. The MTR provides the single-muon and muon-pair triggers.

3.6 A Cosmic Ray Detector (ACORDE)

ACORDE [75, 76, 83], the cosmic ray detector of ALICE, consists of an array of 60 plastic scintillator counters and is placed on the top of the L3 magnet at a radial distance of 850 cm from the interaction point. It has the pseudorapidity range of $|\eta| \leq 1.3$ with azimuthal coverage of $30^\circ < \varphi < 150^\circ$. It detects the atmospheric muons and multi-muon events along with the TPC, TRD and TOF. It also provides a fast trigger signal (L0) for the calibration and alignment of several detectors e.g. the ITS and TPC.

3.7 Trigger

The trigger signals [76] are required to start the process of data taking in ALICE. They are generated by various fast detectors (SPD, TRD, TOF, PHOS, EMCal, ACORDE, V0, T0, ZDC, MTR) having various trigger levels, which is then collected by the Central Trigger Processor (CTP) and sent to other detectors. The input signals are evaluated by the CTP in every $\sim$ 25 ns time interval [76]. In this analysis, the "kINT7" or "V0AND Minimum bias", "kCentral" and "kSemiCentral" triggers are primarily used. These are V0-based trigger signals, which are generated after the particles hit both of the V0A and V0C detectors. The main objective of kINT7 trigger is to record only the collisions between accelerated particles and reject all other events (background) e.g. beam-gas interactions. The kCentral and kSemiCentral triggers are used to select the 0-10% and 30-50% centrality events, respectively [76], by applying a cut to the recorded multiplicity.

3.8 Event and Track reconstruction

The event and track reconstruction are very complex procedures. The primary estimation of the interaction vertex is performed by reconstructing short tracklets using the clusters from the SPD layers and extrapolating those tracklets to the beam line. The point where most of the tracklets converge is tagged as the primary vertex.

The tracks of charged particles are reconstructed in the mid-rapidity region in a three-step process using the Kalman-filter technique in each step [84]. The outer clusters of TPC are used to reconstruct the track seeds, which are then propagated inwards by scanning each pad-row to locate the closest cluster. These "TPC-standalone" tracks are then extrapolated to the outer layer of ITS. For each TPC track, several ITS tracks are reconstructed using the seeds in all six layers of ITS and propagating them inwards. The ITS tracks with highest quality are used to construct the global tracks together with the TPC tracks. In the next step, the tracks are extrapolated outwards from the innermost layer of ITS by refitting the seeds found at the first stage. In this stage, the tracks are propagated beyond the TPC, i.e. to the TRD, TOF, the calorimeters and HMPID. At the last stage, the tracks are again refitted inwards from the outer layer of TPC to the innermost layer of ITS and the global tracks are constructed.

The process of final reconstruction of the primary vertex using the global TPC-ITS tracks is as follow [76]: for each track, the point having closest approach to the beam line is estimated and the points which are very far from others are removed. The vertex position is calculated by taking the average of remaining points. In the final step, the global tracks are weighted according to their closest distances from the preliminary vertex position. The final position of principal-interaction vertex is estimated by fitting the weighted global tracks.

3.9 Centrality determination

The properties of the system produced in collisions of heavy ions depend on the initial collision geometry, which is described in terms of the impact parameter (b) i.e. the minimum distance between the centers of colliding nuclei in the transverse plane [85]. For head-on collisions ("central" collisions), the impact parameter is very small, resulting the overlapping region between two ions to be maximum with the maximum number of participants, whereas, for the collisions with large impact parameters ("peripheral" collisions), the overlapping region is very small with a few participants. Since the impact parameter cannot be measured directly, the "centrality" of a collision is represented as the percentage of total cross-section of hadronic in-

teractions, where the most central collisions correspond to the smallest centrality class (0-5%) and the peripheral events correspond to the larger centrality class (50-90%).

The centrality is mainly estimated by measuring the total amplitude in V0A and V0C detectors. In Fig. 3.9, the distribution of V0 amplitude in Pb–Pb collisions at $\sqrt{s_{\mathrm{NN}}} = 2.76$ TeV is shown, which is fitted using a Glauber Monte Carlo model. The collision geometry in the Glauber model is described using the nuclear density profile, assuming the linear trajectory of nucleons and selecting the binary nucleon–nucleon collisions, which utilises the inelastic nucleon–nucleon cross section [76]. For a given impact parameter, the number of nucleon–nucleon collisions ($\mathrm{N_{coll}}$) and the number of participant nucleons ($\mathrm{N_{part}}$) are estimated, which are used in calculating the number of particle-sources as given in Eq. (3.5).

$$N_{\mathrm{source}} = fN_{\mathrm{part}} + (1 - f)N_{\mathrm{coll}} \tag{3.5}$$

where, f corresponds to the relative contribution from the soft processes while $(1 - f)$ corresponds to the relative contribution from the hard processes. The particle distribution from each source is fitted with a negative binomial distribution (NBD) with fit parameters μ and k. The parameters f, μ and k are shown in Fig. 3.9 [76]. The total number of hadronic interactions is estimated by integrating the fit function. The region that contains up to 90% of the total interaction cross section is pointed out, which is then divided into various centrality classes.

3.10 Data structure

The detectors record the raw data, which is then reconstructed by a software, called AliRoot, developed with C++ based ROOT framework. The reconstructed data is saved as the Event Summary Data (ESD) object. The ESD objects consist of all information regarding the events, tracks along with some detector-level information. However, the ESD objects are very large in size and some of its information are not relevant for the physics analyses. Therefore, ESD files are further filtered to produce Analysis Object Data (AOD) files which are much smaller in size, much faster to process and contain only the relevant information for the physics analyses. The ESD and AOD objects are stored as AliESDs.root and AliAOD.root, respectively.

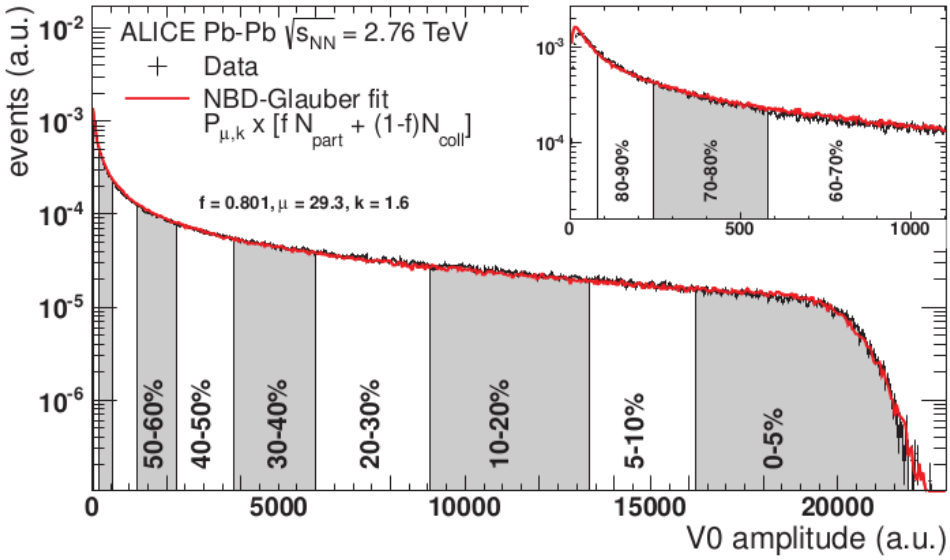

Figure 3.9: The distribution of number of the events as a function of the V0 amplitude, where the red line is the model fitting. The inset shows a magnified version of the most peripheral region [76].

The analysis presented in this thesis has been performed using the AOD objects.

Chapter 4

Pion-kaon femtoscopic correlation in Pb–Pb collisions at $\sqrt{s_{\rm NN}}$ = 5.02 TeV

4.1 Introduction

The femtoscopic correlations of pion-kaon pairs has been explored in Pb–Pb collisions at $\sqrt{s_{\rm NN}}$ = 5.02 TeV with ALICE detector at the LHC. The main objectives of this study are to investigate the dependence of source size ($R_{\rm out}$) and pair-emission asymmetry ($\mu_{\rm out}$) on the beam energy as well as the collectivity of the system by probing the two-particle momentum-correlation functions. The size of pion-kaon system is suggested to be the convolution of radii of the sources emitting pions and kaons with similar velocities[63]. This study also focuses on the dependence of pion-kaon source size on the pair $k_{\rm T}$, $m_{\rm T}$ and pair-transverse velocity ($\beta_{\rm T}$). Additionally, the dependence of $\mu_{\rm out}$ on the $k_{\rm T}$, $m_{\rm T}$ and $\beta_{\rm T}$ is also studied for the first time to understand its behaviour with the collectivity of the system.

4.2 Experimental dataset

The analysis is performed using the datasets (called as "production") for Pb–Pb collision at $\sqrt{s_{\rm NN}}$ = 5.02 TeV, collected in the year 2018 for two different polarities of magnetic field. The datasets are LHC18q_pass3 ((+)ve magnetic field polarity) and LHC18r_pass3 ((-)ve magnetic

field polarity), which can be found in https://alimonitor.cern.ch/production/raw.jsp. Each dataset consists of several run numbers, each run number contains information about some finite number of events.

The General-Purpose Monte Carlo events, associated with each datasets of Pb–Pb events are generated using various models e.g. A Multi-Phase Transport (AMPT) Model, Heavy-Ion Jet INteraction Generator (HIJING), THERMal heavy-IoN generATOR (THERMINATOR) etc. In this analysis, the HIJING Monte Carlo events recorded as the dataset LHC20e3a (anchored to LHC18q,r) are used, where the responses of various detectors are modeled using GEANT4. The Monte Carlo events are analysed to estimate the track-reconstruction efficiency, contamination from secondary particles and particle-identification purity of the pion and kaon samples, which are described in section 4.5.

4.3 Analysis software

The analysis is performed using the AliFemto and AliFemtoUser packages under AliPhysics and AliRoot framework, developed by the ALICE Collaboration. The link to the packages are following:

- https://github.com/alisw/AliPhysics/tree/master/PWGCF/FEMTOSCOPY/AliFemto
- https://github.com/alisw/AliPhysics/tree/master/PWGCF/FEMTOSCOPY/AliFemtoUser.

The configuration file which contains the necessary classes to perform this analysis can be found in https://github.com/alisw/AliPhysics/tree/master/PWGCF/FEMTOSCOPY/macros/Train/NonIdParticleFemto/PionKaonFemto/mixevent_pileupEvent_config/ConfigFemtoAnalysis.C.

4.4 Analysis strategy

4.4.1 Event selection

To perform the physics analysis, the process of selecting the collisions (events) of two heavy ions has to be optimised. Different physics-selection procedures are utilised to select the good events, by which the beam-gas interactions and pile-up events are reduced significantly. The very first step of selecting the events is to apply the physics-selection procedure, by which several collisions are selected according to the trigger class, as discussed in section 3.7. The beam-gas interactions are discarded using the arrival time of the signal in two V0 arrays. In case of Pb–Pb interactions, the collisions of one main and one satellite bunch are rejected using the correlation of arrival times of the signals in neutron ZDCs. In this analysis, the kINT7 (minimum bias), kCentral and kSemiCentral triggers are used.

The next step is to select the primary vertex of the interaction. Only those events for which the primary vertices are reconstructed, are selected for the analysis. There has to be at least one track that contributes to the determination of primary vertex. The z positions of reconstructed vertices ($z_{\rm vtx}$) are taken within 7.0 cm with respect to the nominal interaction point of the ALICE detector. The uniform acceptance of the tracks within $|\eta| < 0.8$ in both the ITS and TPC detector is ensured by selecting $z_{\rm vtx} \leq \pm 7.0$ cm. Also, the pile-up events that are reconstructed at the SPD detector are removed.

The analysis is carried out for 0−5%, 5−10%, 10−20%, 20−30%, 30−40%, 40−50%, 50−60%, 60−70% and 70−80% centrality classes (discussed in section 3.9). The total number of events that are selected for this analysis is $\sim$ 92.8 million. The $z_{\rm vtx}$ distributions of the events are shown in Fig. 4.1.

4.4.2 Track selection

The event-selection criteria is followed by the selection of good tracks. As this analysis focuses on the interactions between primary pions and kaons, a set of conditions are applied to

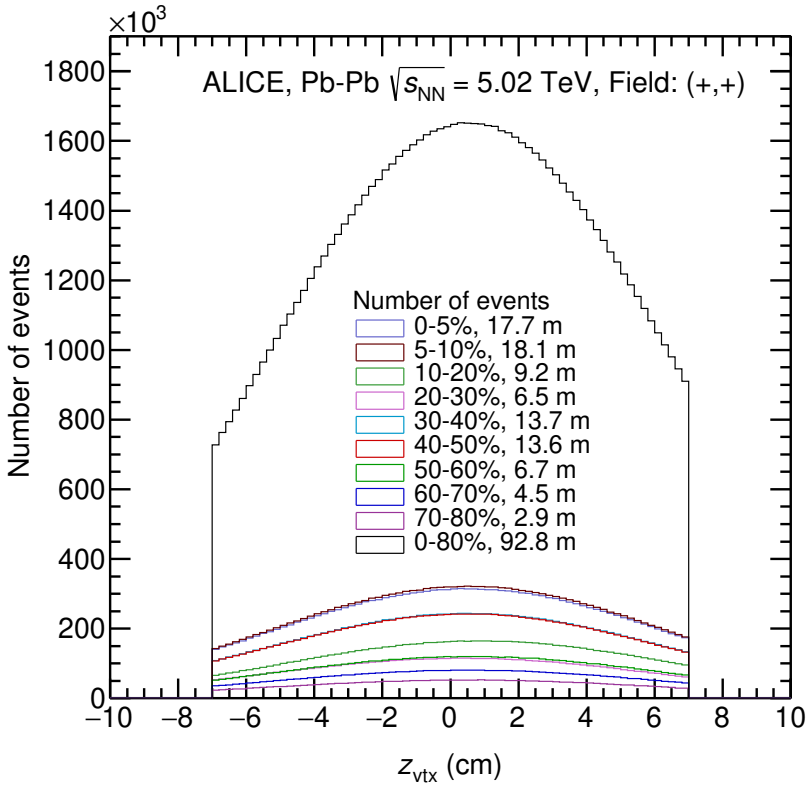

Figure 4.1: The distribution of z position of the primary vertex for Pb–Pb collisions at $\sqrt{s_{\mathrm{NN}}}$ = 5.02 TeV in ALICE.

select the primary-charged particles and also, to reduce the number of secondary tracks, tracks with low quality, false trajectories etc.

In this analysis, the "TPC only tracks", i.e. the tracks of charged particles that are reconstructed using the TPC detector are chosen. A set of pre-defined cuts, named "FilterBit7", is used to select these stand-alone TPC tracks. The details about FilterBit7 can be found in `https://twiki.cern.ch/twiki/bin/view/ALICE/AddTaskInfoAOD145` and `https://twiki.cern.ch/twiki/bin/viewauth/ALICE/PWGPPAODTrackCuts`. The pseudorapidity range is taken to be $|\eta| < 0.8$. The minimum number of TPC clusters which are required to reconstruct a track is taken to be 70 out of 159. The χ^2 per number of cluster of the momentum fit in the TPC is taken to be less than 4.0 to reduce the contribution from uncorrelated combination of clusters. Each track has to have at least one hit in one of the two inner layers of ITS or TOF to reject the track pile-up.

Ideally, all tracks should be reconstructed in such a way that their point of origin should be the primary vertex. But, due to the limitation in detector resolution, there is always a separation between the primary vertex and point of origin of the track. This distance of closest approach (DCA) of the track to the primary vertex is estimated using the Global-track information i.e. combining the tracks reconstructed using the ITS and TPC detectors. The DCA in z direction ($DCA_{\rm z}$) and x-y plane ($DCA_{\rm xy}$) are taken to be less than 0.3 cm. It is ensured that most of the pile-up events are rejected by using the $DCA_{\rm z}$ cut while most of the secondary vertices are rejected by applying the $DCA_{\rm xy}$ cut. This analysis is performed in three parts, which are the following:

- In the first part, the tracks are selected within the transverse-momentum range of 0.19 $<p_{\rm T}$ (GeV)/c <1.5 and no selection cut is applied on the $k_{\rm T}$ of the pair.
- In the second part, the tracks are selected from the same $p_{\rm T}$ range and the following $k_{\rm T}$ ranges: 400−500, 500−600 and 600−700 MeV/c to study the $k_{\rm T}$-dependence of the correlation functions.
- In the third part, the particles are chosen from a relatively broader $p_{\rm T}$ range of 0.1 $<p_{\rm T}$ (GeV)/c <2.5 and $\beta_{\rm T}$ ranges of 0.7−0.75, 0.75−0.8, 0.8−0.85, 0.85−0.9 and 0.9−0.95 to investigate the dependence of correlation function on the $\beta_{\rm T}$.

The selection criteria for the charged-particle tracks are listed in Table 4.1.

4.4.3 Particle identification

In this analysis, the identification of particles is performed using the information from both TPC and TOF detectors. The primary objective of this process is to identify relevant tracks with high purity and reduce the contamination from misidentified particles to a feasible extent.

The information on the specific-energy loss (dE/dx) of a track inside the TPC detector (discussed in section 3.3.2) and the time of flight of a track inside the TOF detector (discussed in section 3.3.4) are used to identify pions and kaons. The sampling of the tracks in various momentum ranges is performed using the $n\sigma$ method, which can be explained in the following

Kinematic limit	
$\|\eta\|$	≤ 0.8
p_{T}	[0.19, 1.5] GeV/c [0.1, 2.5] GeV/c
Track selection and uality	
FilterBit	7 (TPC only tracks)
χ^2/clusters of the momentum fit in the TPC	≤ 4
DCA_{XY}	0.3 cm
DCA_{Z}	0.3 cm
Minimum number of TPC clusters	70 out of 159
Track pile-up rejection	kTRUE

Table 4.1: The selection criteria for the charged-particle tracks

way: if A_{m} is a measured variable in a detector, A_{p} is the predicted value of that variable and σ_{resol} is the resolution of the detector, then $n\sigma$ can be defined as:

$$n\sigma = \frac{A_{\mathrm{m}} - A_{\mathrm{p}}}{\sigma_{\mathrm{resol}}} \tag{4.1}$$

A track is identified after applying a specific $n\sigma$ cut (e.g. 2σ, 3σ etc.) on that variable.

In case of the TPC detector, the difference of the measured specific energy loss of a track with the predicted one from the Bethe-Bloch parametrisation is calculated, which is used to estimate the $n\sigma_{\mathrm{TPC}}$ as given in Eq. (4.2).

$$n\sigma_{\mathrm{TPC}} = \frac{\mathrm{d}E/\mathrm{d}x_{\mathrm{measured}} - \mathrm{d}E/\mathrm{d}x_{\mathrm{predicted}}}{\sigma_{\mathrm{TPC}}} \tag{4.2}$$

where, $\mathrm{dE/dx}_{\mathrm{measured}}$ is the specific-energy loss inside the TPC detector, $\mathrm{dE/dx}_{\mathrm{predicted}}$ is the predicted specific-energy loss and σ_{TPC} is the TPC-dE/dx resolution.

Similarly, the $n\sigma_{\mathrm{TOF}}$ for a track is estimated by computing the difference of the measured time of flight of that track inside the TOF detector with the predicted one as given in Eq. (4.3).

$$n\sigma_{\mathrm{TOF}} = \frac{TOF_{\mathrm{measured}} - TOF_{\mathrm{predicted}}}{\sigma_{\mathrm{TOF}}} \tag{4.3}$$

where, TOF_{measured} and $TOF_{\text{predicted}}$ are the measured and predicted time of flight of the track inside the TOF detector, respectively and σ_{TOF} is the TOF-time resolution.

To select the identified track within some $n\sigma$ value, two conditions are always taken care of:

- A very wide $n\sigma$ cut is not applied to ensure that the contamination from misidentified tracks is less.
- A very narrow $n\sigma$ cut is not chosen to ensure that the selected sample has enough statistics.

Pion identification

The following $n\sigma_{TPC}$ and $n\sigma_{TOF}$ cuts are applied for pion selection:

- $|n\sigma_{TPC}| < 3.0$ for $|p|$ <500 MeV/c,
- $\sqrt{(n\sigma^2_{TPC} + n\sigma^2_{TPC})} < 3.0$ for $|p|$ >500 MeV/c.

Kaon identification

The following $n\sigma_{TPC}$ and $n\sigma_{TOF}$ cuts are applied for kaon selction:

- $|n\sigma_{TPC}| < 2.0$ for $|p|$ <400 MeV/c,
- $|n\sigma_{TPC}| < 1.0$ for 400 MeV/c < $|p|$ <450 MeV/c,
- $|n\sigma_{TPC}| < 3.0$ and $n\sigma_{TOF} < 2.0$ for 450 MeV/c < $|p|$ <800 MeV/c,
- $|n\sigma_{TPC}| < 3.0$ and $n\sigma_{TOF} < 1.5$ for 800 MeV/c < $|p|$ <1000 MeV/c,
- $|n\sigma_{TPC}| < 3.0$ and $n\sigma_{TOF} < 1.0$ for $|p|$ >1000 MeV/c.

The TPC-dE/dx distribution and TOF-time distribution for pions and kaons as a function of momentum are shown in Fig. 4.2 and Fig. 4.3, respectively. The p_{T}, η and ϕ distributions of pions and kaons are given in Fig. 4.4-4.5.

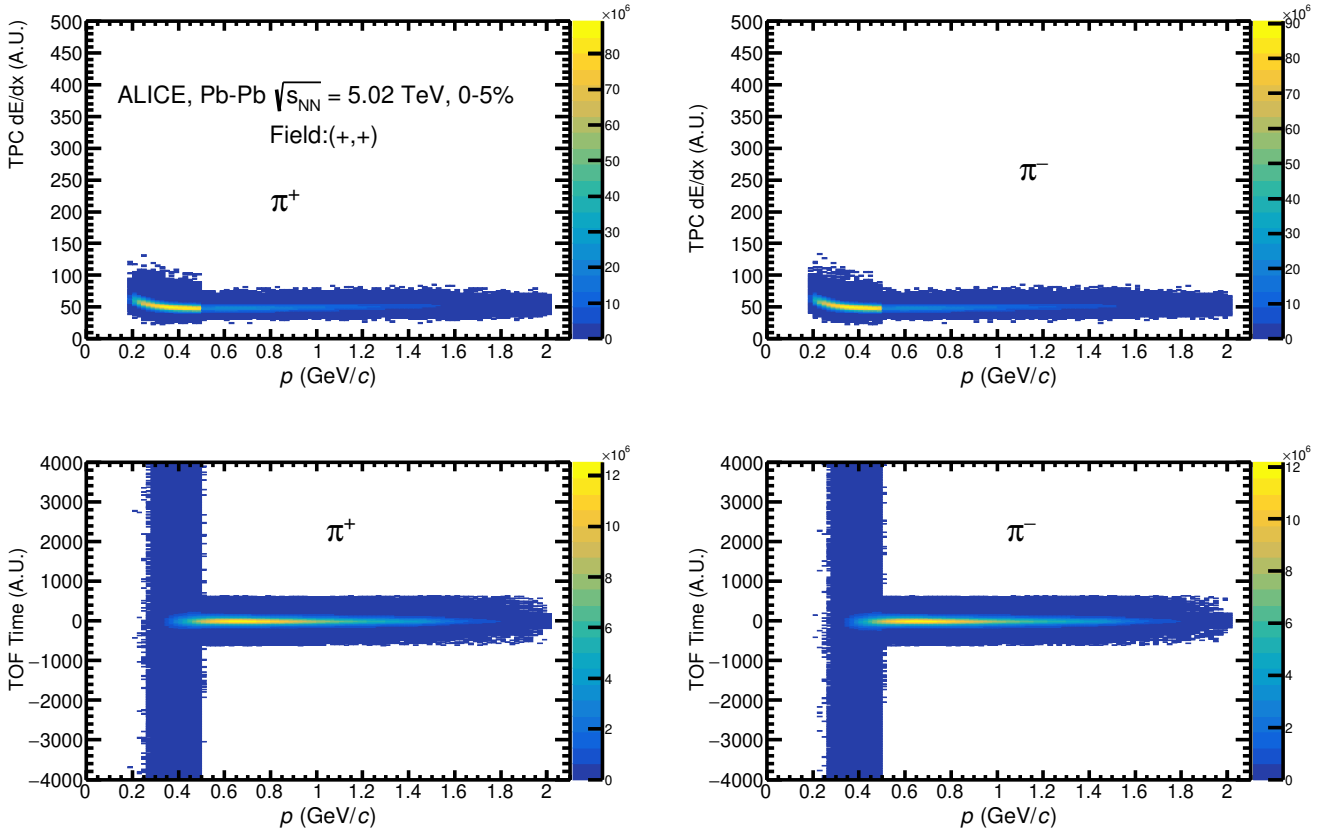

Figure 4.2: The TPC-dE/dx and TOF-Time distribution for pions as a function of momentum in Pb–Pb collisions at $\sqrt{s_{\mathrm{NN}}}$ = 5.02 TeV in ALICE.

After identifying the tracks, a pair is formed by selecting one track of pion and one track of kaon from the bunch of accepted tracks. Eventually the relevant variables are computed, which are used further in the analysis.

4.5 Track-reconstruction efficiency, secondary contamination and particle-identification purity

The track-reconstruction efficiency, secondary contamination and the particle purity are estimated using the Monte Carlo events, generated (and reconstructed) by the HIJING event generator. The event- and track-selection criteria that are used for this purpose are similar to the ones, used in the analysis of real events.

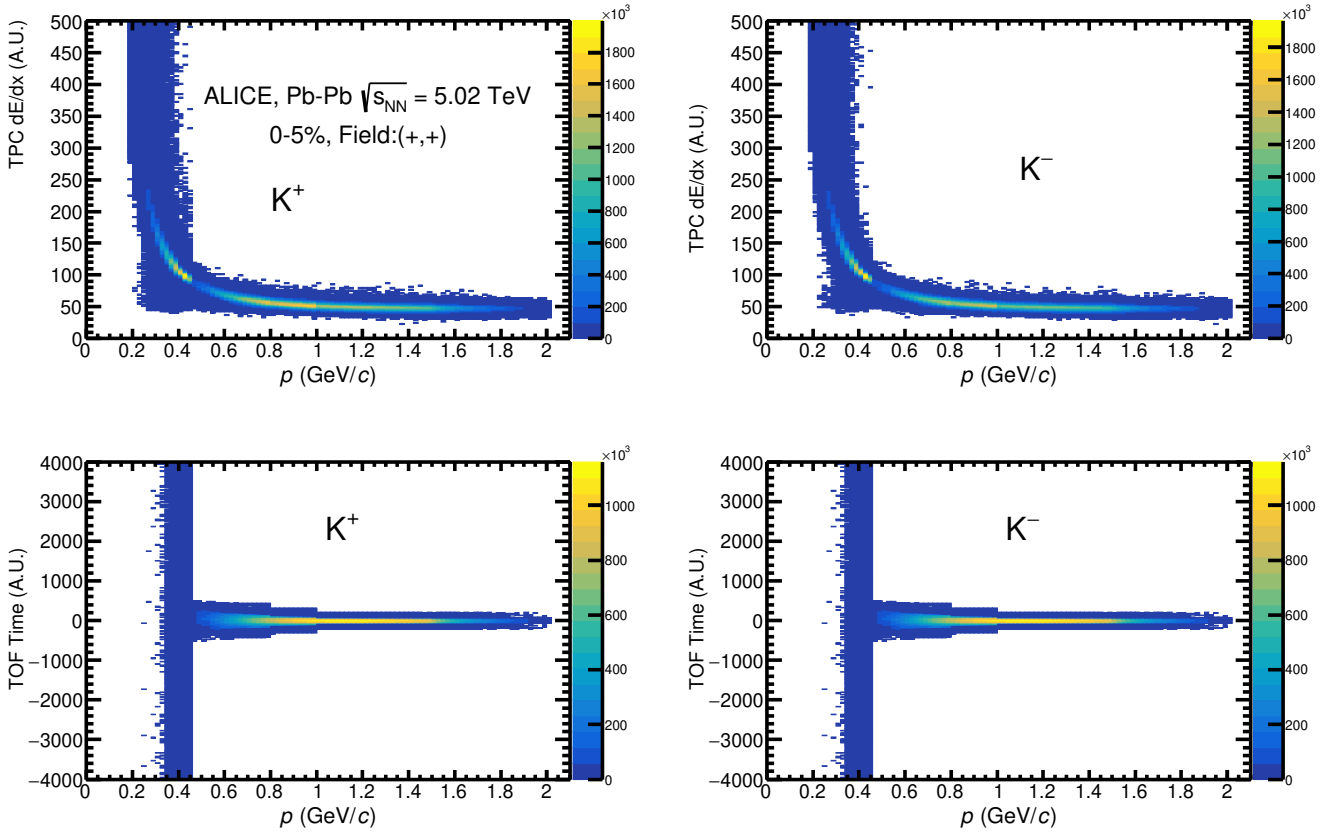

Figure 4.3: The TPC-dE/dx and TOF-Time distribution for kaons as a function of momentum in Pb–Pb collisions at $\sqrt{s_{\rm NN}}$ = 5.02 TeV in ALICE.

The track-reconstruction efficiency, ϵ, is the ratio of number of the measured primary particles (reconstructed-primary tracks) to the number of primary particles that would be measured in an ideal detector (generated-primary tracks):

$$\epsilon = \frac{N^{reconstructed}_{primaries}}{N^{generated}_{primaries}}. \tag{4.4}$$

The tracking efficiency for pions in two $p_{\rm T}$ ranges are shown in Fig. 4.6 and the same for kaons are shown in Fig. 4.7. It is observed that in each centrality class, the efficiency decreases significantly when the $p_{\rm T}$ is greater than 0.5 GeV/c. This is the region where the information from the TOF detector is also used. Moreover, the efficiency decreases from most central to peripheral events for both pions and kaons.

The contamination from secondary particles, C_{sec}, is a ratio of the number of reconstructed (measured) secondary particle i.e the particles produced from weak decays, to the total number

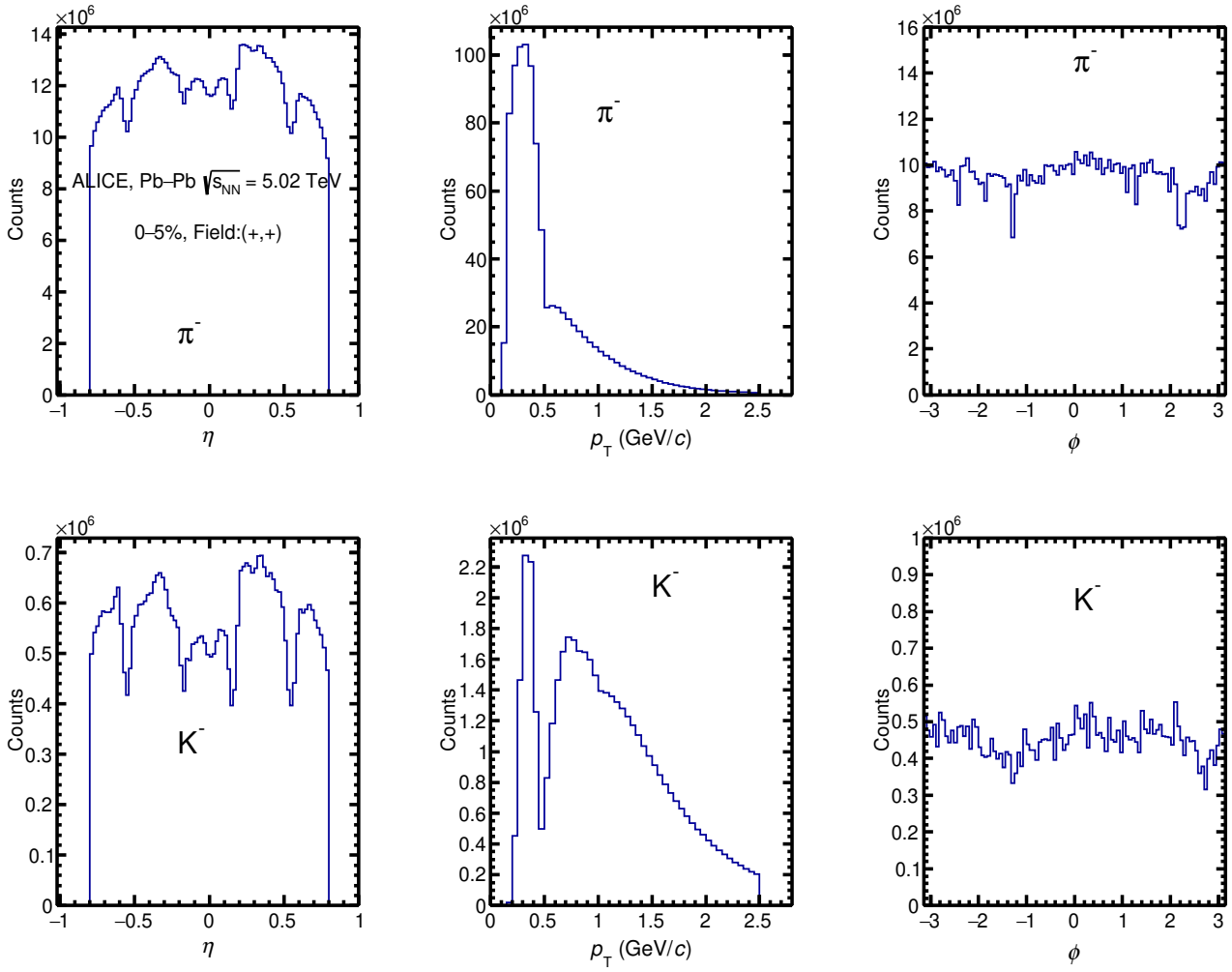

Figure 4.4: The η, p_T & ϕ distribution for the π^- (upper panels) and K^- (bottom panels) in Pb–Pb collisions at $\sqrt{s_{NN}}$ = 5.02 TeV in ALICE.

of reconstructed particles. The values of C_{sec} as a function of p_T for pions and kaons are shown in Fig. 4.8. The secondary contamination of kaons is very negligible. For pions, the contamination is less than 2% in the higher p_T region, however, it varies from 5% in 0−5% central to 3% in 60−70% central collisions in the lower p_T region.

$$C_{sec} = \frac{N^{reconstructed}_{secondaries}}{N^{reconstructed}_{primaries} + N^{measured}_{secondaries}}. \tag{4.5}$$

The particle-identification (PID) purity can be estimated by taking the ratio of truly identified particles to the total (sum of truly and falsely) identified particles. The purity for pions and kaon as the function of p_T is shown in Fig. 4.9. The purities of both pions and kaons are around 99% in the lower p_T region, however, it decreases significantly in the higher p_T region.

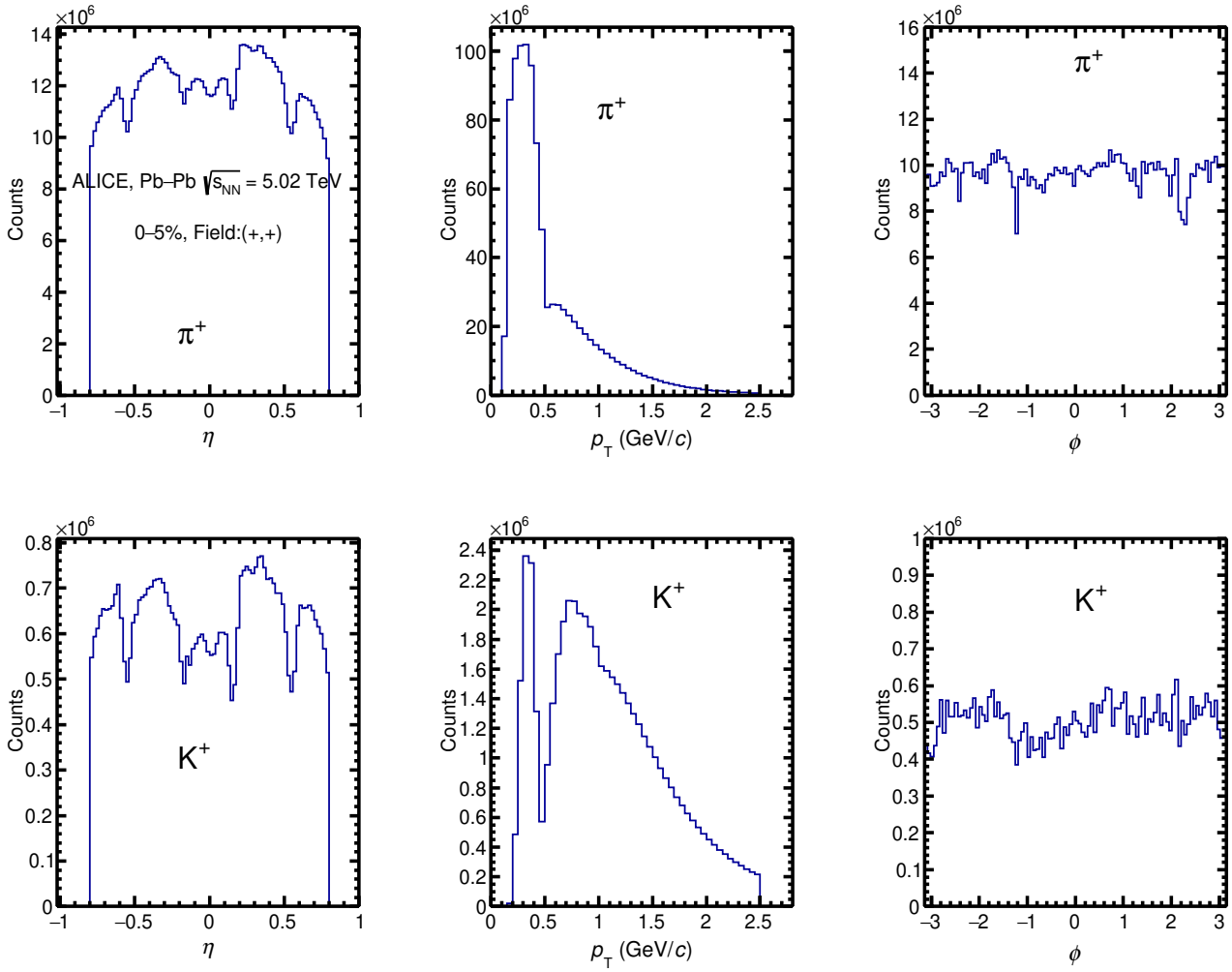

Figure 4.5: The η, p_T & ϕ distribution for the π^+ (upper panels) and K^+ (bottom panels) in Pb–Pb collisions at $\sqrt{s_{NN}}$ = 5.02 TeV in ALICE.

4.6 Experimental correlation functions

The spherical harmonics representation of the correlation functions calculated using the experimental data for all charged combinations of pion-kaon pairs for 0−5% central Pb–Pb collisions at $\sqrt{s_{NN}}$ = 5.02 TeV in ALICE in both (+)ve and (-)ve magnetic-field polarities are shown in Fig. 4.10.

The C_0^0 components are observed to deviate from unity in the lower k^* region. For the like-signed pairs, the C_0^0 goes below unity due to the dominance of repulsive Coulomb interaction, while it goes above unity for the unlike-signed pairs due to the attractive Coulomb interaction.

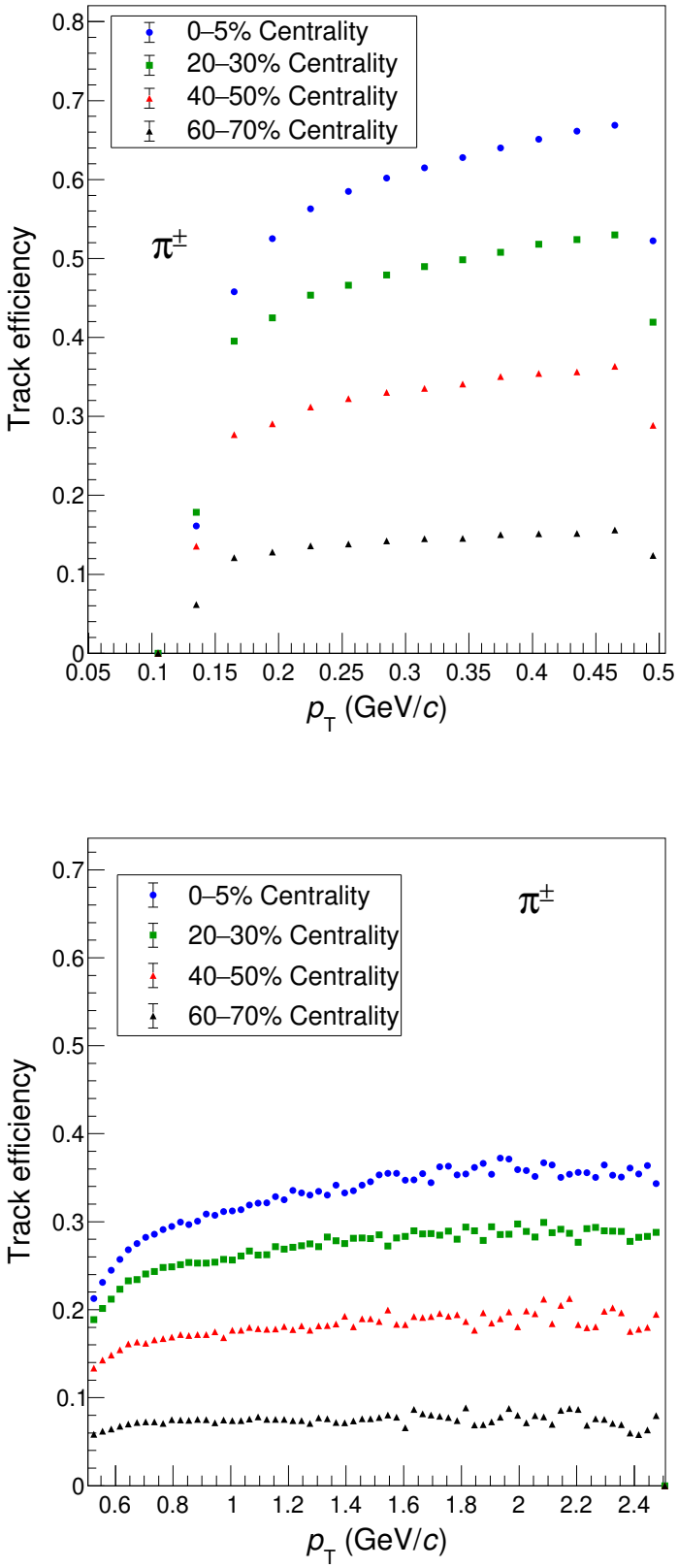

Figure 4.6: The track-reconstruction efficiency as a function of p_{T} for pions in the range of 0.0< p_{T} (GeV/c)< 0.5 (upper panel) and 0.5< p_{T} (GeV/c)< 2.5 (bottom panel) in Pb–Pb collisions at $\sqrt{s_{\mathrm{NN}}}$ = 5.02 TeV in ALICE, generated by HIJING Monte Carlo simulator.

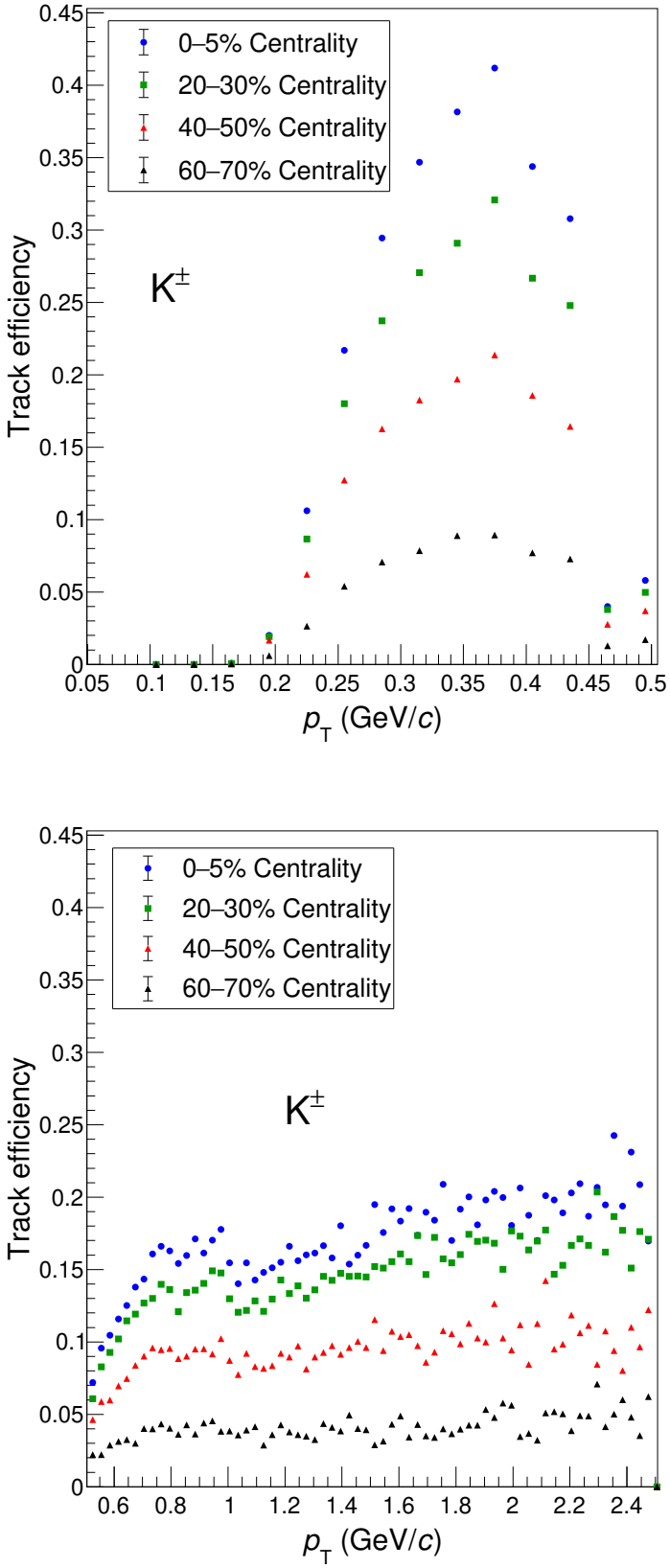

Figure 4.7: The track-reconstruction efficiency as a function of p_{T} for kaons in the range of 0.0< p_{T}(GeV/c)< 0.5 (upper panel) and 0.5< p_{T}(GeV/c)< 2.5 (bottom panel) in Pb–Pb collisions at $\sqrt{s_{\mathrm{NN}}}$ = 5.02 TeV in ALICE, generated by HIJING Monte Carlo simulator.

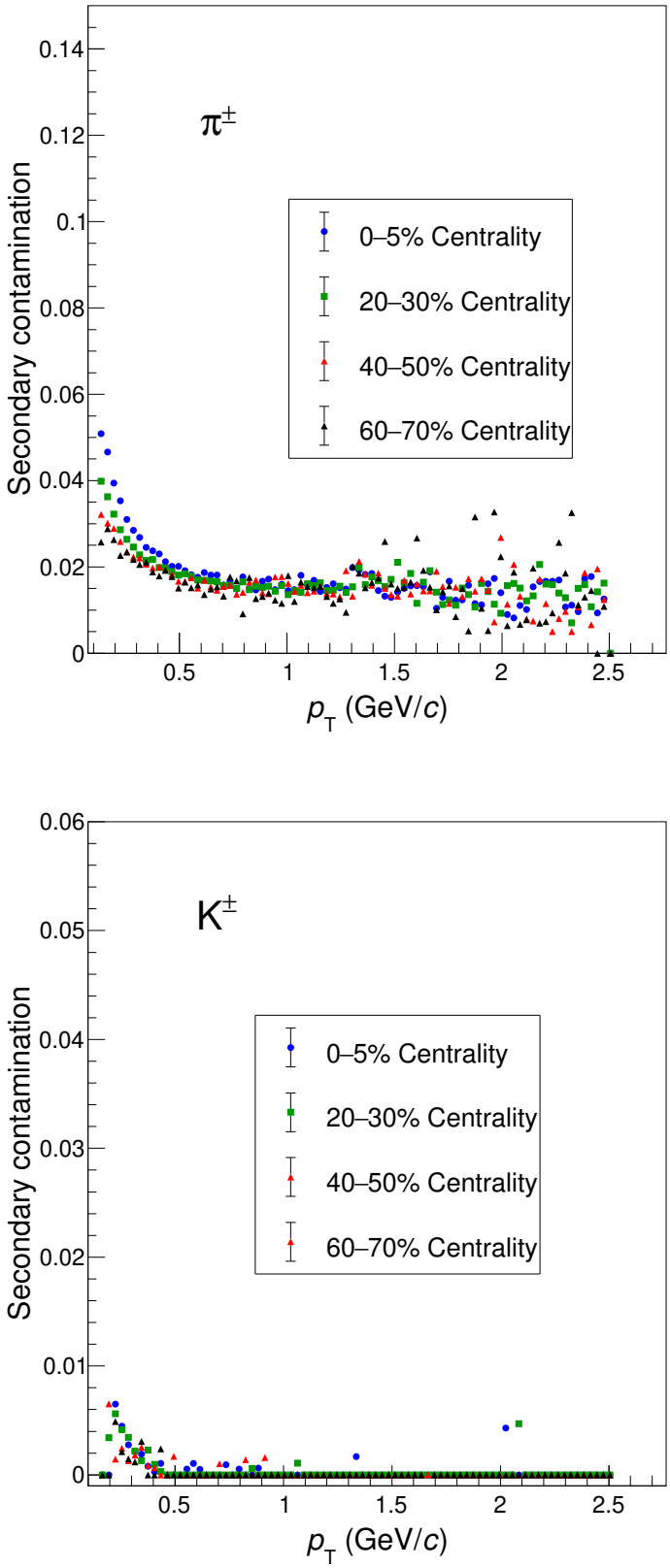

Figure 4.8: The secondary contamination as a function of p_{T} for pions (upper panel) and kaons (bottom panel) in Pb–Pb collisions at $\sqrt{s_{\mathrm{NN}}} = 5.02$ TeV in ALICE, generated by HIJING Monte Carlo simulator.

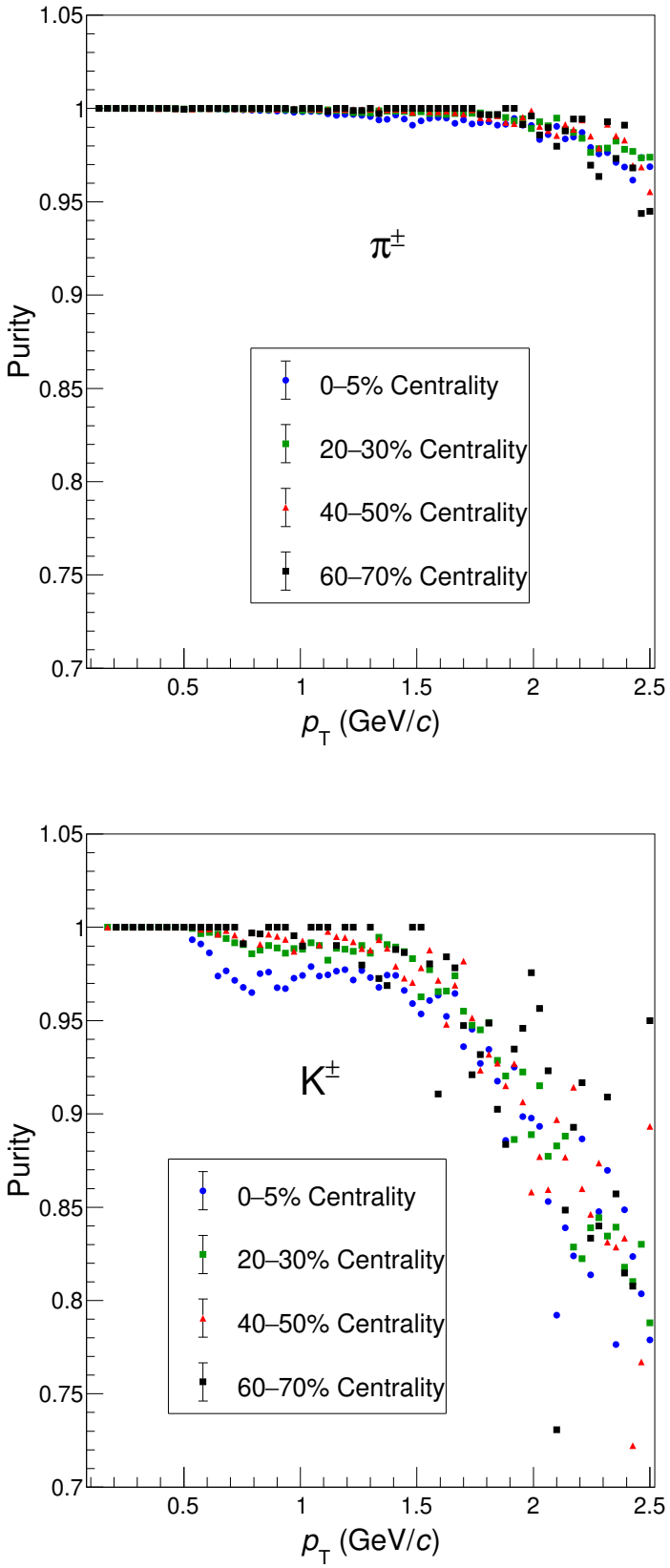

Figure 4.9: The PID purity as a function of p_T for pions (upper panel) and kaons (bottom panel) in Pb–Pb collisions at $\sqrt{s_{NN}}$ = 5.02 TeV in ALICE, generated by HIJING Monte Carlo simulator.

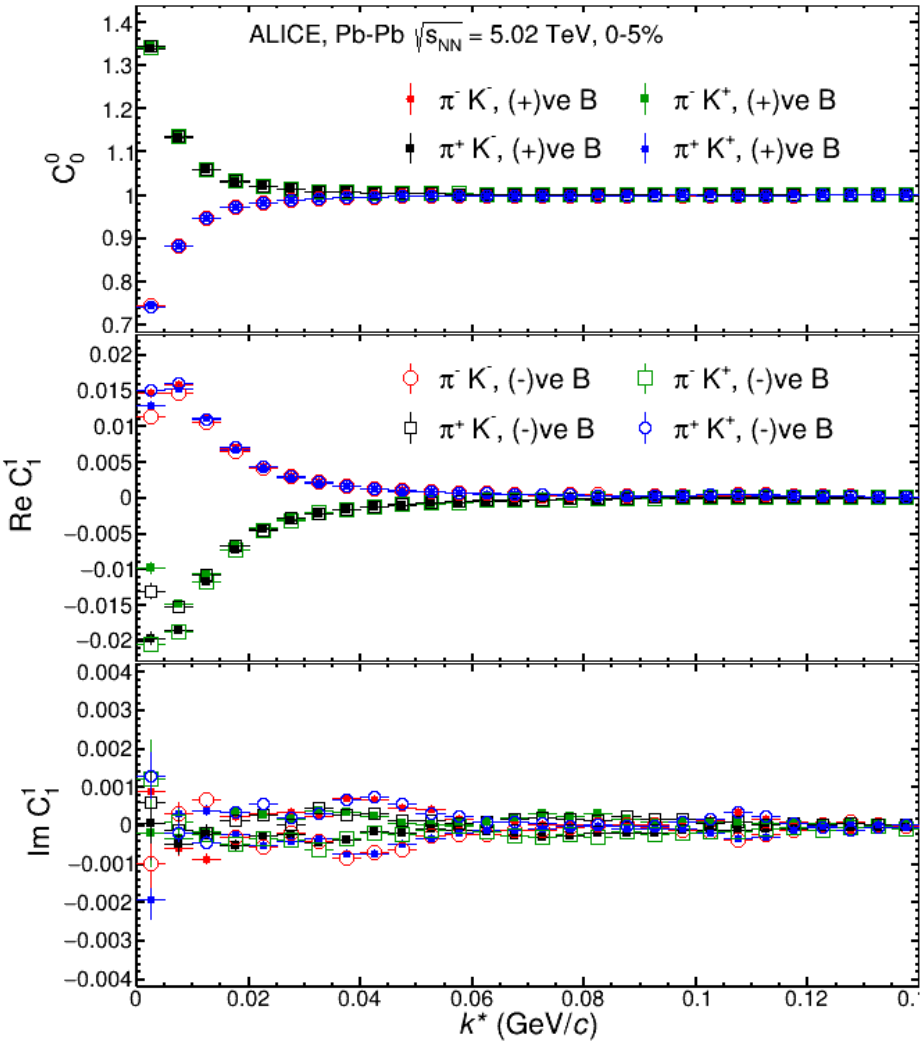

Figure 4.10: The spherical harmonics representation of the correlation functions for all charged combinations of pion-kaon pairs for 0–5% central Pb–Pb collisions at $\sqrt{s_{\rm NN}}$ = 5.02 TeV in ALICE in both (+)ve and (-)ve magnetic-field polarities.

The ReC_1^1 components also deviate from zero in the lower k^* region which suggests the possible existence of pair-emission asymmetry along the *out* direction. The ImC_1^1 components that should ideally vanish due to the intrinsic symmetries, deviate slightly from zero and their polarities change with the magnetic-field polarities. The non-zero values of ImC_1^1 may indicate the track-reconstruction issues[60]. The pairs that are formed with the tracks having very small angular differences are mostly affected due to the limitations in track-reconstruction process. The pair cuts or two-tracks cuts that are applied to minimise the detector effects are discussed in section 4.6.1.

4.6.1 Pair cuts

Cut for fraction of shared clusters

Generally a large number of particles are produced in heavy-ion collisions and the region enclosing the TPC detector is heavily populated with the tracks. The particles traversing through the TPC detector may be very close to each another and therefore, it may happen that the clusters created in the TPC for multiple particles can be merged into one. Hence, some of the pairs may be reconstructed as only one track instead of two separate tracks. A cut is applied to reduce this effect by removing those reconstructed pairs whose constituents share more than 5% of the total number of hits in the TPC.

Pair quality cut

It may happen that a track is segmented into two pieces in the TPC [86]. While reconstructing a single track, such pieces should be properly linked. However, in some cases, a split track may by observed and the tracks which form a pair may have few TPC clusters. Moreover, in most of the cases, these two tracks would not have clusters in the same TPC pad-row. To reject these type of tracks, the number of times the tracks of a particle-pair have non-shared cluster in a TPC pad-row is counted and those pairs for which this number is less then half of the total number of clusters (if both have clusters in the same row) are removed.

Anti-gamma cut

During the pair-production, an electron-positron pair is produced from a gamma ray having energy more than $2m_e$, where m_e is the rest mass of an electron. If this process occurs at any place between the interaction point and TPC detector, the produced electron-positron pair may be misidentified as the oppositely charged pairs of pion and kaon and may affect the analysis. To remove this pair, the following criteria should be fulfilled simultaneously:

- The invariant mass $M_{\text{inv}} = 2m_e^2 + 2(E_1E_2 - \bar{p_1}\bar{p_2})$ of pion-kaon pair with momenta p_1 and p_2 and with assumed m_e is lower than 0.002 GeV/c.

- The polar-angle difference $\Delta\theta = |\theta_1 - \theta_2|$ between the particles in a pair, where θ is the angle between the beam axis and momentum of the particle, is lower than 0.008 rad.

Merged fraction cut

When two tracks traverse very close to each other inside the TPC detector, it is possible that the clusters of those two tracks may overlap in some pad-rows. This may affect the track-reconstruction process in such way that the two tracks may be reconstructed as one track ("merging" effect) or on the contrary, one track may be split into two tracks ("splitting" effect), which modifies the correlations between the particles in a pair and eventually affects the femtoscopic parameters. To observe this effect, the $\Delta\phi^* - \Delta\eta$ correlation function of π^+K^+ and π^+K^- pairs, selected from the same and mixed events are shown in the upper panels of Fig. 4.11-4.12, respectively. The merging and splitting of the tracks are very prominent within the pseudorapidity difference of $|\Delta\eta| < 0.01$ for the pairs that are selected from the same events. For the pairs from the mixed events, the splitting effect is very prominent.

To remove this effect, an additional cut, called "merged fraction cut" (MF) is applied for the pairs having $|\Delta\eta| < 0.01$. The trajectories of two particles are propagated for a set of radii, from 0.8 to 2.5 m in steps of 0.01 m and are projected on the plane perpendicular to the beam axis. The separation between these two projected tracks are calculated at each step. If the distance is less than 3 cm at any step, that step is marked as "merged". Then the fraction of merged points is calculated by taking the ratio between the "merged" points and total number of points i.e. 170. If this ratio is greater than a specific limit, the pair is not considered for further analysis.

The $\Delta\phi^* - \Delta\eta$ correlations for π^+K^+ and π^+K^- pairs, selected from the same and mixed events, with 3% MF+ anti-gamma cuts are shown in the bottom panels of Fig. 4.11-4.12. It is observed that the merging effect is minimised for the pairs with $|\Delta\phi^*| = 0.025$ and $|\Delta\eta| < 0.01$ at a radial distance of 1.2 m.

To observe the track-merging/splitting effect on the femtoscopic correlation functions, the C_0^0, ReC_1^1 and ImC_1^1 for π^+K^+ and π^+K^- pairs with no MF+$\bar{\gamma}$ cuts and with different MF (1%, 3%

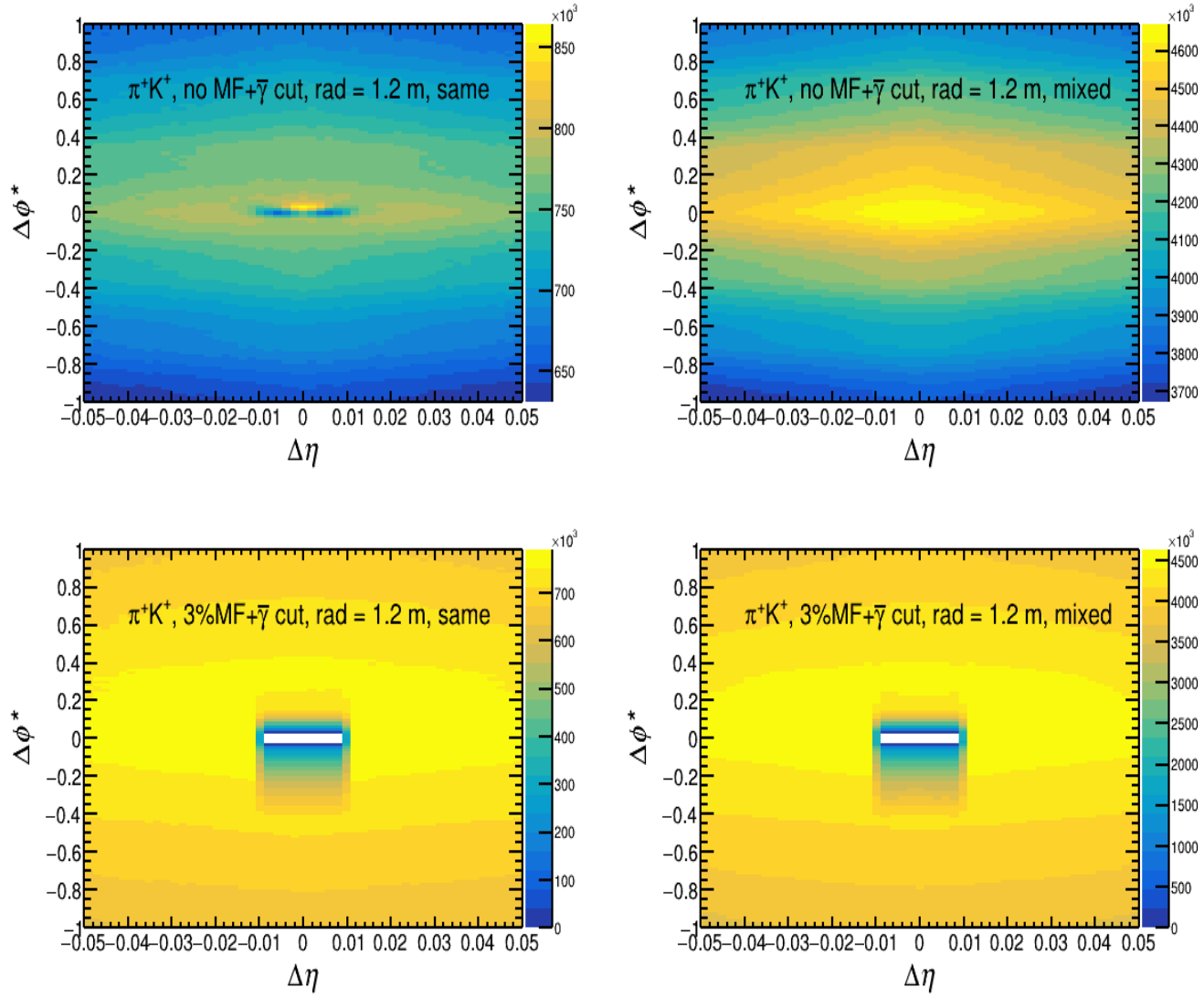

Figure 4.11: The $\Delta\phi^* - \Delta\eta$ correlation functions for π^+K^+ pairs selected from the same and different events with no MF and no $\bar{\gamma}$ cuts (upper panels) and 3% MF+$\bar{\gamma}$ cuts (bottom panels) for 0−5% central Pb–Pb collisions at $\sqrt{s_{\rm NN}}$ = 5.02 TeV in ALICE.

and 5%)+$\bar{\gamma}$ cuts are shown in Fig. 4.13-4.14. All the three correlation functions with different MF cuts almost overlap each other. For the π^+K^+ pair, the ImC_1^1 does not vary significantly after applying the MF cut, however, the merging effect in the C_0^0 and ReC_1^1 in the region of 90 MeV/c $< k^* <$ 120 MeV/c is slightly improved. For the π^+K^- pair, the ImC_1^1 becomes close to zero in the lower k^* region and the magnitudes of C_0^0 and ReC_1^1 are affected with the application of MF cut.

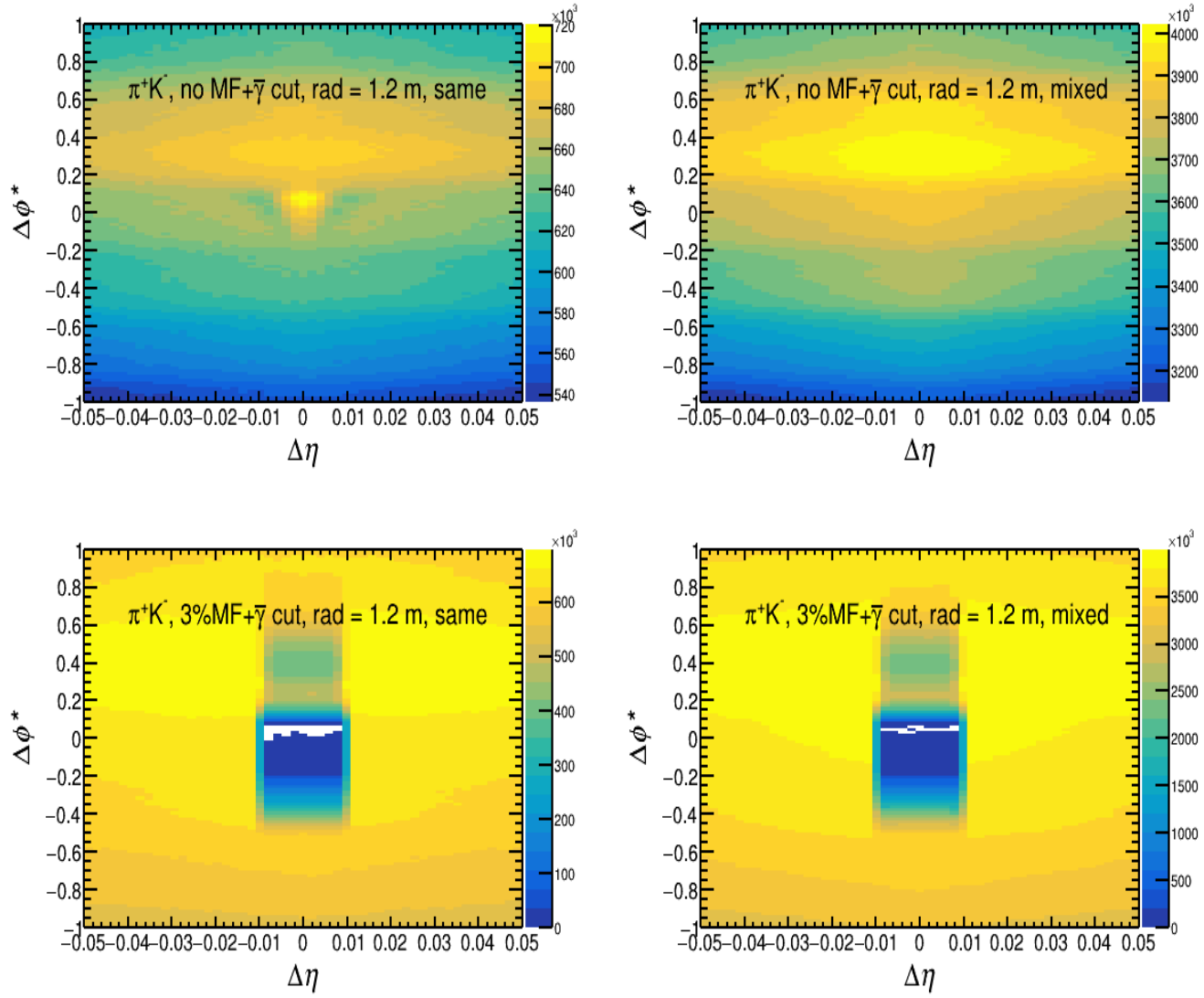

Figure 4.12: The $\Delta\phi^* - \Delta\eta$ correlation functions for π^+K^- pairs selected from the same and different events with no MF and no $\bar{\gamma}$ cuts (upper panels) and 3% MF+$\bar{\gamma}$ cuts (bottom panels) for 0−5% central Pb–Pb collisions at $\sqrt{s_{\rm NN}}$ = 5.02 TeV in ALICE.

The correlation functions are observed to improve with the application of MF cut, however, there is no significant change in the correlation function for 1%, 3% and 5% MF cut. Hence, the cut of 3% MF which takes care of the merging/splitting effect without reducing the statistics of pairs significantly, is chosen to proceed further in the analysis.

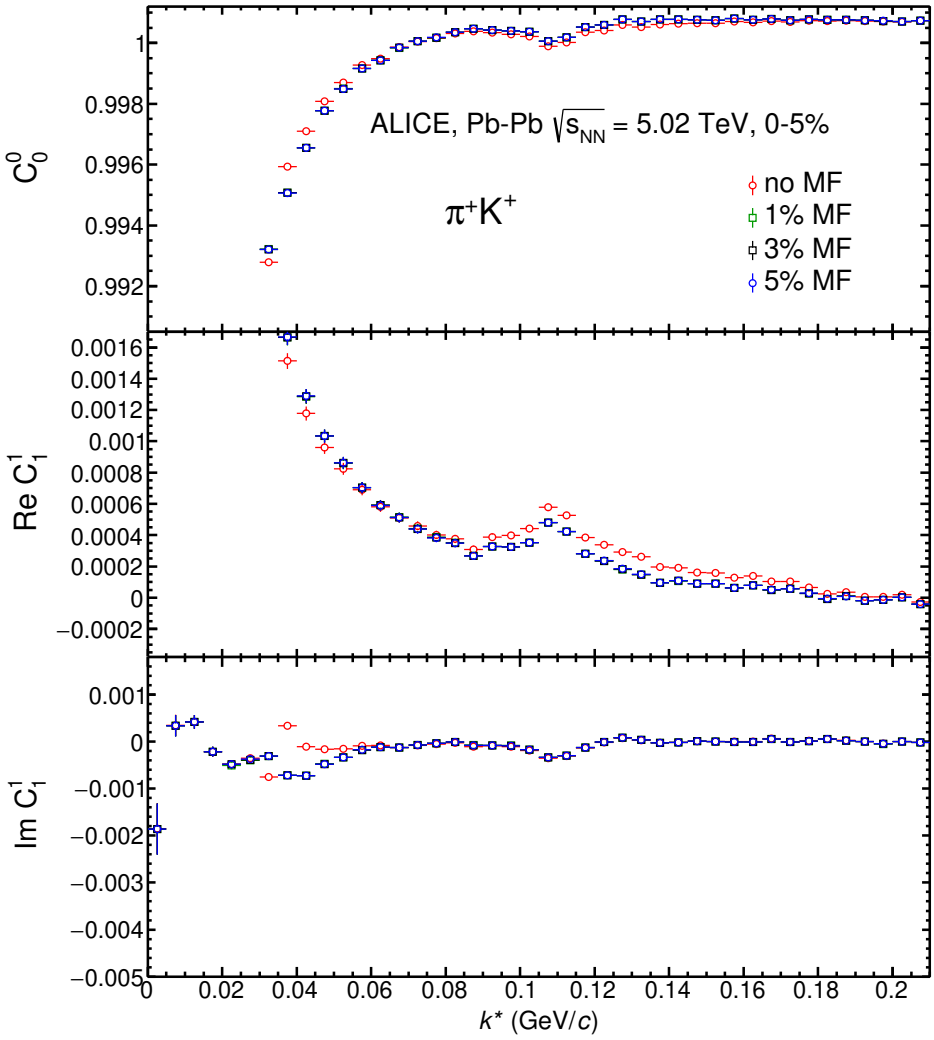

Figure 4.13: The correlation functions for π^+K^+ pairs with different merged-fraction cuts for 0–5% central Pb–Pb collisions at $\sqrt{s_{\rm NN}}$ = 5.02 TeV in ALICE.

4.7 Non-femtoscopic background correction

In Fig. 4.15, it can be seen that the C_0^0 and ReC_1^1 components of the correlation functions are not uniform in the higher k^* region. This suggests that along with the femtoscopic correlation, the non-femtoscopic correlations are also present in the pion-kaon correlation functions. The non-femtoscopic background may arise due to the presence of elliptic flow, residual correlations, resonance decay etc. [87, 88] and it has to be minimised before estimating the femtoscopic parameters. The experimental correlation function can be represented as the addition of real

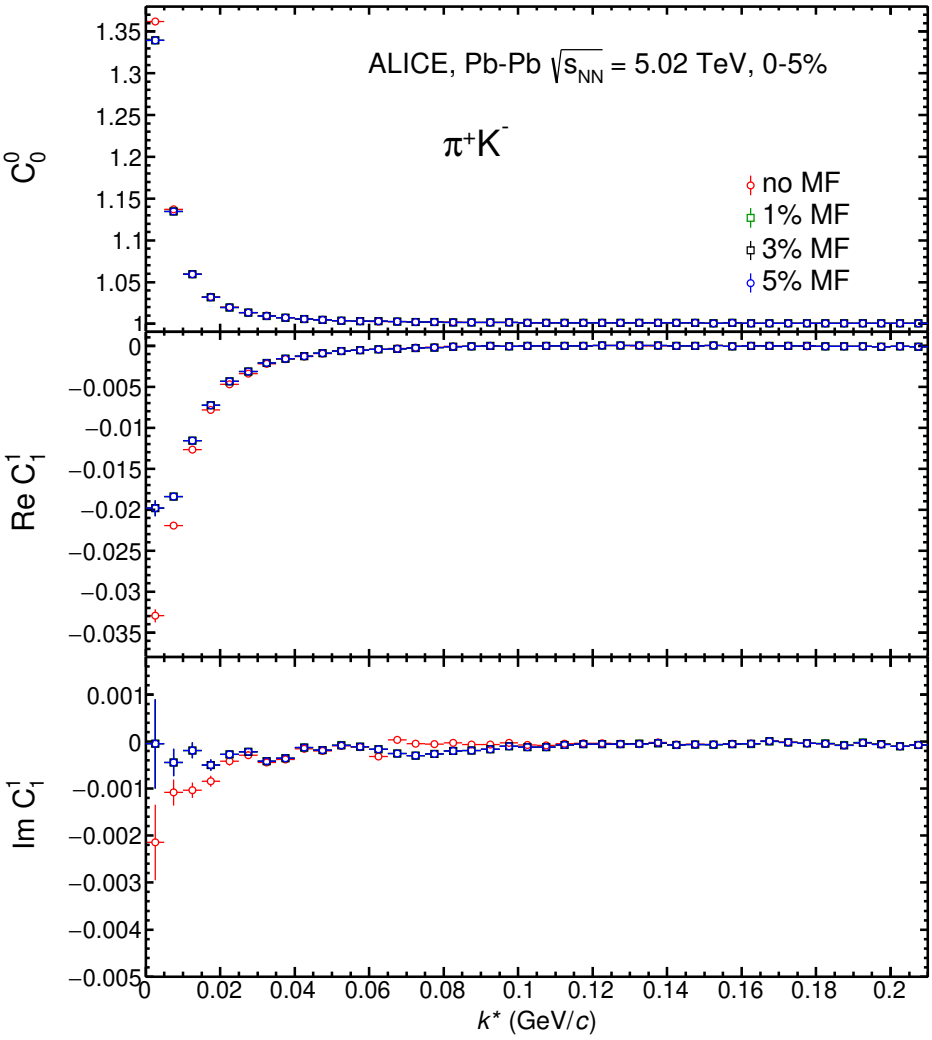

Figure 4.14: The correlation functions for π^+K^- pairs with different merged-fraction cuts for 0–5% central Pb–Pb collisions at $\sqrt{s_{\mathrm{NN}}}$ = 5.02 TeV in ALICE.

femtoscopic correlation and background as given in Eq. (4.6).

$$C_{exp}^{ij} = C_{real}^{ij} + B^{ij}, \tag{4.6}$$

where C_{exp}^{ij} is the experimental correlation function, C_{real}^{ij} is the real femtoscopic correlation, B^{ij} is the background and i, j are the positive and negative charge of the particles. The real correlation function can be filtered out from the measured one by the formula given in Eq. (4.7).

$$C_{real}^{ij} = C_{exp}^{ij} - B^{ij}. \tag{4.7}$$

Before minimising the background, it is imperative to check whether it is similar for all charged-pair combinations of pions and kaons. Fig. 4.16 shows the ratio of correlation functions of the

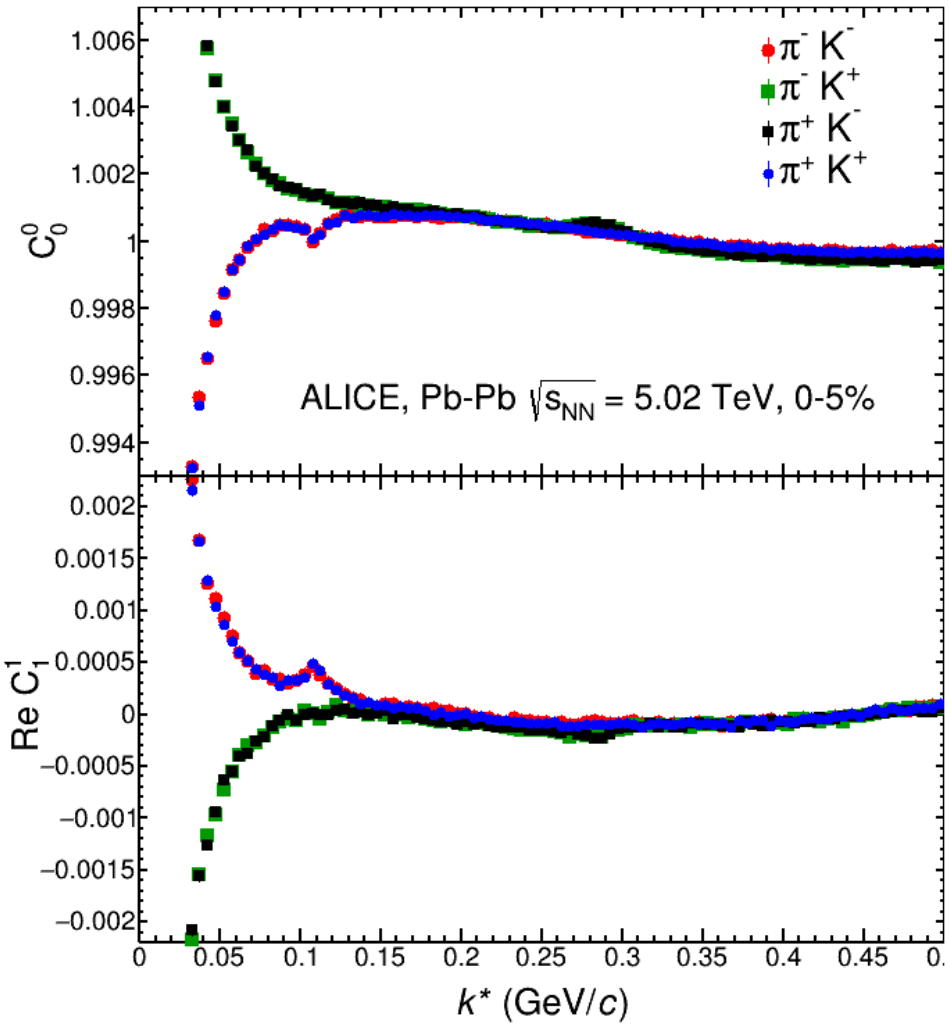

Figure 4.15: The correlation functions of pion-kaon pairs (zoomed) for 0–5% central Pb–Pb collisions at $\sqrt{s_{\rm NN}}$ = 5.02 TeV in ALICE.

like-signed and unlike-signed pairs. It is seen that the ratio is ≈ 1 in the higher k^* region, which suggests that the background is similar for all charged pairs.

The background estimation is a complicated procedure. In this analysis, two approaches are used to measure the non-femtoscopic background. In the first approach, the background is compared with the pion-kaon correlation functions in Pb–Pb events at $\sqrt{s_{\rm NN}}$ = 5.02 TeV, obtained from AMPT ([89]) event generator. Since AMPT model does not include the femtoscopic correlation between the particles, it can be utilised to estimate the background present in the experimentally measured data. The comparisons of correlation functions, obtained from the real data and AMPT events are shown in Fig. 4.17 and Fig. 4.18. It can be observed that the

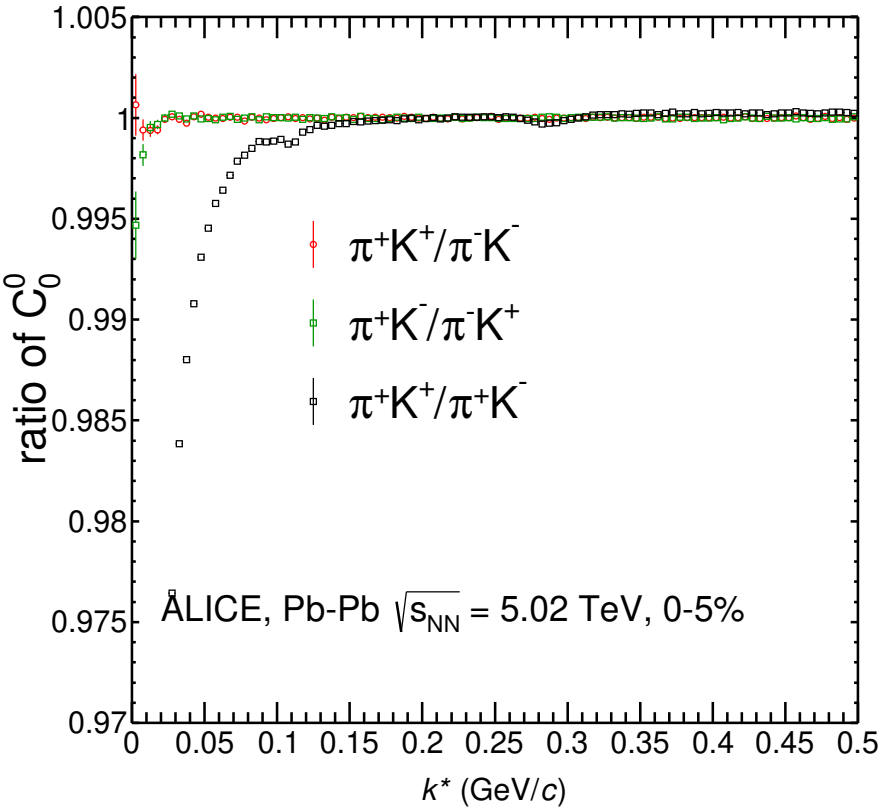

Figure 4.16: The ratio of correlation functions of different charged-pair combinations of pions and kaons (zoomed) for 0−5% central Pb–Pb collisions at $\sqrt{s_{\rm NN}}$ = 5.02 TeV in ALICE.

correlations functions for both unlike- and like-signed pairs, obtained from the AMPT events do not have the slope similar to that of the real data in the higher k^* region. Therefore, the AMPT events were not used to estimate the background, present in pion-kaon correlation functions.

The second approach of background estimation is based on the observation of similar background for all charge combinations of pions and kaons[88]. It is assumed that for C_0^0,

$$(C^{like} - B) = \frac{1}{(C^{unlike} - B)} \tag{4.8}$$

where *like* corresponds to + +, - - and *unlike* corresponds to + -, - + charged-pair combinations. The background function is assumed to be a 6^{th} order polynomial as given in Eq. (4.9):

$$B^{ij} = a_0^{ij} + \sum_{l=1}^{5} a_l z^{(l+1)} \tag{4.9}$$

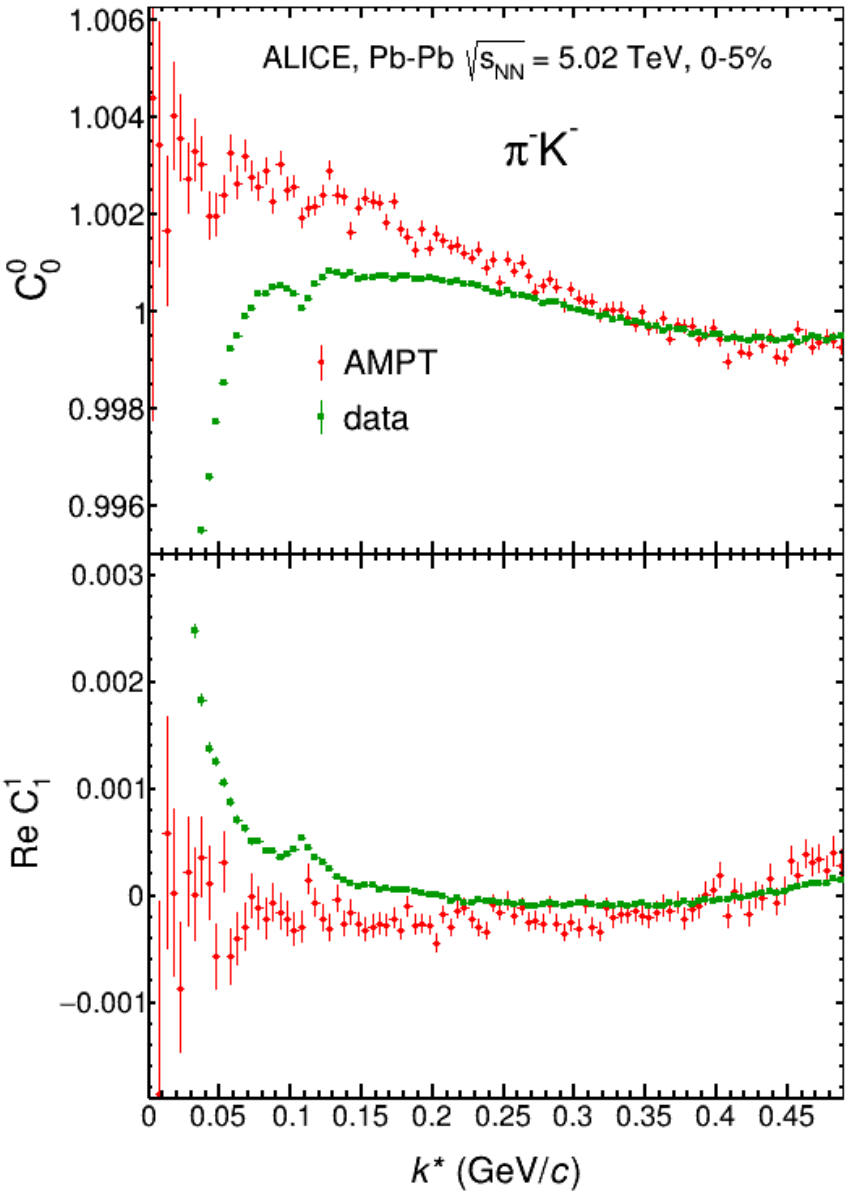

Figure 4.17: The comparisons of correlation functions for $\pi^- K^-$ obtained from the data and AMPT for 0−5% central Pb–Pb collisions at $\sqrt{s_{\rm NN}}$ = 5.02 TeV in ALICE.

where z corresponds to the k^* of pion-kaon pair. The parametrisation of the background is performed for all centrality classes separately by minimizing the $\chi^2_{background}$ as given in Eq. (4.10) [87].

$$\chi^2_{background} = \frac{1}{\sigma^2_{tot}}\left[(C^{++} - B) - \frac{1}{(C^{+-} - B)}\right]^2 + \frac{1}{\sigma^2_{tot}}\left[(C^{--} - B) - \frac{1}{(C^{+-} - B)}\right]^2 + \frac{1}{\sigma^2_{tot}}\left[(C^{++} - B) - \frac{1}{(C^{-+} - B)}\right]^2 + \frac{1}{\sigma^2_{tot}}\left[(C^{--} - B) - \frac{1}{(C^{-+} - B)}\right]^2. \tag{4.10}$$

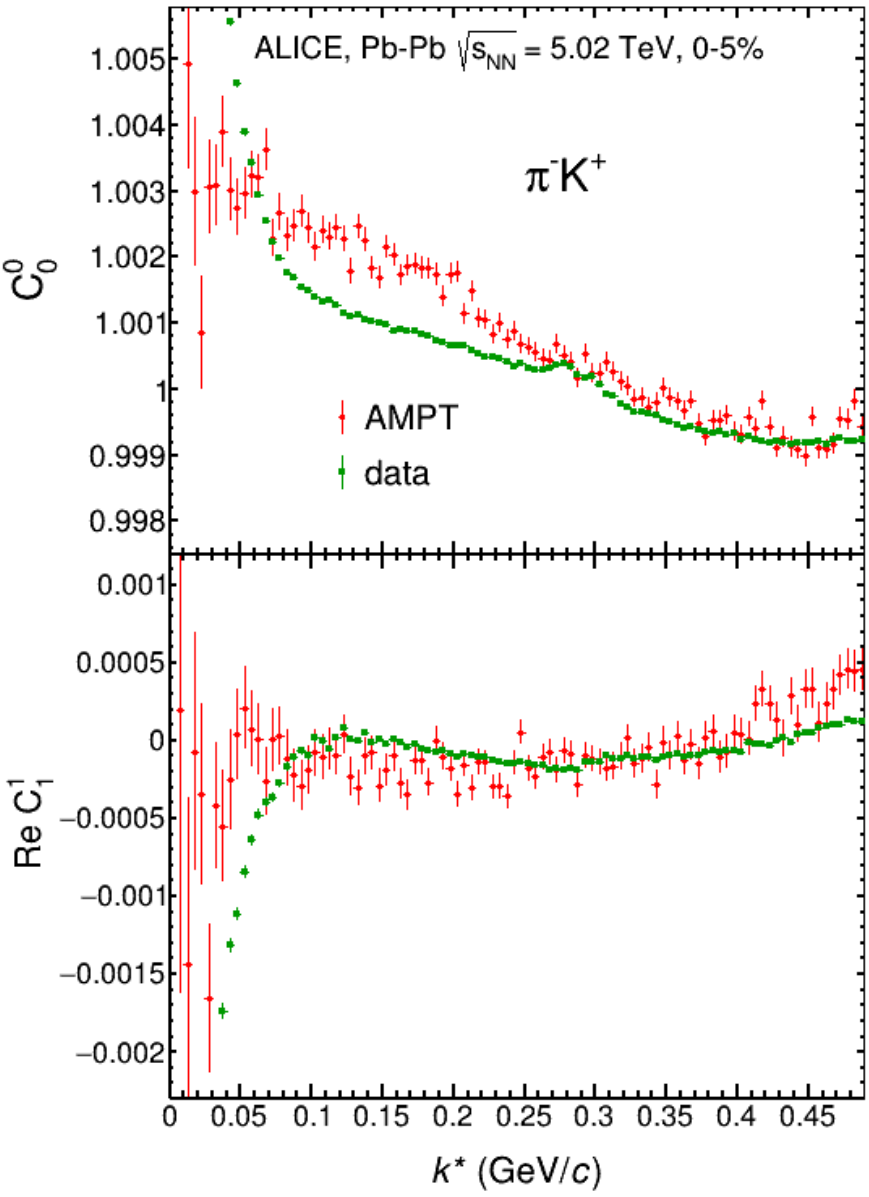

Figure 4.18: The comparisons of correlation functions for $\pi^- K^+$ obtained from the data and AMPT for 0−5% central Pb–Pb collisions at $\sqrt{s_{\rm NN}}$ = 5.02 TeV in ALICE.

Here, σ_{tot} is the sum of σ's for all the pairs in each k^* bin. The χ^2 is minimised for all the pairs together in such a way that all the coefficients of B^{ij} i.e. a_l are same for all pairs but the four $pol0$ terms, ($a_0^{++}, a_0^{+-}, a_0^{-+}$ and a_0^{--}) are different. The background in ReC_1^1 can be minimised in the similar way, assuming that the background-minimised ReC_1^1 of unlike-signed and like-signed pairs will have the same magnitudes but opposite signs.

In Fig. 4.19-4.20, the experimental correlation functions for pion-kaon pairs with 6^{th} order polynomial functions, estimated as the background, are shown for 0−5% and 20−30% centrality classes, respectively. The estimated background functions describe the experimental correlation functions quite well.

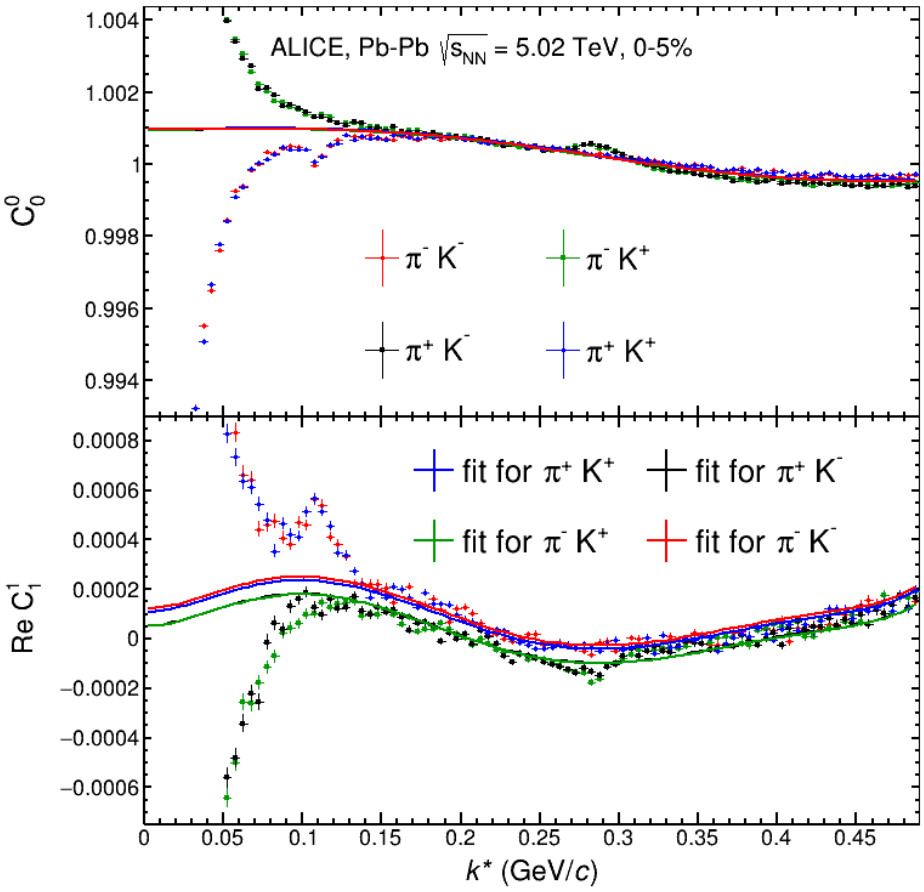

Figure 4.19: The correlation functions for pion-kaon pairs with the 6^{th} order polynomial functions as the non-femtoscopic background for 0−5% centrality Pb–Pb collisions at $\sqrt{s_{NN}}$ = 5.02 TeV in ALICE.

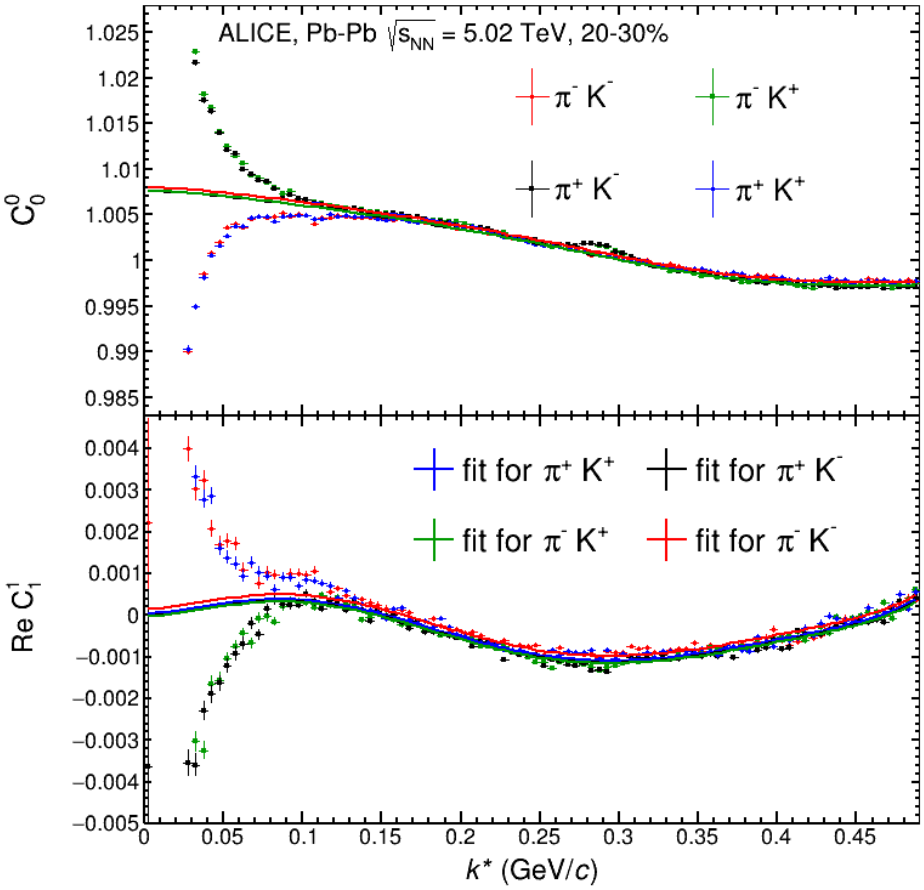

Figure 4.20: The correlation functions for pion-kaon pairs with the 6^{th} order polynomial functions as the non-femtoscopic background for 20−30% centrality Pb–Pb collisions at $\sqrt{s_{\rm NN}}$ = 5.02 TeV in ALICE.

4.8 Systematic uncertainty estimation

4.8.1 Systematic uncertainty due to variations in selection cuts

The measured correlation function might be affected by the biases, present in the selection process of the events, tracks, pairs etc. To investigate the possible systematic effects in the correlation functions due to the selection criteria, the values of selection cuts are varied from the baseline to some other values as listed in the third and fourth columns of Table. 4.2.

In each set, only one selection cut is changed and rest of the cuts are kept same as the default values.

Selection cut	Default	Variation 1	Variation 2
$\|z_{\rm vtx}\|$	$\leq$ 7.0 cm	$\leq$ 8.0 cm	$\leq$ 6.0 cm
$\|\eta\|$	$\leq$ 0.8	$\leq$ 0.7	$\leq$ 0.85
$DCA_{\rm XY}$	$\leq$ 0.3 cm	$\leq$ 0.25 cm	$\leq$ 0.35 cm
$DCA_{\rm Z}$	$\leq$ 0.3 cm	$\leq$ 0.25 cm	$\leq$ 0.35 cm
Minimum number of TPC clusters	70	60	80
Number of events to be mixed	3	4	$--$
$\Delta\eta_{max}$	0.01	0.011	0.009
Mag. field polarity	(+)ve	(-)ve	$--$

Table 4.2: The variations in selection criteria to check for the systematic uncertainties.

The results obtained for each of the variations are further analysed using the Barlow's criteria [90] to decide whether the variation is contributing to the systematic or not. The description of Barlow's criteria is briefly outlined:

Let $D \pm \sigma_{\rm D}$ and $A \pm \sigma_{\rm A}$ be the values of correlation functions in the *default* and *alternate* (variation) set of selection cuts, respectively. For a given k^*, the difference $\Delta = (A - D)$ is determined. The resultant uncertainty, σ is considered to be $\sqrt{|\sigma_A^2 - \sigma_D^2|}$ and $\sqrt{|\sigma_A^2 + \sigma_D^2|}$ for the correlated and uncorrelated samples, respectively. In this analysis, the considered cut variations are correlated since they belong to the same dataset except the variations in magnetic field polarity, where two different datasets are compared. The Δ/σ's for each variation is obtained as a function of k^*. For $|\Delta/\sigma| \leq 2$, the corresponding variation is not considered as a source of systematic uncertainty.

The Δ/σ as a function of k^* for the DCA and $z_{\rm vtx}$ variations for π^+K^+ are shown in Fig. 4.21. In case of the DCA variation, the Δ/σ for C_0^0 and ReC_1^1 are observed to have distinct trends and most of the points are on/beyond the border of statistical limit. Hence, it is considered for the systematic effect while the contribution for $z_{\rm vtx}$ are not. The variations of

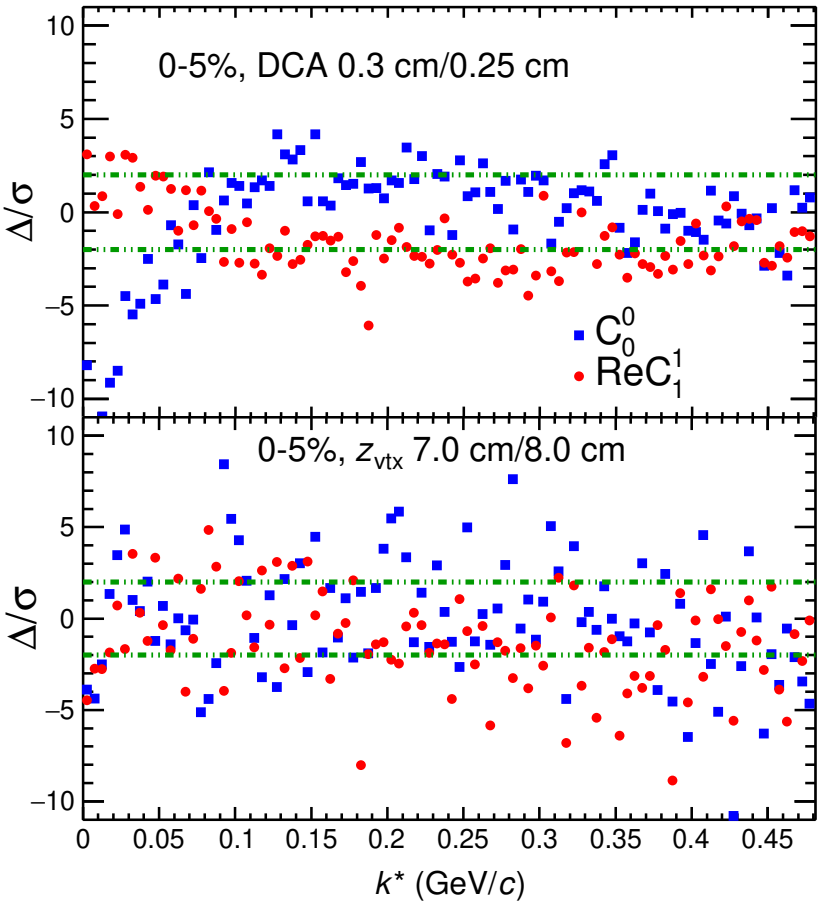

Figure 4.21: The Δ/σ as a function of k^* for the variations in DCA (upper panel) and z_{vtx} (bottom panel) for the π^+K^+ for 0−5% central Pb–Pb collisions at $\sqrt{s_{\text{NN}}} = 5.02$ TeV in ALICE.

Δ/σ as a function of k^* for all the considered cut variations are shown in Appendix A. The variations due to DCA, η, minimum number of TPC clusters and magnetic-field polarity are considered to be the source of systematic uncertainty, while the variations in z_{vtx}, $\Delta\eta_{\text{max}}$ and number of mixed events are not considered.

The relative systematic uncertainty due to the selection cut in each k^* bin is calculated using Eq. (4.11).

$$\frac{\Delta s_{cut}(k^*)}{D(k^*)} = \sqrt{\sum_i \left(\frac{A_i(k^*) - D(k^*)}{D(k^*)}\right)^2} \tag{4.11}$$

where i corresponds to each set of selection criteria.

4.8.2 Systematic uncertainty in estimation of non-femtosocpic background

The systematic effects due to the background-estimation process are obtained in the following way.

- The background function is fitted in three different fit-ranges of k^*, which are following:
  - $0 < k^*$ (MeV/c) <500 (default)
  - $25 < k^*$ (MeV/c) <500
  - $50 < k^*$ (MeV/c) <500
- The background function is changed to a 5^{th} order polynomial, which is used for fitting in the range of $0 < k^*$ (MeV/c) <500

It is clear from the background variations, shown in Fig. 4.22, that the fits are consistent and cover the higher k^* region very well.

The correlation functions for pion-kaon pairs for 0−5%, 5−10%, 10−20%, 20−30%, 30−40% and 40−50% central collisions with statistical uncertainties along with the systematic uncertainties due to the selection cuts and background variations are shown in Fig. 4.23-4.28. It is observed that the estimated background functions are in good agreement with the measured correlation functions in the higher k^* region.

4.9 Background minimised correlation function

After the background minimisation, the resultant correlation functions from 0−5% to 40−50% centrality classes are shown in Fig. 4.29-4.34. The total systematic uncertainty in C_0^0 and ReC_1^1 in each k^* bin is the quadrature-sum of systematic uncertainty due to the cut selection and non-femtoscopic background and is given by Eq. (4.12).

$$\Delta s_{total}(k^*) = \sqrt{(\Delta s_{cut}(k^*))^2 + (\Delta s_{BG}(k^*))^2}. \tag{4.12}$$

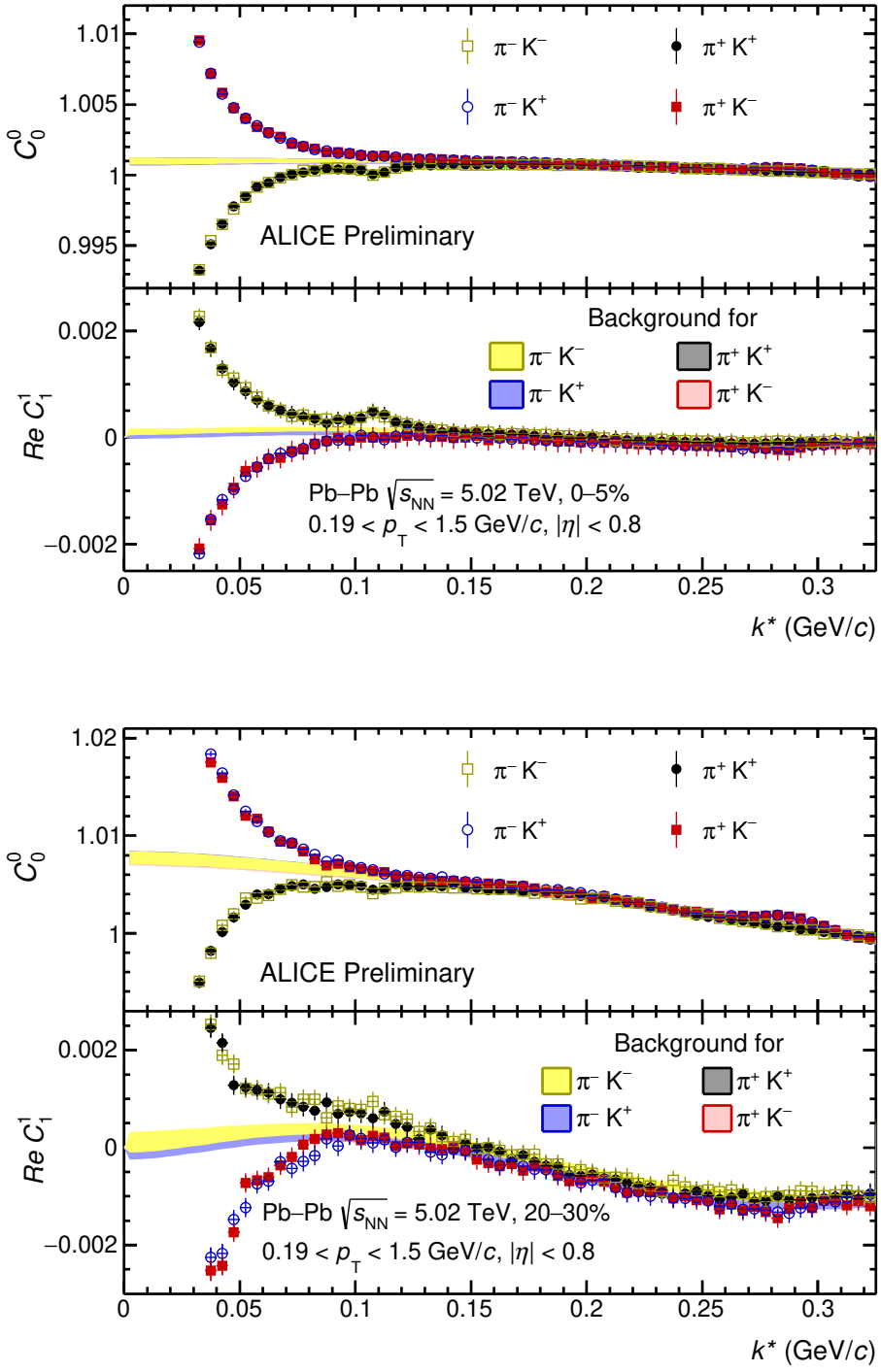

Figure 4.22: The correlation functions for pion-kaon pairs with the 6^{th} order polynomial functions as the non-femtoscopic background for 0−5% (upper panel) and 20−30% central (bottom panel) Pb–Pb collisions at $\sqrt{s_{\rm NN}}$ = 5.02 TeV in ALICE.

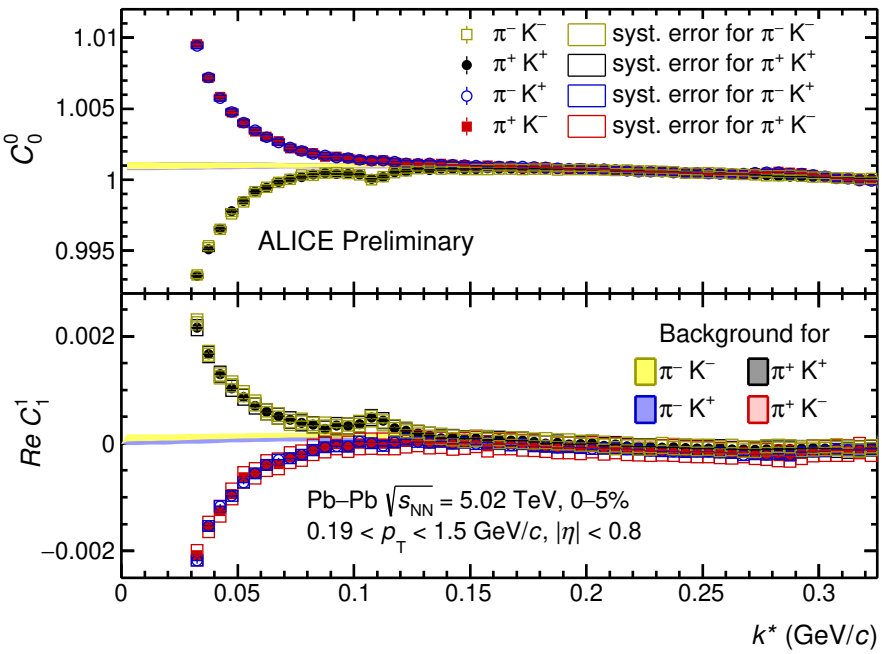

Figure 4.23: The correlation functions for pion-kaon pairs with the non-femtoscopic background for 0−5% central Pb–Pb collisions at $\sqrt{s_{\mathrm{NN}}}$ = 5.02 TeV in ALICE.

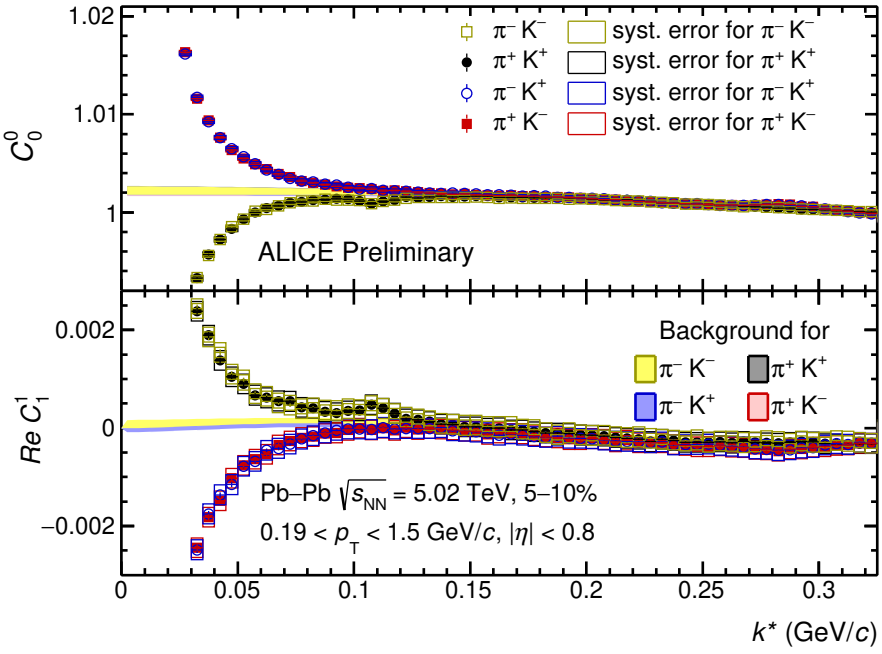

Figure 4.24: The correlation functions for pion-kaon pairs with the non-femtoscopic background for 5−10% central Pb–Pb collisions at $\sqrt{s_{\mathrm{NN}}}$ = 5.02 TeV in ALICE.

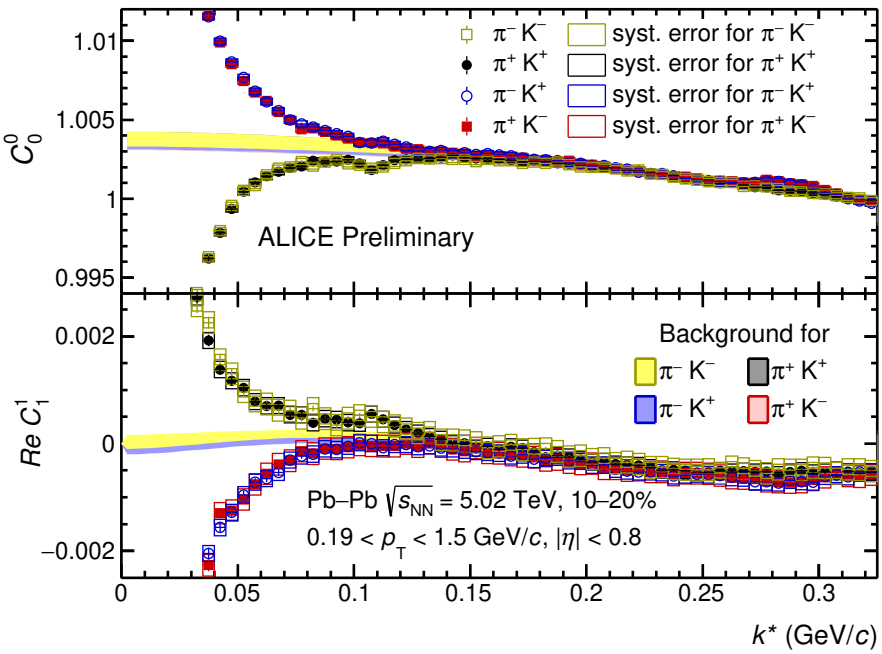

Figure 4.25: The correlation functions for pion-kaon pairs with the non-femtoscopic background for 10−20% central Pb–Pb collisions at $\sqrt{s_{NN}}$ = 5.02 TeV in ALICE.

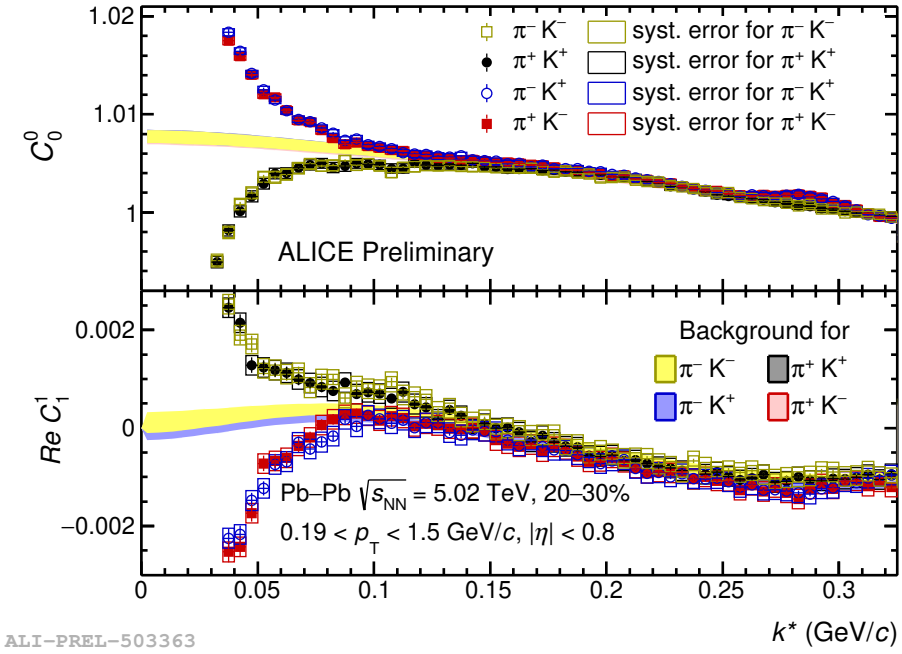

Figure 4.26: The correlation functions for pion-kaon pairs with the non-femtoscopic background for 20−30% central Pb–Pb collisions at $\sqrt{s_{NN}}$ = 5.02 TeV in ALICE. [91]

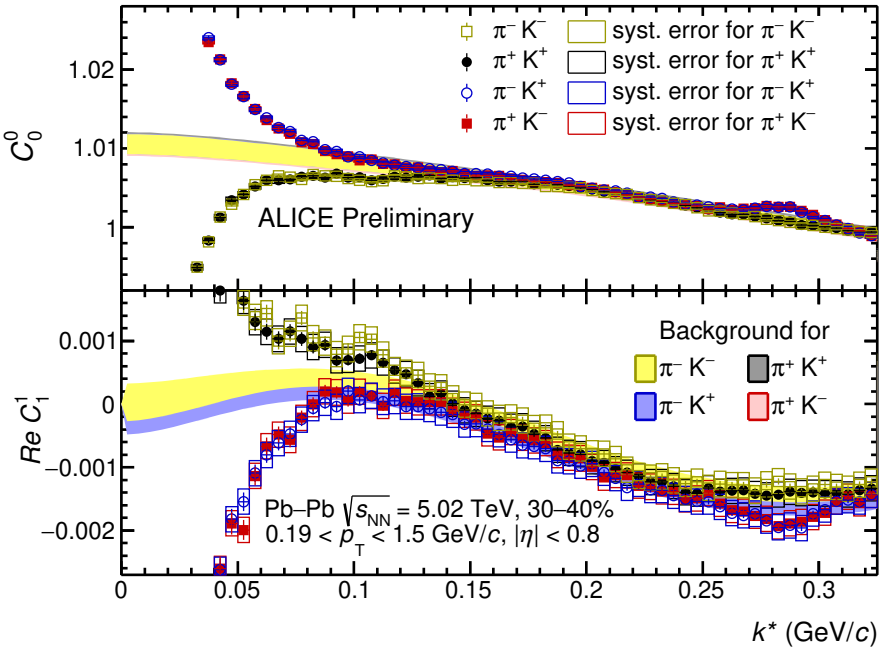

Figure 4.27: The correlation functions for pion-kaon pairs with the non-femtoscopic background for 30−40% central Pb–Pb collisions at $\sqrt{s_{\mathrm{NN}}}$ = 5.02 TeV in ALICE.

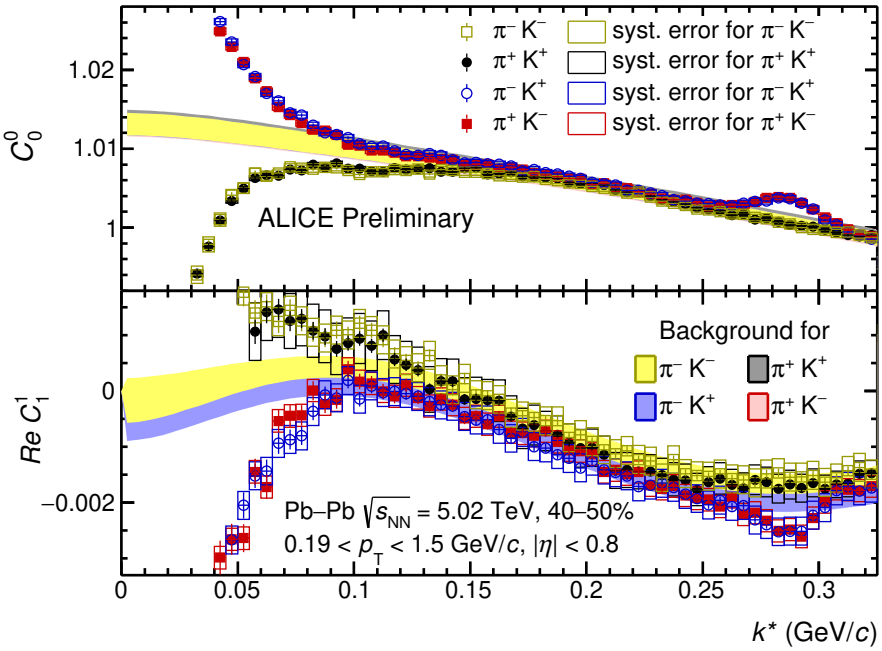

Figure 4.28: The correlation functions for pion-kaon pairs with the non-femtoscopic background for 40−50% central Pb–Pb collisions at $\sqrt{s_{\mathrm{NN}}}$ = 5.02 TeV in ALICE.

Here, $\Delta s_{cut}(k^*)$ and $\Delta s_{BG}(k^*)$ are the systematic uncertainty in each k^* bin due to the cut selections and non-femtoscopic background, respectively.

After the background minimisation, the correlation functions are used to extract the femtoscopic parameters which is discussed in section 4.12.

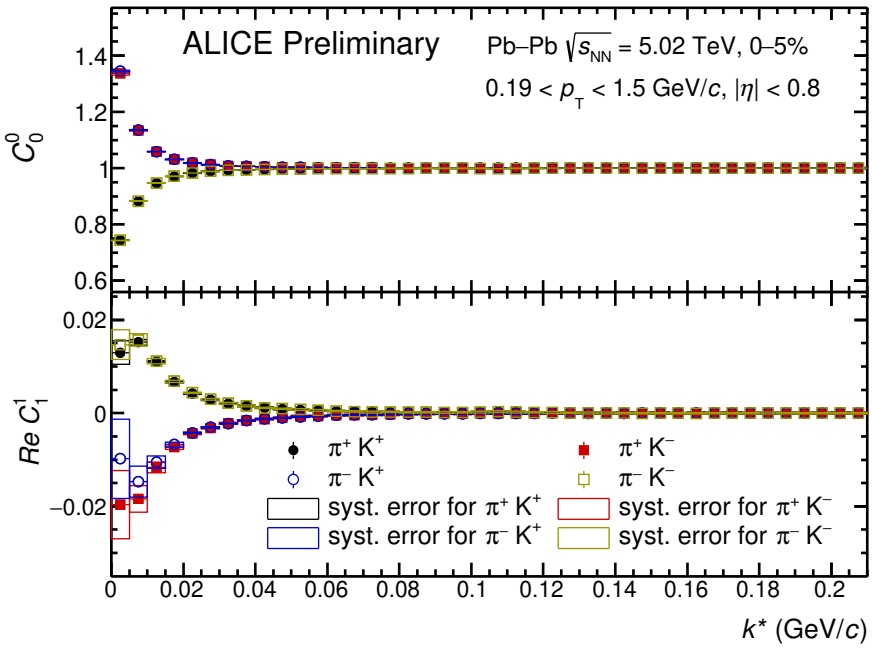

Figure 4.29: The background-minimised correlation functions of pion-kaon pairs for 0–5% central Pb–Pb collisions at $\sqrt{s_{NN}}$ = 5.02 TeV in ALICE.

4.10 k_T-dependent correlation functions

The correlation functions in three k_T ranges: 400–500, 500-600 and 600-700 MeV/c are obtained to observe the k_T dependence of the femtoscpic parameters. The correlation functions from 0–5% to 40–50% centrality classes in three k_T ranges with the statistical and systematic uncertainties are shown in Fig. 4.35 - 4.52.

The background-minimised correlation functions from 0–5% to 40–50% centrality classes in the three k_T ranges are shown in Fig. 4.53-4.70.

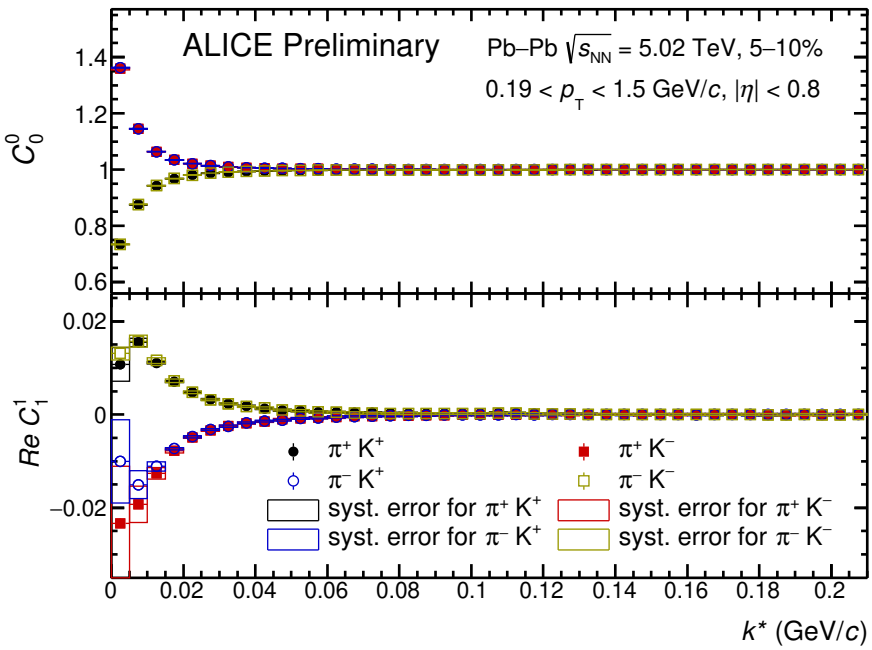

Figure 4.30: The background-minimised correlation functions of pion-kaon pairs for 5−10% central Pb–Pb collisions at $\sqrt{s_{NN}}$ = 5.02 TeV in ALICE.

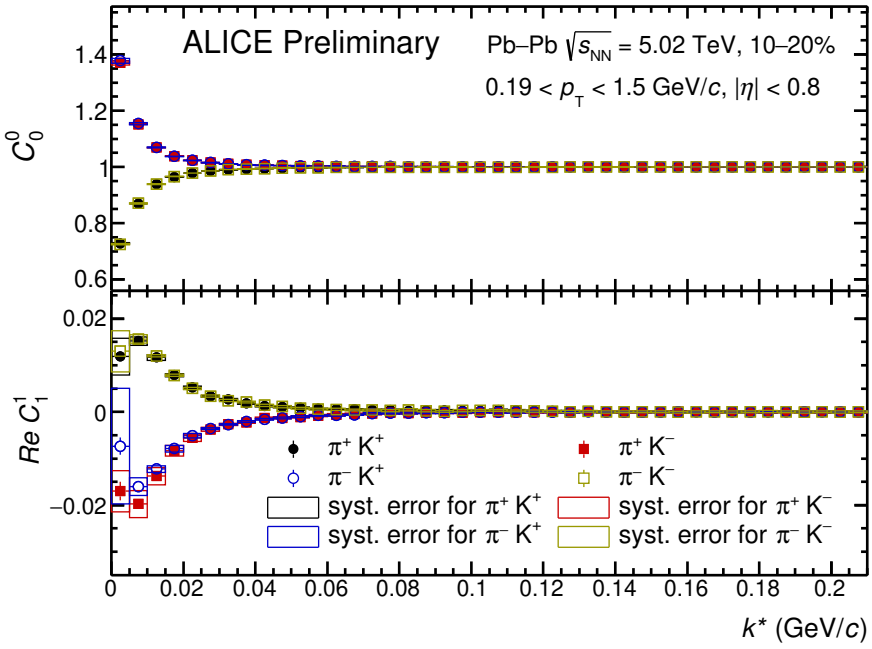

Figure 4.31: The background-minimised correlation functions of pion-kaon pairs for 10−20% central Pb–Pb collisions at $\sqrt{s_{NN}}$ = 5.02 TeV in ALICE.

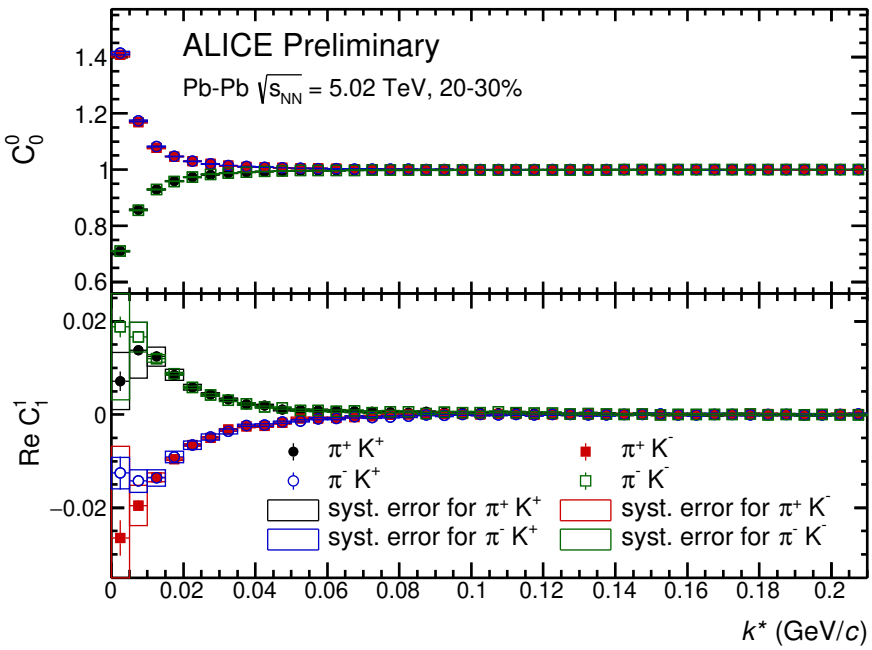

Figure 4.32: The background-minimised correlation functions of pion-kaon pairs for 20–30% central Pb–Pb collisions at $\sqrt{s_{NN}}$ = 5.02 TeV in ALICE.

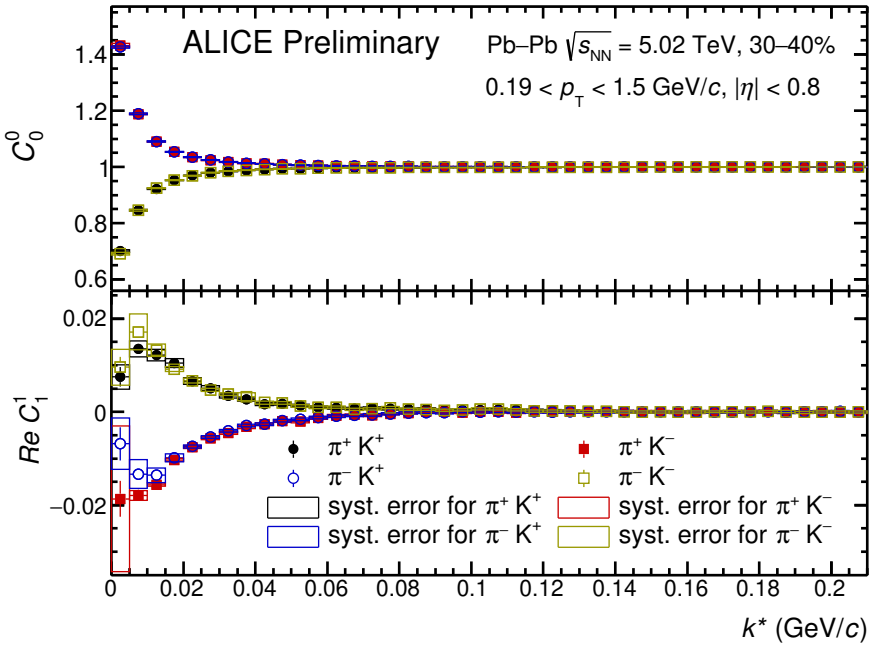

Figure 4.33: The background-minimised correlation functions of pion-kaon pairs for 30–40% central Pb–Pb collisions at $\sqrt{s_{NN}}$ = 5.02 TeV in ALICE.

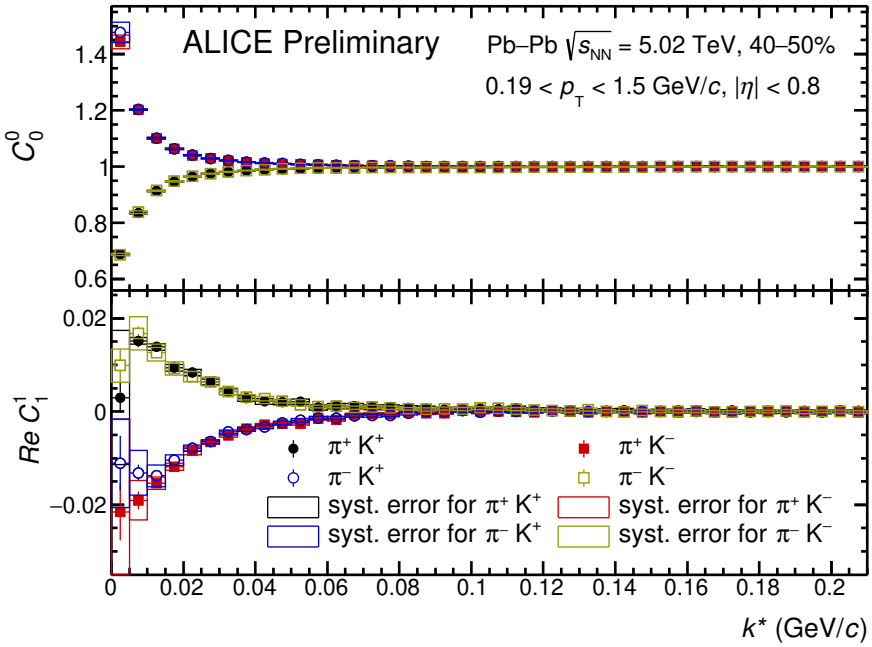

Figure 4.34: The background-minimised correlation functions of pion-kaon pairs for 40–50% central Pb–Pb collisions at $\sqrt{s_{NN}}$ = 5.02 TeV in ALICE.

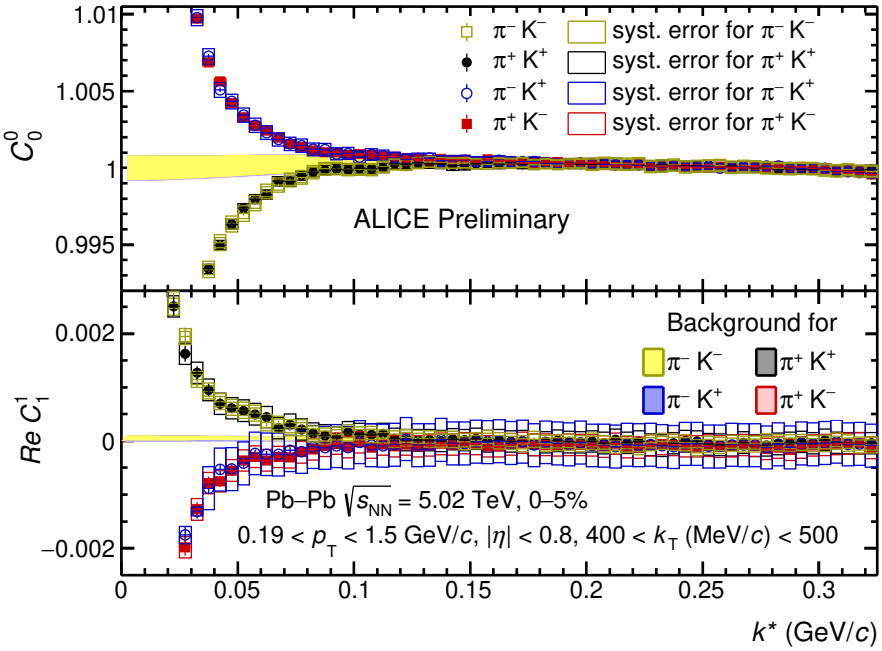

Figure 4.35: The pion-kaon correlation functions within 400 <k_T (MeV/c)< 500 with the non-femtoscopic background for 0–5% central Pb–Pb collisions at $\sqrt{s_{NN}}$ = 5.02 TeV in ALICE.

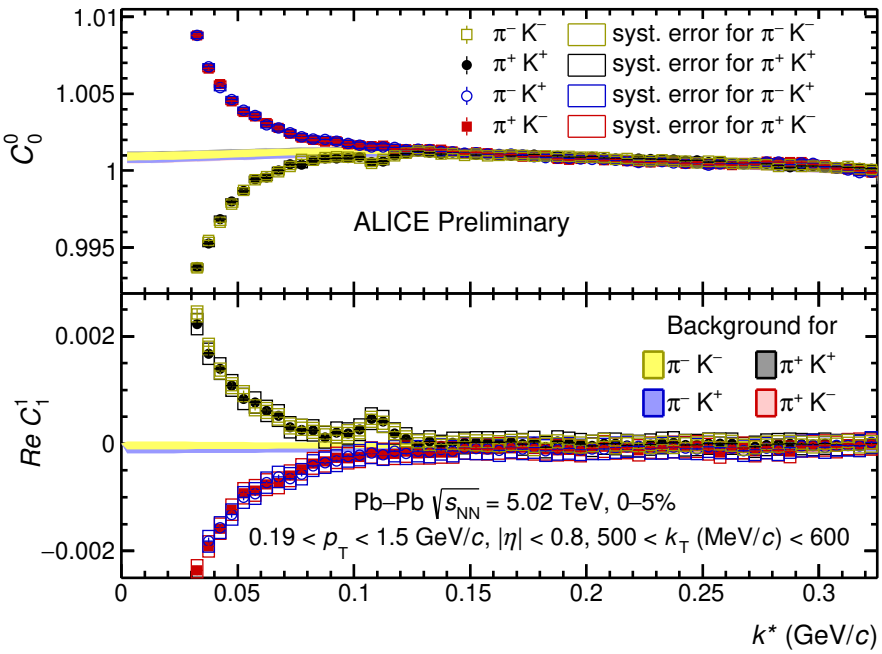

Figure 4.36: The pion-kaon correlation functions within 500 $<k_T$ (MeV/c)$<$ 600 with the non-femtoscopic background for 0−5% central Pb–Pb collisions at $\sqrt{s_{NN}}$ = 5.02 TeV in ALICE.

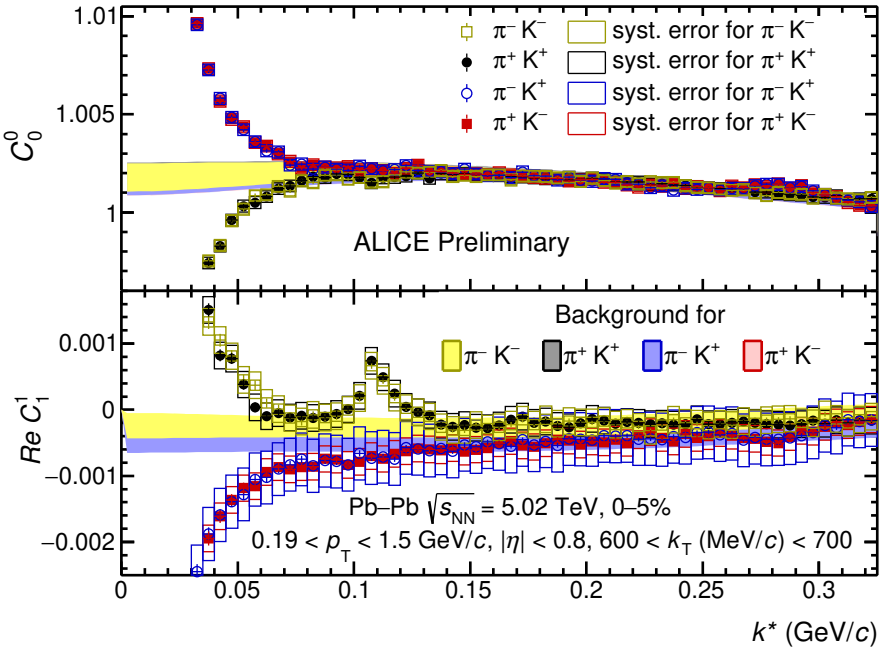

Figure 4.37: The pion-kaon correlation functions within 600 $<k_T$ (MeV/c)$<$ 700 with the non-femtoscopic background for 0−5% central Pb–Pb collisions at $\sqrt{s_{NN}}$ = 5.02 TeV in ALICE.

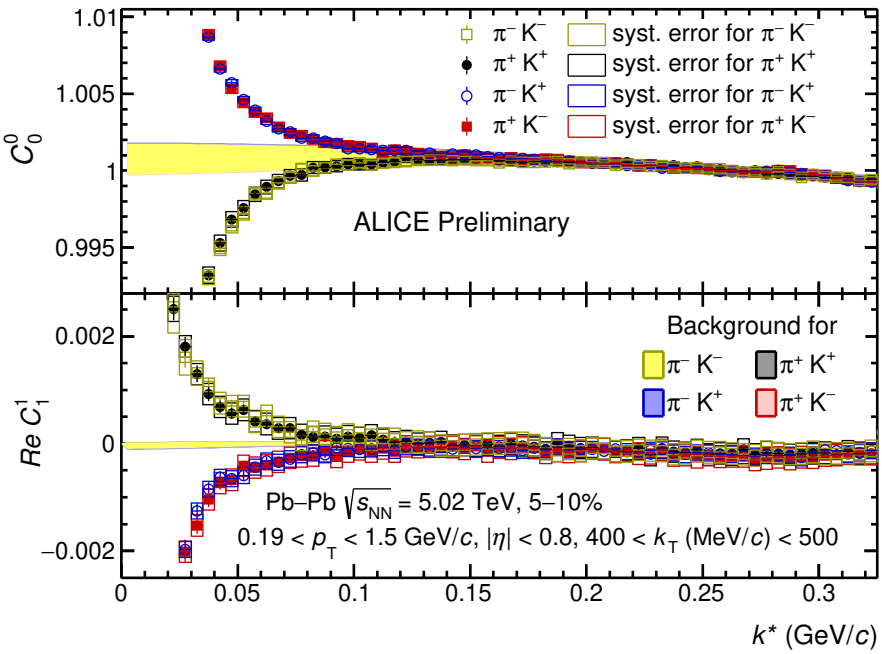

Figure 4.38: The pion-kaon correlation functions within 400 $<k_T$ (MeV/c)$<$ 500 with the non-femtoscopic background for 5−10% central Pb–Pb collisions at $\sqrt{s_{NN}}$ = 5.02 TeV in ALICE.

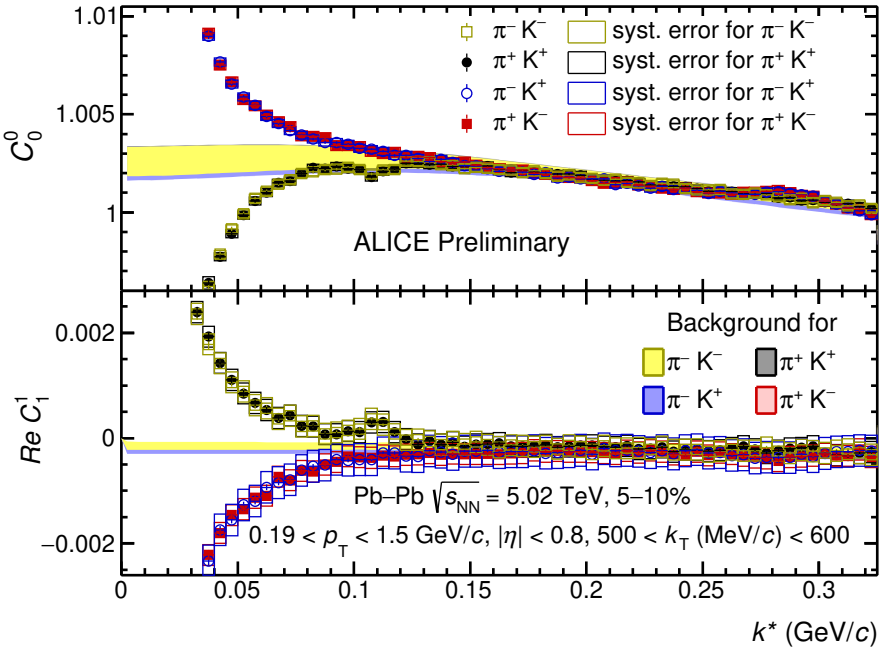

Figure 4.39: The pion-kaon correlation functions within 500 $<k_T$ (MeV/c)$<$ 600 with the non-femtoscopic background for 5−10% central Pb–Pb collisions at $\sqrt{s_{NN}}$ = 5.02 TeV in ALICE.

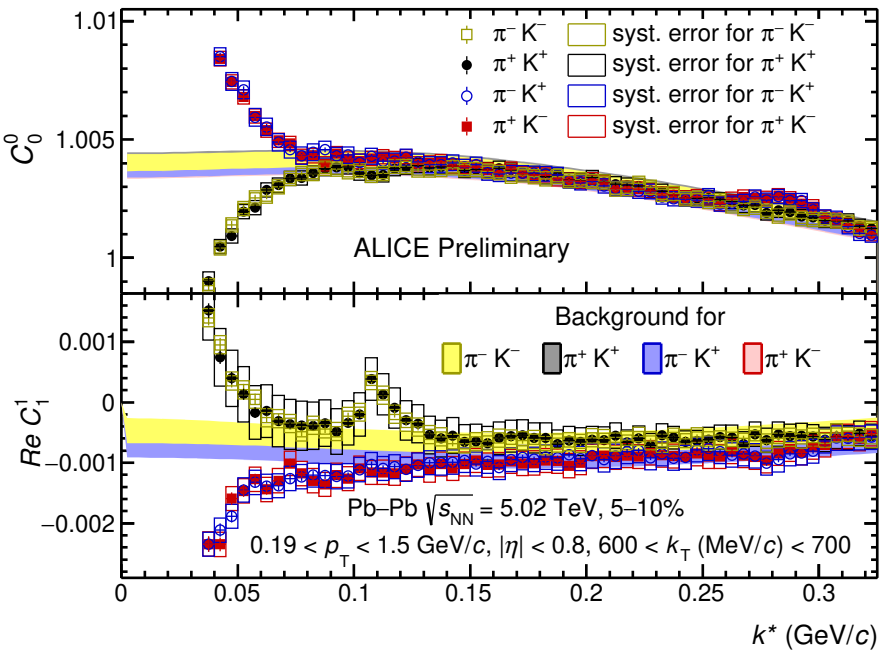

Figure 4.40: The pion-kaon correlation functions within 600 $<k_T$ (MeV/c)$<$ 700 with the non-femtoscopic background for 5−10% central Pb–Pb collisions at $\sqrt{s_{NN}}$ = 5.02 TeV in ALICE.

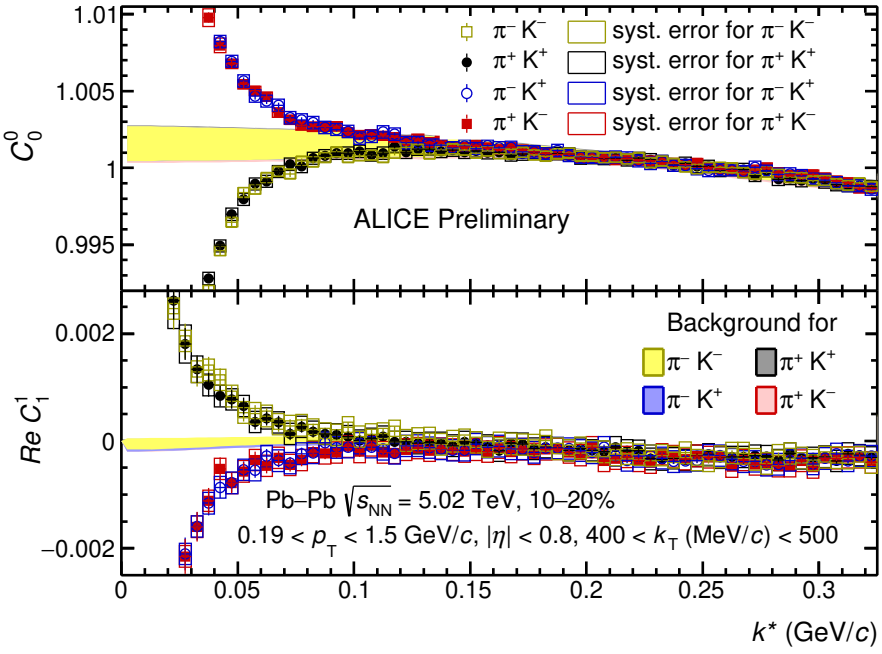

Figure 4.41: The pion-kaon correlation functions within 400 $<k_T$ (MeV/c)$<$ 500 with the non-femtoscopic background for 10−20% central Pb–Pb collisions at $\sqrt{s_{NN}}$ = 5.02 TeV in ALICE.

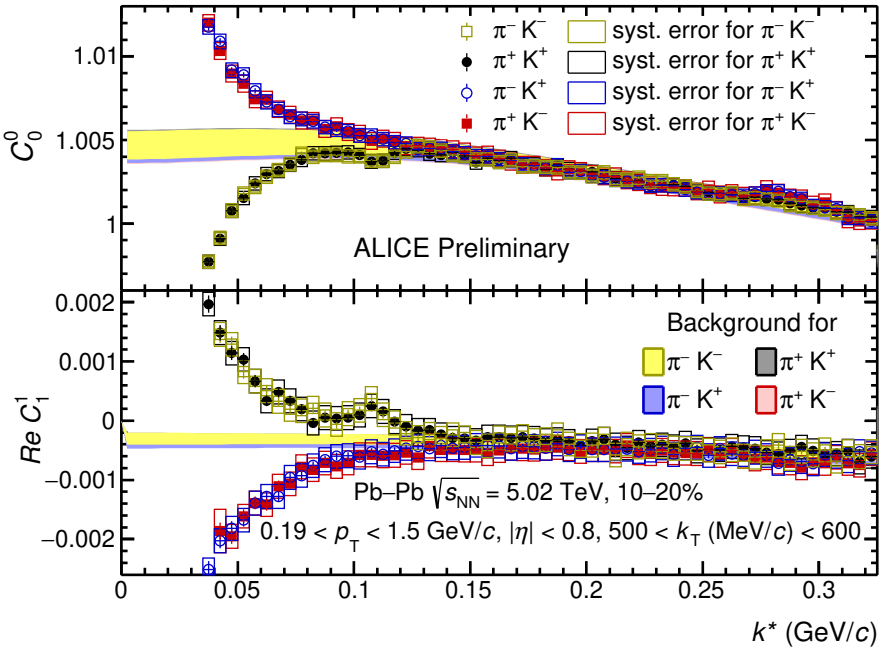

Figure 4.42: The pion-kaon correlation functions within 500 $<k_T$ (MeV/c)$<$ 600 with the non-femtoscopic background for 10−20% central Pb–Pb collisions at $\sqrt{s_{NN}}$ = 5.02 TeV in ALICE.

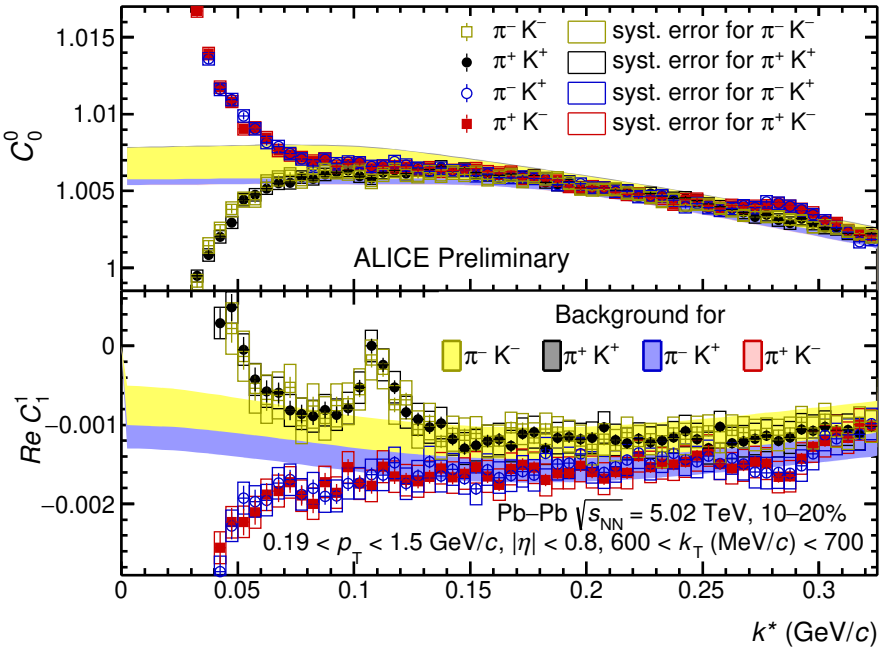

Figure 4.43: The pion-kaon correlation functions within 600 $<k_T$ (MeV/c)$<$ 700 with the non-femtoscopic background for 10−20% central Pb–Pb collisions at $\sqrt{s_{NN}}$ = 5.02 TeV in ALICE.

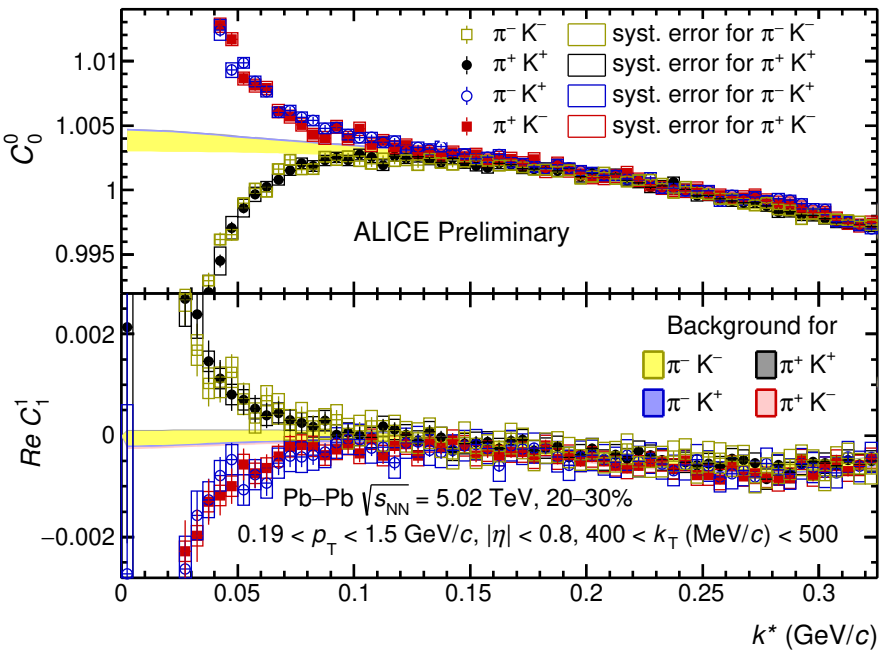

Figure 4.44: The pion-kaon correlation functions within 400 $<k_T$ (MeV/c)$<$ 500 with the non-femtoscopic background for 20−30% central Pb–Pb collisions at $\sqrt{s_{NN}}$ = 5.02 TeV in ALICE.

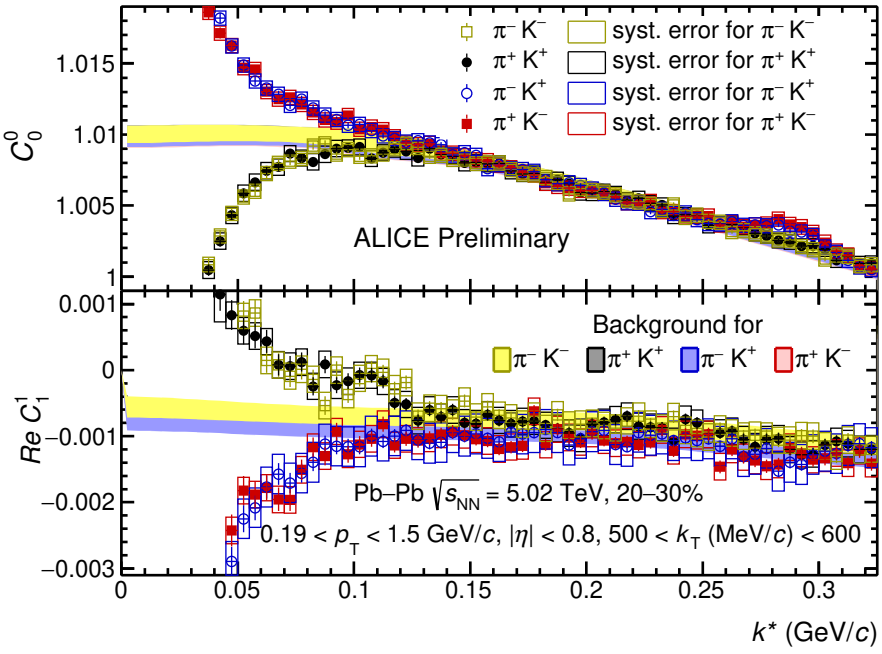

Figure 4.45: The pion-kaon correlation functions within 500 $<k_T$ (MeV/c)$<$ 600 with the non-femtoscopic background for 20−30% central Pb–Pb collisions at $\sqrt{s_{NN}}$ = 5.02 TeV in ALICE.

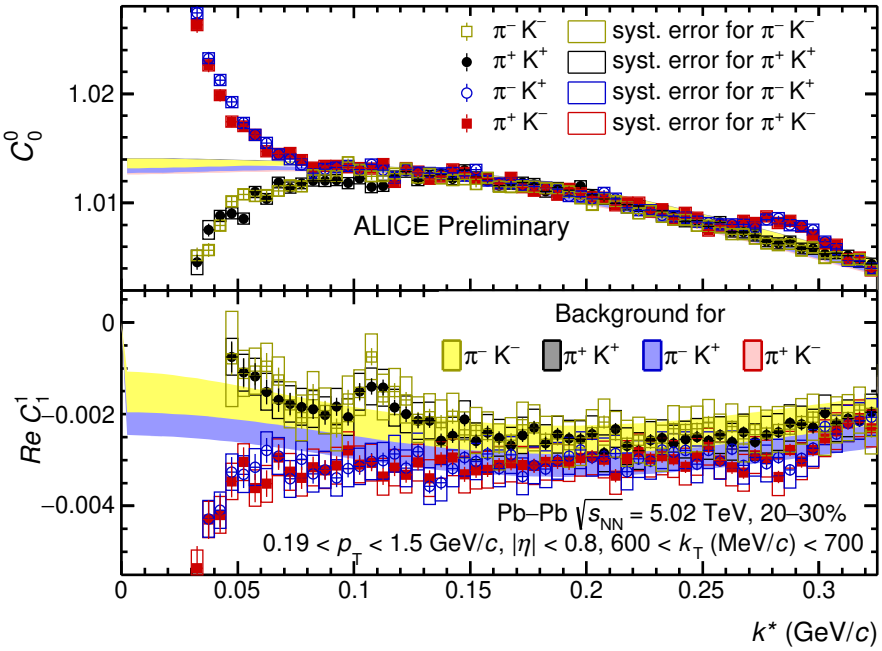

Figure 4.46: The pion-kaon correlation functions within 600 $<k_T$ (MeV/c)$<$ 700 with the non-femtoscopic background for 20−30% central Pb–Pb collisions at $\sqrt{s_{NN}}$ = 5.02 TeV in ALICE.

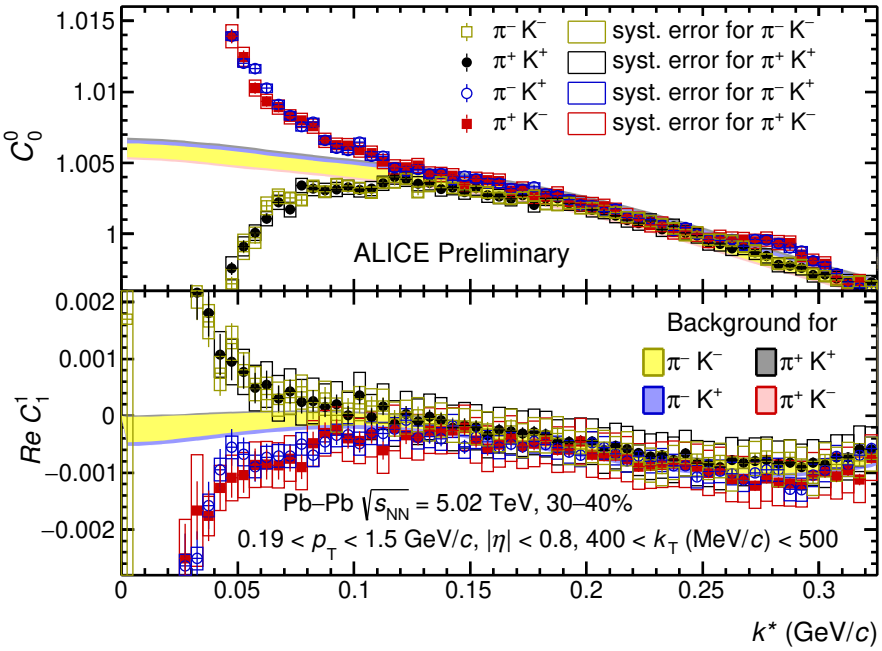

Figure 4.47: The pion-kaon correlation functions within 400 $<k_T$ (MeV/c)$<$ 500 with the non-femtoscopic background for 30−40% central Pb–Pb collisions at $\sqrt{s_{NN}}$ = 5.02 TeV in ALICE.

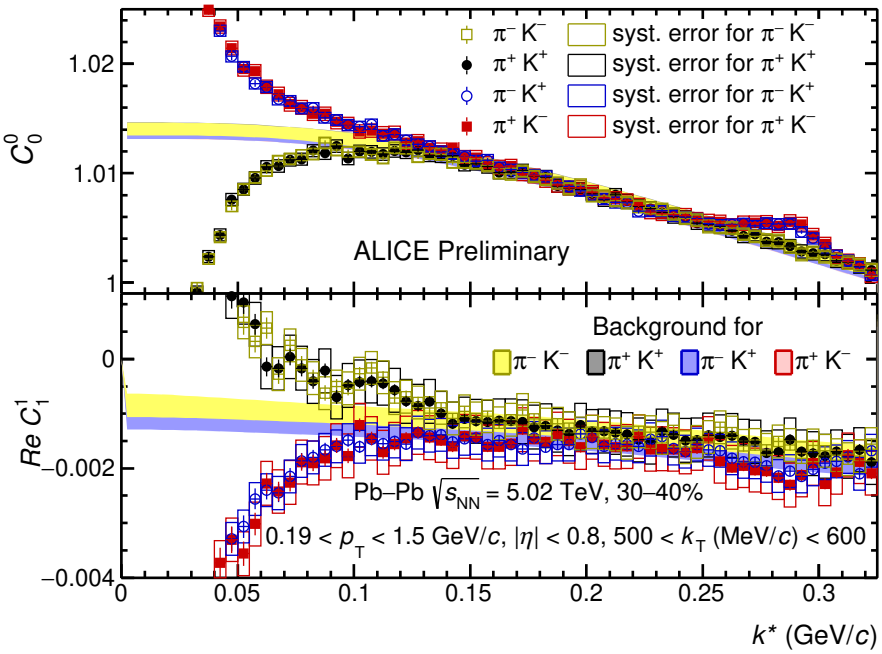

Figure 4.48: The pion-kaon correlation functions within 500 <k_T (MeV/c)< 600 with the non-femtoscopic background for 30−40% central Pb–Pb collisions at $\sqrt{s_{NN}}$ = 5.02 TeV in ALICE.

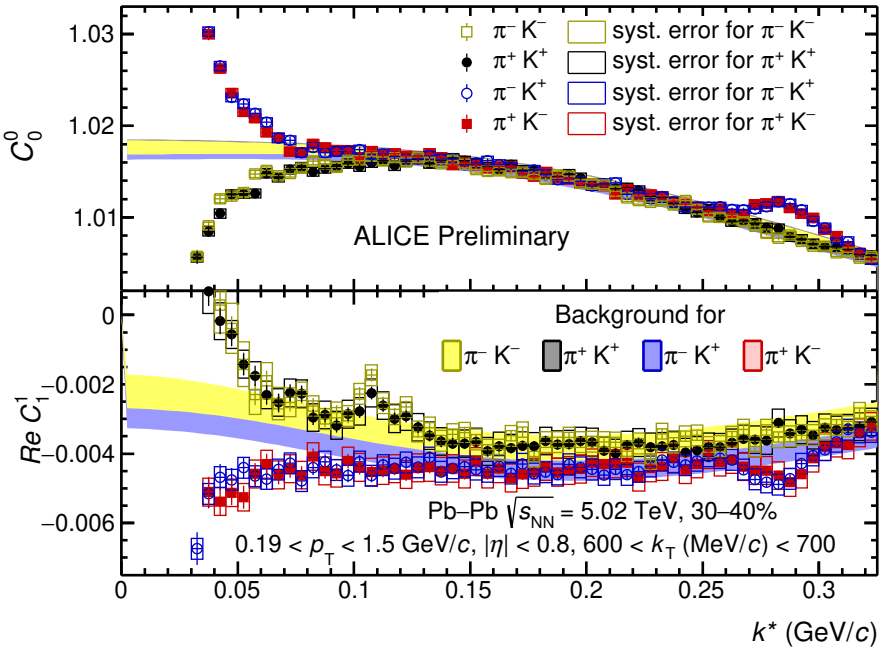

Figure 4.49: The pion-kaon correlation functions within 600 <k_T (MeV/c)< 700 with the non-femtoscopic background for 30−40% central Pb–Pb collisions at $\sqrt{s_{NN}}$ = 5.02 TeV in ALICE.

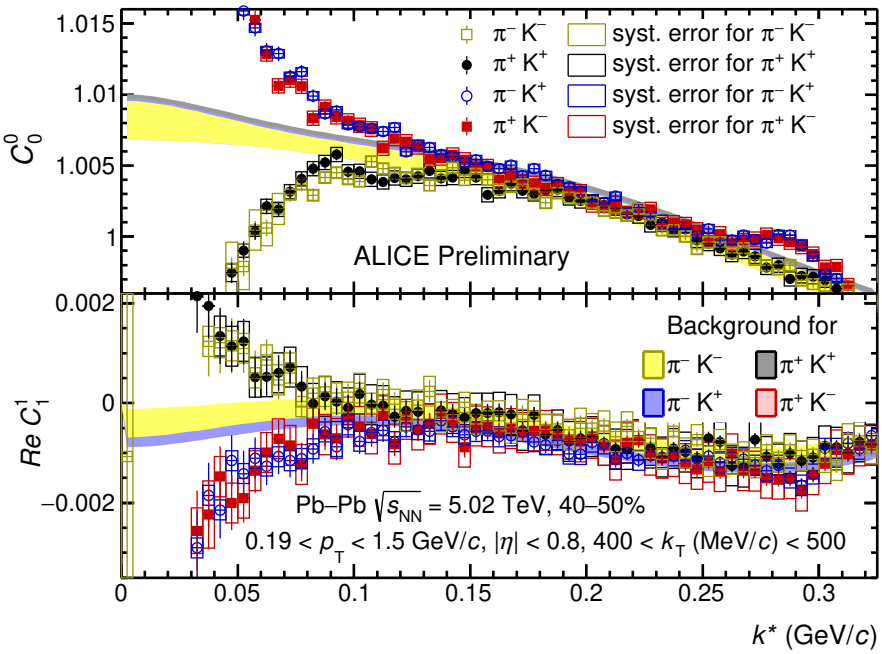

Figure 4.50: The pion-kaon correlation functions within 400 $<k_T$ (MeV/c)$<$ 500 with the non-femtoscopic background for 40–50% central Pb–Pb collisions at $\sqrt{s_{NN}}$ = 5.02 TeV in ALICE.

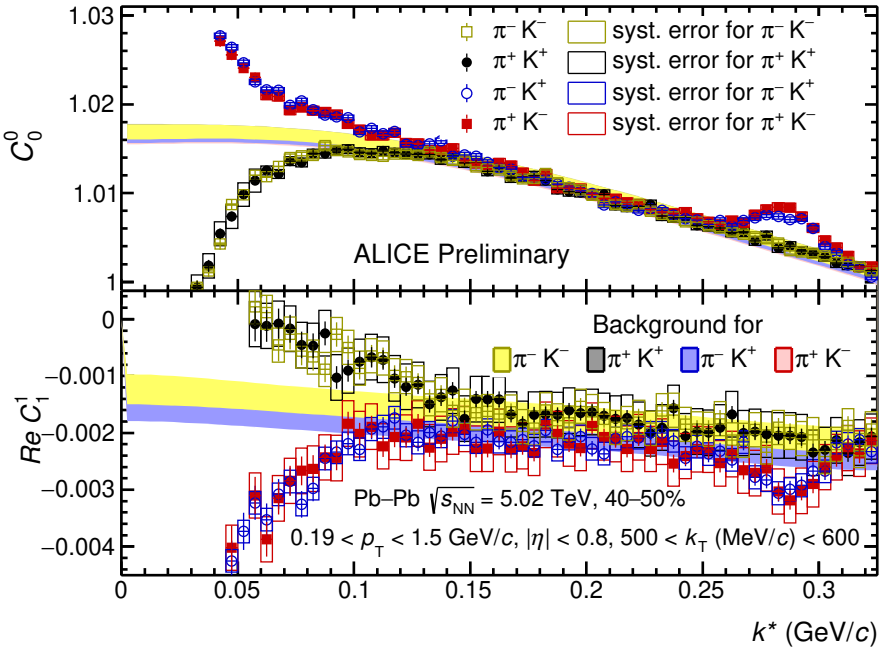

Figure 4.51: The pion-kaon correlation functions within 500 $<k_T$ (MeV/c)$<$ 600 with the non-femtoscopic background for 40–50% central Pb–Pb collisions at $\sqrt{s_{NN}}$ = 5.02 TeV in ALICE.

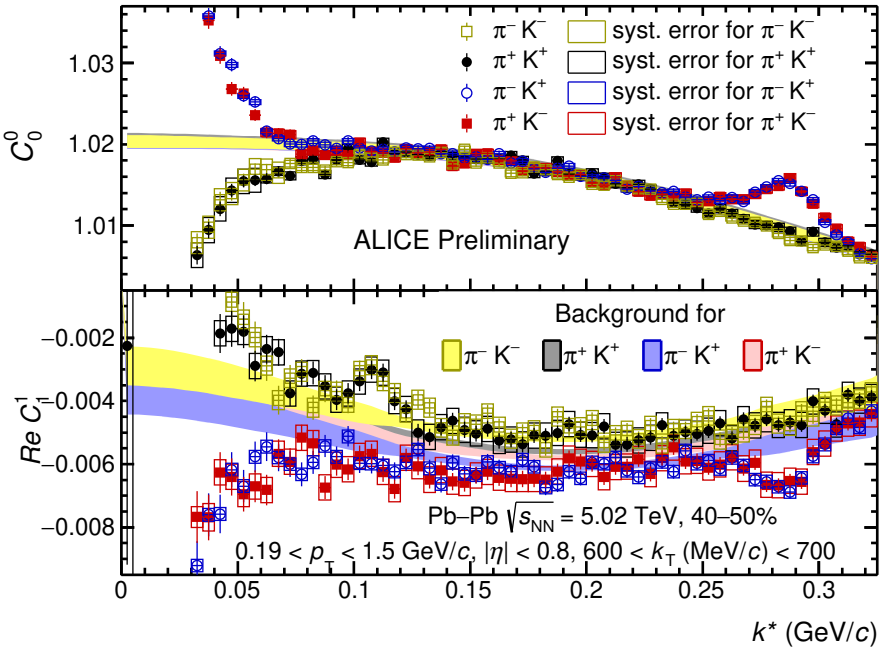

Figure 4.52: The pion-kaon correlation functions within 600 <k_T (MeV/c)< 700 with the non-femtoscopic background for 40−50% central Pb–Pb collisions at $\sqrt{s_{NN}}$ = 5.02 TeV in ALICE.

4.11 β_T-dependent correlation functions

The femtoscopic parameters are heavily influenced by the collectivity of the system, mostly the radial flow. The relative pair separation between the particles, when boosted to PRF, is directly related to the pair-transverse velocity as given by Eq. (4.13) [60].

$$r^*_{out} = \gamma_T(r_{out} - \beta_T \Delta t) \tag{4.13}$$

where, r_{out} and Δt are the space−time separation between particles, β_T is the pair-transverse velocity, $\gamma_T = 1/\sqrt{1-\beta_T^2}$. The β_T can be estimated by taking the ratio of pair-k_T to the transverse mass of the pair. It will be interesting to study the dependence of the pion-kaon correlation functions on the pair-transverse velocity. The primary objective of this study is to probe the evolution of the femtoscopic parameters directly with the collectivity of the system.

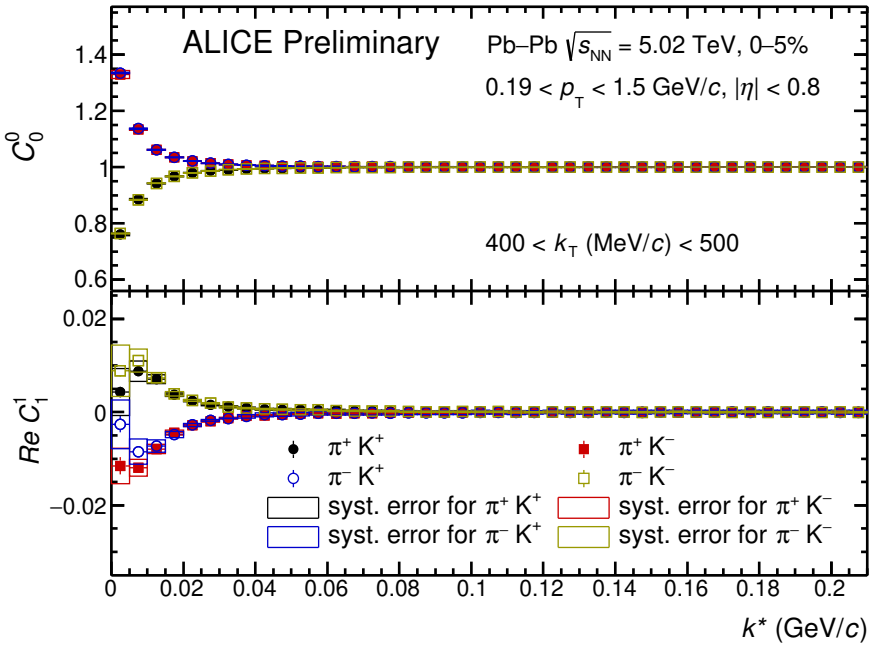

Figure 4.53: The background-minimised correlation functions of pion-kaon pairs within 400 $<k_T$ (MeV/c)$<$ 500 for 0−5% central Pb–Pb collisions at $\sqrt{s_{NN}}$ = 5.02 TeV in ALICE.

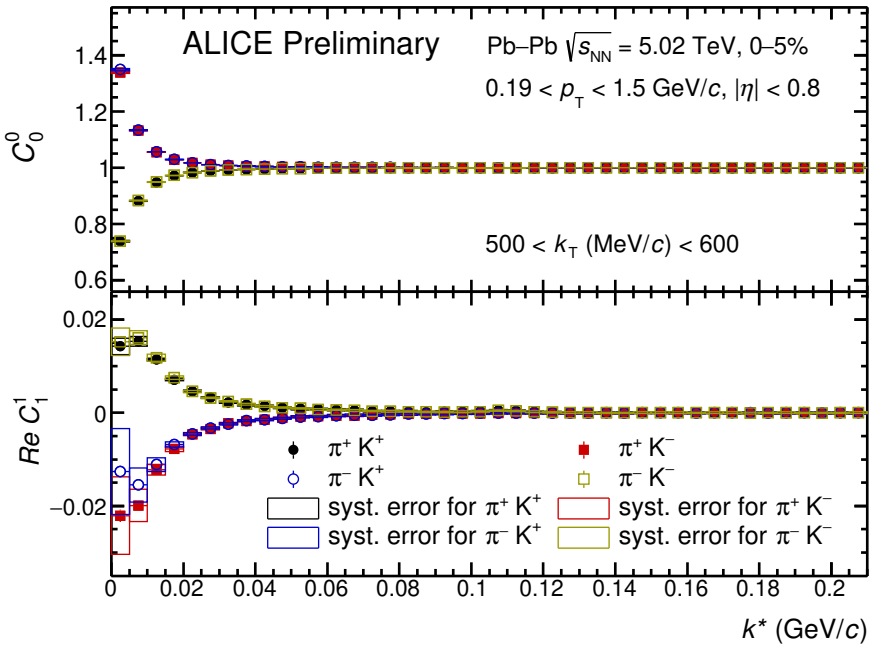

Figure 4.54: The background-minimised correlation functions of pion-kaon pairs within 500 $<k_T$ (MeV/c)$<$ 600 for 0−5% central Pb–Pb collisions at $\sqrt{s_{NN}}$ = 5.02 TeV in ALICE.

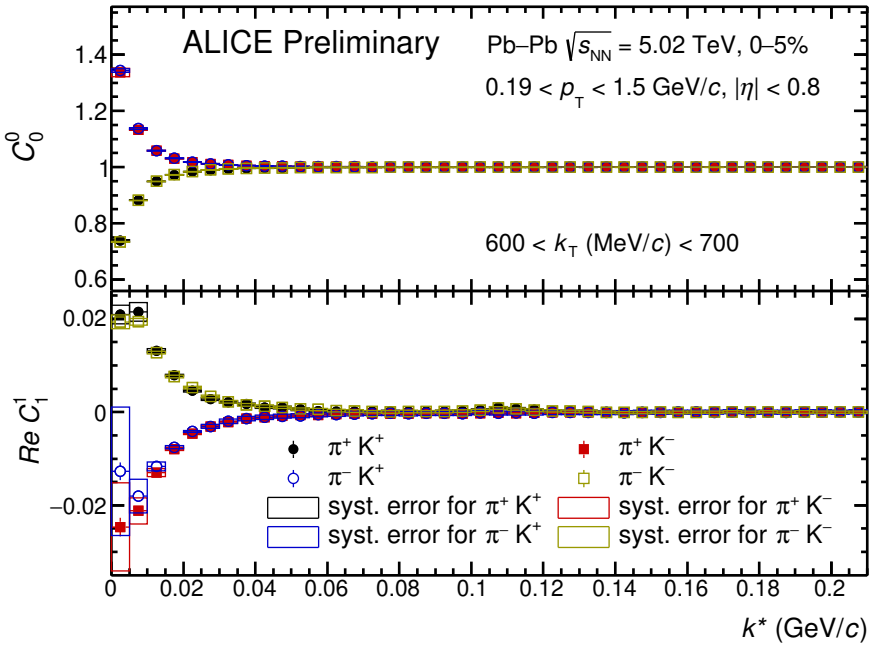

Figure 4.55: The background-minimised correlation functions of pion-kaon pairs within 600 $<k_T$ (MeV/c)$<$ 700 for 0−5% central Pb–Pb collisions at $\sqrt{s_{NN}}$ = 5.02 TeV in ALICE.

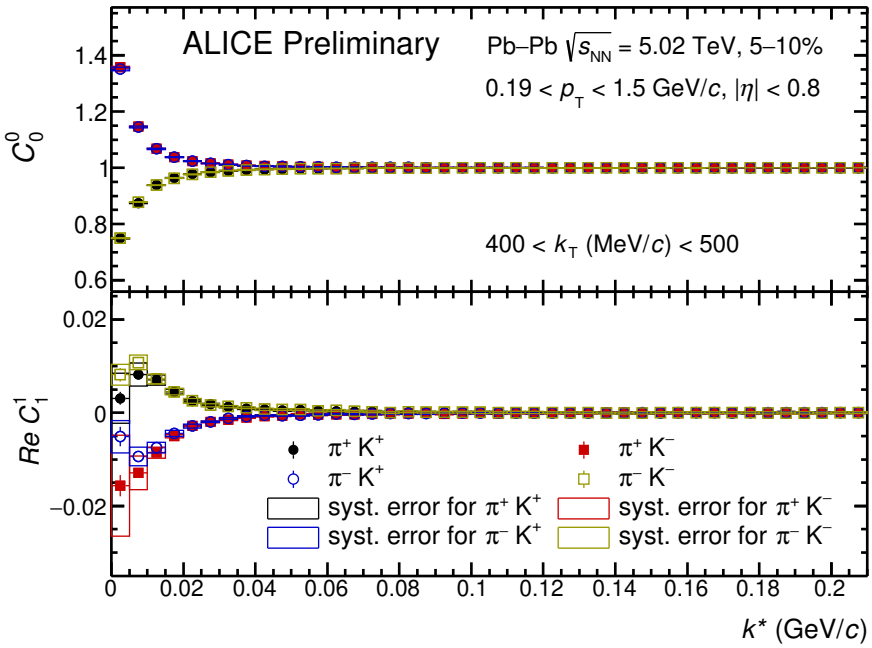

Figure 4.56: The background-minimised correlation functions of pion-kaon pairs within 400 $<k_T$ (MeV/c)$<$ 500 for 5−10% central Pb–Pb collisions at $\sqrt{s_{NN}}$ = 5.02 TeV in ALICE.

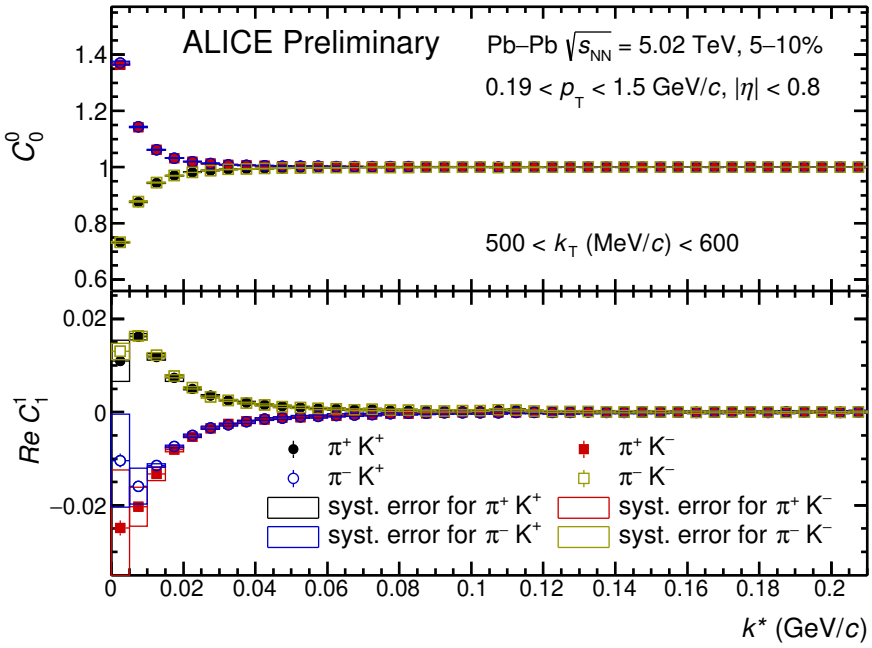

Figure 4.57: The background-minimised correlation functions of pion-kaon pairs within 500 $<k_T$ (MeV/c)$<$ 600 for 5−10% central Pb–Pb collisions at $\sqrt{s_{NN}}$ = 5.02 TeV in ALICE.

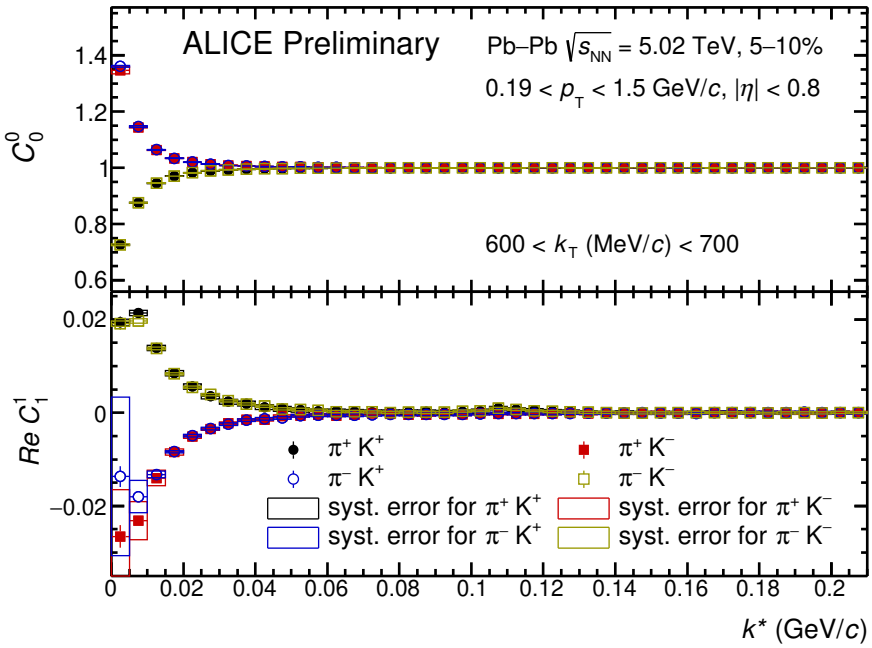

Figure 4.58: The background-minimised correlation functions of pion-kaon pairs within 600 $<k_T$ (MeV/c)$<$ 700 for 5−10% central Pb–Pb collisions at $\sqrt{s_{NN}}$ = 5.02 TeV in ALICE.

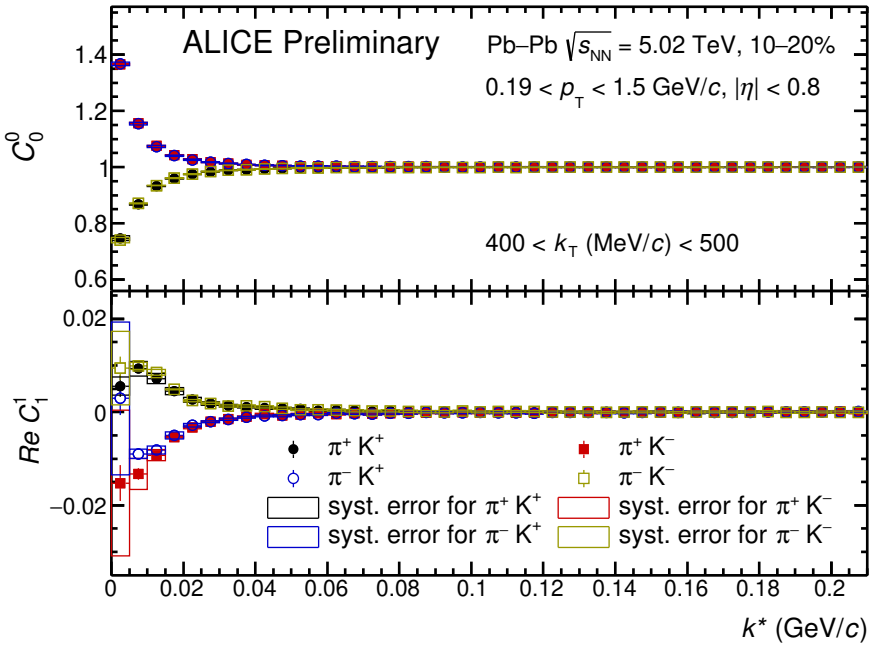

Figure 4.59: The background-minimised correlation functions of pion-kaon pairs within 400 $<k_T$ (MeV/c)$<$ 500 for 10−20% central Pb–Pb collisions at $\sqrt{s_{NN}}$ = 5.02 TeV in ALICE.

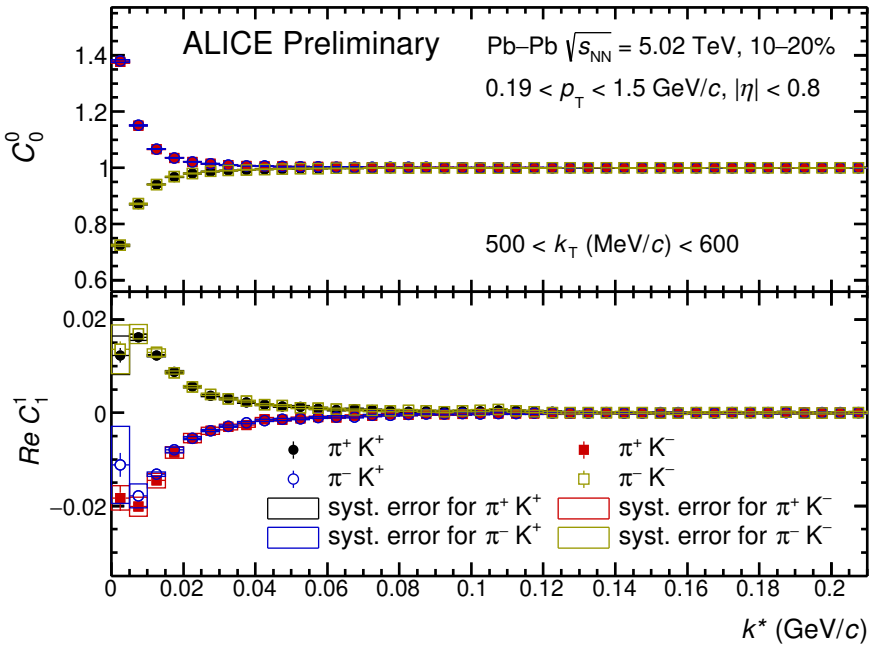

Figure 4.60: The background-minimised correlation functions of pion-kaon pairs within 500 $<k_T$ (MeV/c)$<$ 600 for 10−20% central Pb–Pb collisions at $\sqrt{s_{NN}}$ = 5.02 TeV in ALICE.

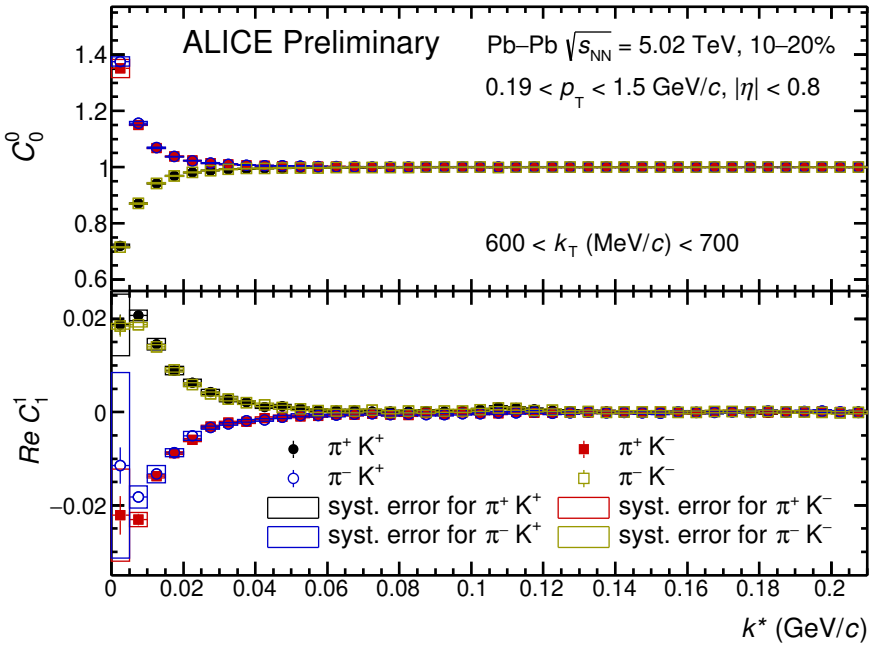

Figure 4.61: The background-minimised correlation functions of pion-kaon pairs within 600 $<k_T$ (MeV/c)$<$ 700 for 10−20% central Pb–Pb collisions at $\sqrt{s_{NN}}$ = 5.02 TeV in ALICE.

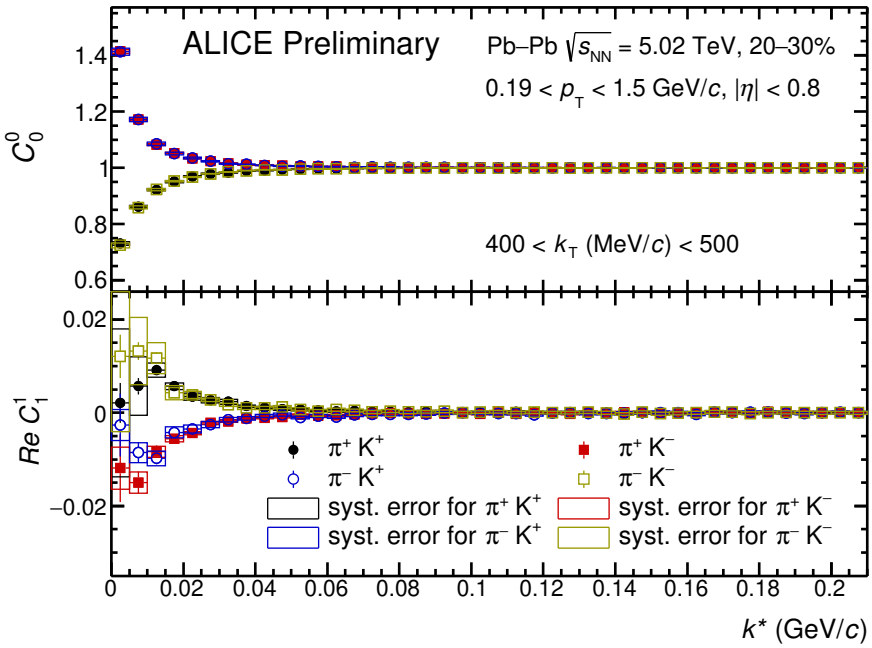

Figure 4.62: The background-minimised correlation functions of pion-kaon pairs within 400 $<k_T$ (MeV/c)$<$ 500 for 20−30% central Pb–Pb collisions at $\sqrt{s_{NN}}$ = 5.02 TeV in ALICE.

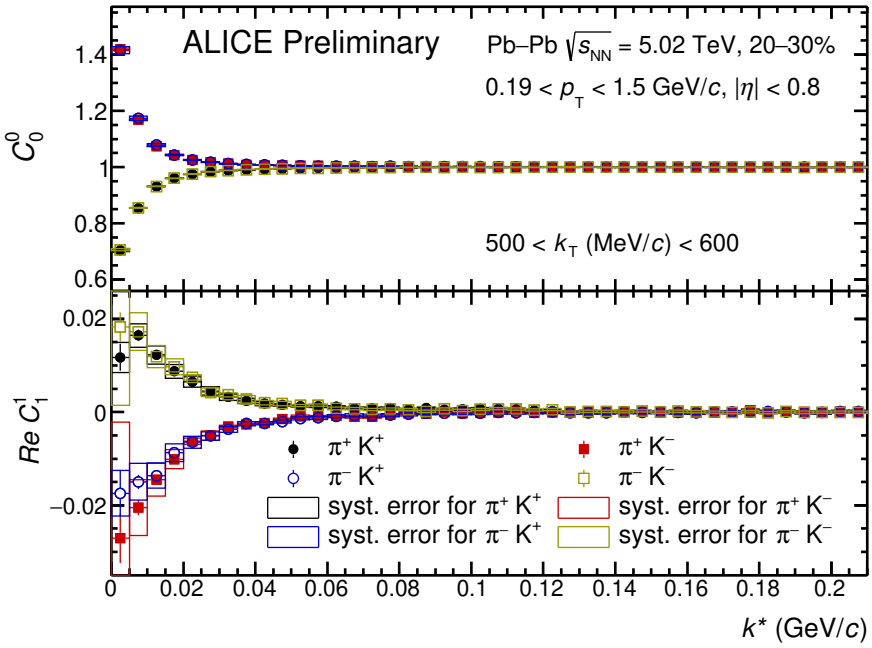

Figure 4.63: The background-minimised correlation functions of pion-kaon pairs within 500 $<k_T$ (MeV/c)$<$ 600 for 20−30% central Pb–Pb collisions at $\sqrt{s_{NN}}$ = 5.02 TeV in ALICE.

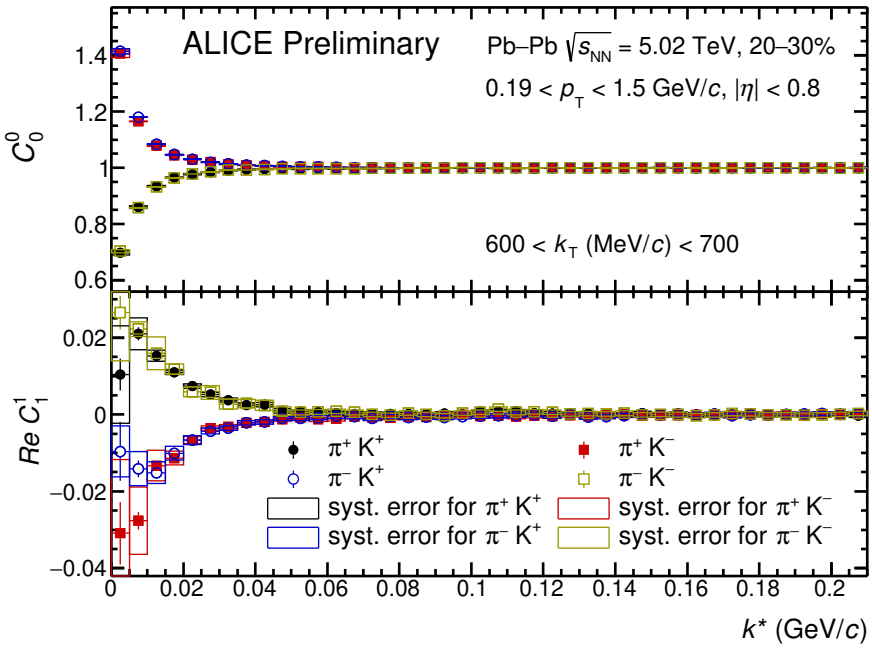

Figure 4.64: The background-minimised correlation functions of pion-kaon pairs within 600 $<k_T$ (MeV/c)$<$ 700 for 20−30% central Pb–Pb collisions at $\sqrt{s_{NN}}$ = 5.02 TeV in ALICE.

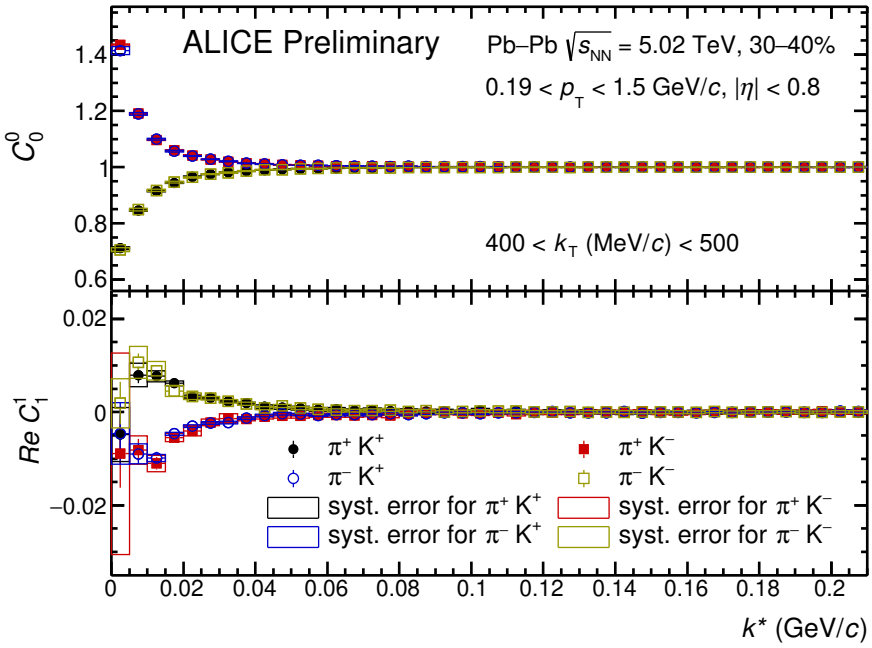

Figure 4.65: The background-minimised correlation functions of pion-kaon pairs within 400 $<k_T$ (MeV/c)$<$ 500 for 30−40% central Pb–Pb collisions at $\sqrt{s_{NN}}$ = 5.02 TeV in ALICE.

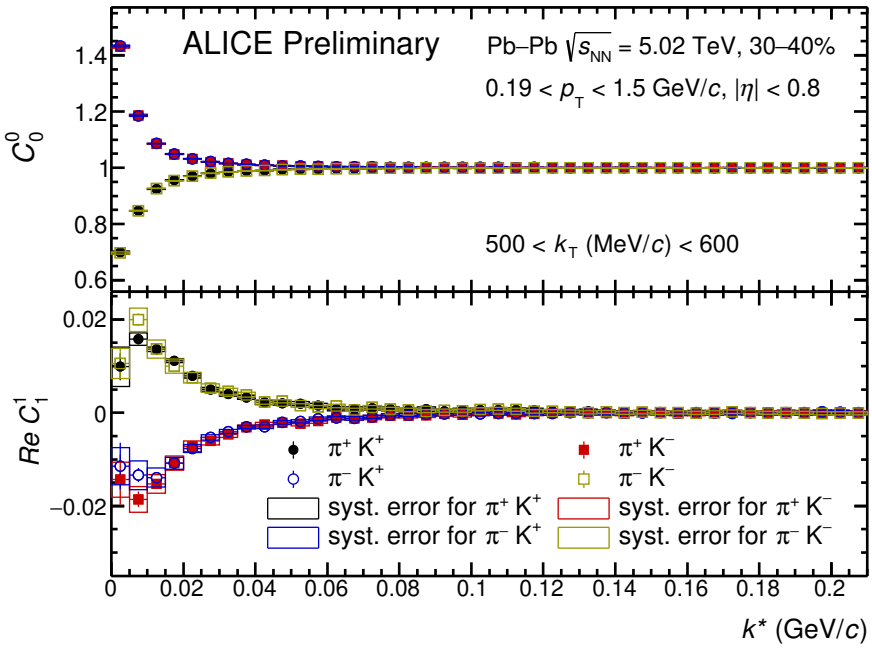

Figure 4.66: The background-minimised correlation functions of pion-kaon pairs within 500 $<k_T$ (MeV/c)$<$ 600 for 30−40% central Pb–Pb collisions at $\sqrt{s_{NN}}$ = 5.02 TeV in ALICE.

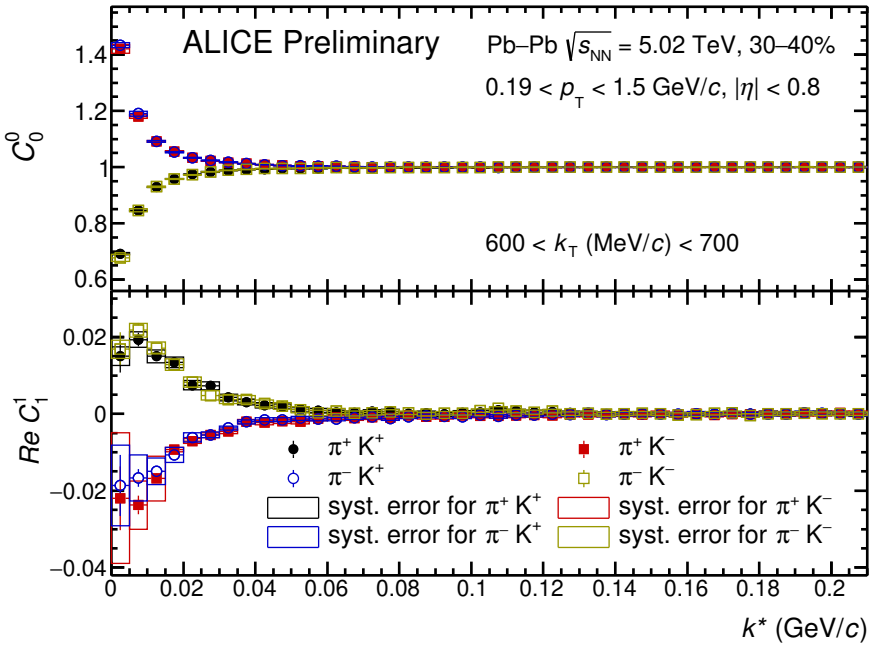

Figure 4.67: The background-minimised correlation functions of pion-kaon pairs within 600 $<k_T$ (MeV/c)$<$ 700 for 30−40% central Pb–Pb collisions at $\sqrt{s_{NN}}$ = 5.02 TeV in ALICE.

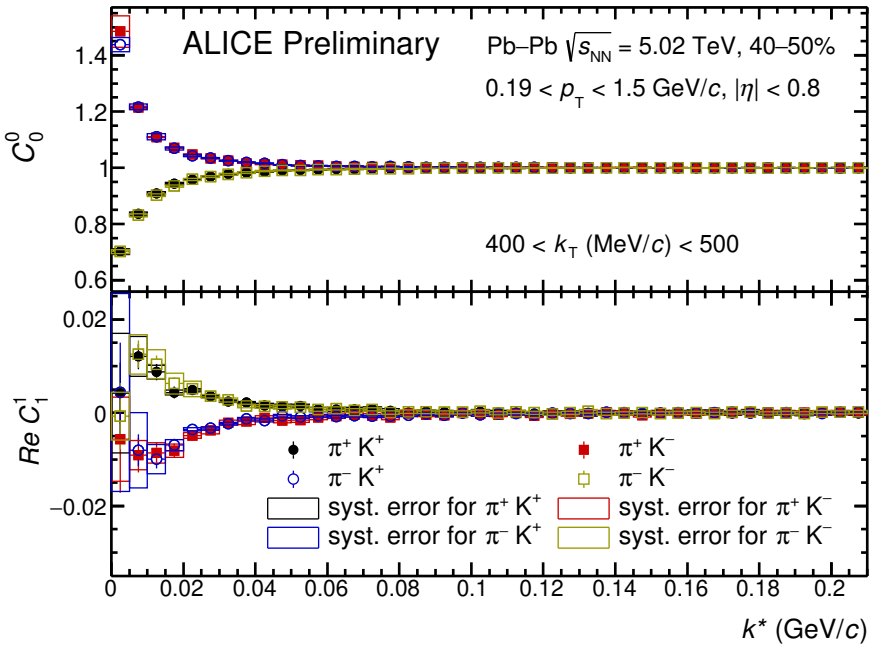

Figure 4.68: The background-minimised correlation functions of pion-kaon pairs within 400 $<k_T$ (MeV/c)$<$ 500 for 40−50% central Pb–Pb collisions at $\sqrt{s_{NN}}$ = 5.02 TeV in ALICE.

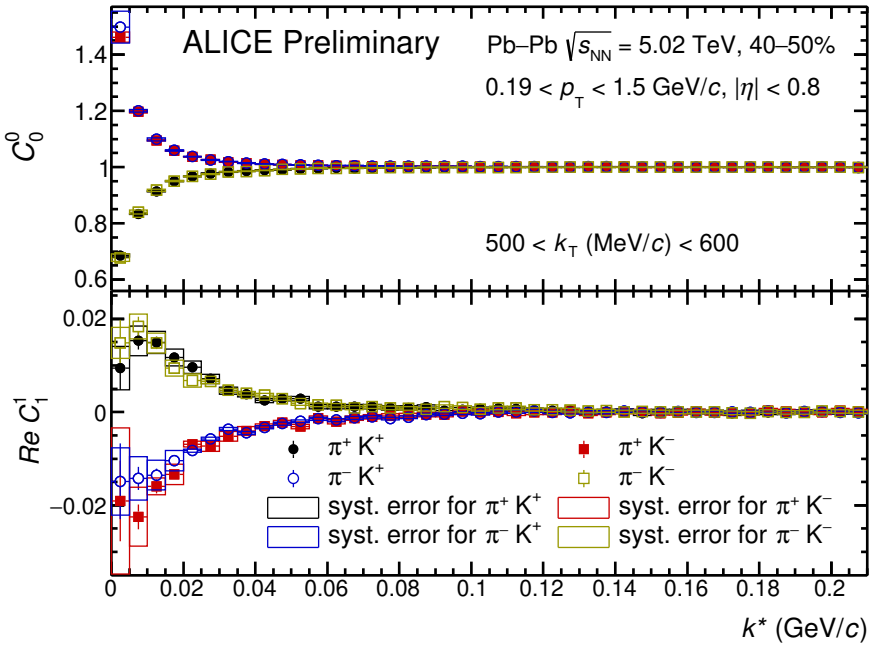

Figure 4.69: The background-minimised correlation functions of pion-kaon pairs within 500 $<k_T$ (MeV/c)$<$ 600 for 40−50% central Pb–Pb collisions at $\sqrt{s_{NN}}$ = 5.02 TeV in ALICE.

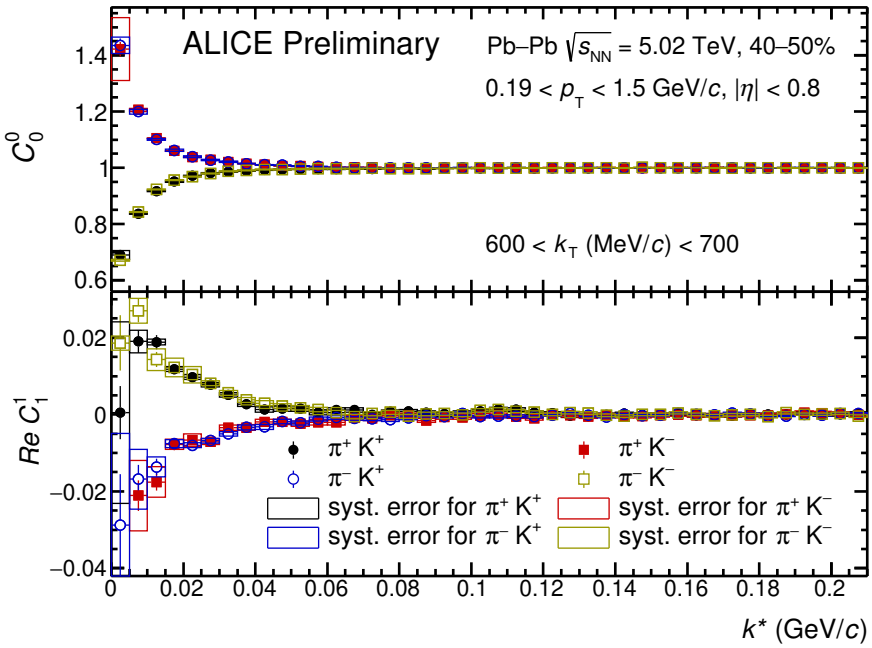

Figure 4.70: The background-minimised correlation functions of pion-kaon pairs within 600 $<k_T$ (MeV/c)$<$ 700 for 40−50% central Pb–Pb collisions at $\sqrt{s_{NN}}$ = 5.02 TeV in ALICE.

4.11.1 Estimation of electron-contamination

To study the β_T-dependence of the correlation functions of pion-kaon pairs, the particles are chosen from 0.1 $<p_T$ (GeV)/c <2.5. The TPC-dEdx distribution for pions as a function of p_T with large $n\sigma$ values are shown in Fig. 4.71, where it is observed that the pion sample is contaminated with the electrons in the lower p_T region. To quantify the fraction of electrons in the pion sample, the following approach is used.

The TPC-dEdx distribution is projected in various p_T bins as shown in Fig. 4.72. The electron sample is distinctively separated from that of the pion in the region of $p_T > 0.24$ GeV/c and is fitted with a Gaussian function as given by Eq. (4.14).

$$y_{\text{elec}} = a_{\text{elec}} e^{\left(\frac{-(x-\mu_{\text{elec}})^2}{4\sigma^2_{\text{elec}}}\right)} \tag{4.14}$$

where, μ_{elec} and σ_{elec} are the mean and standard deviation of the distribution, respectively and a_{elec} is the normalising constant. In the region of $p_T < 0.24$ GeV/c, the TPC-dEdx distribution has the contribution from both electrons and pions. Hence, the TPC-dEdx distribution in the region of $p_T < 0.24$ GeV/c can be fitted with a double Gaussian function as given in Eq. (4.15).

$$y_{\text{total}} = a_{\text{elec}} e^{\left(\frac{-(x-\mu_{\text{elec}})^2}{4\sigma^2_{\text{elec}}}\right)} + a_{\text{pi}} e^{\left(\frac{-(x-\mu_{\text{pi}})^2}{4\sigma^2_{\text{pi}}}\right)}. \tag{4.15}$$

Here, μ_{pi} and σ_{pi} are the mean and standard deviation, respectively of the Gaussian distribution of pion sample, which can be expressed as

$$y_{\text{pi}} = a_{\text{pi}} e^{\left(\frac{-(x-\mu_{\text{pi}})^2}{4\sigma^2_{\text{pi}}}\right)}. \tag{4.16}$$

The previously obtained parameters μ_{elec} and σ_{elec} are used as the input parameters in Eq. (4.15).

The pion sample is chosen within 3σ of the TPC-dEdx distribution in the respective momentum ranges, as discussed in section 4.4.3. In Fig. 4.72, the 3σ of the TPC-dEdx distributions in respective p_T bins are denoted as vertical black lines. The total number of pions and electrons in the respective TPC-dEdx distributions are calculated by integrating the y_{pi} and y_{elec}, respectively within the 3σ. The fraction of electrons over pions (f_e) in the respective p_T bins are given in Table 4.3.

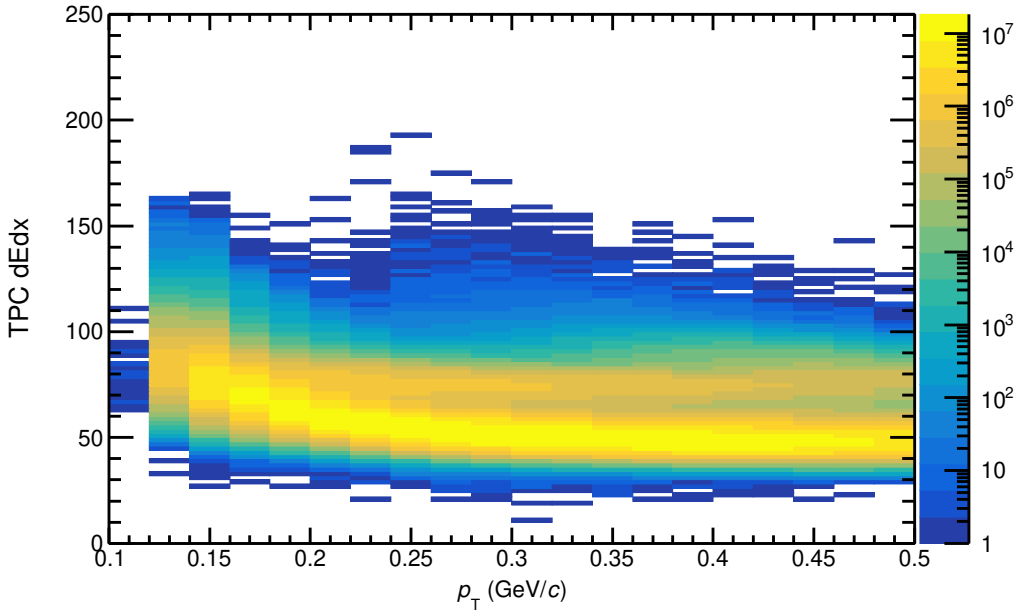

Figure 4.71: The TPC-dEdx distribution for pions as a function of p_T for 0–5% central Pb–Pb collisions at $\sqrt{s_{NN}}$ = 5.02 TeV in ALICE.

Centrality (%)	Fraction of electron contamination for p_T ranges (GeV/c)					
	0.12–0.14	0.14–0.16	0.16–0.18	0.18–0.20	0.20–0.22	0.22–0.24
0–5	0.03	0.05	0.05	0.08	0.04	0.01
5–10	0.05	0.05	0.05	0.07	0.03	0.01
10–20	0.05	0.05	0.04	0.06	0.03	0.01
20–30	0.04	0.04	0.04	0.05	0.02	0.00
30–40	0.04	0.04	0.03	0.05	0.02	0.00
40–50	0.03	0.03	0.03	0.04	0.02	0.00
50–60	0.03	0.03	0.03	0.04	0.01	0.00
60–70	0.03	0.03	0.02	0.03	0.01	0.00
70–80	0.03	0.02	0.02	0.03	0.01	0.00

Table 4.3: The fractions of electron in the pion sample in various centrality classes and p_T bins.

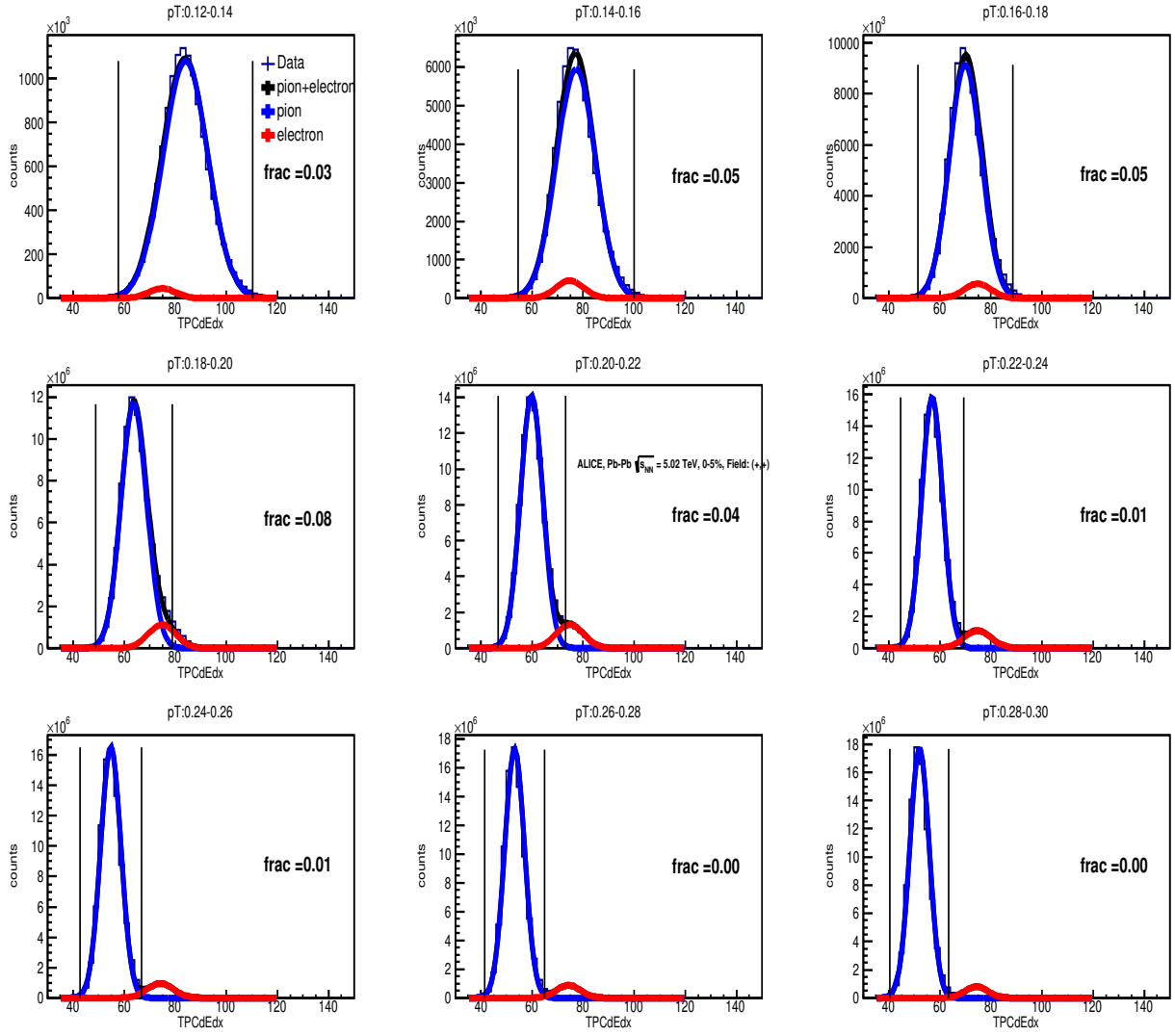

Figure 4.72: The projection of TPC-dEdx distribution for pions in various p_T bins for 0−5% central Pb–Pb collisions at $\sqrt{s_{NN}}$ = 5.02 TeV in ALICE.

The correlation functions of pion-kaon pairs, selected within the β_T bins: 0.7−0.75, 0.8−0.85 and 0.9−0.95 for centrality classes: 0−5%, 20−30%, 40−50% and 60−70% in Pb–Pb collisions at $\sqrt{s_{NN}}$ = 5.02 TeV, with the statistical and systematic uncertainties are shown in Fig. 4.73 -4.84.

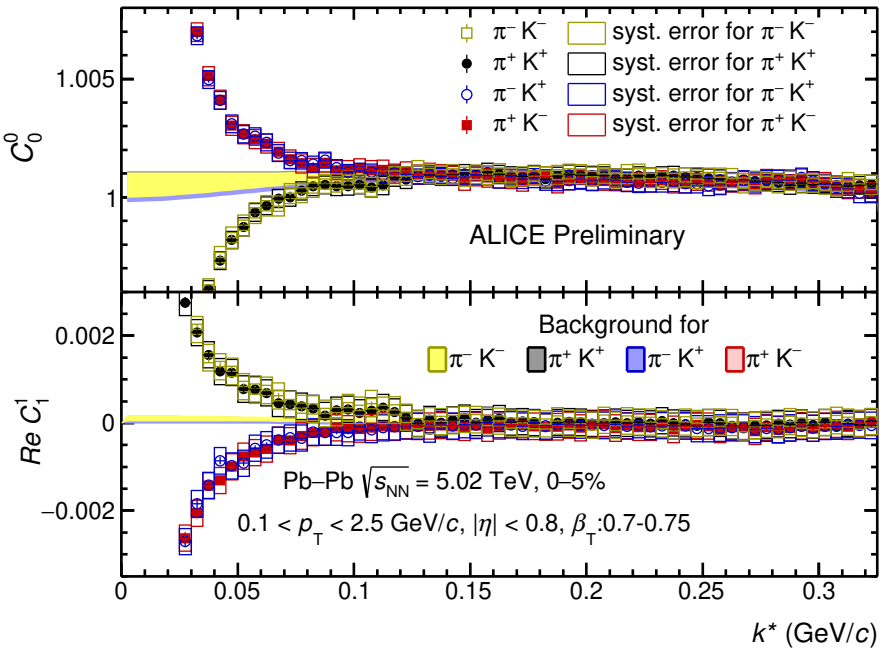

Figure 4.73: The pion-kaon correlation functions within 0.7<β_T<0.75 with the non-femtoscopic background for 0−5% central Pb–Pb collisions at $\sqrt{s_{NN}}$ = 5.02 TeV in ALICE.

The background minimised correlation functions for 0−5%, 20−30%, 40−50% and 60−70% central collisions in the β_T ranges: 0.7−0.75, 0.8−0.85 and 0.9−0.95 are shown in Fig. 4.85-4.96. The systematic uncertainty of the correlation functions in each k^* bin is estimated using Eq. (4.12) by including the uncertainties due to the variations in DCA, η, minimum no. of TPC clusters and magnetic-field polarity, and non-femtoscopic background variation as discussed in the section 4.9.

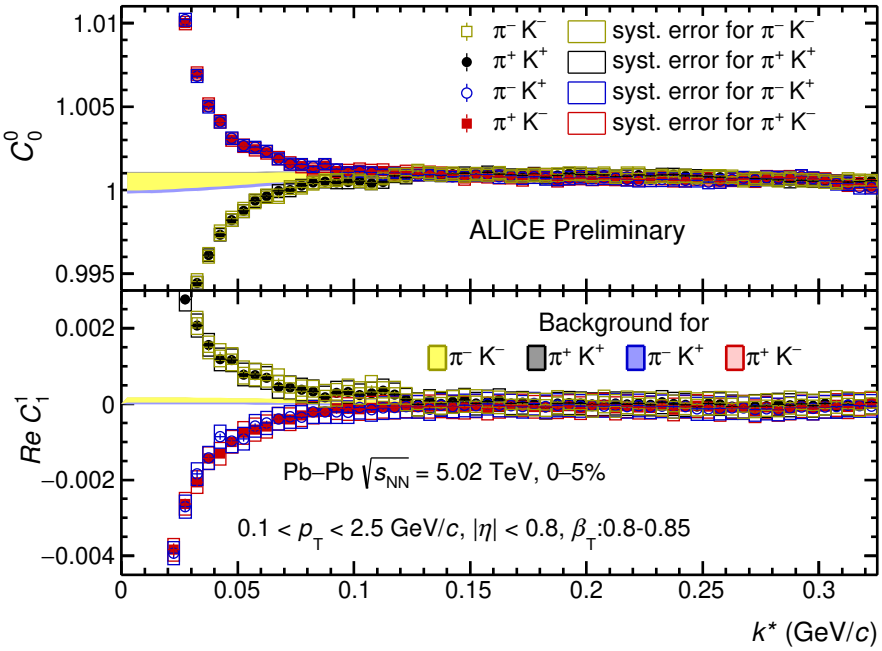

Figure 4.74: The pion-kaon correlation functions within $0.8<\beta_T<0.85$ with the non-femtoscopic background for 0–5% central Pb–Pb collisions at $\sqrt{s_{NN}}$ = 5.02 TeV in ALICE.

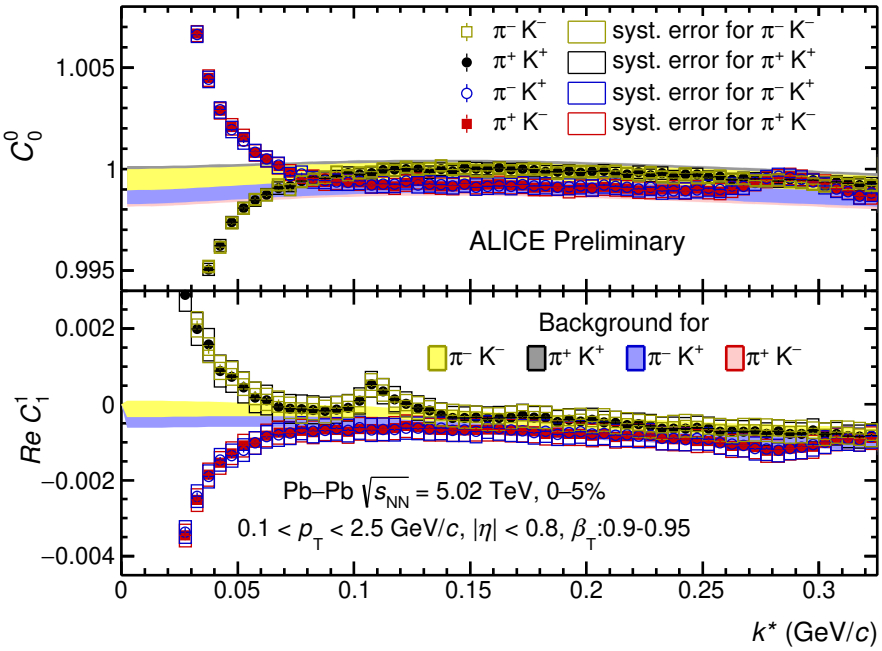

Figure 4.75: The pion-kaon correlation functions within $0.9<\beta_T<0.95$ with the non-femtoscopic background for 0–5% central Pb–Pb collisions at $\sqrt{s_{NN}}$ = 5.02 TeV in ALICE.

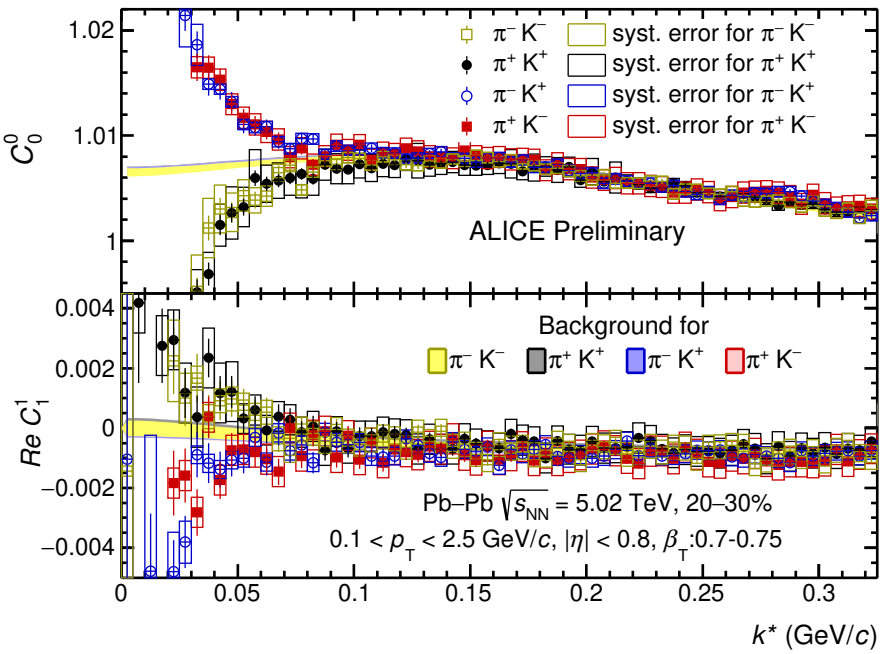

Figure 4.76: The pion-kaon correlation functions within $0.7<\beta_T<0.75$ with the non-femtoscopic background for 20−30% central Pb–Pb collisions at $\sqrt{s_{NN}}$ = 5.02 TeV in ALICE.

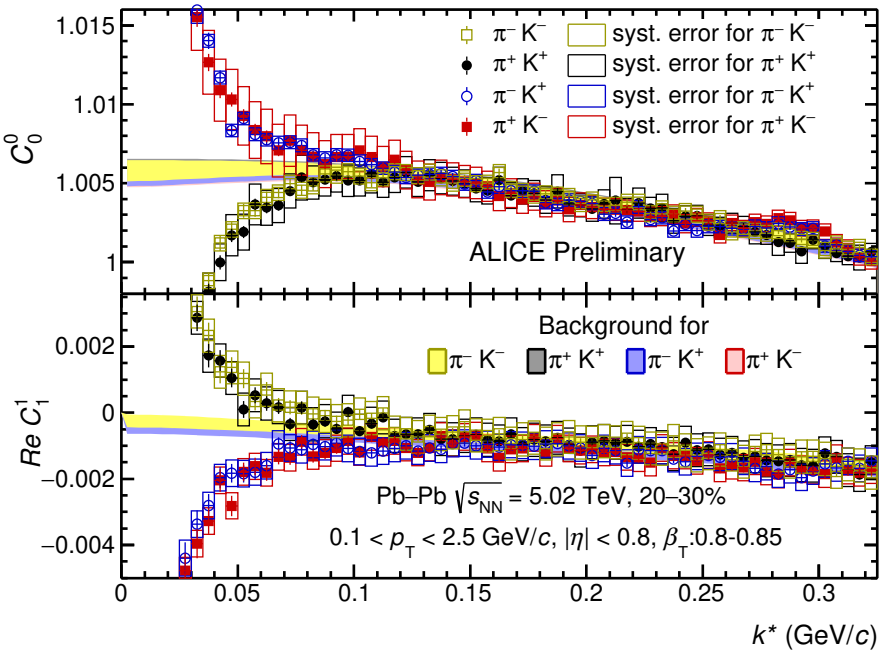

Figure 4.77: The pion-kaon correlation functions within $0.8<\beta_T<0.85$ with the non-femtoscopic background for 20−30% central Pb–Pb collisions at $\sqrt{s_{NN}}$ = 5.02 TeV in ALICE.

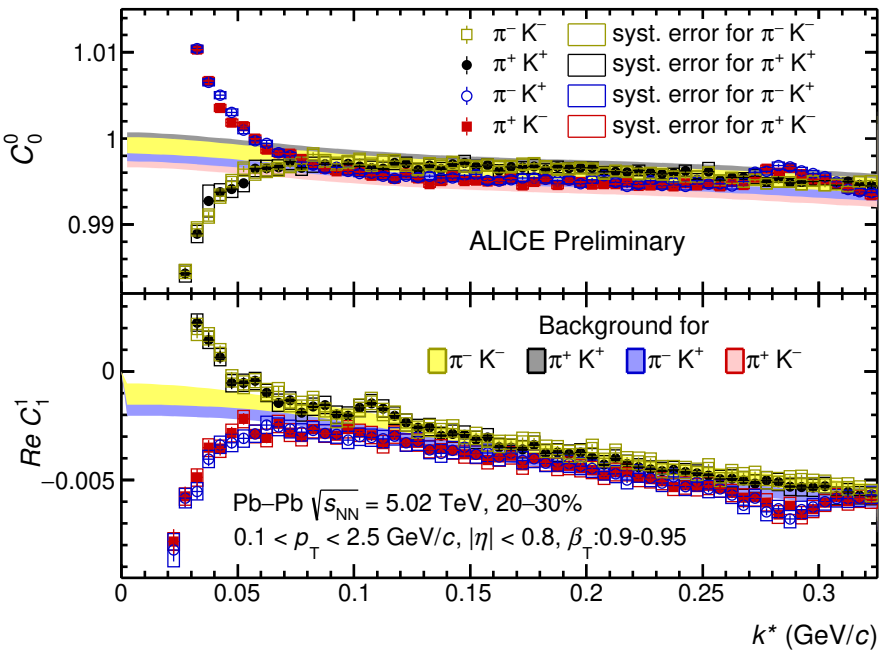

Figure 4.78: The pion-kaon correlation functions within $0.9<\beta_T<0.95$ with the non-femtoscopic background for 20−30% central Pb–Pb collisions at $\sqrt{s_{NN}}$ = 5.02 TeV in ALICE.

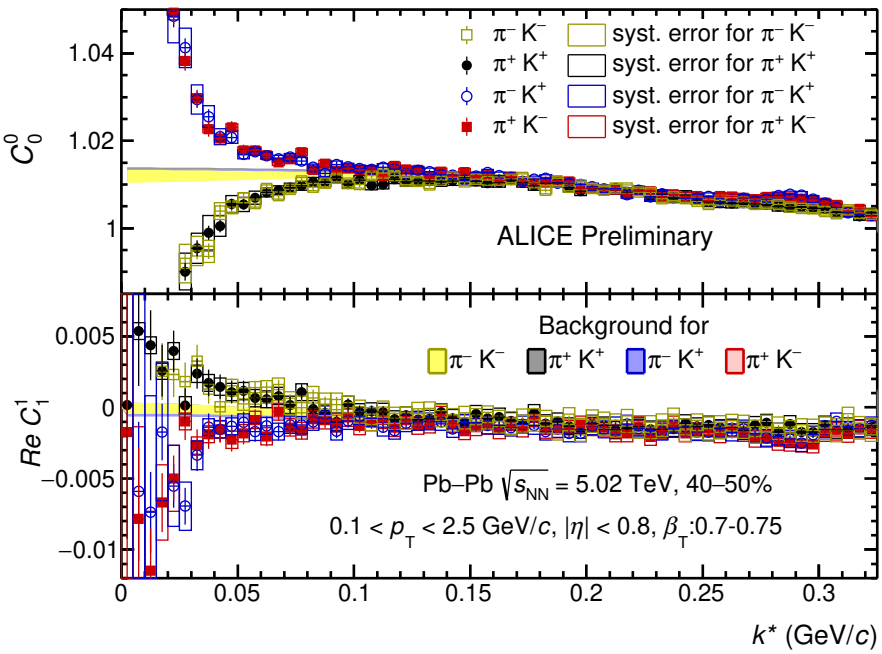

Figure 4.79: The pion-kaon correlation functions within $0.7<\beta_T<0.75$ with the non-femtoscopic background for 40−50% central Pb–Pb collisions at $\sqrt{s_{NN}}$ = 5.02 TeV in ALICE.

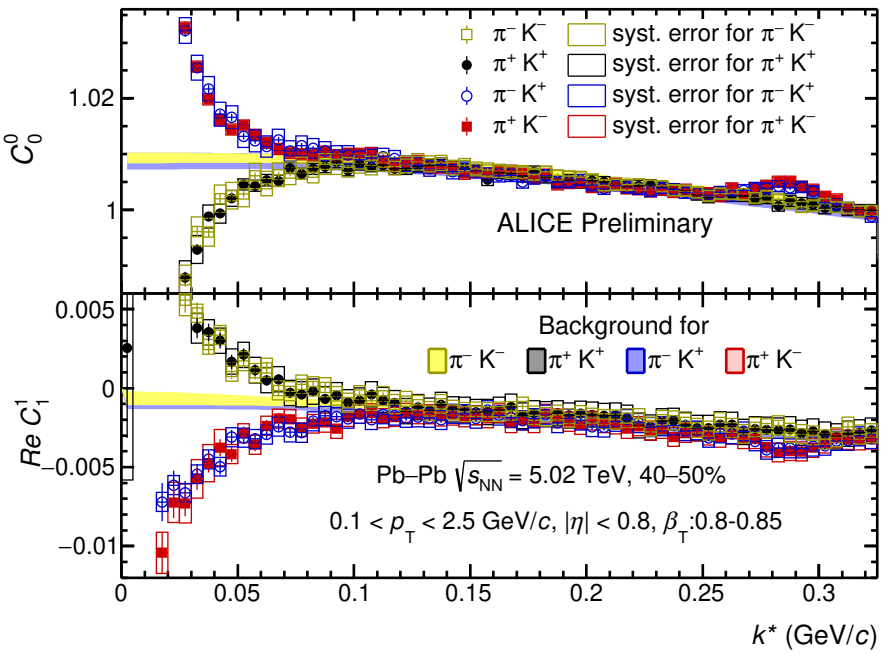

Figure 4.80: The pion-kaon correlation functions within $0.8<\beta_T<0.85$ with the non-femtoscopic background for 40−50% central Pb–Pb collisions at $\sqrt{s_{NN}}$ = 5.02 TeV in ALICE.

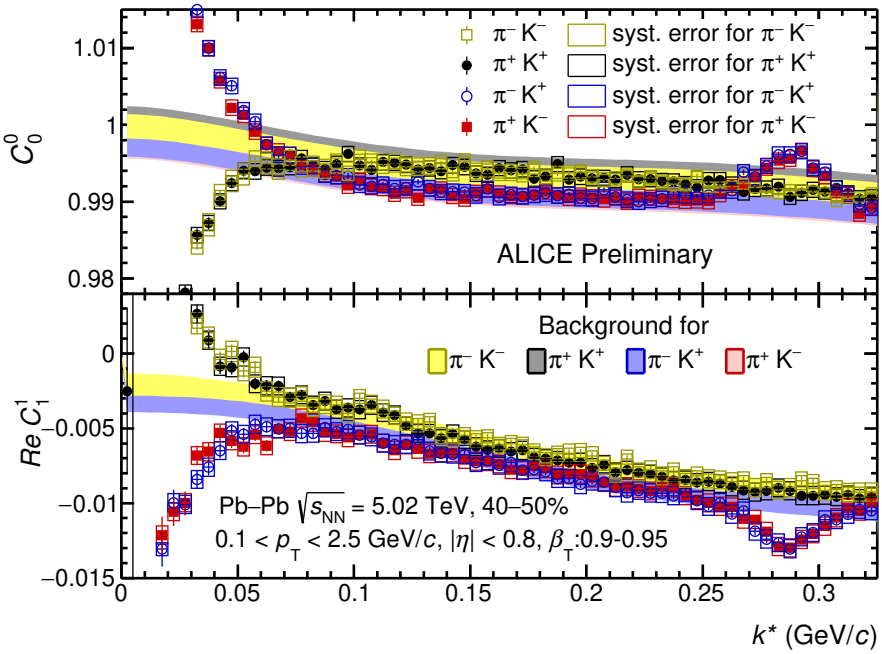

Figure 4.81: The pion-kaon correlation functions within $0.9<\beta_T<0.95$ with the non-femtoscopic background for 40−50% central Pb–Pb collisions at $\sqrt{s_{NN}}$ = 5.02 TeV in ALICE.

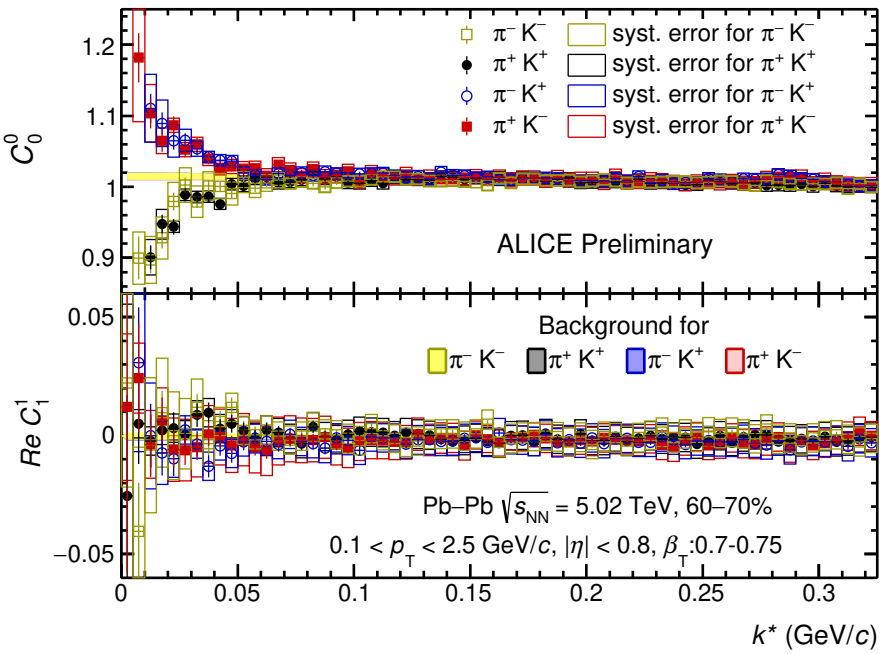

Figure 4.82: The pion-kaon correlation functions within $0.7<\beta_T<0.75$ with the non-femtoscopic background for 60−70% central Pb–Pb collisions at $\sqrt{s_{NN}}$ = 5.02 TeV in ALICE.

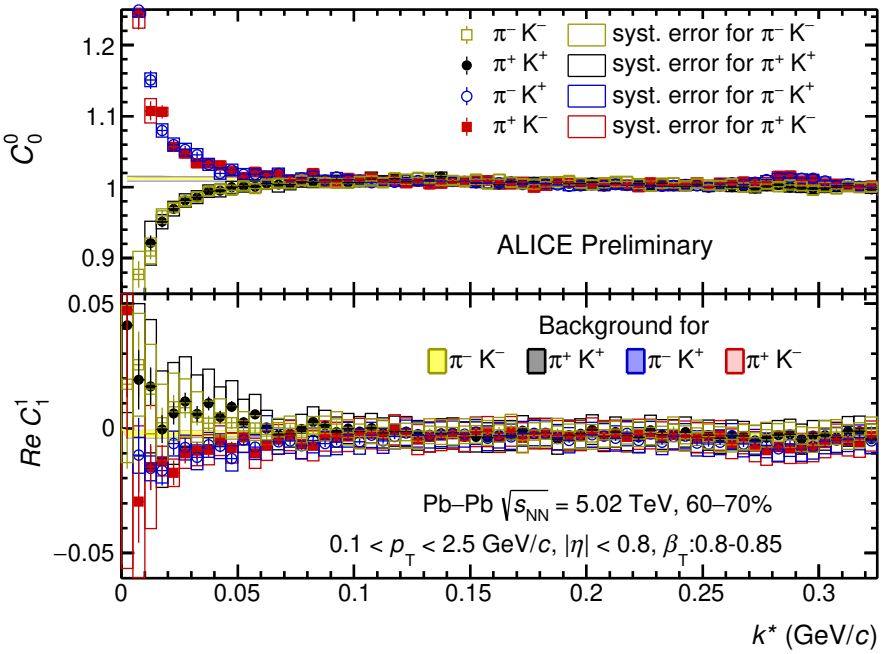

Figure 4.83: The pion-kaon correlation functions within $0.8<\beta_T<0.85$ with the non-femtoscopic background for 60−70% central Pb–Pb collisions at $\sqrt{s_{NN}}$ = 5.02 TeV in ALICE.

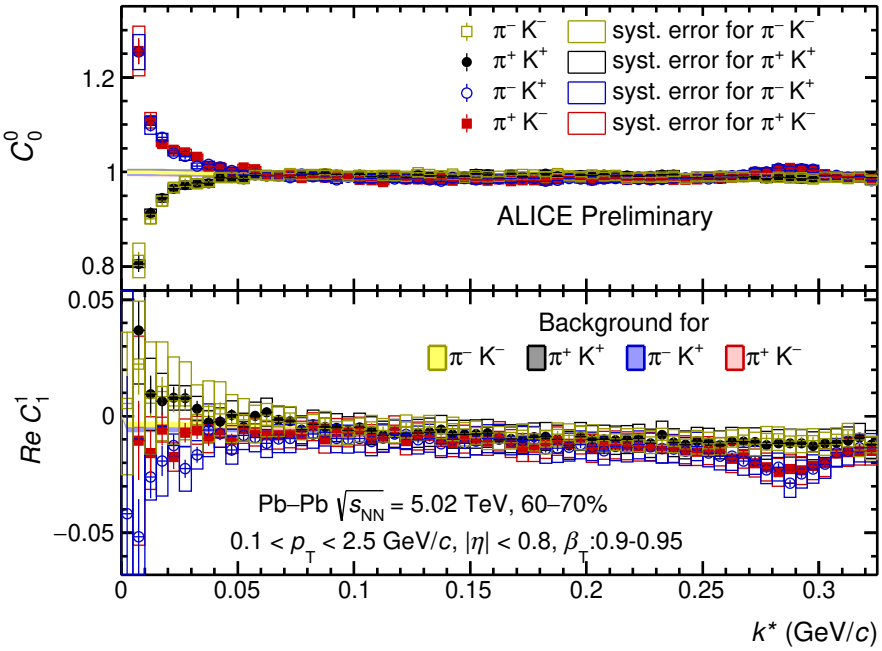

Figure 4.84: The pion-kaon correlation functions within $0.9<\beta_T<0.95$ with the non-femtoscopic background for 60−70% central Pb–Pb collisions at $\sqrt{s_{NN}}$ = 5.02 TeV in ALICE.

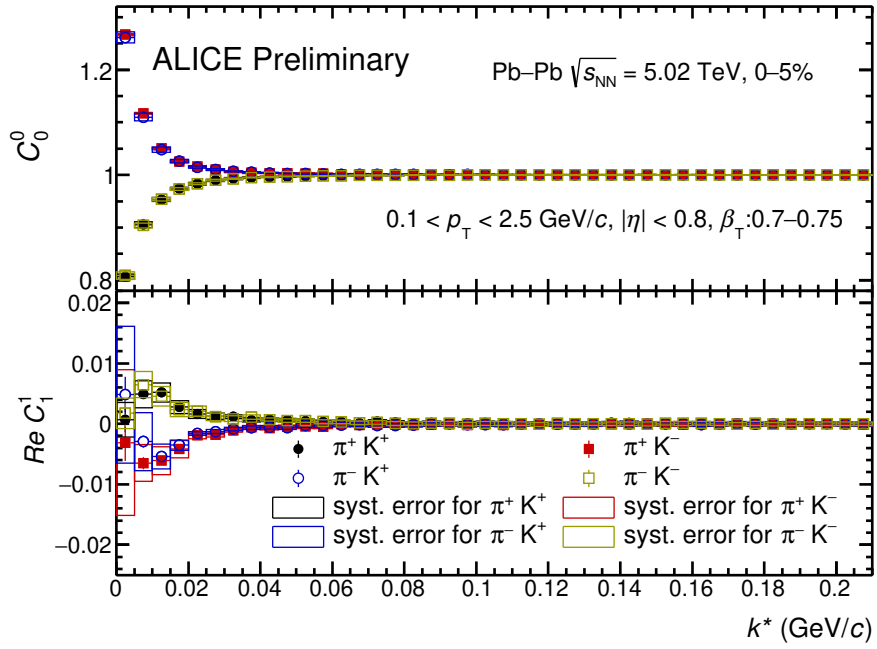

Figure 4.85: The background-minimised correlation functions for pion-kaon pairs in $0.7<\beta_T<0.75$ for 0-5% central Pb–Pb collisions at $\sqrt{s_{NN}}$ = 5.02 TeV in ALICE.

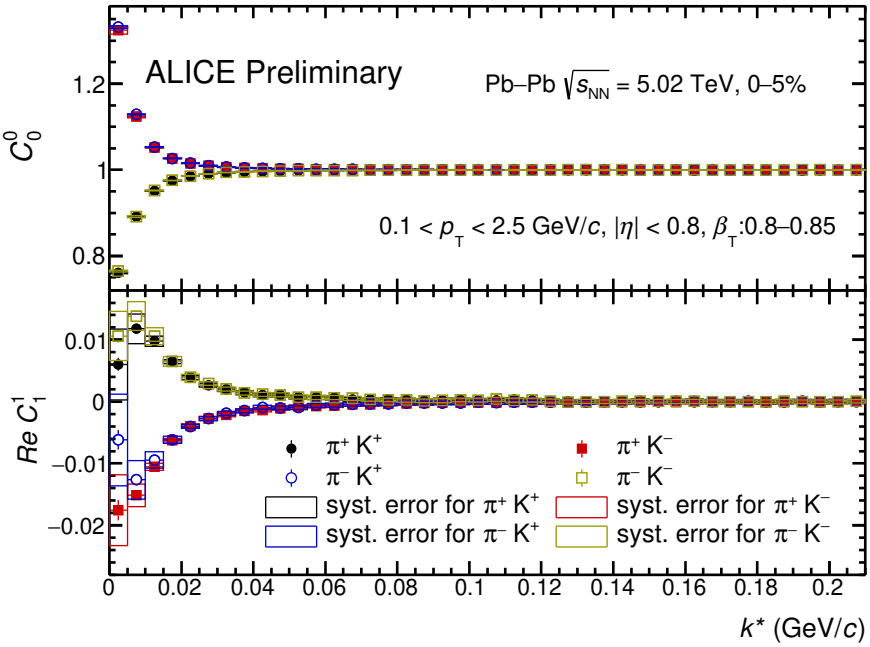

Figure 4.86: The background-minimised correlation functions for pion-kaon pairs in $0.8<\beta_T<0.85$ for 0-5% central Pb–Pb collisions at $\sqrt{s_{NN}}$ = 5.02 TeV in ALICE.

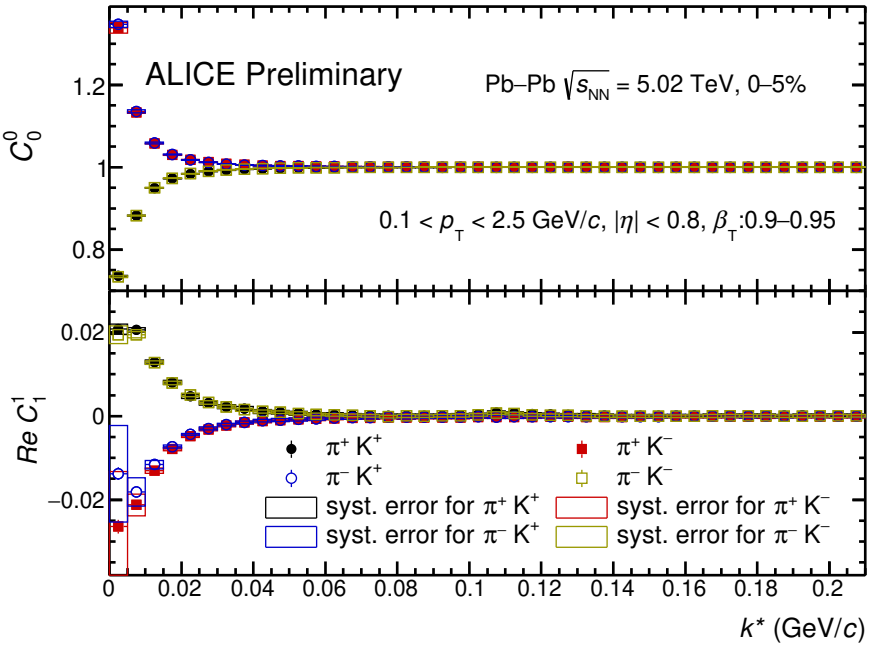

Figure 4.87: The background-minimised correlation functions for pion-kaon pairs in $0.9<\beta_T<0.95$ for 0-5% central Pb–Pb collisions at $\sqrt{s_{NN}}$ = 5.02 TeV in ALICE.

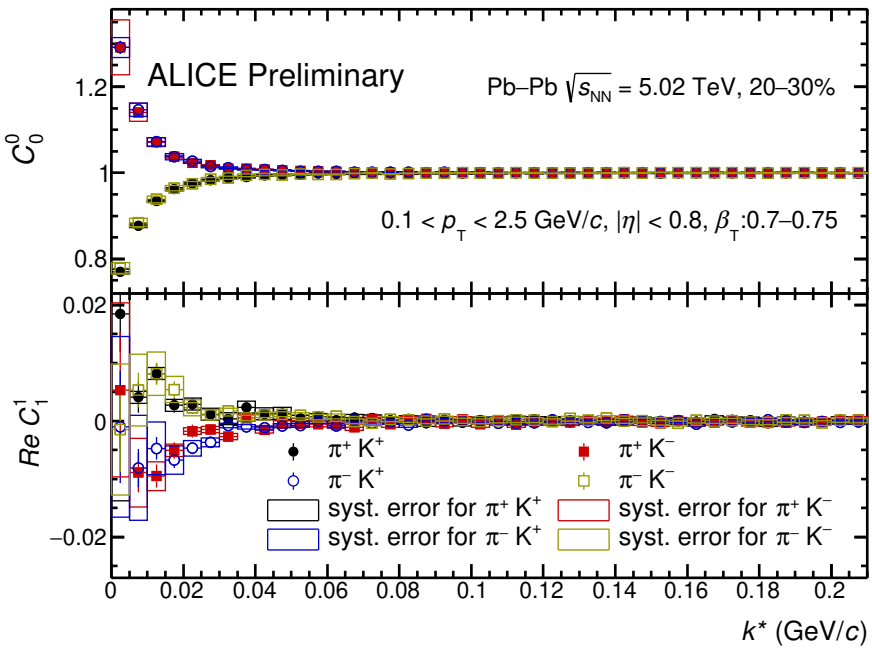

Figure 4.88: The background-minimised correlation functions for pion-kaon pairs in $0.7<\beta_T<0.75$ for 20-30% central Pb–Pb collisions at $\sqrt{s_{NN}}$ = 5.02 TeV in ALICE.

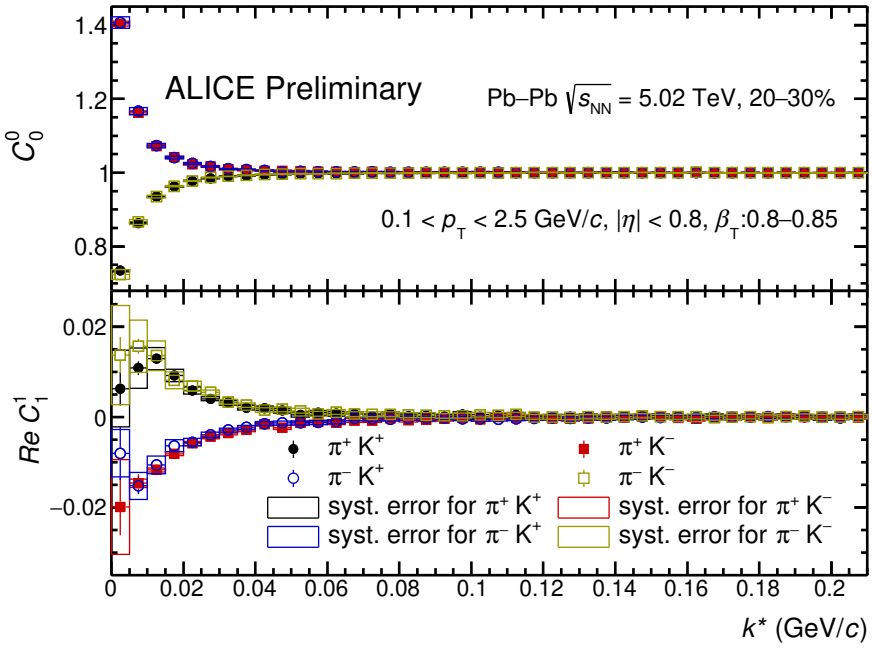

Figure 4.89: The background-minimised correlation functions for pion-kaon pairs in $0.8<\beta_T<0.85$ for 20-30% central Pb–Pb collisions at $\sqrt{s_{NN}}$ = 5.02 TeV in ALICE.

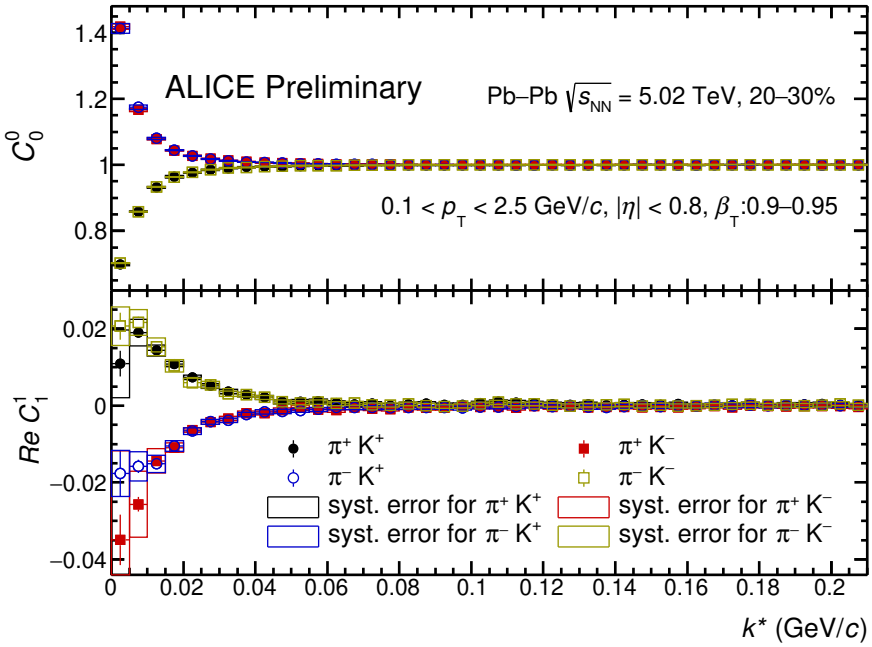

Figure 4.90: The background-minimised correlation functions for pion-kaon pairs in $0.9<\beta_T<0.95$ for 20-30% central Pb–Pb collisions at $\sqrt{s_{NN}}$ = 5.02 TeV in ALICE.

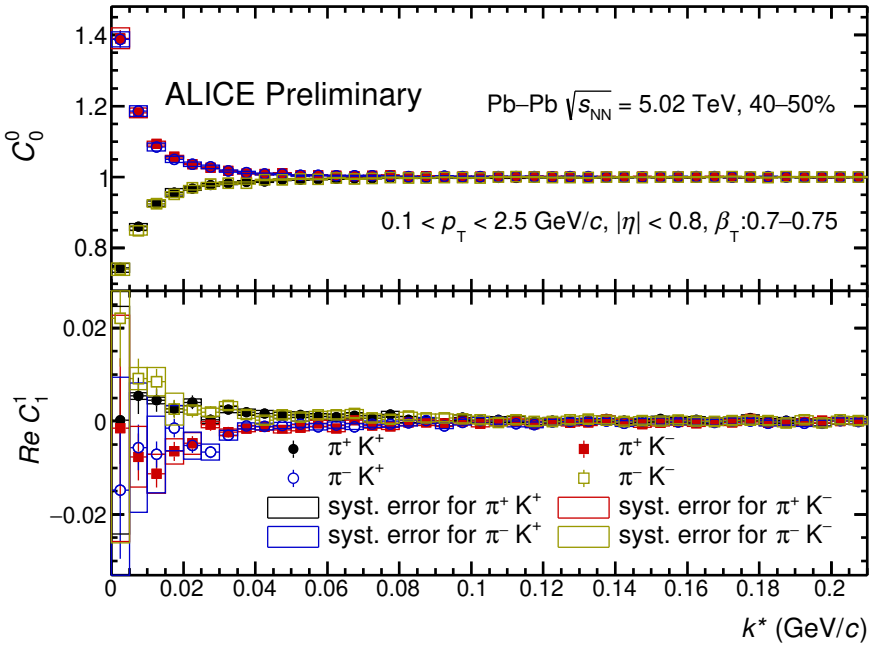

Figure 4.91: The background-minimised correlation functions for pion-kaon pairs in $0.7<\beta_T<0.75$ for 40-50% central Pb–Pb collisions at $\sqrt{s_{NN}}$ = 5.02 TeV in ALICE.

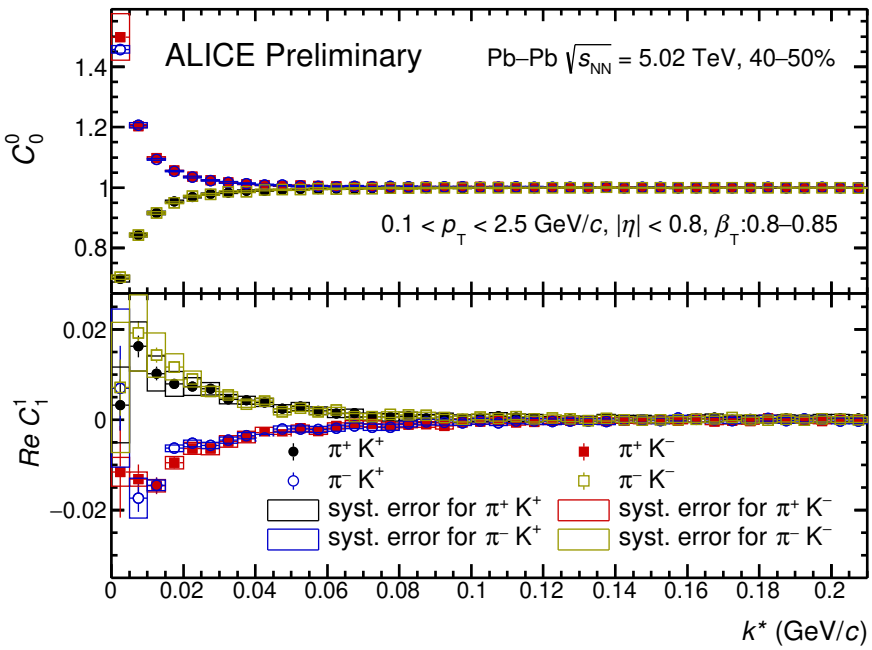

Figure 4.92: The background-minimised correlation functions for pion-kaon pairs in $0.8<\beta_T<0.85$ for 40-50% central Pb–Pb collisions at $\sqrt{s_{NN}}$ = 5.02 TeV in ALICE.

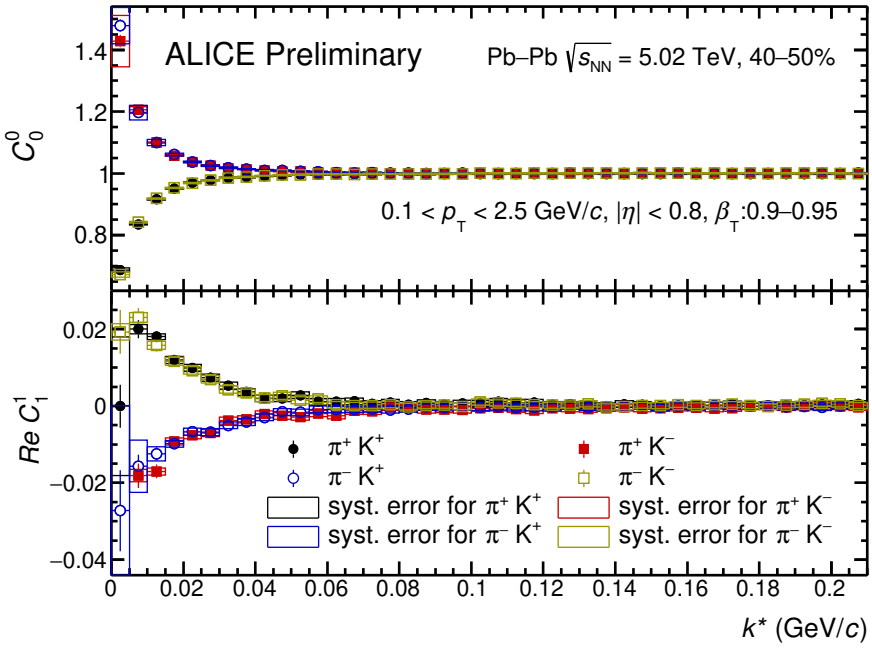

Figure 4.93: The background-minimised correlation functions for pion-kaon pairs in $0.9<\beta_T<0.95$ for 40-50% central Pb–Pb collisions at $\sqrt{s_{NN}}$ = 5.02 TeV in ALICE.

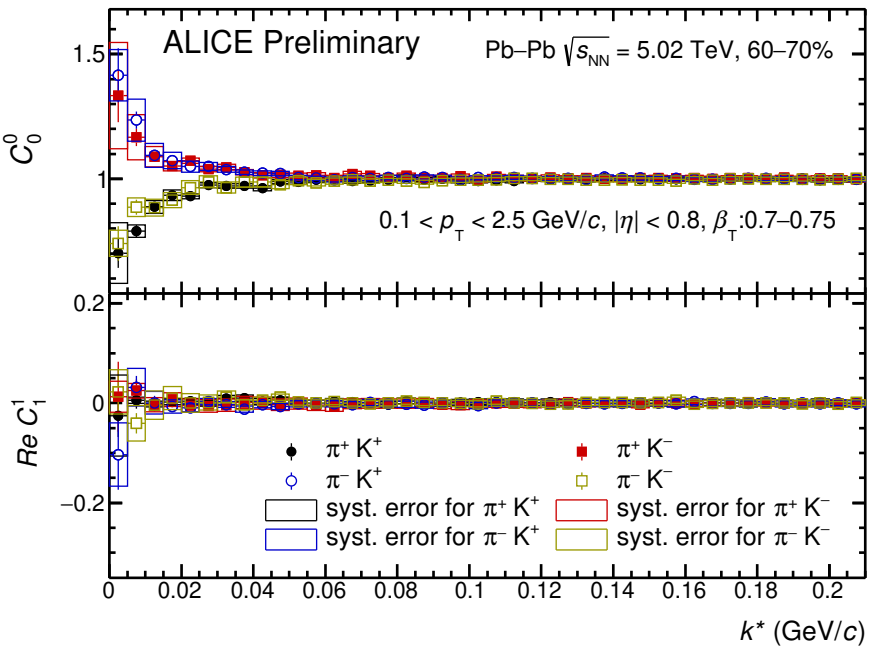

Figure 4.94: The background-minimised correlation functions for pion-kaon pairs in $0.7<\beta_T<0.75$ for 60-70% central Pb–Pb collisions at $\sqrt{s_{NN}}$ = 5.02 TeV in ALICE.

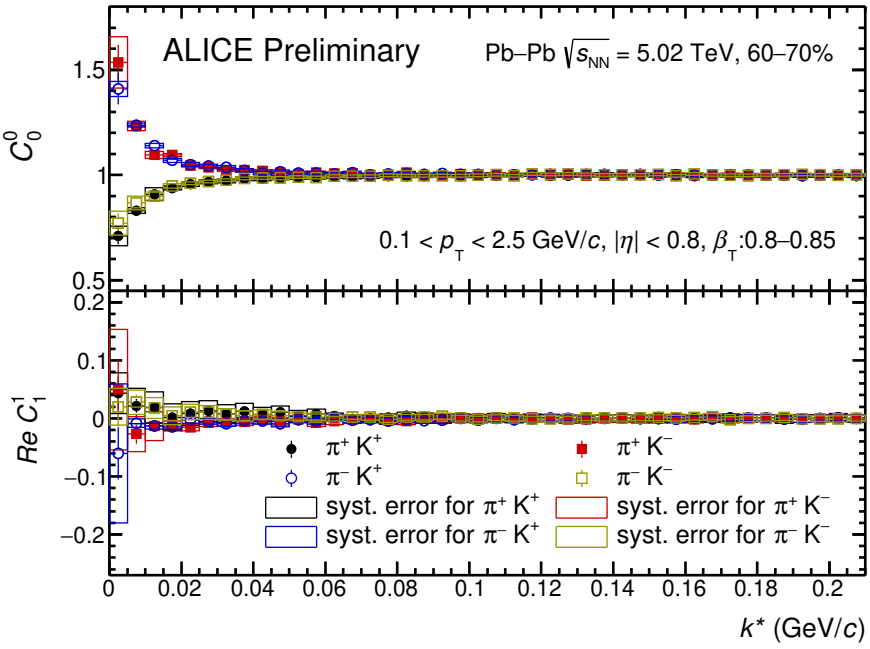

Figure 4.95: The background-minimised correlation functions for pion-kaon pairs in $0.8<\beta_T<0.85$ for 60-70% central Pb–Pb collisions at $\sqrt{s_{NN}}$ = 5.02 TeV in ALICE.

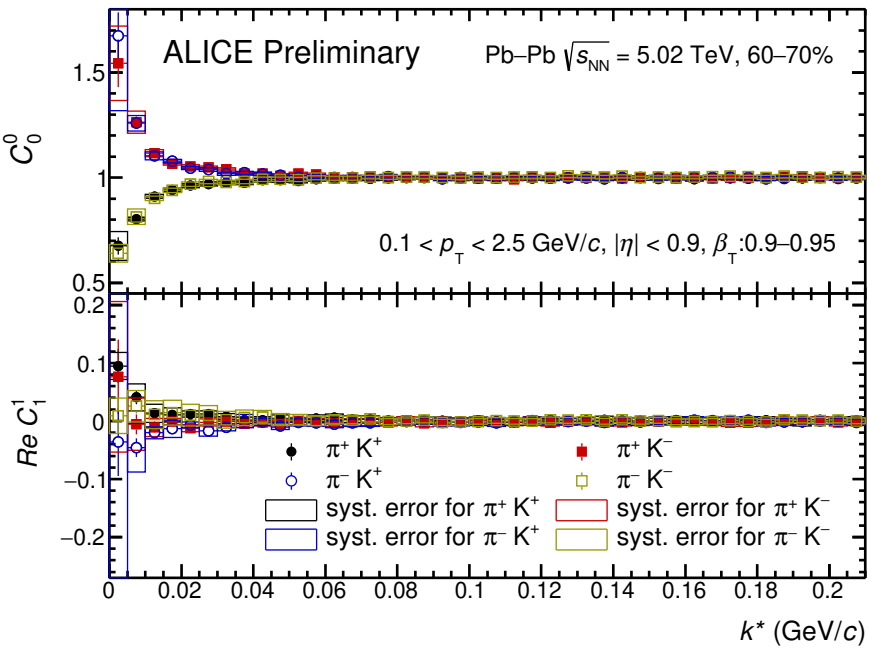

Figure 4.96: The background-minimised correlation functions for pion-kaon pairs in $0.9<\beta_T<0.95$ for 60-70% central Pb–Pb collisions at $\sqrt{s_{NN}}$ = 5.02 TeV in ALICE.

4.12 Fitting of correlation function

The procedure to fit the background-minimised correlation functions and extract the femtoscopic parameters is discussed in section 2.6. A software package, called CorrFit[92], is used to fit the correlation functions. This package is mainly developed to extract the source parameters from the pion-kaon correlation functions in the STAR experiment for Au–Au events at $\sqrt{s_{NN}}$ = 200 GeV and recently used in the ALICE experiment for Pb–Pb events at $\sqrt{s_{NN}}$ = 2.76 TeV. It can be used to fit the one-dimensional and three-dimensional correlation function in the Cartesian and Spherical harmonics representations. The package consists of different source models and pair interactions which can be chosen appropriately depending on the correlation analysis.

The theoretical correlation functions, generated by the CorrFit package are needed to be scaled with two important factors, Pair purity and Momentum-resolution factor, which take care of the detector effects and some model-dependent factors. These two factors are discussed below in detail.

4.12.1 Pair purity

The femtoscopic parameters are highly sensitive to the purity of particle pairs which depends on various experimental and model-dependent factors. Two important experimental factors are the PID purity of detector and the fraction of primary particles. The former takes care of the misidentified particles while the later considers the contribution from primary particles only, minimising the effect of secondary-decay products(discussed in section 4.5). The first step towards estimating these factors is to calculate the average p_{T} of the pion and kaon sample that contribute to the lower k^* region.

The upper panels of Fig. 4.97 and Fig. 4.98, shows the p_{T} distribution of π^+ and K^+, respectively as a function of k^*. The projection of p_{T} in the lower k^* range (0−0.05 GeV/c) are shown in the bottom panels of Fig. 4.97 and Fig. 4.98 for π^+ and K^+, respectively. The mean of these p_{T} distributions are estimated. The PID purity and secondary-contamination factors of pions and kaons corresponding to the extracted mean are estimated from the distributions shown in section 4.5. For the analysis of k_{T}-dependent correlation functions, the correction factors are estimated for the average p_{T} of pions and kaons obtained within the specified k_{T} ranges.

Additionally, there can be contributions from long-lived strongly-decaying resonance particles which also affect the correlation functions. If one particle of the pair is produced from the decay of a long-lived resonance particle, then the source function deviates from a perfect Gaussian and is associated with a long tail. This effect is observed in the analyses of identical-particle correlations at STAR and PHENIX experiments at RHIC [93, 94] and therefore, has to be accounted before fitting the correlation functions.

To quantify the contribution from resonance particles, the pair distributions for charged pions and kaons in Pb–Pb collisions at $\sqrt{s_{\mathrm{NN}}} = 5.02$ TeV are simulated in (3+1)D hydrodynamics coupled to THERMINATOR 2 event generator. THERMINATOR 2 [95] is a Monte Carlo event simulator that is developed to analyse the statistical hadronisation in relativistic heavy-ion collisions. The model uses different freeze-out hypersurfaces and velocity profiles, generated externally by using different hydrodynamic codes. It is widely used to study the femtoscopic

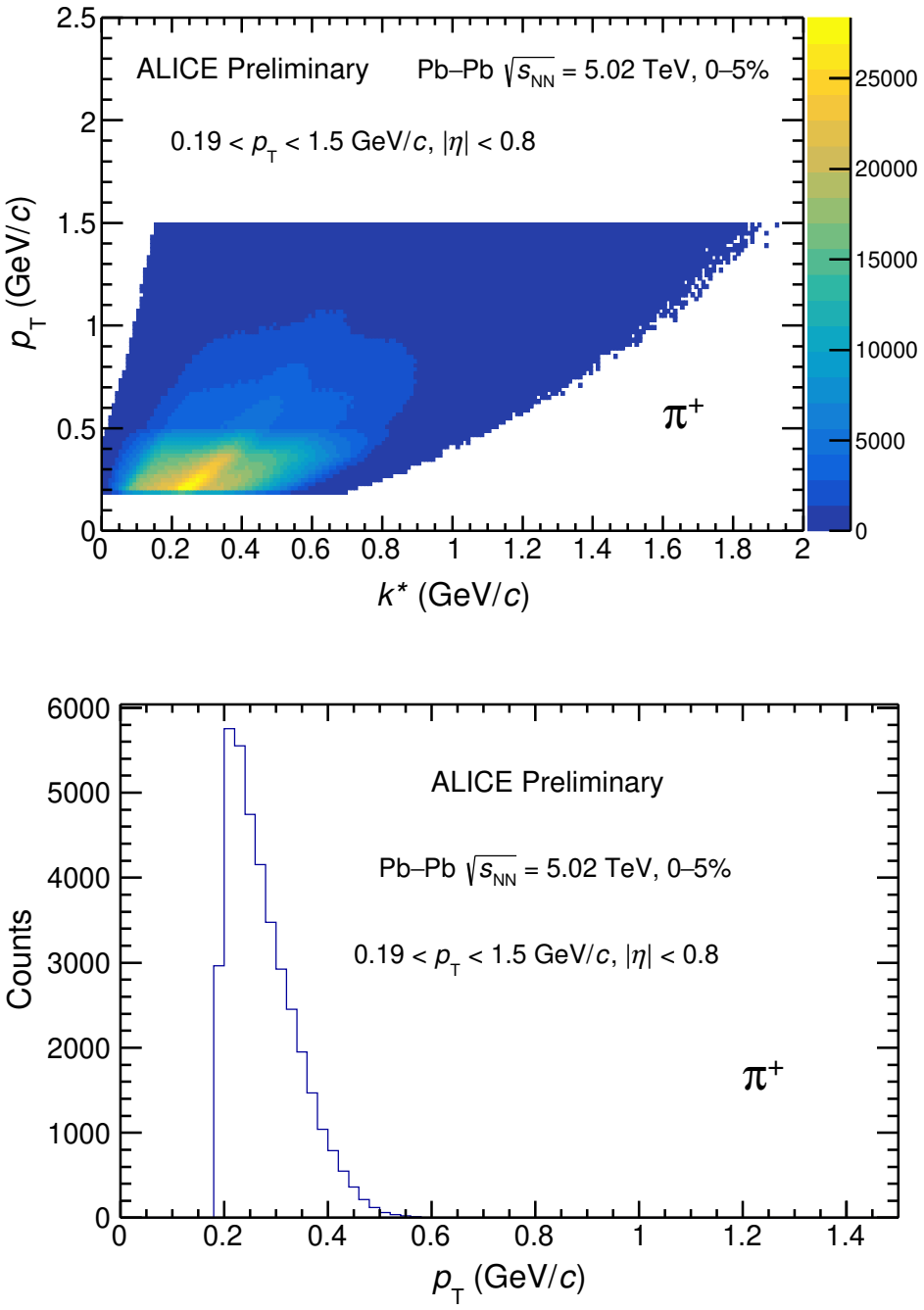

Figure 4.97: The p_T distribution of pions as a function of k^* (upper panel) and projection of p_T in the k^* range: 0–0.05 GeV/c (bottom panel) for π^+ for 0–5% central Pb–Pb collisions at $\sqrt{s_{NN}}$ = 5.02 TeV in ALICE.

correlations between the particles. It can also be used to investigate the p_T-spectra of particles, elliptic-flow coefficient, and compute the number of elastic scattering after the freeze-out.

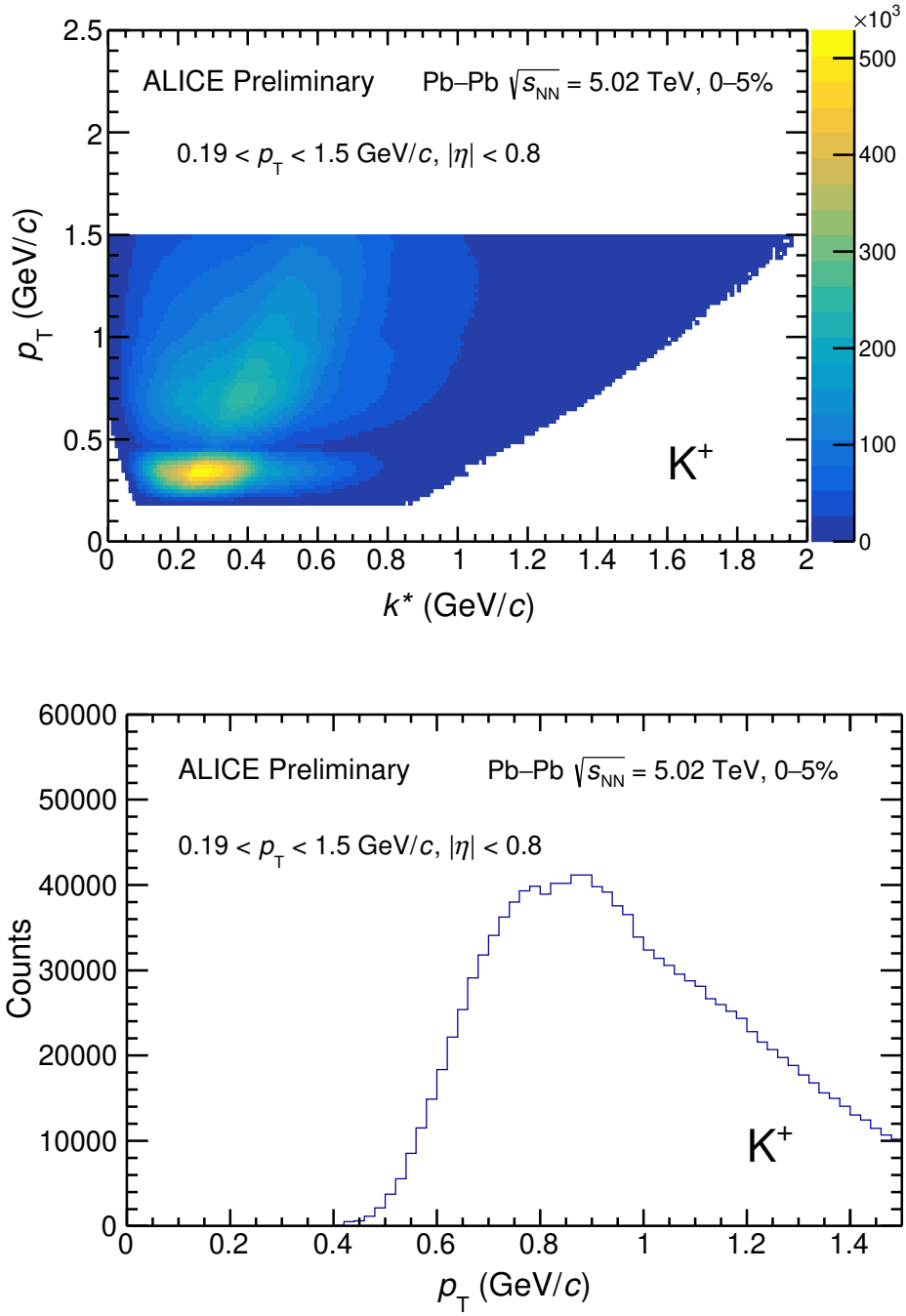

Figure 4.98: The p_{T} distribution of kaons as a function of k^* (upper panel) and projection of p_{T} in the k^* range: 0−0.05 GeV/c (bottom panel) for K^+ for 0−5% central Pb–Pb collisions at $\sqrt{s_{\mathrm{NN}}}$ = 5.02 TeV in ALICE.

The r_{inv} distribution of pion-kaon pairs selected within the k_{T} range of 500 < k_{T} (MeV/c) < 600 for 0−5% central Pb–Pb collisions, simulated in THERMINATOR 2 is shown in Fig. 4.99, where a prominent non-Gaussian tail is observed. To separate the non-Gaussian region, the

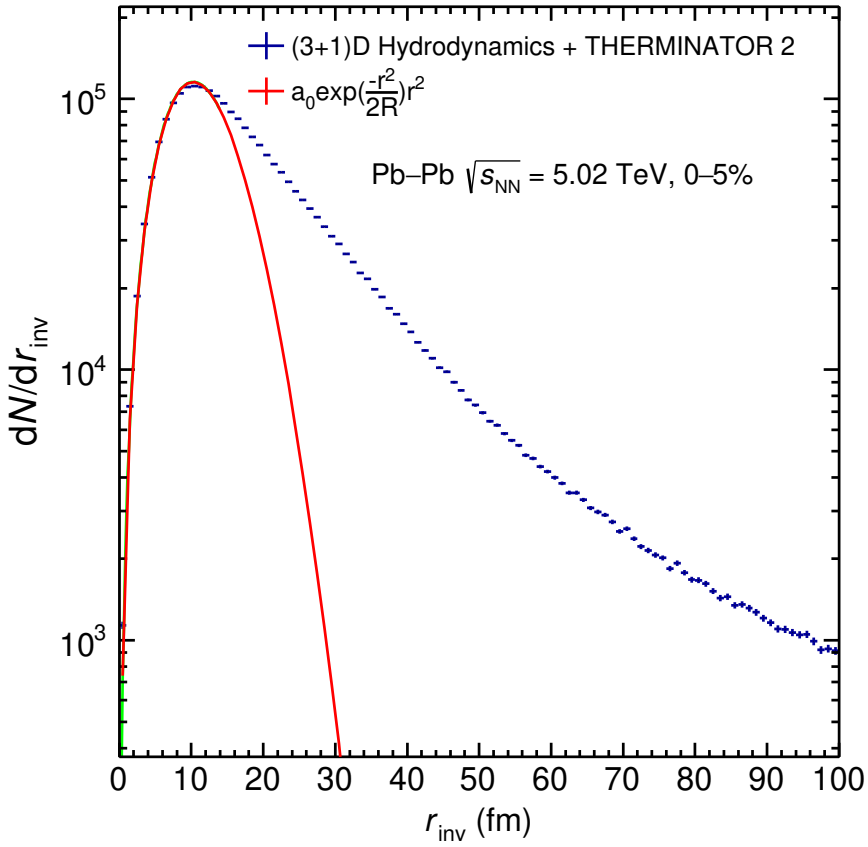

Figure 4.99: The r_{inv} distribution (blue points) of pion-kaon pairs within $500 < k_{\mathrm{T}}$ (MeV/c) < 600 with the fit function (red curve) for 0–5% central Pb–Pb collisions at $\sqrt{s_{\mathrm{NN}}} = 5.02$ generated in (3+1)D hydrodynamics coupled to THERMINATOR 2 model.

distribution is fitted with a function as given by Eq. (4.17) [60].

$$y = a_0 r^2 e^{(-\frac{r^2}{2R})} \tag{4.17}$$

where, r corresponds to the separation of particles in a pair, R is the size of one-dimensional source function and a_0 is the normalisation constant. The pairs which are inside the fitted-function profile are considered to be "femtoscopically correlated"[60]. The fraction of correlated particles ($g(C)$) is estimated by taking the ratio of femtoscopically correlated pairs to all pairs. The values of $g(C)$ for k_{T}-integrated pion-kaon pairs in different centrality classes are taken from [60], whereas for k_{T}-dependent analysis, the $g(C)$ is estimated and the values are

given in Table 4.4. The $g(C)$ is also estimated in different β_T bins for 0−5% to 70−80% central classes, which are listed in Table 4.5. The values of $g(C)$ are found to be decreasing as the multiplicity decreases in all the k_T bins and most of the β_T bins, although they do not vary much in the regions 0.85 <β_T< 0.9 and 0.9<β_T<0.95.

Centrality (%)	Fraction of femtoscopically correlated pairs ($g(C)$) for k_T ranges (MeV/c)		
	400−500	500-600	600-700
0−5	0.85	0.80	0.76
5−10	0.81	0.75	0.72
10−20	0.76	0.71	0.68
20−30	0.73	0.70	0.67
30−40	0.72	0.70	0.66
40−50	0.72	0.70	0.66

Table 4.4: The fraction of femtoscopically correlated pion-kaon pairs ($g(C)$) in different k_T bins and centrality classes of Pb–Pb collisions at $\sqrt{s_{NN}}$ = 5.02 TeV.

The overall purity of pion-kaon pair (F) is calculated using the Eq. (4.18).

$$F_{\pi^{\pm}K^{\pm}} = p_{\pi}^{\pm}(C) * p_{K}^{\pm}(C) * f_{\pi^{\pm}}(C) * f_{K^{\pm}}(C) * g(C) \tag{4.18}$$

where, $p_{\pi}^{\pm}(C)$ and $p_{K}^{\pm}(C)$ are the PID purity of pions and kaons, respectively, $f_{\pi^{\pm}}(C)$ and $f_{K^{\pm}}(C)$ are the fractions of primary pions and kaons, respectively, $g(C)$ is the fraction of correlated particles, and C is the centrality. The variation of F as a function of centrality class for the pairs selected in integrated-k_T ranges is shown in Fig. 4.100. It is observed that the F decreases from most central to peripheral collisions. Fig. 4.101 shows the variation of $F(C)$ as a function of k_T for different centrality classes and it is observed that the F decreases from low k_T to high k_T region. However, in case of the β_T-dependent correlation functions, the F is scaled with (1-f_e) to take care of the contamination from electrons in the pion sample. The values of f_e are listed in Table 4.3. The F as a function of β_T for 0−5% to 70−80% central Pb–Pb collisions

Centrality (%)	Fraction of femtoscopically correlated pairs ($g(C)$) for β_T ranges:				
	0.7–0.75	0.75–0.8	0.8–0.85	0.85–0.9	0.9–0.95
0–5	0.71	0.68	0.65	0.59	0.51
10–20	0.70	0.67	0.64	0.59	0.51
20–30	0.68	0.65	0.63	0.59	0.51
30–40	0.67	0.64	0.61	0.57	0.51
40–50	0.65	0.63	0.60	0.56	0.51
50–60	0.64	0.63	0.60	0.56	0.51
60–70	0.63	0.61	0.58	0.56	0.51
70–80	0.63	0.61	0.58	0.56	0.51

Table 4.5: The fraction of femtoscopically correlated pion-kaon pairs ($g(C)$) in different β_T bins and centrality classes of Pb–Pb collisions at $\sqrt{s_{NN}}$ = 5.02 TeV.

at $\sqrt{s_{NN}}$ = 5.02 TeV is shown in Fig. 4.102, where it is observed that the F decreases with increasing β_T.

The measured correlation function can be corrected by F using the following expression [60]:

$$C_{\text{corrected}} = \frac{C_{\text{measured}} - 1}{F} + 1. \tag{4.19}$$

This correction is not applied to the measured correlation function directly. Instead, the theoretical correlation functions generated randomly in CorrFit are scaled with the purity factor.

4.12.2 Momentum-resolution factor

The momentum resolution of the detectors can also affect the correlation functions. As the reconstructed momenta of the particles vary from the true momenta, the estimated k^* and hence, the correlation functions are modified. To estimate this effect, Monte Carlo events generated by HIJING event generator (discussed in section 4.2) are analysed. The generated particles with the true momentum p_{gen} is passed through the reconstruction algorithm to give the reconstructed

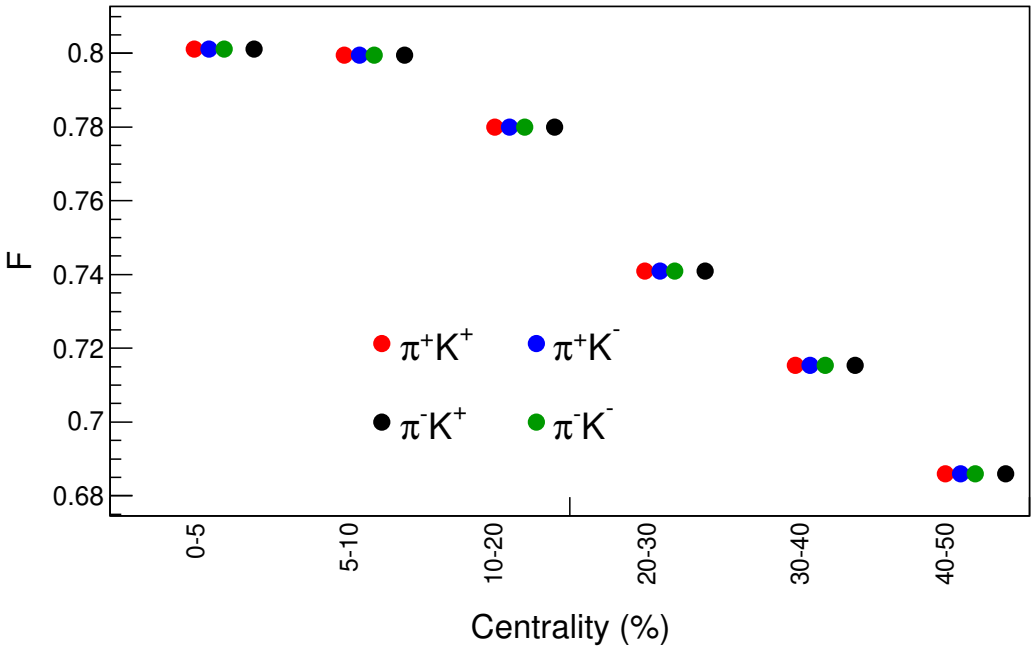

Figure 4.100: The overall purity of pion-kaon pairs selected in the integrated-k_{T} range, as a function of centrality class in Pb–Pb collisions at $\sqrt{s_{\mathrm{NN}}}$ = 5.02 TeV.

momentum, p_{reco}. The p_{gen} and p_{reco} are decomposed into $|p_{\mathrm{gen}}|$, $\theta_{p_{\mathrm{gen}}}$, $\phi_{p_{\mathrm{gen}}}$ and $|p_{\mathrm{reco}}|$, $\theta_{p_{\mathrm{reco}}}$, $\phi_{p_{\mathrm{reco}}}$, respectively. The standard deviation of each component of the $(p_{\mathrm{gen}} - p_{\mathrm{reco}})$, namely σ_p, σ_θ and σ_ϕ are obtained for each p_{reco} bin by fitting them with a linear combination of Gaussian and Laplace function and estimating the value of standard deviation of the fits. The obtained standard deviations are then fitted with the following functions and are shown in Fig. 4.103.

$$f_p(p_{\mathrm{reco}}) = a_p + b_p p_{\mathrm{reco}} + c_p (p_{\mathrm{reco}})^{d_p}, \tag{4.20}$$

$$f_\theta(p_{\mathrm{reco}}) = a_\theta + b_\theta p_{\mathrm{reco}} + c_\theta (p_{\mathrm{reco}})^{d_\theta}, \tag{4.21}$$

$$f_\phi(p_{\mathrm{reco}}) = a_\phi + b_\phi p_{\mathrm{reco}} + c_\phi (p_{\mathrm{reco}})^{d_\phi} \tag{4.22}$$

4.12.3 Input parameters for fitting

In the present analysis, the following model parameters are used to fit the correlation functions (C_0^0 and ReC_1^1).

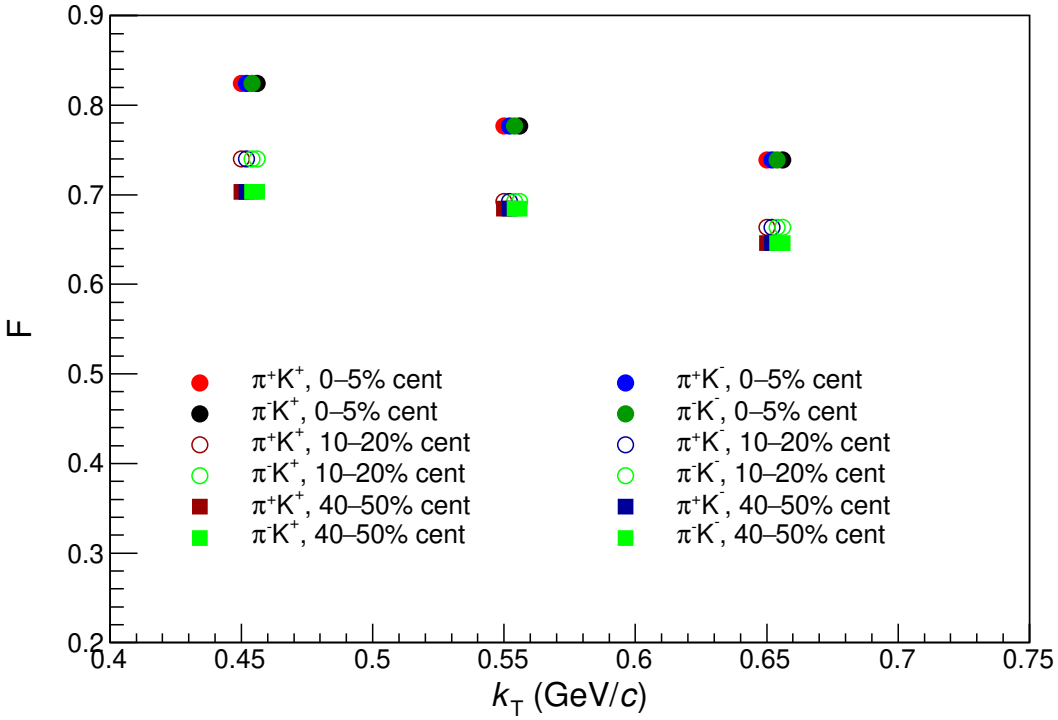

Figure 4.101: The overall purity of pion-kaon pairs as a function of k_T in different centrality classes of Pb–Pb collisions at $\sqrt{s_{NN}}$ = 5.02 TeV. The points for different pairs in each k_T bin are shifted deliberately.

- It is assumed that the source function is a three-dimensional Gaussian function as given in Eq. (2.15).
- A condition of $R_{side} = R_{out}$ and $R_{long} = 1.3R_{out}$, based on the results obtained for three-dimensional identical-particle femtoscopy for pions in ALICE [96], is applied to reduce the amount of computation, as one is left with the task of extracting two independent parameters, R_{out} and μ_{out} from the fit.
- The momentum distributions of pions and kaons from the real data are used as the input distributions.
- The FSI (Coulomb and strong) between the particles in a pair is computed using the approach based on the R. Lednicky [64, 97] model.
- The correlation functions are fitted within the range of 0.0 $<k^*$ (MeV/c) $<$100.0.

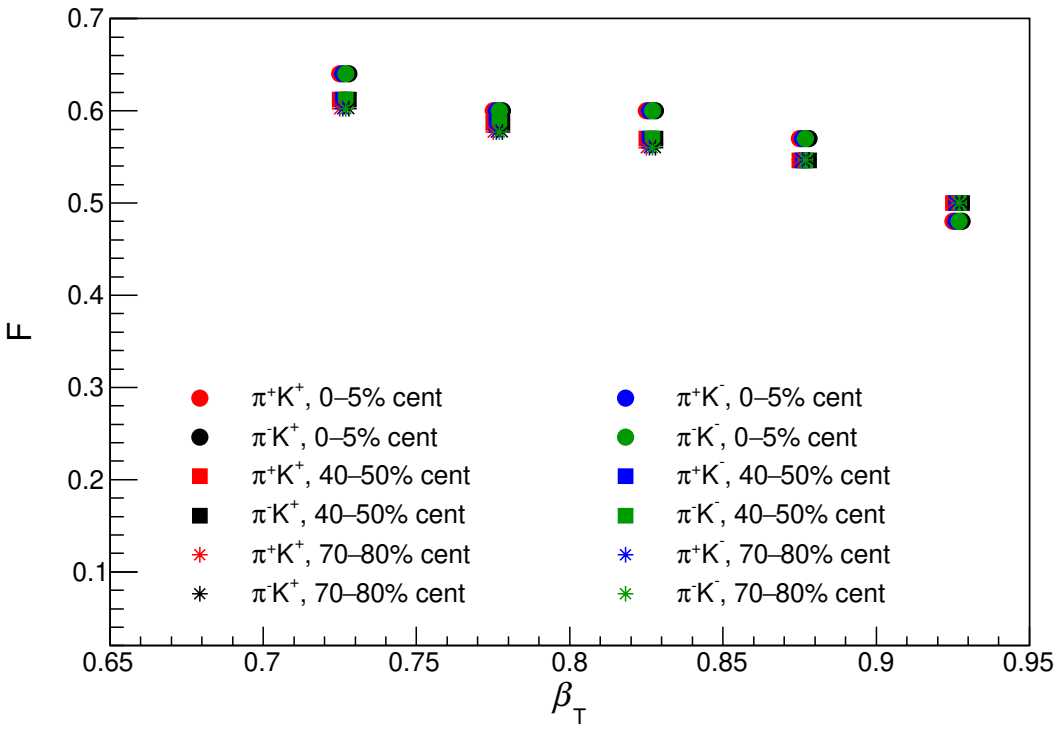

Figure 4.102: The overall purity of pion-kaon pairs as a function of β_T in different centrality classes of Pb–Pb collisions at $\sqrt{s_{NN}}$ = 5.02 TeV. The points for different pairs in each β_T bin are shifted deliberately.

- The correlation functions are normalised within the range of 150.0 $<k^*$ (MeV/c) <200.0.
- The pair purity, discussed in section 4.12.1, is estimated and used as an input parameter.
- The momentum-resolution correction, discussed in section 4.12.2 is used as an input parameter.

4.12.4 Correlation functions with fit results

The k_T-integrated correlation functions for all four different charged pairs of pions and kaons and their fit results from 0−5% to 40−50% central Pb–Pb collisions at $\sqrt{s_{NN}}$ = 5.02 TeV are shown in Fig. 4.104-4.109. Moreover, the fitted correlation functions for three different k_T bins are shown in Fig. 4.110-4.127. It is observed that there is a good agreement between the experimental correlation functions and the fits obtained from the CorrFit package.

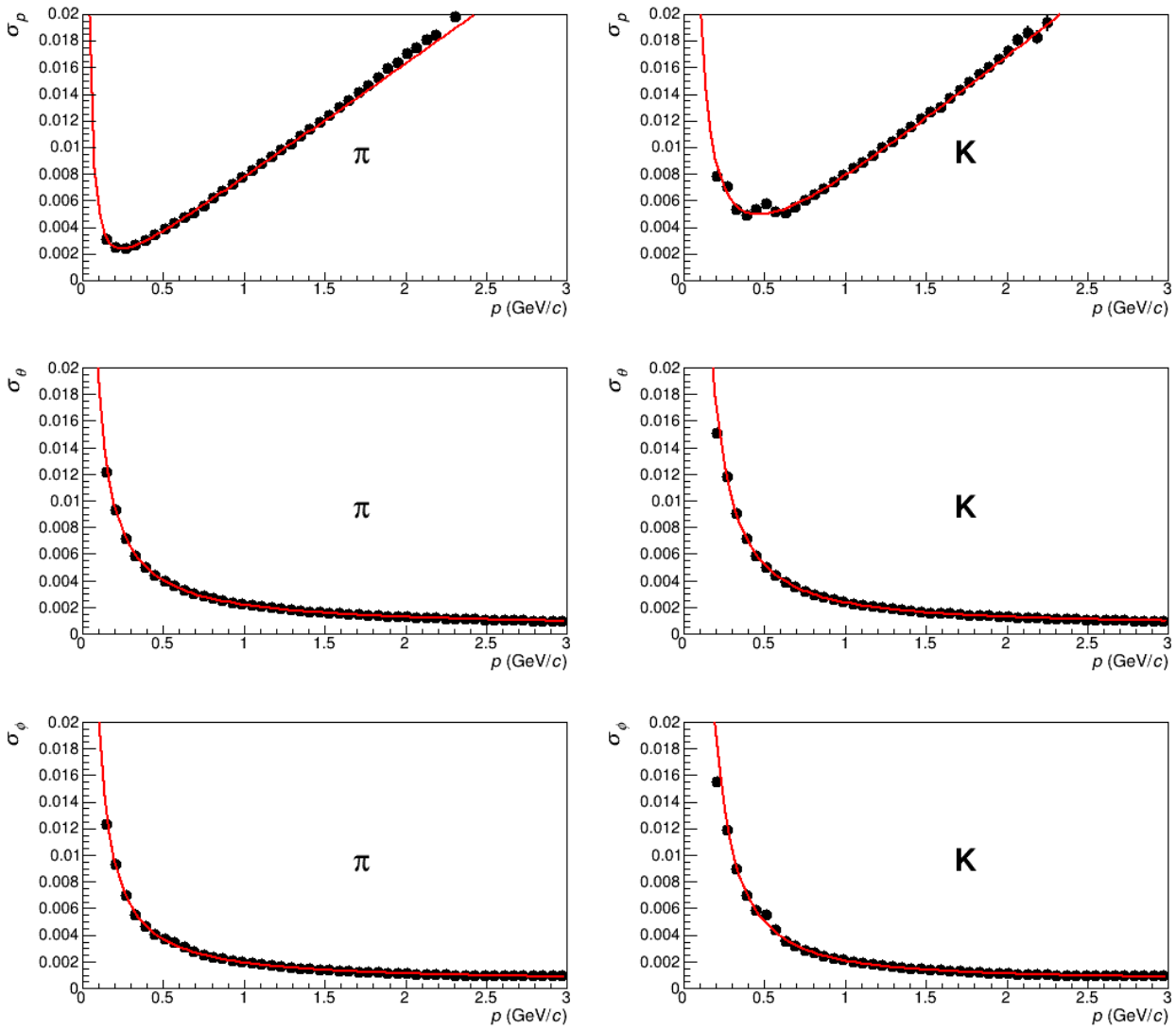

Figure 4.103: The values of σ_p (upper panels), σ_θ (middle panels) and σ_ϕ (bottom panels) estimated from the differences between true and reconstructed momentum, together with the fit results for pions (left column) and kaons (right column)

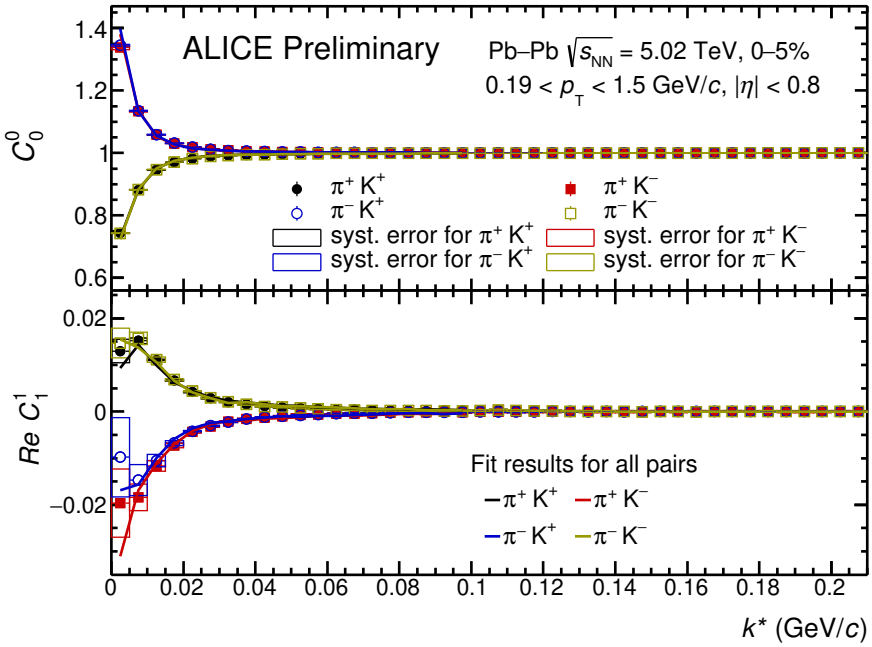

Figure 4.104: The pion-kaon correlation functions with the fit results from *CorrFit* for 0–5% central Pb–Pb collisions at $\sqrt{s_{NN}}$ = 5.02 TeV in ALICE.

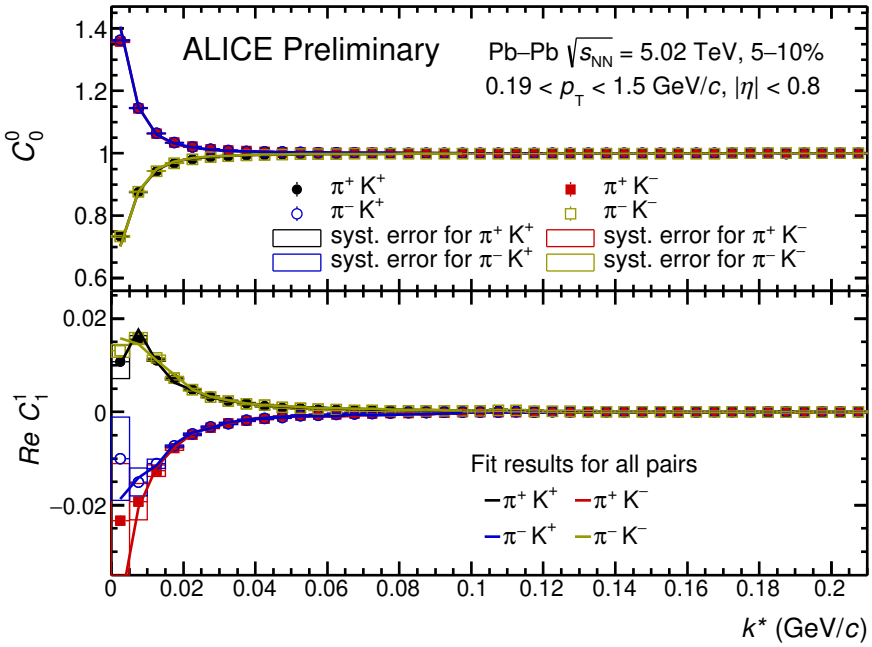

Figure 4.105: The pion-kaon correlation functions with the fit results from *CorrFit* for 5–10% central Pb–Pb collisions at $\sqrt{s_{NN}}$ = 5.02 TeV in ALICE.

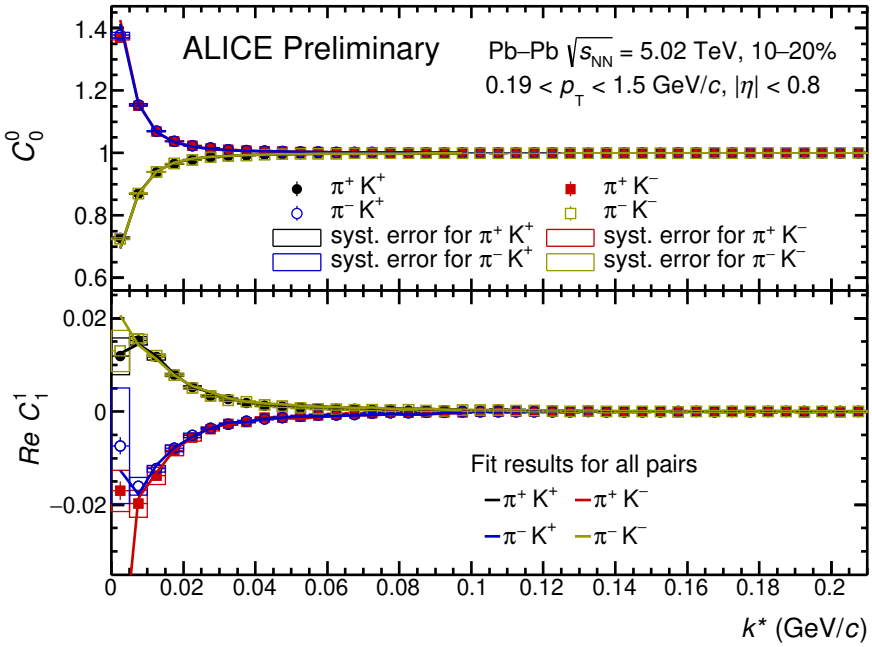

Figure 4.106: The pion-kaon correlation functions with the fit results from *CorrFit* for 10−20% central Pb–Pb collisions at $\sqrt{s_{NN}}$ = 5.02 TeV in ALICE.

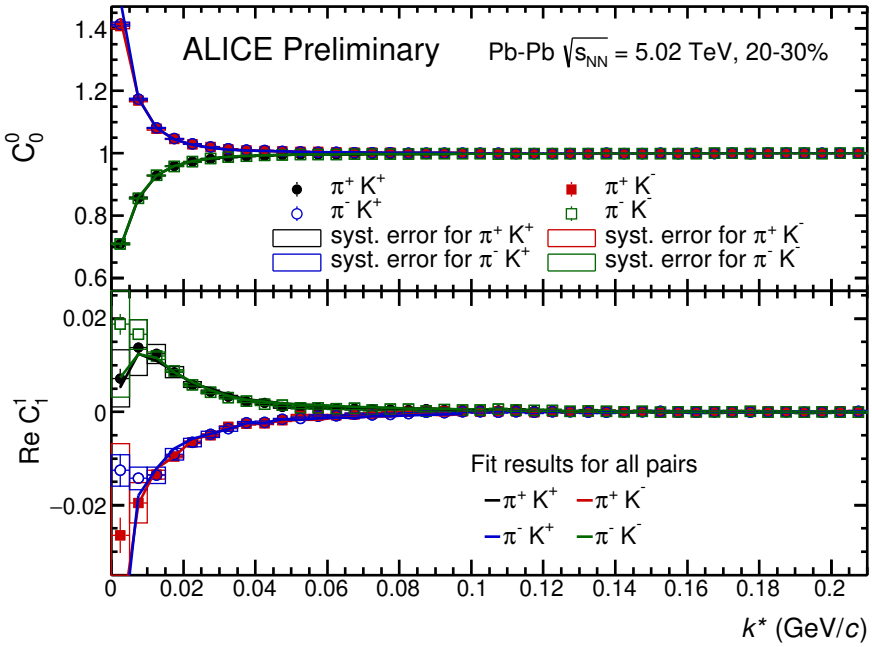

Figure 4.107: The pion-kaon correlation functions with the fit results from *CorrFit* for 20−30% central Pb–Pb collisions at $\sqrt{s_{NN}}$ = 5.02 TeV in ALICE. [91]

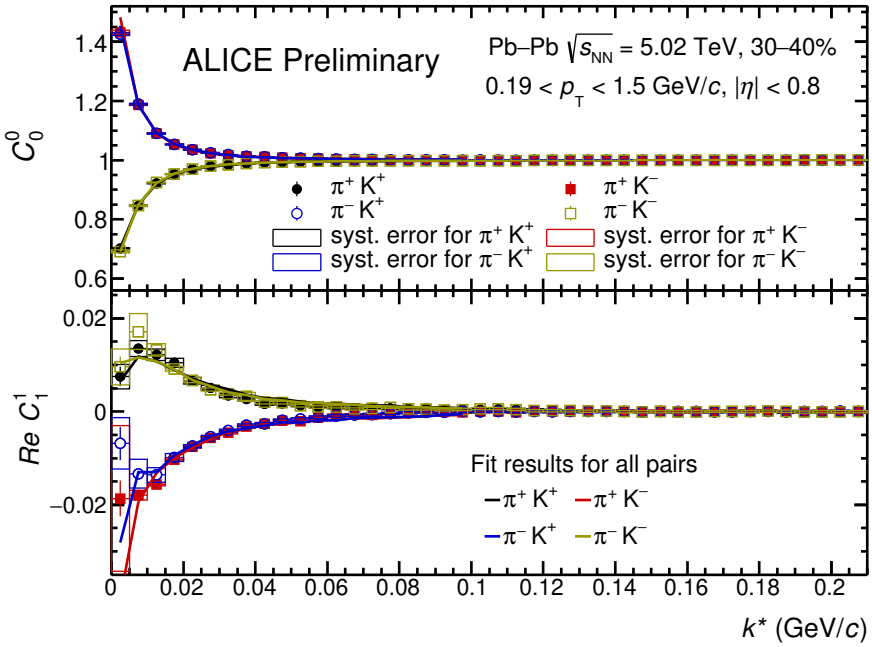

Figure 4.108: The pion-kaon correlation functions with the fit results from *CorrFit* for 30–40% central Pb–Pb collisions at $\sqrt{s_{NN}}$ = 5.02 TeV in ALICE.

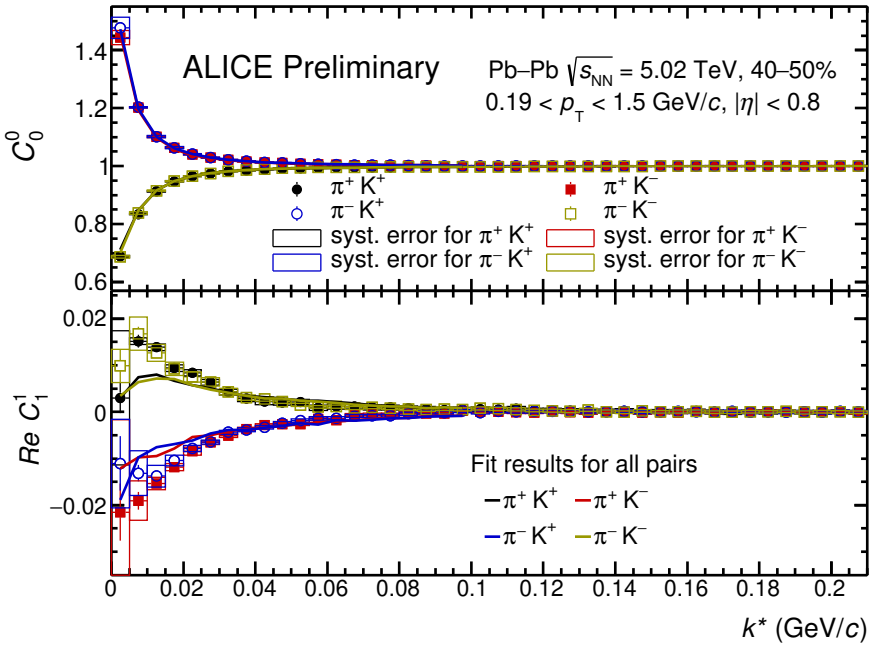

Figure 4.109: The pion-kaon correlation functions with the fit results from *CorrFit* for 40–50% central Pb–Pb collisions at $\sqrt{s_{NN}}$ = 5.02 TeV in ALICE.

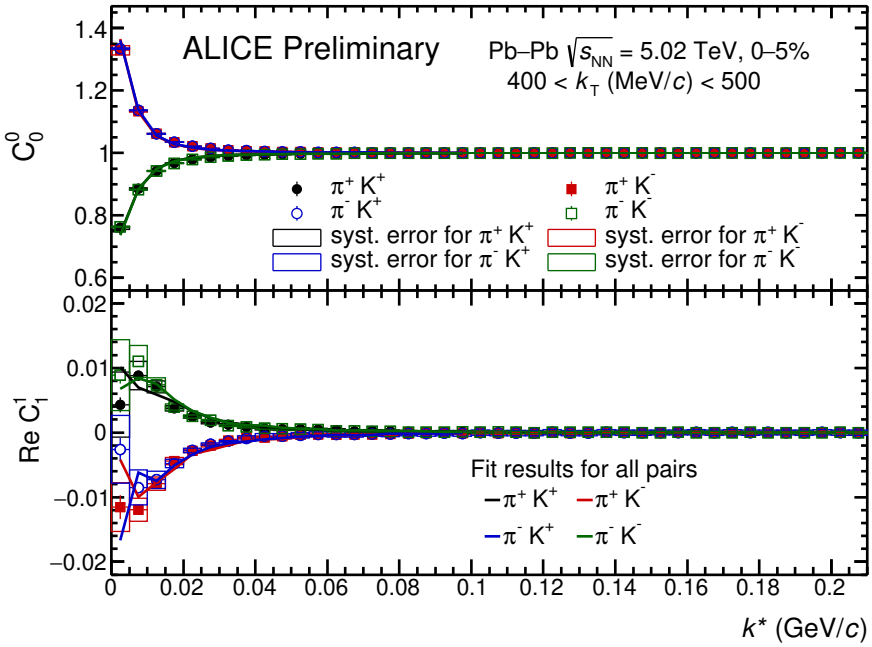

Figure 4.110: The pion-kaon correlation functions with the fit results from *CorrFit* within 400 $<k_T$ (MeV/c)$<$ 500 for 0−5% central Pb–Pb collisions at $\sqrt{s_{NN}}$ = 5.02 TeV in ALICE.

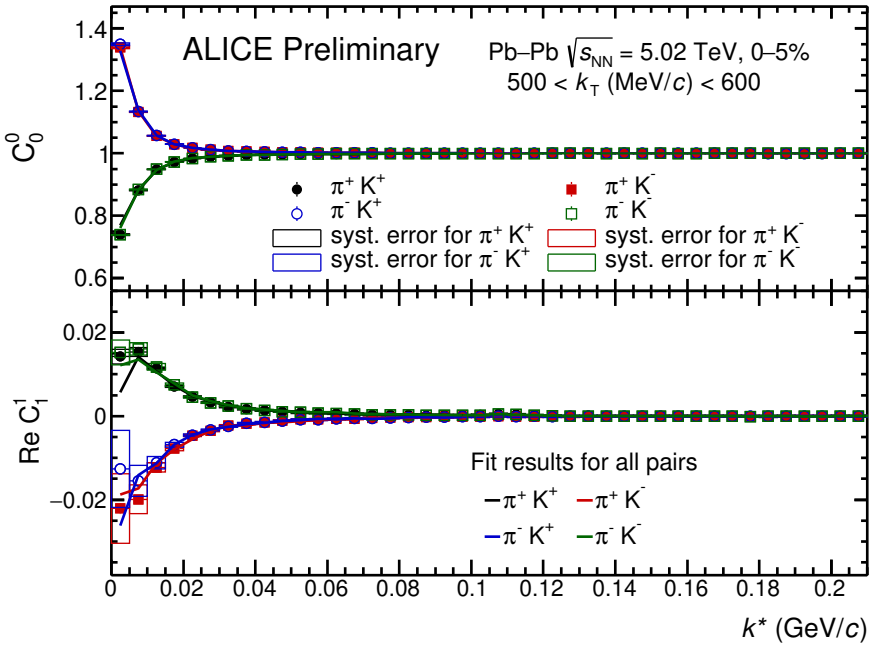

Figure 4.111: The pion-kaon correlation functions with the fit results from *CorrFit* within 500 $<k_T$ (MeV/c)$<$ 600 for 0−5% central Pb–Pb collisions at $\sqrt{s_{NN}}$ = 5.02 TeV in ALICE.

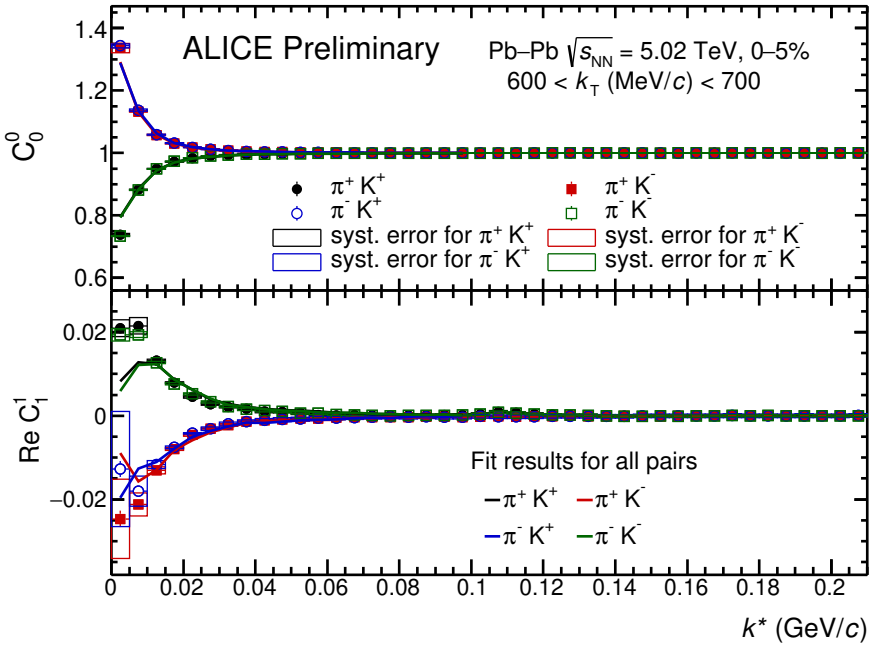

Figure 4.112: The pion-kaon correlation functions with the fit results from *CorrFit* within 600 $<k_T$ (MeV/c)$<$ 700 for 0−5% central Pb–Pb collisions at $\sqrt{s_{NN}}$ = 5.02 TeV in ALICE.

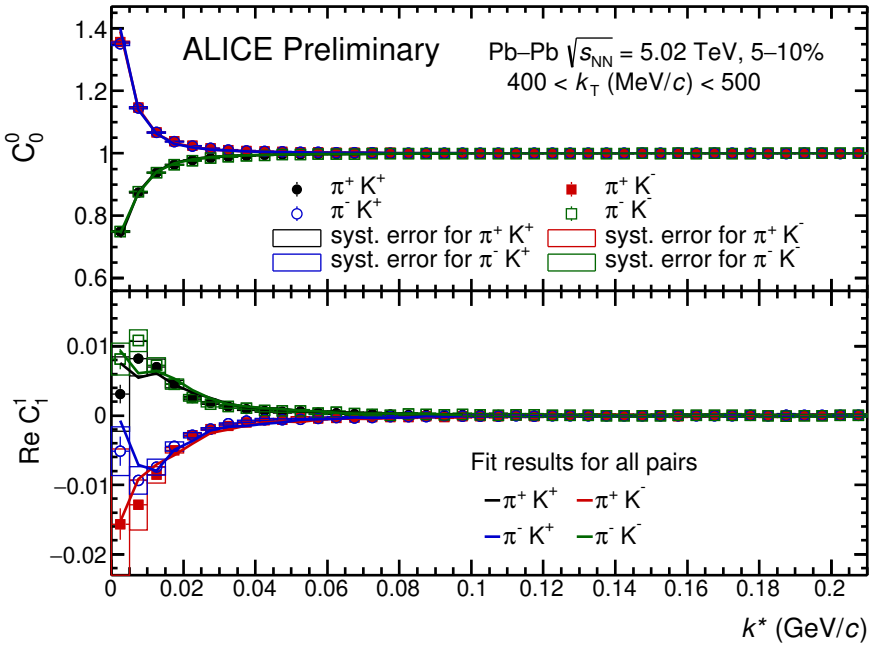

Figure 4.113: The pion-kaon correlation functions with the fit results from *CorrFit* within 400 $<k_T$ (MeV/c)$<$ 500 for 5−10% central Pb–Pb collisions at $\sqrt{s_{NN}}$ = 5.02 TeV in ALICE.

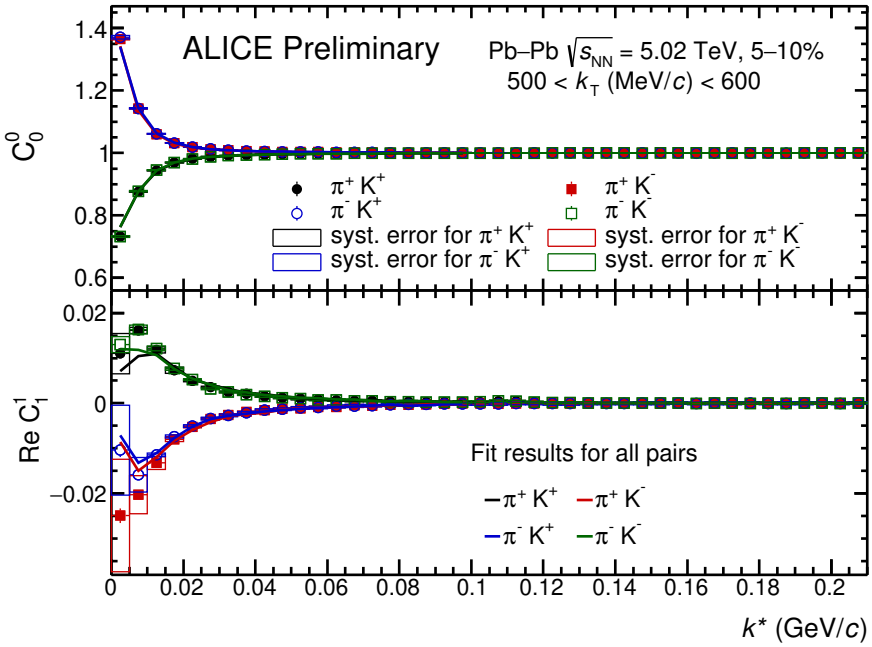

Figure 4.114: The pion-kaon correlation functions with the fit results from *CorrFit* within 500 $<k_T$ (MeV/c)$<$ 600 for 5−10% central Pb–Pb collisions at $\sqrt{s_{NN}}$ = 5.02 TeV in ALICE.

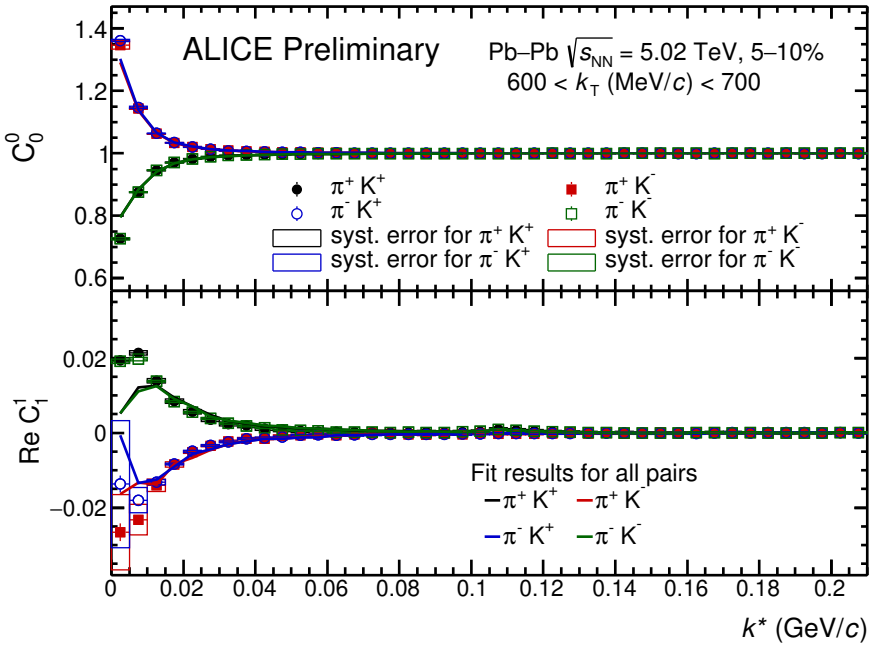

Figure 4.115: The pion-kaon correlation functions with the fit results from *CorrFit* within 600 $<k_T$ (MeV/c)$<$ 700 for 5−10% central Pb–Pb collisions at $\sqrt{s_{NN}}$ = 5.02 TeV in ALICE.

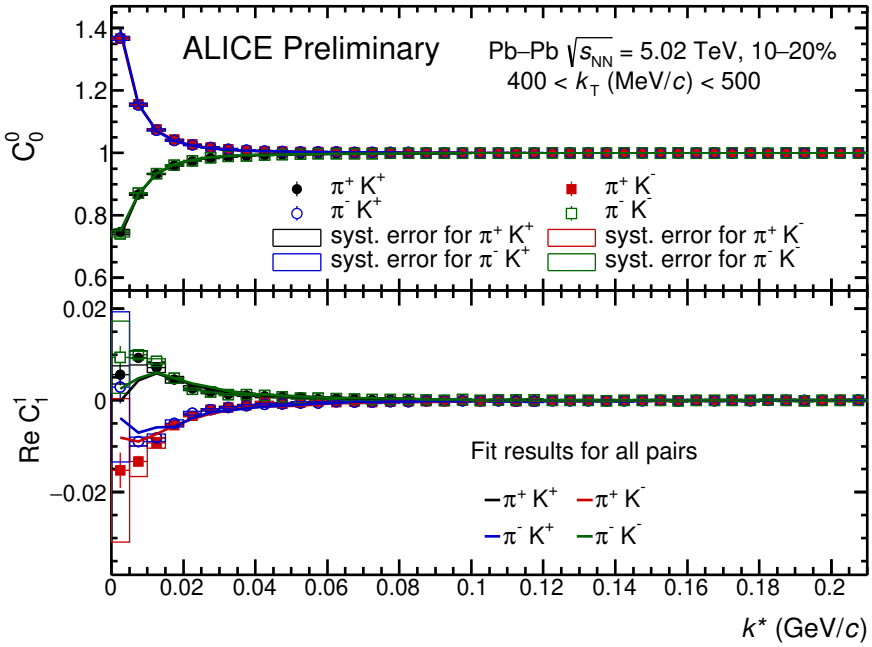

Figure 4.116: The pion-kaon correlation functions with the fit results from *CorrFit* within 400 $<k_T$ (MeV/c)$<$ 500 for 10−20% central Pb–Pb collisions at $\sqrt{s_{NN}}$ = 5.02 TeV in ALICE.

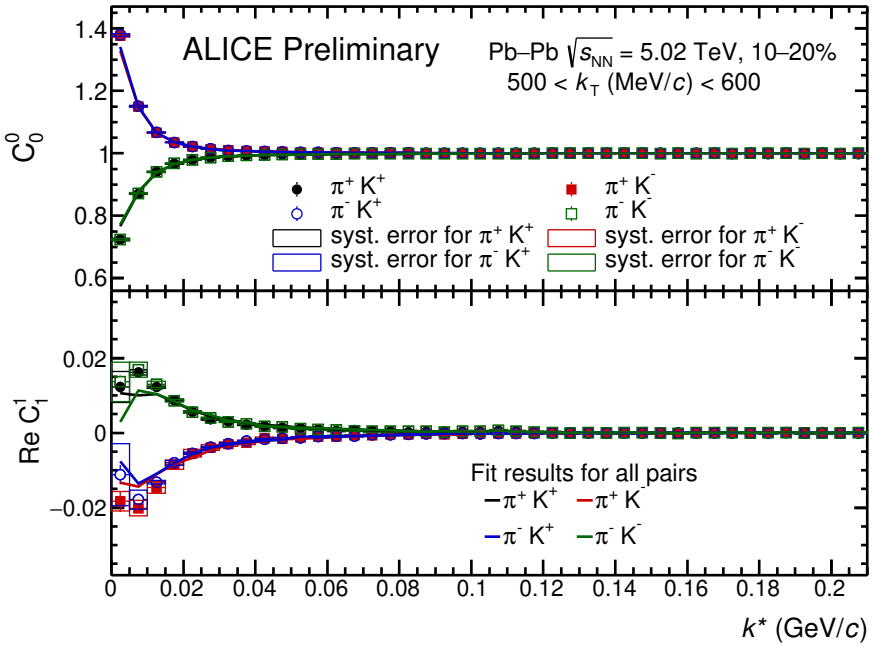

Figure 4.117: The pion-kaon correlation functions with the fit results from *CorrFit* within 500 $<k_T$ (MeV/c)$<$ 600 for 10−20% central Pb–Pb collisions at $\sqrt{s_{NN}}$ = 5.02 TeV in ALICE.

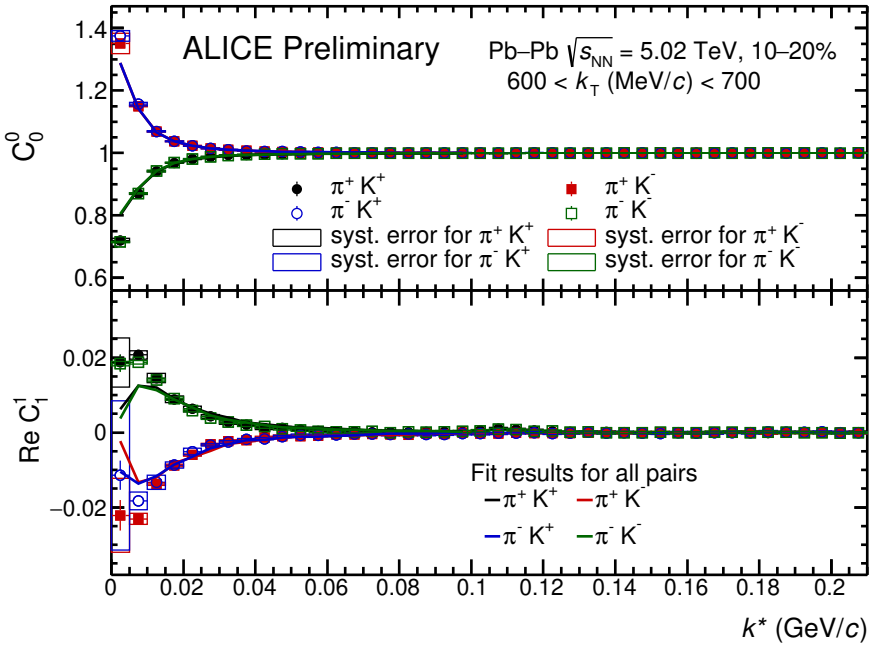

Figure 4.118: The pion-kaon correlation functions with the fit results from *CorrFit* within 600 $<k_T$ (MeV/c)$<$ 700 for 10−20% central Pb–Pb collisions at $\sqrt{s_{NN}}$ = 5.02 TeV in ALICE.

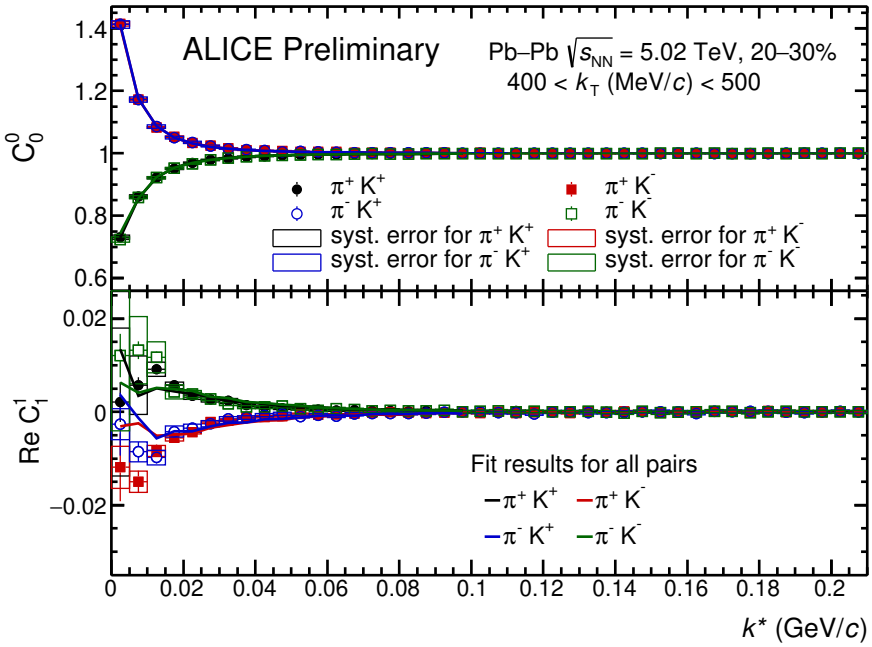

Figure 4.119: The pion-kaon correlation functions with the fit results from *CorrFit* within 400 $<k_T$ (MeV/c)$<$ 500 for 20−30% central Pb–Pb collisions at $\sqrt{s_{NN}}$ = 5.02 TeV in ALICE.

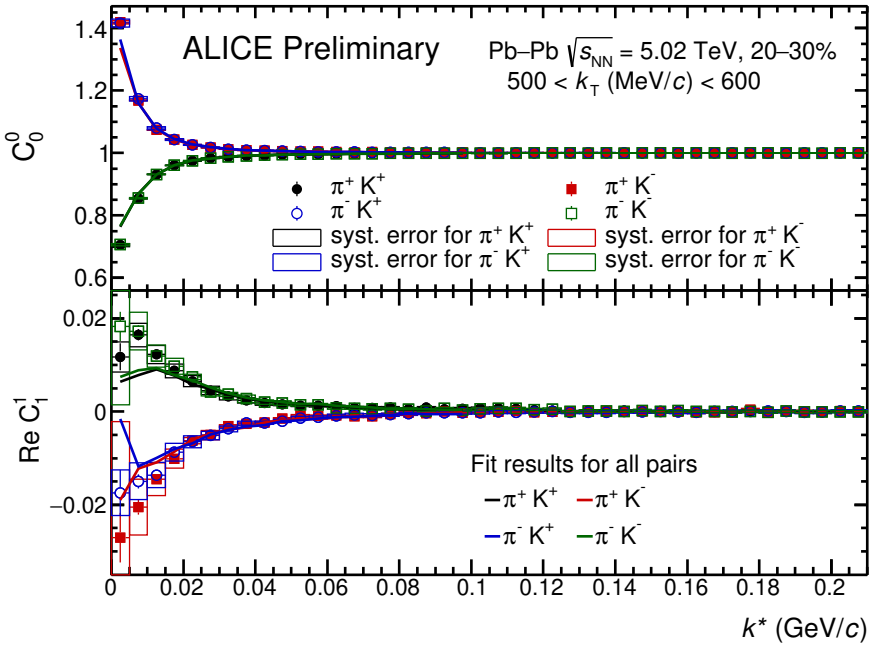

Figure 4.120: The pion-kaon correlation functions with the fit results from *CorrFit* within 500 $<k_T$ (MeV/c)$<$ 600 for 20−30% central Pb–Pb collisions at $\sqrt{s_{NN}}$ = 5.02 TeV in ALICE.

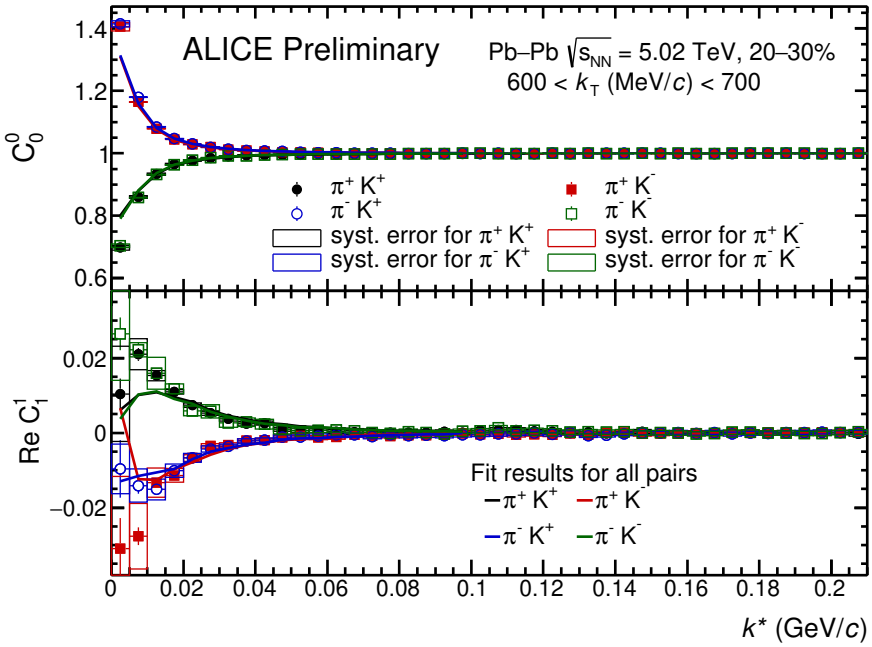

Figure 4.121: The pion-kaon correlation functions with the fit results from *CorrFit* within 600 $<k_T$ (MeV/c)$<$ 700 for 20−30% central Pb–Pb collisions at $\sqrt{s_{NN}}$ = 5.02 TeV in ALICE.

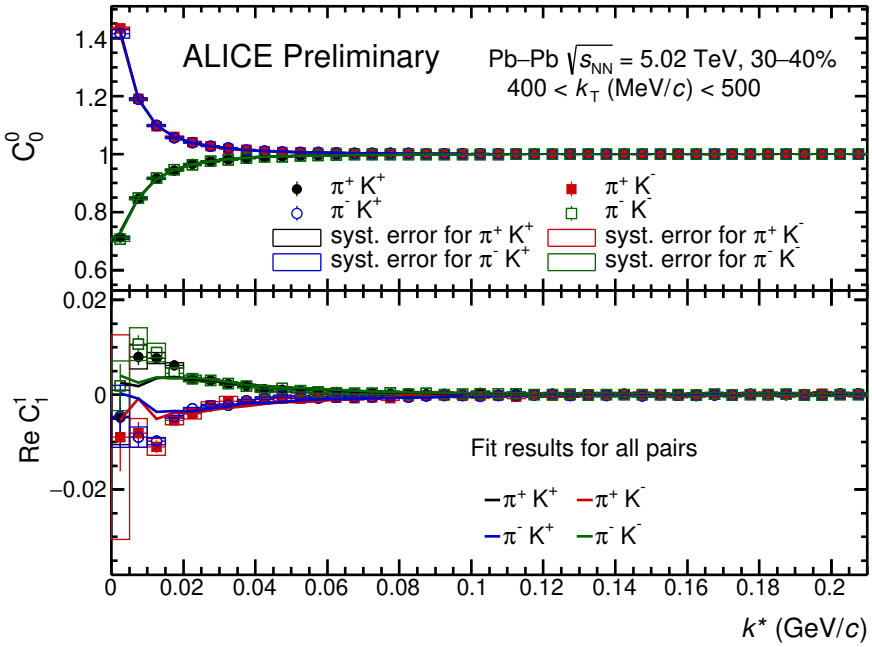

Figure 4.122: The pion-kaon correlation functions with the fit results from *CorrFit* within 400 $<k_T$ (MeV/c)$<$ 500 for 30−40% central Pb–Pb collisions at $\sqrt{s_{NN}}$ = 5.02 TeV in ALICE.

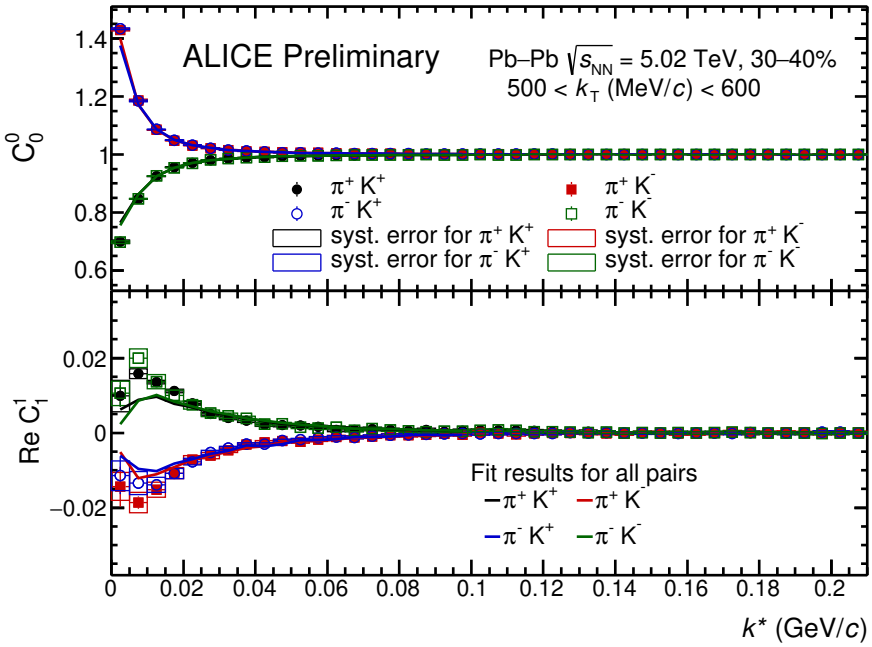

Figure 4.123: The pion-kaon correlation functions with the fit results from *CorrFit* within 500 $<k_T$ (MeV/c)$<$ 600 for 30−40% central Pb–Pb collisions at $\sqrt{s_{NN}}$ = 5.02 TeV in ALICE.

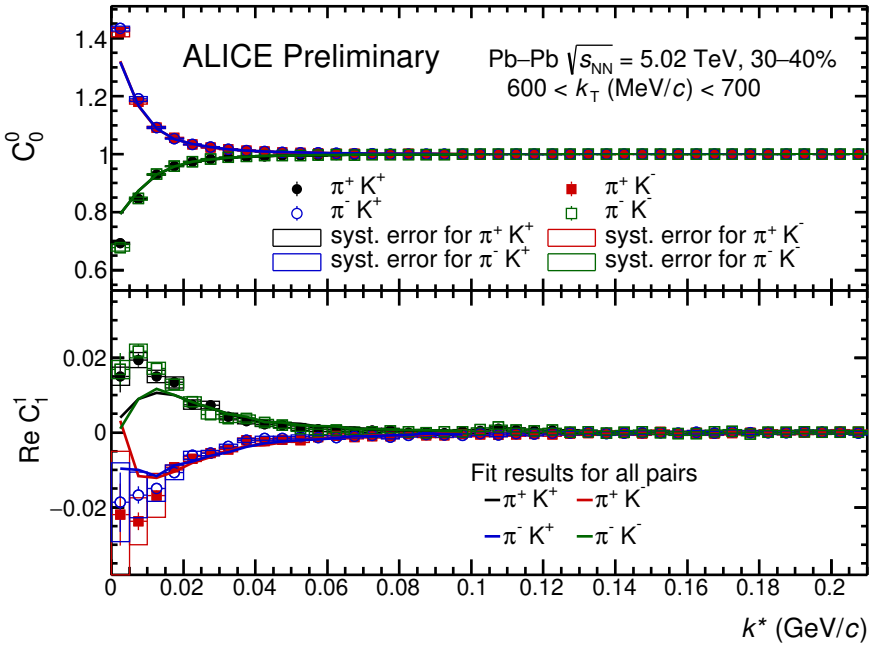

Figure 4.124: The pion-kaon correlation functions with the fit results from *CorrFit* within 600 $<k_T$ (MeV/c)$<$ 700 for 30−40% central Pb–Pb collisions at $\sqrt{s_{NN}}$ = 5.02 TeV in ALICE.

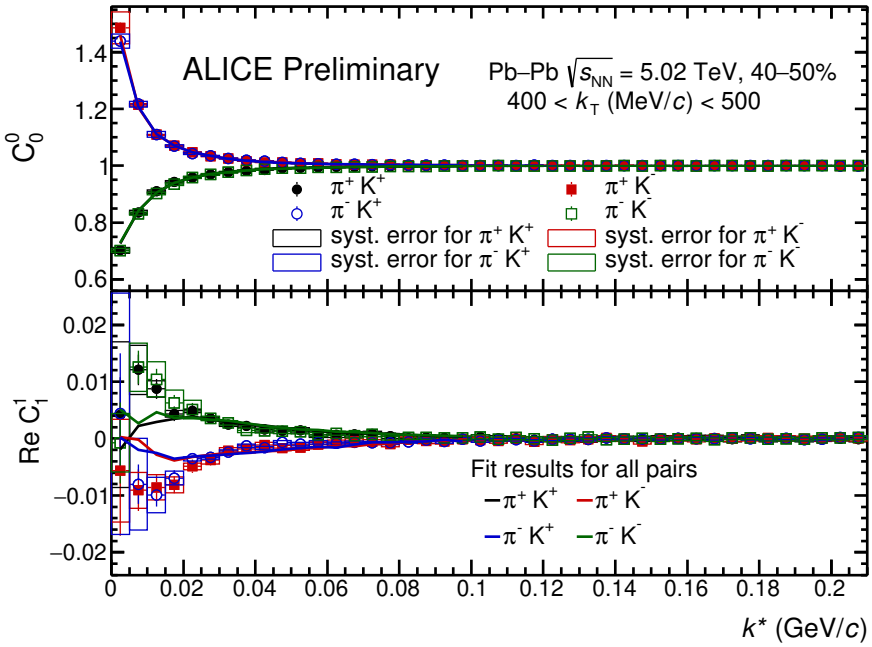

Figure 4.125: The pion-kaon correlation functions with the fit results from *CorrFit* within 400 $<k_T$ (MeV/c)$<$ 500 for 40−50% central Pb–Pb collisions at $\sqrt{s_{NN}}$ = 5.02 TeV in ALICE.

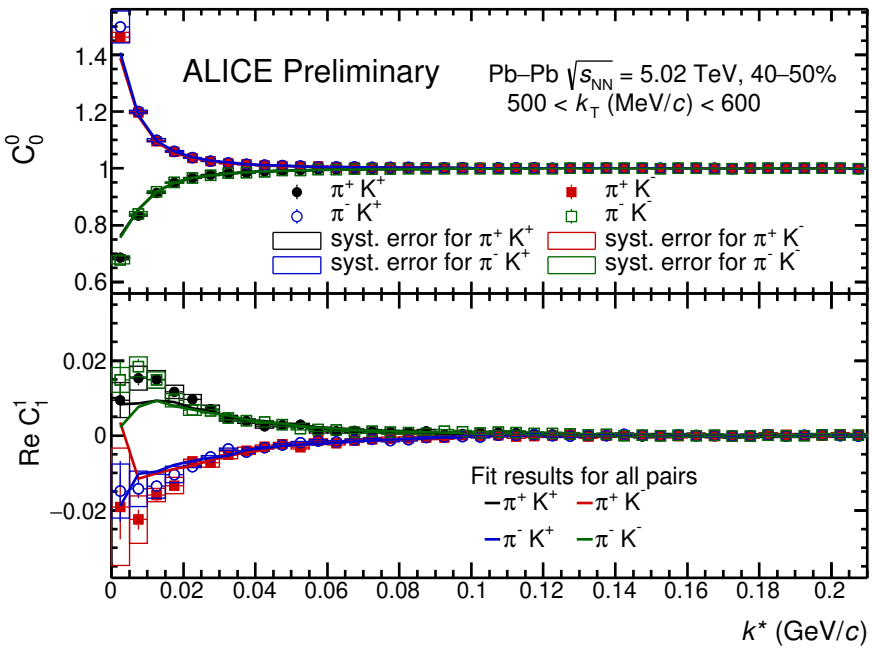

Figure 4.126: The pion-kaon correlation functions with the fit results from *CorrFit* within 500 $<k_T$ (MeV/c)$<$ 600 for 40−50% central Pb–Pb collisions at $\sqrt{s_{NN}}$ = 5.02 TeV in ALICE.

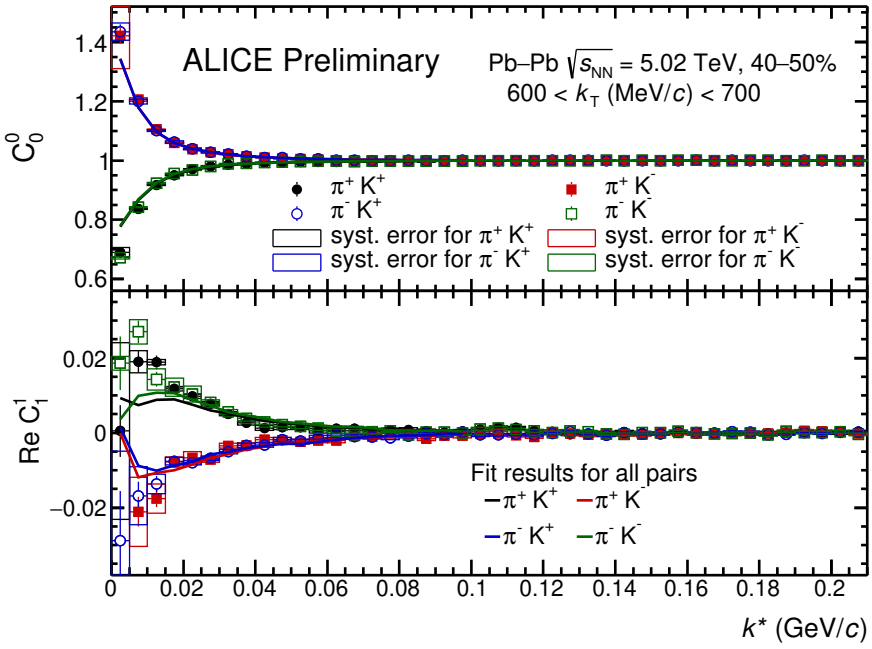

Figure 4.127: The pion-kaon correlation functions with the fit results from *CorrFit* within 600 $<k_T$ (MeV/c)$<$ 700 for 40−50% central Pb–Pb collisions at $\sqrt{s_{NN}}$ = 5.02 TeV in ALICE.

The background-minimised pion-kaon correlation functions with fit results, obtained from the CorrFit package for 0−5%, 20−30%, 40−50% and 60−70% central Pb–Pb collisions in the β_T ranges: 0.7−0.75, 0.8−0.85 and 0.9−0.95 are shown in Fig. 4.128-4.139. It is observed that the fit functions are in well agreement with the experimental correlation functions.

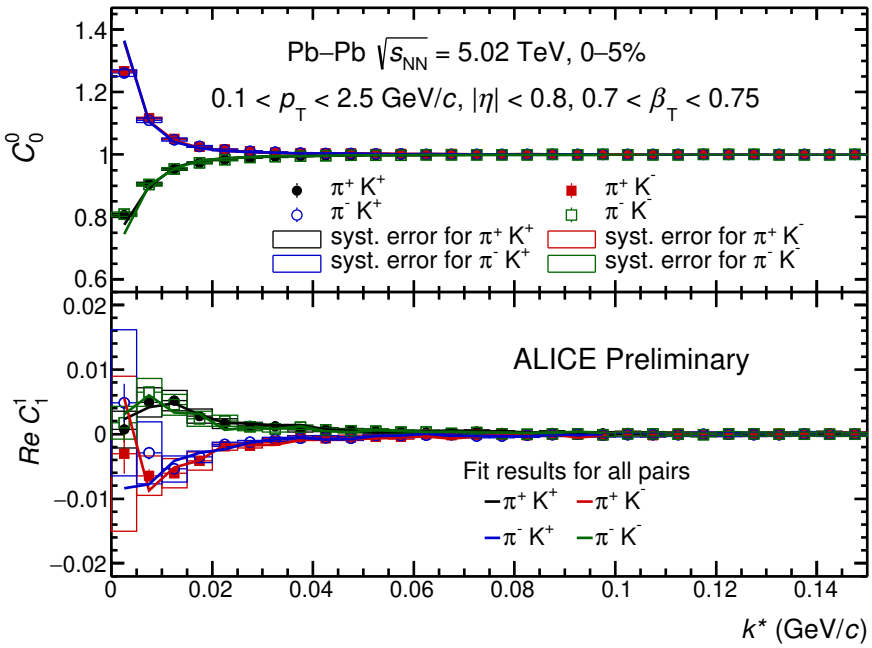

Figure 4.128: The pion-kaon correlation functions with the fit results from *CorrFit* in 0.7<β_T<0.75 for 0-5% central Pb–Pb collisions at $\sqrt{s_{NN}}$ = 5.02 TeV in ALICE.

The femtosocpic parameters, extracted from these fits are discussed extensively in chapter 5.

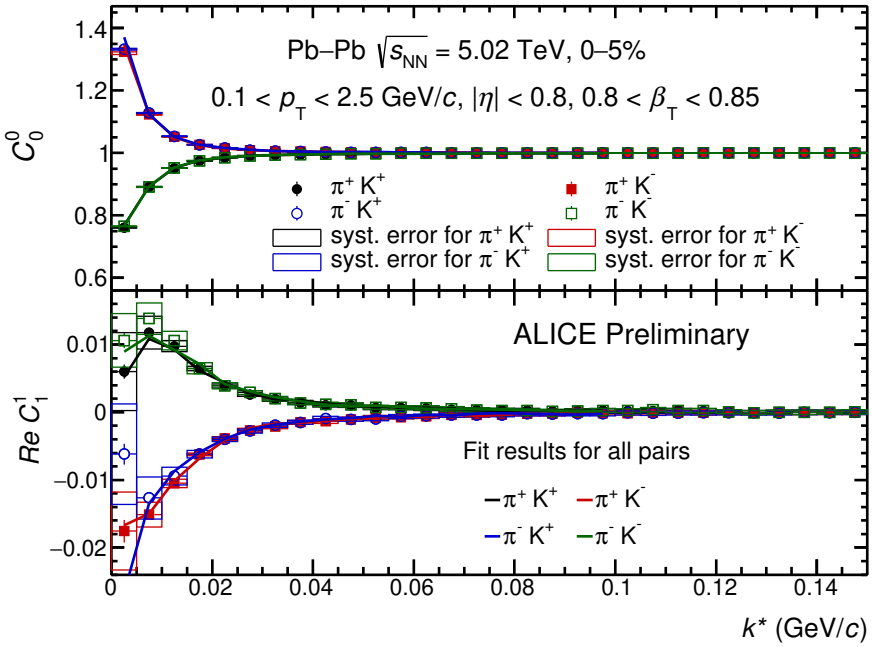

Figure 4.129: The pion-kaon correlation functions with the fit results from *CorrFit* in $0.8<\beta_T<0.85$ for 0-5% central Pb–Pb collisions at $\sqrt{s_{NN}}$ = 5.02 TeV in ALICE.

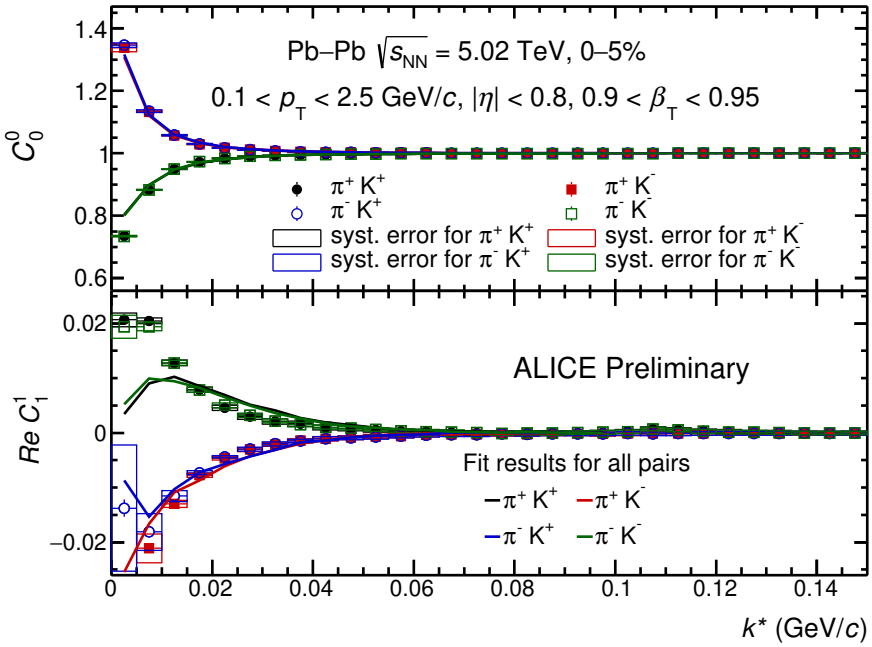

Figure 4.130: The pion-kaon correlation functions with the fit results from *CorrFit* in $0.9<\beta_T<0.95$ for 0-5% central Pb–Pb collisions at $\sqrt{s_{NN}}$ = 5.02 TeV in ALICE.

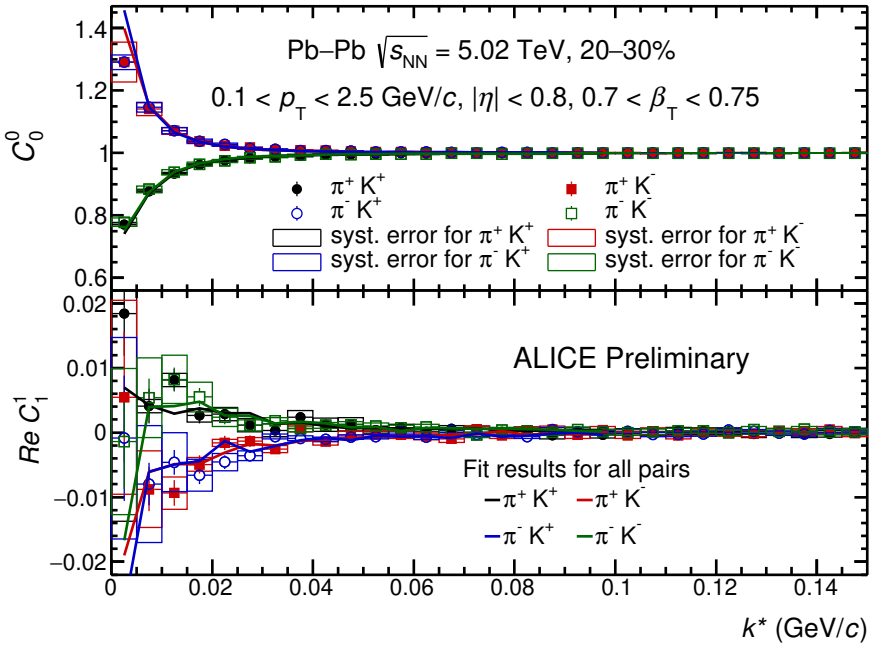

Figure 4.131: The pion-kaon correlation functions with the fit results from *CorrFit* in $0.7<\beta_T<0.75$ for 20-30% central Pb–Pb collisions at $\sqrt{s_{NN}}$ = 5.02 TeV in ALICE.

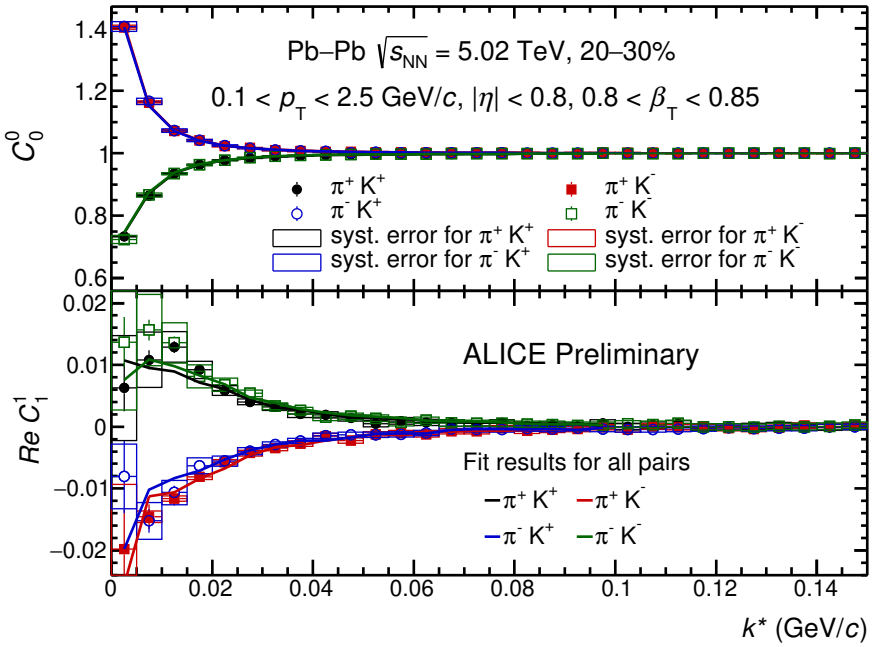

Figure 4.132: The pion-kaon correlation functions with the fit results from *CorrFit* in $0.8<\beta_T<0.85$ for 20-30% central Pb–Pb collisions at $\sqrt{s_{NN}}$ = 5.02 TeV in ALICE.

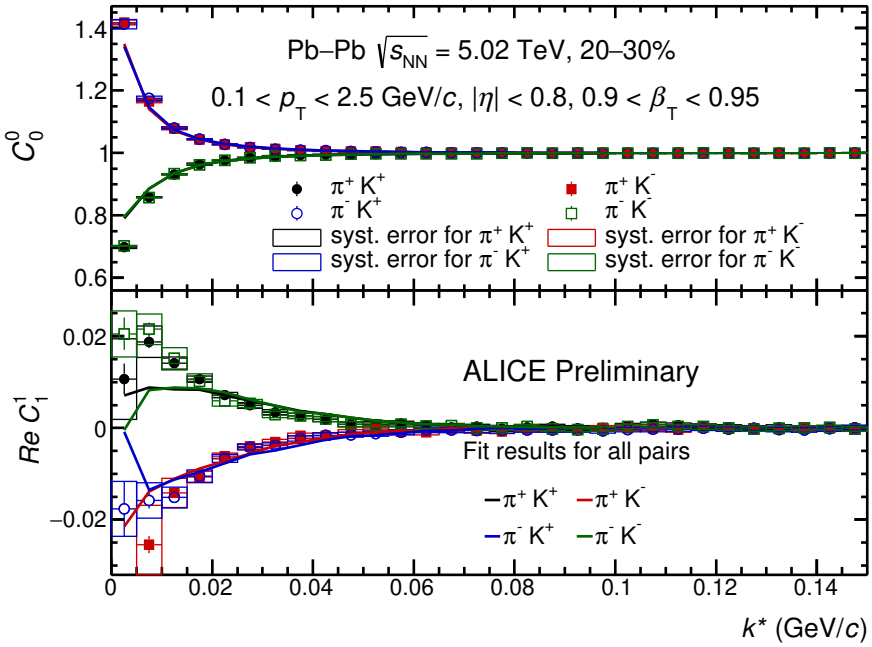

Figure 4.133: The pion-kaon correlation functions with the fit results from *CorrFit* in 0.9<β_T<0.95 for 20-30% central Pb–Pb collisions at $\sqrt{s_{NN}}$ = 5.02 TeV in ALICE.

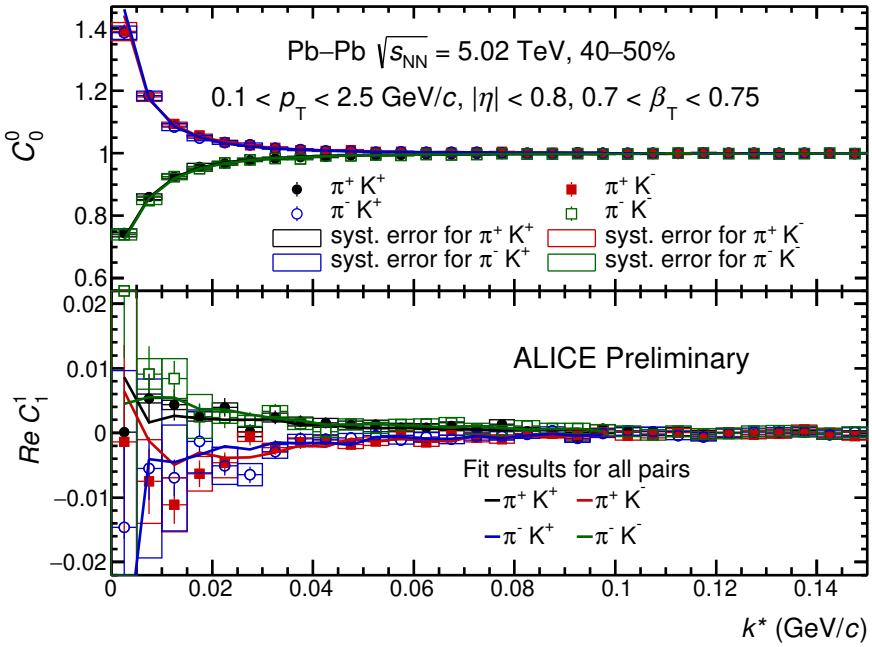

Figure 4.134: The pion-kaon correlation functions with the fit results from *CorrFit* in 0.7<β_T<0.75 for 40-50% central Pb–Pb collisions at $\sqrt{s_{NN}}$ = 5.02 TeV in ALICE.

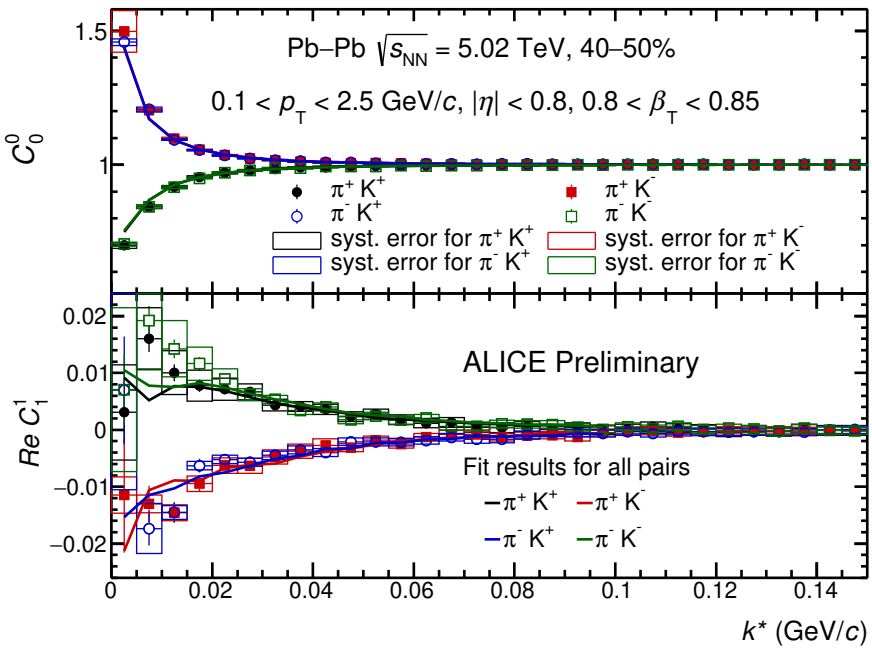

Figure 4.135: The pion-kaon correlation functions with the fit results from *CorrFit* in $0.8<\beta_T<0.85$ for 40-50% central Pb–Pb collisions at $\sqrt{s_{NN}}$ = 5.02 TeV in ALICE.

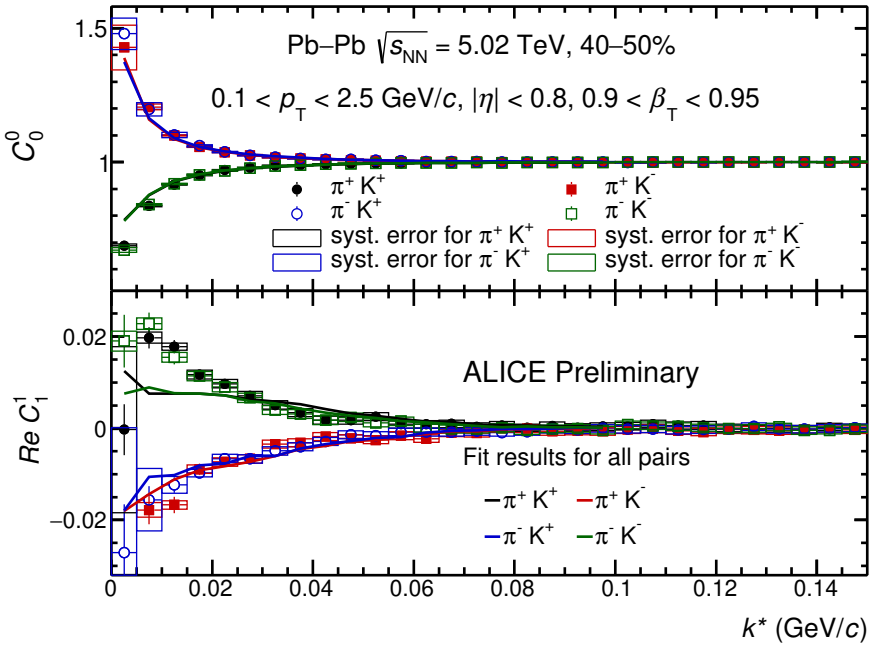

Figure 4.136: The pion-kaon correlation functions with the fit results from *CorrFit* in $0.9<\beta_T<0.95$ for 40-50% central Pb–Pb collisions at $\sqrt{s_{NN}}$ = 5.02 TeV in ALICE.

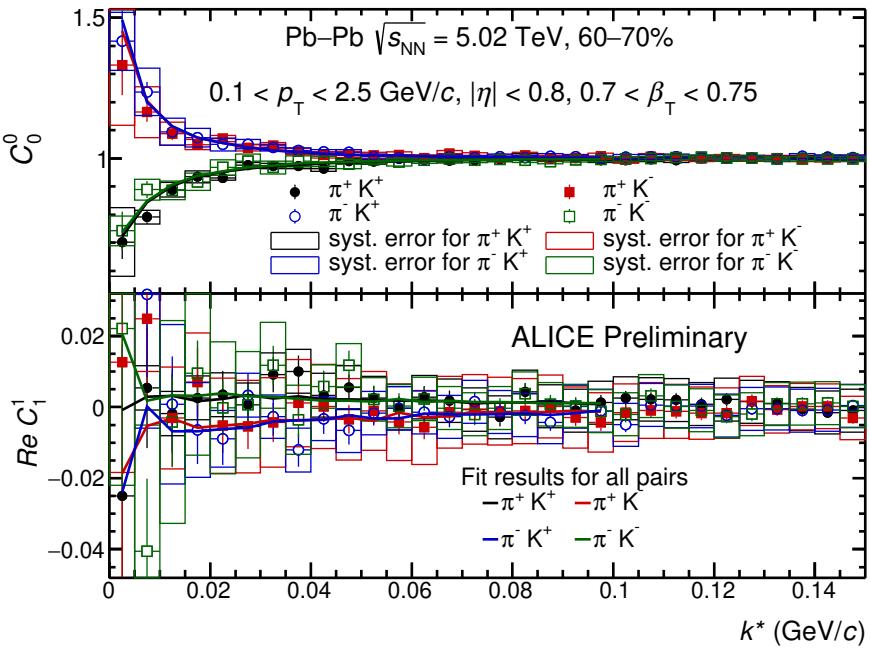

Figure 4.137: The pion-kaon correlation functions with the fit results from *CorrFit* in $0.7<\beta_T<0.75$ for 60-70% central Pb–Pb collisions at $\sqrt{s_{NN}}$ = 5.02 TeV in ALICE.

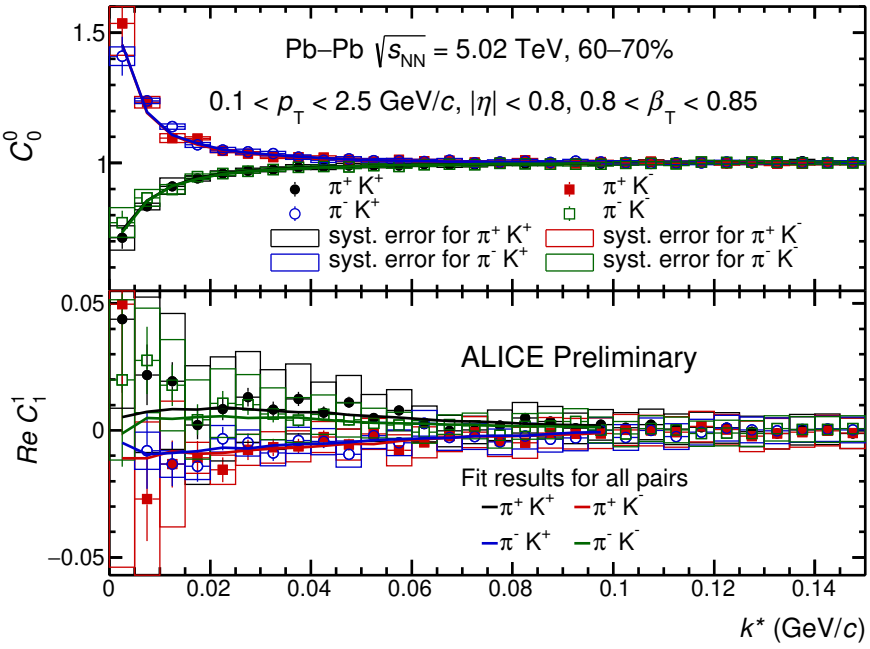

Figure 4.138: The pion-kaon correlation functions with the fit results from *CorrFit* in $0.8<\beta_T<0.85$ for 60-70% central Pb–Pb collisions at $\sqrt{s_{NN}}$ = 5.02 TeV in ALICE.

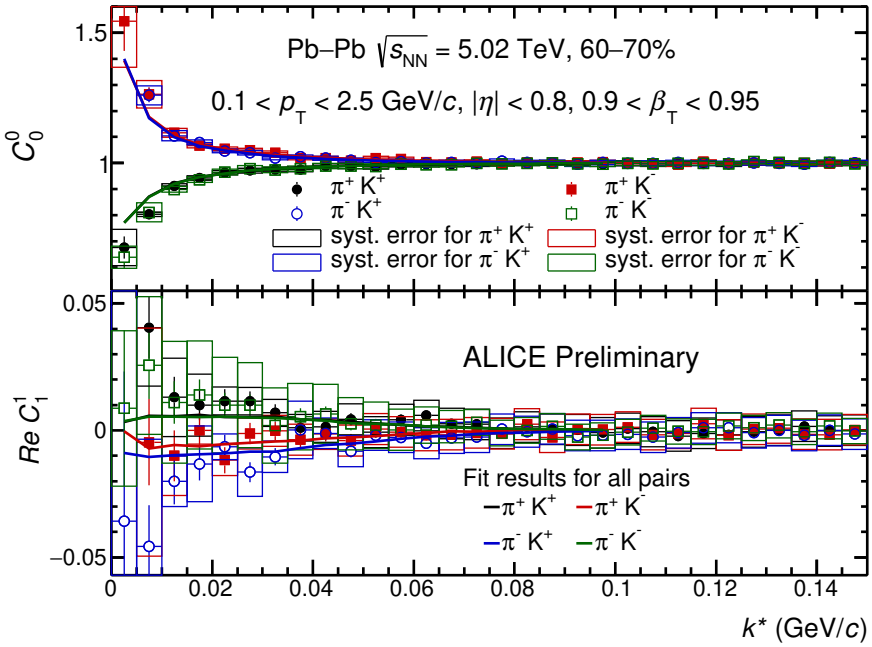

Figure 4.139: The pion-kaon correlation functions with the fit results from *CorrFit* in $0.9<\beta_T<0.95$ for 60-70% central Pb–Pb collisions at $\sqrt{s_{NN}}$ = 5.02 TeV in ALICE.

Chapter 5

Results and discussion

In the previous chapter, it is shown that the measured pion-kaon correlation functions are well described by the theoretical fit from *CorrFit* package. The extracted fit parameters can therefore be considered as the best estimate of the femtoscopic parameters associated with the particle emitting source. In this chapter, the dependence of femtoscopic parameters on various properties of the system is discussed in detail.

5.1 Femtoscopic parameters (k_{T} integrated)

The centrality dependence of R and μ in the *out* direction obtained from the pion-kaon correlation functions from 0−5% to 40−50% central Pb–Pb collisions at $\sqrt{s_{\mathrm{NN}}}$ = 5.02 TeV is shown in Fig. 5.1. The analysis is performed separately for four different charged-pair combinations of pions and kaons and two magnetic-field polarities (total eight functions) for each $<\mathrm{d}N_{\mathrm{ch}}/\mathrm{d}\eta>^{\frac{1}{3}}$ bin in the integrated k_{T} range. Each $<\mathrm{d}N_{\mathrm{ch}}/\mathrm{d}\eta>^{\frac{1}{3}}$ bin consists of the results obtained from two magnetic field polarities and each magnetic-field polarity includes four charged-pair combinations of pions and kaons. It is observed that the R increases from the peripheral to most central events. The μ also increases from the peripheral to central collisions. However, a systematic difference in the values of R (and μ) in each $<\mathrm{d}N_{\mathrm{ch}}/\mathrm{d}\eta>^{\frac{1}{3}}$ bin is observed for different charged-pairs and magnetic-field polarities.

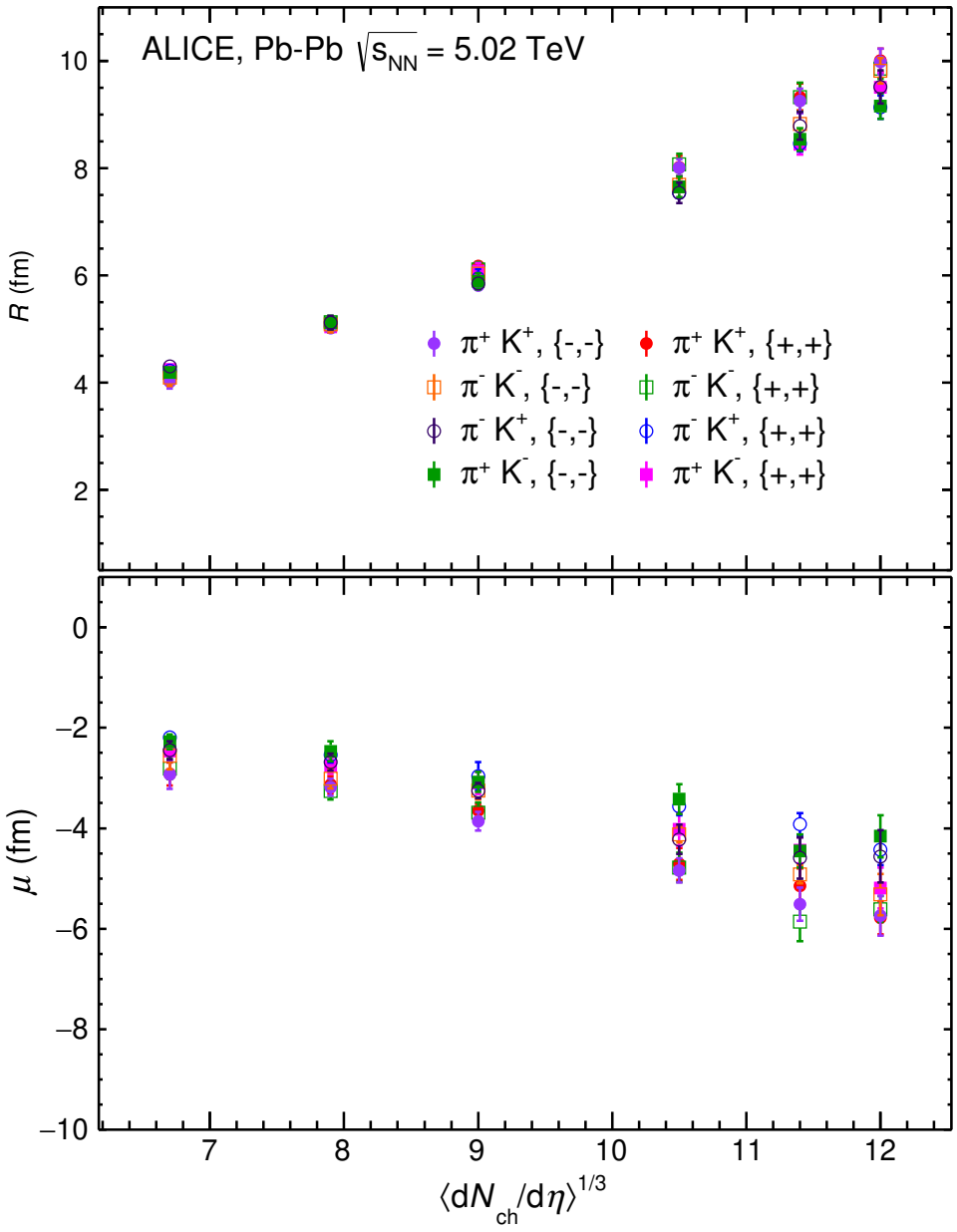

Figure 5.1: The radii, R (upper panel) and pair-emission asymmetry, μ (bottom panel) in the *out* direction as a function of $<\mathrm{d}N_{\mathrm{ch}}/\mathrm{d}\eta>^{\frac{1}{3}}$ for all charged-pair combinations of pions and kaons in both magnetic-field polarities in Pb–Pb collisions at $\sqrt{s_{\mathrm{NN}}}$ = 5.02 TeV in ALICE.

The resultant values of the source size and pair-emission asymmetry in each $<\mathrm{d}N_{\mathrm{ch}}/\mathrm{d}\eta>^{\frac{1}{3}}$ bin is estimated as the weighted mean of all the eight points [87] using the following equations:

$$R_{\mathrm{out}} = \left(\sum_{i=1}^{8} \frac{R_{\mathrm{i}}}{\sigma(R)_{\mathrm{i}}^2}\right) \Big/ \left(\sum_{\mathrm{i}=1}^{8} \frac{1}{\sigma(R)_{\mathrm{i}}^2}\right), \tag{5.1}$$

$$\mu_{\mathrm{out}} = \left(\sum_{\mathrm{i}=1}^{8} \frac{\mu_{\mathrm{i}}}{\sigma(\mu)_{\mathrm{i}}^2}\right) \Big/ \left(\sum_{\mathrm{i}=1}^{8} \frac{1}{\sigma(\mu)_{\mathrm{i}}^2}\right). \tag{5.2}$$

The statistical uncertainty is calculated as:

$$\Delta R_{\text{out}} = 1/\sqrt{\sum_{i=1}^{8} \frac{1}{\sigma(R)_i^2}} \tag{5.3}$$

$$\Delta \mu_{\text{out}} = 1/\sqrt{\sum_{i=1}^{8} \frac{1}{\sigma(\mu)_i^2}} \tag{5.4}$$

where, σ_i is the respective error in each point.

5.1.1 Systematic uncertainties

The fitting of the correlation functions might be affected by various input parameters, which might contribute to the systematic uncertainties in the extracted source parameters. The variations in the input parameters are given in Table 5.1.

Single parameter variation	**Default**	**Variation 1**	**Variation 2**
Fitting range (MeV/c)	0−100	0−80	0−120
Normalisation range (MeV/c)	150−200	180−230	200−250
Pair purity (% of the default value)	100	98.5	101.5
Momentum-resolution correction	100%	80%	−−
Mag. field polarity × charged-pairs	−−	2×4	−−
Multiple parameter variation			
Fitting range (MeV/c)	0−100	0−80	−−
Pair purity (% of the default value)	100	98.5	−−
Normalisation range (MeV/c)	150−200	180−230	−−
Pair purity (% of the default value)	100	101.5	−−
Fitting range (MeV/c)	0−100	0−120	−−
Normalisation range (MeV/c)	150−200	200−250	−−

Table 5.1: The variations in the input conditions for fitting the correlation functions.

The relative-systematic uncertainty in each $<dN_{ch}/d\eta>^{\frac{1}{3}}$ bin for each of the variations can be calculated by the following formulae:

$$\Delta R_{syst} = (R_D - R_A)/R_D, \tag{5.5}$$

$$\Delta \mu_{syst} = (\mu_D - \mu_A)/\mu_D, \tag{5.6}$$

where, R_D and R_A are the mean of R_{out}, obtained in the default input condition and any of the variations, respectively. Similarly, μ_D and μ_A are the mean of μ_{out} obtained in default input condition and any of the variations, respectively. The relative systematic uncertainties, averaged over all multiplicity classes for different variations in the fit conditions are given in Table 5.2.

Femtoscopic parameter	Error (%) in fit range: MeV/c		Error (%) in normalisation range: MeV/c		Error (%) in purity		Error (%) in 80% mom. resol.	Error (%) in mag. field polarity and charged pairs
	0−80	0−120	180−230	200−250	+1.5%	-1.5%		
R_{out}	1.0	1.0	1.1	1.0	2.7	3.6	2.1	2.6
μ_{out}	1.9	2.3	1.0	1.0	3.0	2.9	1.0	5.0

Table 5.2: The average systematic uncertainties in the R_{out} and μ_{out} for different variations of the input parameters for fitting the pion-kaon correlation functions in Pb–Pb collisions at $\sqrt{s_{NN}}$ = 5.02 TeV in ALICE.

The total systematic uncertainty of the femtoscopic parameter is estimated using the following approach. For each of the variation considered, there are eight values of the estimated parameter in each $<dN_{ch}/d\eta>^{\frac{1}{3}}$ bin. As the number of variations considered is 10, there are 80 values in each $<dN_{ch}/d\eta>^{\frac{1}{3}}$ bin. The RMS of these eighty points is calculated and quoted as the total systematic uncertainty associated with the estimated parameter.

Fig. 5.2 shows the R_{out} and μ_{out} as a function of $<dN_{ch}/d\eta>^{\frac{1}{3}}$. It is observed that the R_{out} increases with multiplicity which is expected as the system size increases with increase in number of the participants. The μ_{out} is found to be universally negative which suggests that pions

are always emitted from closer proximity of the center of source than kaons. The magnitude of μ_{out} also increases with increasing multiplicity. The non-zero values of μ_{out} also indicate the presence of radial flow in the system. The values of R_{out} and μ_{out} are compared with the results obtained in Pb–Pb collisions at $\sqrt{s_{\mathrm{NN}}} = 2.76$ TeV and are found to be consistent. Moreover, the study suggests that there is no significant dependence of R_{out} and μ_{out} on the beam energy.

The predictions from THERMINATOR 2 model are compared with the results as shown in Fig. 5.2. THERMINATOR 2 does not incorporate the hadronic-rescattering phase of the fireball after freeze-out. Therefore, a study is performed by introducing a set of additional time delays in the emission of kaons to mimic the presence of a possible rescattering phase. The lines in Fig. 5.2 correspond to different values of additional delay in the emission of kaons. It is observed that there is a good agreement between the measured radii and predicted ones in the peripheral events. However, the predictions of THERMINATOR 2 underestimates the measured values from mid-central to central events. The slope of centrality dependence of μ_{out} as predicted by THERMINATOR 2 follows a similar trend as the measured ones. The measured values of μ_{out} lie between the lines corresponding to the time delay of 0.0 and 1.0 fm/c. This indicates the presence of hadronic-rescattering phase along with the radial flow in the system.

5.2 k_{T}- and m_{T}-dependent correlation functions

The femtoscopic parameters are extracted from the pion-kaon correlation functions in three k_{T} ranges as discussed in section 4.10. The values of source size and pair-emission asymmetry in *out* direction as a function of $<\mathrm{d}N_{\mathrm{ch}}/\mathrm{d}\eta>^{\frac{1}{3}}$ for all charged combinations of pion-kaon pairs in both the magnetic-field polarities are shown in Fig. 5.3-5.5. The values of source size and pair-emission asymmetry are observed to decrease with increasing multiplicity in all the three k_{T} ranges.

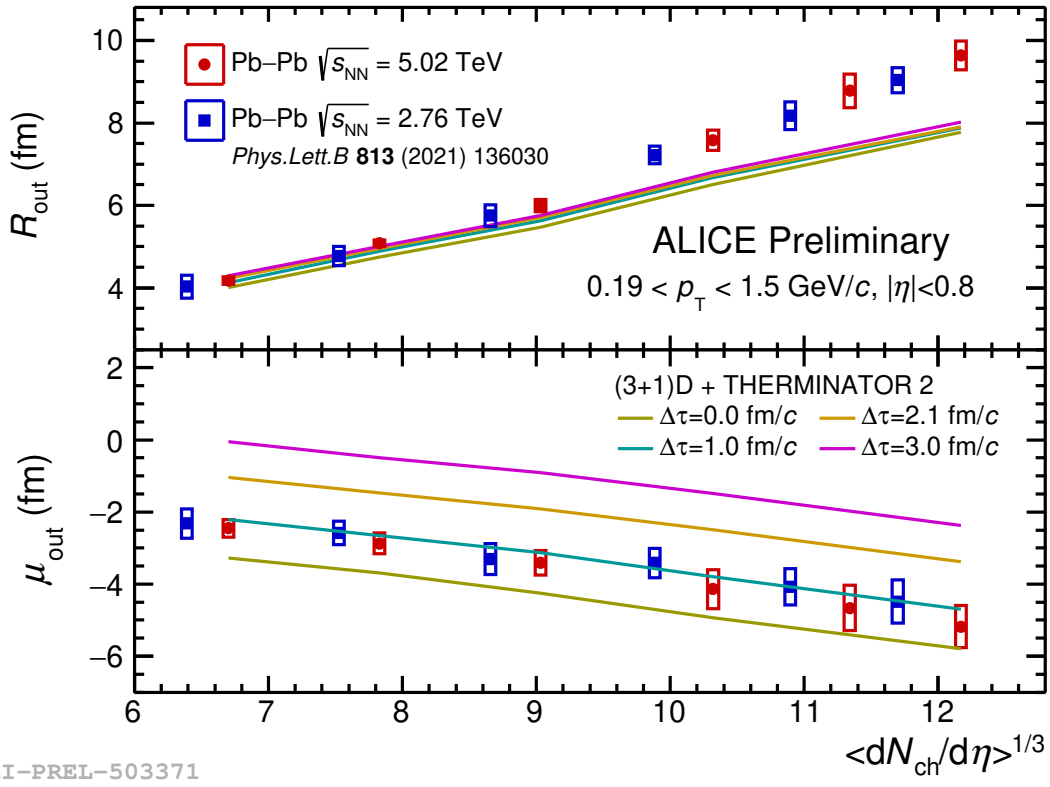

Figure 5.2: The R_{out} (upper panel) and μ_{out} (bottom panel) as a function of the $<dN_{ch}/d\eta>^{\frac{1}{3}}$ in Pb–Pb collisions at $\sqrt{s_{NN}}$ = 5.02 TeV in ALICE. The solid lines show the predictions of R_{out} and μ_{out} from THERMINATOR 2 model with the default and selected values of additional delay ($\Delta\tau$) in kaon emission. [91]

5.2.1 Systematic uncertainties

The variations of input parameters for fitting the correlation functions, discussed in section 5.1.1 are also applied to estimate the systematic uncertainties in the femtoscopic parameters in different k_T ranges for all multiplicity classes. The systematic uncertainties due to the variations in fit conditions in the three k_T bins, averaged over the centrality classes, are given in Table 5.3.

The resultant systematic uncertainty in the R_{out} and μ_{out} in each k_T bin and centrality class is estimated using the procedure discussed in 5.1.1. The R_{out} and μ_{out} as a function of $<k_T>$ for different centrality classes are shown in Fig. 5.6. It is observed that the R_{out} decreases with increasing k_T. In a given centrality class, the pairs with larger k_T are mostly formed by high-p_T

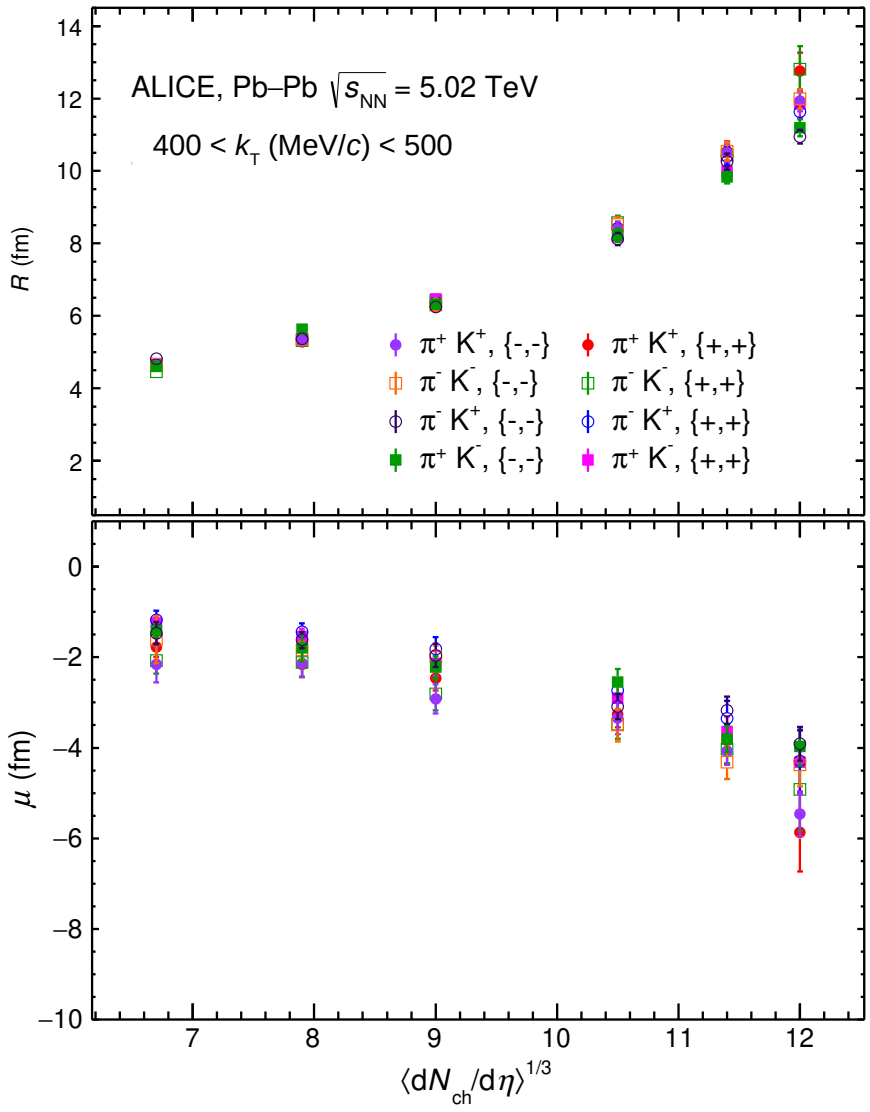

Figure 5.3: The radii (upper panel) and pair-emission asymmetry (bottom panel) in *out* direction as the function of $<dN_{ch}/d\eta>^{\frac{1}{3}}$ for all charged combinations of pion-kaon pairs in both the magnetic fields and 400<k_T (MeV/c) <500 in Pb–Pb collisions at $\sqrt{s_{NN}}$ = 5.02 TeV in ALICE.

particles which are emitted in the vicinity of each other. Hence, the region of homogeneity for the larger-k_T pairs is less compared to the ones with lower k_T. The values of μ_{out} decrease from the most central to peripheral events irrespective of the k_T values and its magnitude is observed

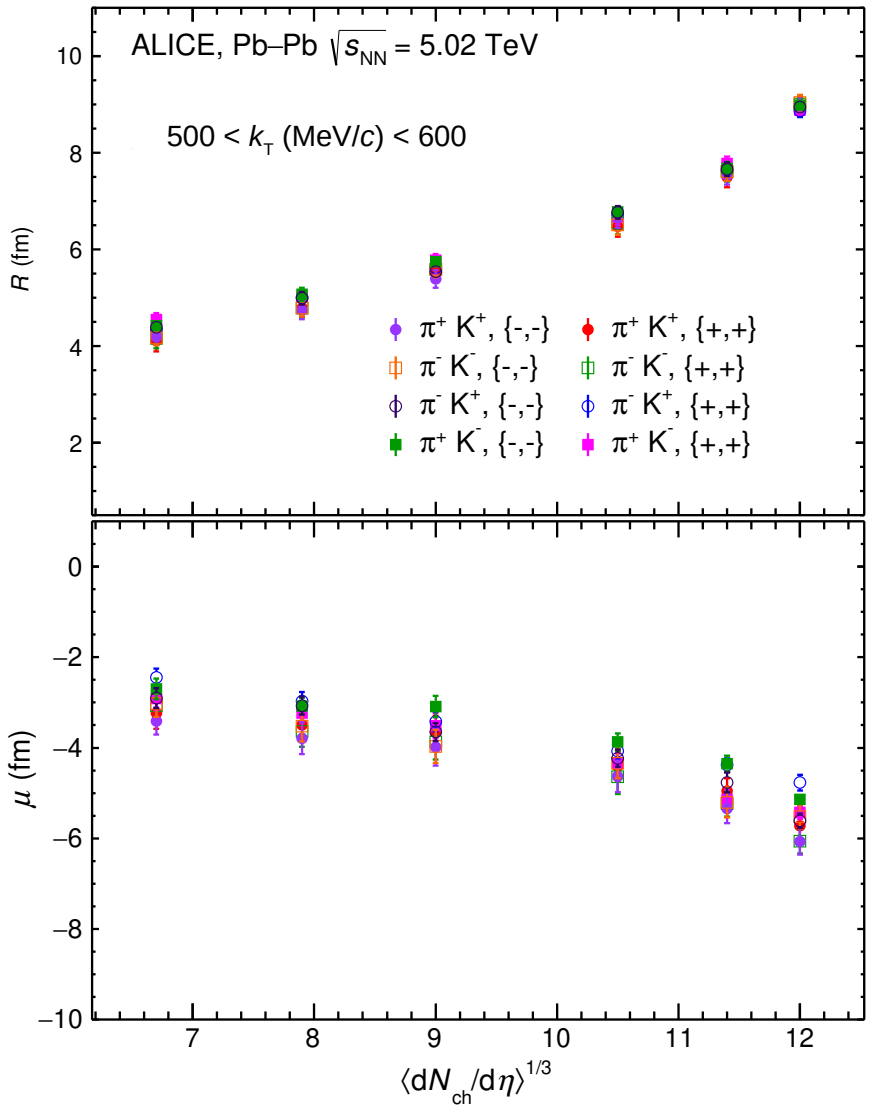

Figure 5.4: The radii (upper panel) and pair-emission asymmetry (bottom panel) in *out* direction as the function of $<dN_{ch}/d\eta>^{\frac{1}{3}}$ for all charged combinations of pion-kaon pairs in both the magnetic fields and 500<k_T (MeV/c) <600 in Pb–Pb collisions at $\sqrt{s_{NN}}$ = 5.02 TeV in ALICE.

to be lowest at 400<k_T (MeV/c)<500 for each centrality class. However, the correlation functions are needed to be analysed in more k_T bins to understand the behaviour of μ_{out} more clearly. This would be possible by selecting the particles from broader p_T ranges.

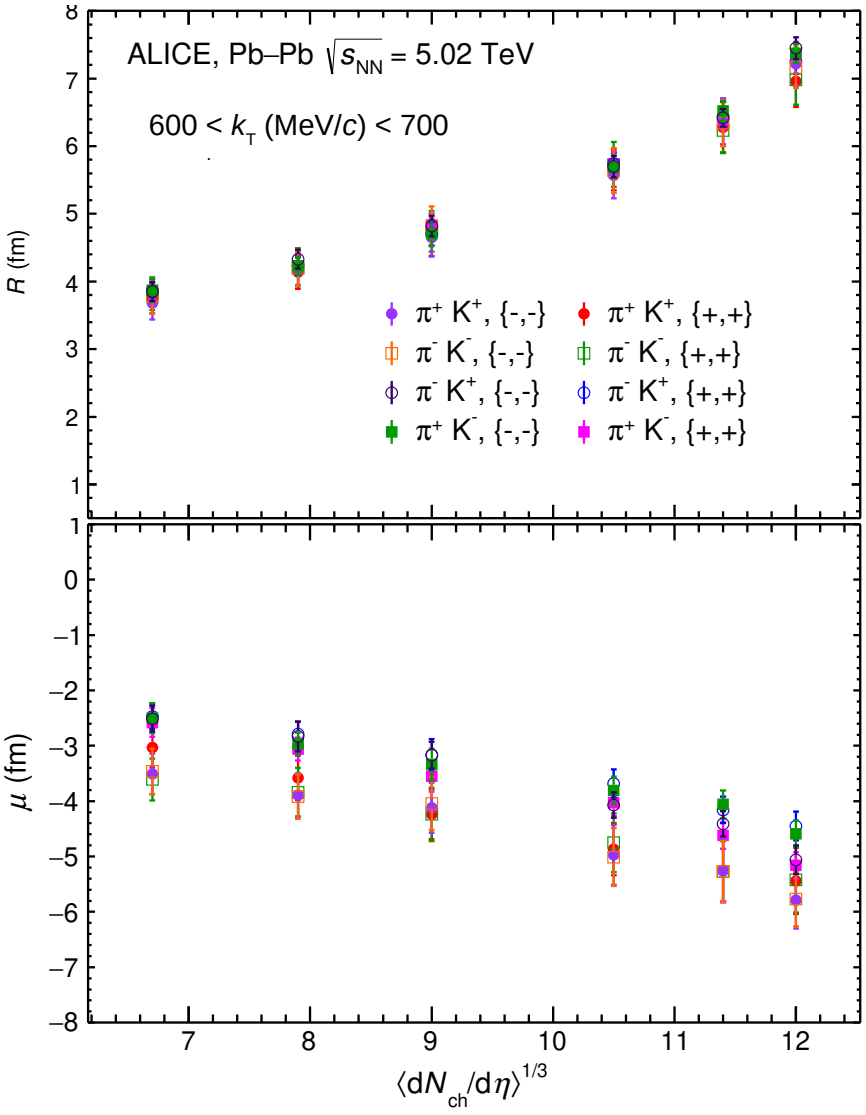

Figure 5.5: The radii (upper panel) and pair-emission asymmetry (bottom panel) in *out* direction as the function of $<dN_{ch}/d\eta>^{\frac{1}{3}}$ for all charged combinations of pion-kaon pairs in both the magnetic fields and 600<k_T (MeV/c) <700 in Pb–Pb collisions at $\sqrt{s_{NN}}$ = 5.02 TeV in ALICE.

Fig. 5.7 shows the R_{out} and μ_{out} as a function of the transverse mass of the pair (<m_T>) and centrality class. The m_T is estimated using Eq. (5.7).

$$m_T = \sqrt{m_r^2 + k_T^2} \tag{5.7}$$

Variation in input setting	Error in 400<k_T (MeV/c)<500		Error in 500<k_T (MeV/c) <600		Error in 600<k_T (MeV/c)<700	
	R_{out}(%)	μ_{out}(%)	R_{out}(%)	μ_{out}(%)	R_{out}(%)	μ_{out}(%)
Fit range: 0-120 MeV/c	1.0	4.3	1.0	1.0	1.0	1.8
Fit range: 0-80 MeV/c	1.0	5.2	1.0	1.6	1.0	3.1
Norm. range: 180-230 MeV/c	1.0	1.7	1.0	1.0	1.0	1.0
Norm. range: 200-250 MeV/c	1.0	1.1	1.0	1.0	1.0	1.0
Purity: 98.5% of default	3.6	6.3	2.7	2.6	3.0	3.9
Purity: 101.5% of default	2.9	4.8	2.8	3.0	2.7	1.2
Momentum resolution: 80%	1.0	3.2	1.6	2.8	3.4	5.4
Mag. field and charge combination	2.5	15.4	1.8	8.1	1.4	9.5

Table 5.3: Average systematic uncertainties in the R_{out} and μ_{out} in the three k_T ranges for different variations of input conditions for fitting the pion-kaon correlation functions in Pb–Pb collisions at $\sqrt{s_{NN}}$ = 5.02 TeV in ALICE.

where, $m_r = \frac{m_{\pi^\pm} m_{K^\pm}}{(m_{\pi^\pm} + m_{K^\pm})}$ is the reduced mass of pion-kaon pair. It is observed that the R_{out} decreases as m_T increases due to the increase in k_T. This observation can be attributed to the presence of strong collectivity in the system.

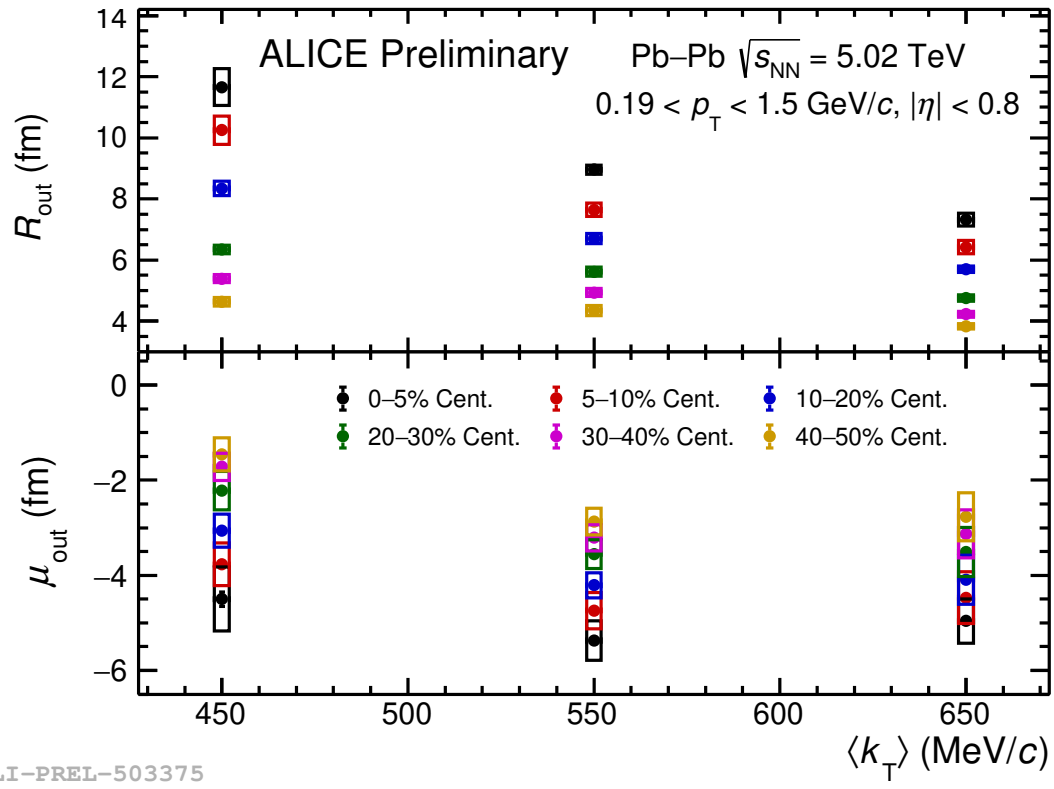

Figure 5.6: The R_{out} (upper plot) and μ_{out} (bottom plot) as a function of $<k_T>$ for different centrality classes in Pb–Pb collisions at $\sqrt{s_{NN}}$ = 5.02 TeV in ALICE. [91]

5.3 β_T-dependent correlation functions

The values of R_{out} and μ_{out} are extracted from the pion-kaon correlation functions in Pb–Pb collisions at $\sqrt{s_{NN}}$ = 5.02 TeV from 0–5% to 70–80% centrality classes in the β_T ranges of 0.7–0.75, 0.75–0.8, 0.8–0.85, 0.85–0.9 and 0.9–0.95. Fig. 5.8 shows the R_{out} and μ_{out} as a function of $<\beta_T>$ for different centrality classes. The values of $<\beta_T>$ are the weighted averages of respective β_T bins. The values of systematic uncertainties in R_{out} and μ_{out}, listed in Table 5.4-5.5, are estimated using the same sets of variations in the input parameters, as discussed in section 5.1.1.

The R_{out} and μ_{out} as a function of $<\beta_T>$ for different centrality classes are shown in Fig. 5.8. In the upper panel of Fig. 5.8, it is shown that the R_{out} decreases with increasing $<\beta_T>$ for all centrality classes. The β_T is directly related to the collective flow of the system along the transverse

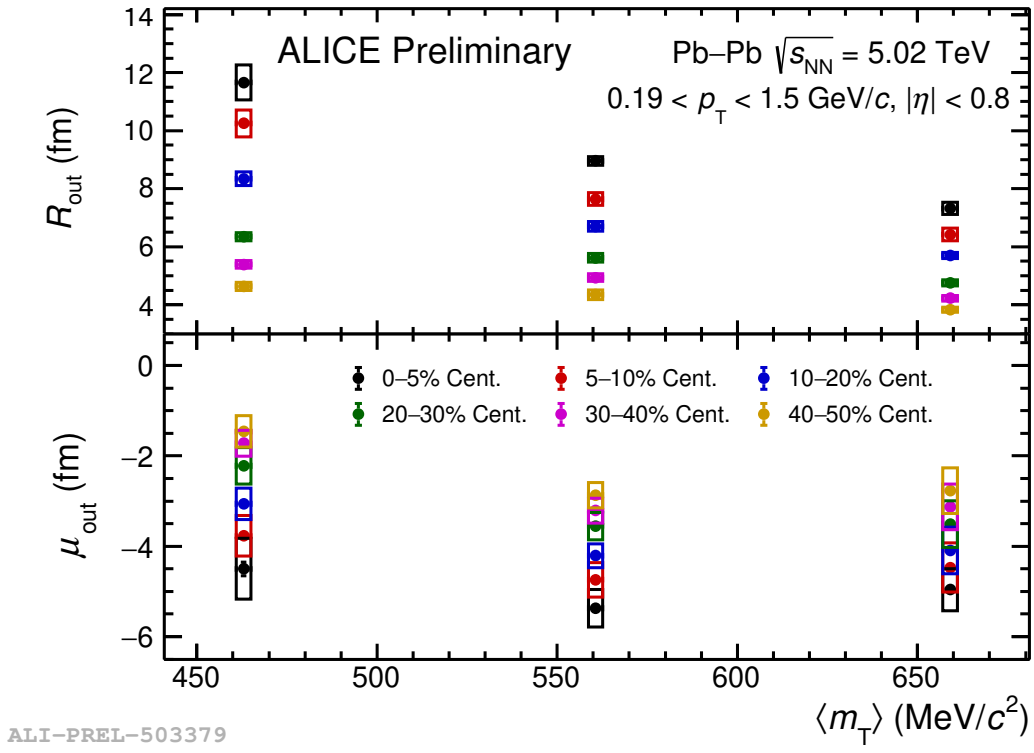

Figure 5.7: The R_{out} (upper plot) and μ_{out} (bottom plot) as a function of $<m_T>$ for different centrality classes in Pb–Pb collisions at $\sqrt{s_{NN}}$ = 5.02 TeV in ALICE.

direction. Hence, this observation infers that for a given centrality class (or similar collectivity), the source size decreases with increasing β_T as the region of homogeneity decreases for the pairs with higher p_T. The results are compared with the predicted values from THERMINATOR 2 events with kaon-emission delay $\Delta\tau$ = 0 fm/c. The predictions underestimate the values of R_{out} in the higher multiplicity events as observed earlier in 5.1.

In the bottom panel of Fig. 5.8, it is observed for a given bin of β_T, the emission asymmetry increases from the peripheral to central collisions. This is expected due to the presence of collectivity. However, the variation of μ_{out} as a function of mean β_T does not follow a particular trend across all centrality classes. It is observed that the μ_{out} decreases as β_T increases in the most central events. This is expected because the pair-emission asymmetry arises when both the collective and thermal velocities are comparable in magnitude and as the β_T increases, the contribution from collectivity becomes larger than the random thermal velocities. However,

Variation in input setting	Error in $0.7<\beta_T<0.75$		Error in $0.75<\beta_T<0.8$		Error in $0.8<\beta_T<0.85$	
	$R_{out}(\%)$	$\mu_{out}(\%)$	$R_{out}(\%)$	$\mu_{out}(\%)$	$R_{out}(\%)$	$\mu_{out}(\%)$
Fit range: 0-120 MeV/c	1.5	9.7	1.0	2.0	1.0	2.7
Fit range: 0-80 MeV/c	1.6	15.1	1.0	3.0	1.0	2.5
Norm. range: 180-230 MeV/c	1.0	3.0	1.0	1.4	1.0	1.9
Norm. range: 200-250 MeV/c	1.0	6.1	1.0	1.1	1.0	2.4
Purity: 98.5% of default	4.2	12.3	1.9	3.1	1.3	3.3
Purity: 101.5% of default	1.7	13.2	1.3	3.7	1.5	3.3
Momentum resolution: 80%	1.0	3.0	1.0	1.0	1.0	2.8
Mag. field and charge combination	5.0	20.7	2.6	9.7	3.1	9.6

Table 5.4: The systematic uncertainties in the R_{out} and μ_{out} in $0.7<\beta_T<0.75$, $0.75<\beta_T<0.8$ and $0.8<\beta_T<0.85$ for different variations of input conditions for fitting the pion-kaon correlation function in Pb–Pb collisions at $\sqrt{s_{NN}}$ = 5.02 TeV in ALICE.

in the lower-multiplicity events, the magnitude of μ_{out} increases with β_T, attains the maximum around $<\beta_T>$ = 0.825 and then gradually decreases with increasing β_T of the pairs. Moreover, the value μ_{out} in 70−80% centrality class reaches very close to zero at $<\beta_T>$ = 0.725, which suggests that the asymmetry between the average emission points of pions and kaons is very small. The predictions from THERMINATOR 2 underestimates the results in the lower β_T

Variation in input setting	Error in $0.85<\beta_T<0.9$		Error in $0.9<\beta_T<0.95$	
	$R_{out}(\%)$	$\mu_{out}(\%)$	$R_{out}(\%)$	$\mu_{out}(\%)$
Fit range: 0-120 MeV/c	1.0	1.3	1.0	1.3
Fit range: 0-80 MeV/c	1.0	1.6	1.0	2.1
Norm. range: 180-230 MeV/c	1.0	1.4	1.0	1.0
Norm. range: 200-250 MeV/c	1.0	2.8	1.0	1.4
Purity: 98.5% of default	1.4	2.1	2.0	1.8
Purity: 101.5% of default	1.7	2.3	1.9	1.7
Momentum resolution: 80%	1.0	1.1	1.0	1.0
Mag. field and charge combination	3.8	9.2	6.2	6.5

Table 5.5: The systematic uncertainties in the R_{out} and μ_{out} for $0.85<\beta_T<0.9$ and $0.9<\beta_T<0.95$ for different variations of input conditions for fitting the pion-kaon correlation function in Pb–Pb collisions at $\sqrt{s_{NN}}$ = 5.02 TeV in ALICE.

region. There might be a significant contribution from the rescattering of resonances in the lower β_T region which is not incorporated in THERMINATOR 2 model. Therefore, it will be imperative to compare the results with the predictions, obtained by simulating the correlation functions after scaling the respective p_T spectra of pions and kaons with the real data.

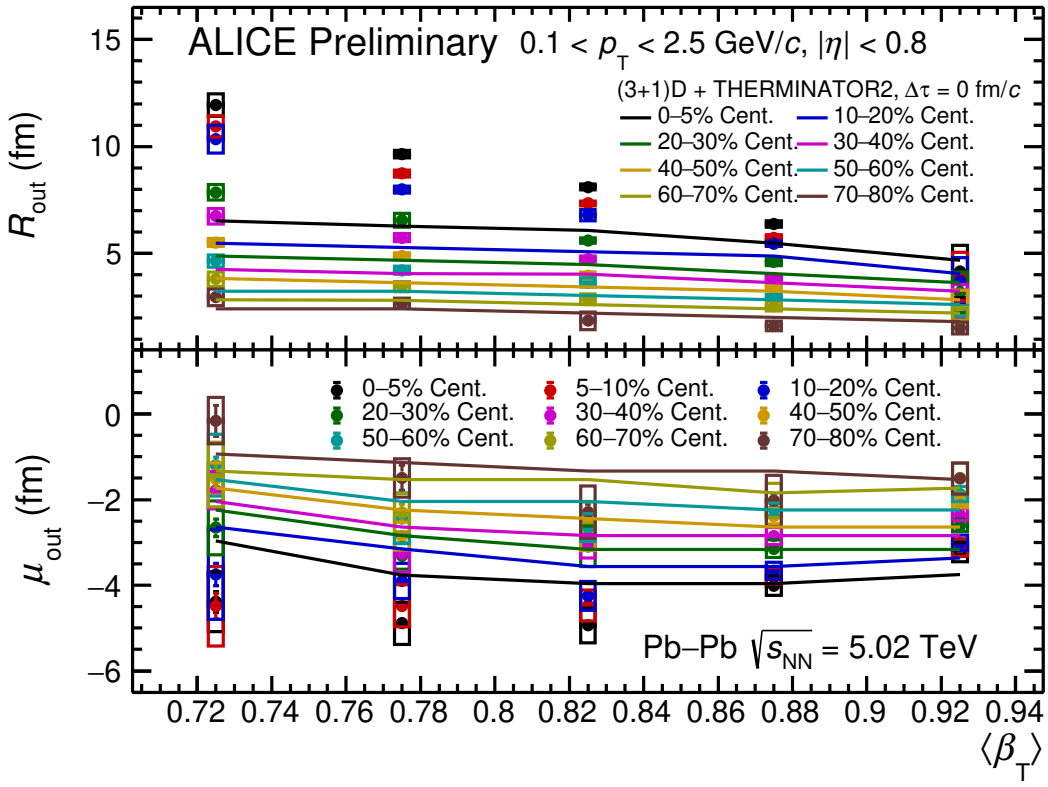

Figure 5.8: The R_{out} (upper plot) and μ_{out} (bottom plot) as a function of β_T and centrality class in Pb–Pb collisions at $\sqrt{s_{NN}}$ = 5.02 TeV in ALICE with the predictions from (3 + 1)D viscous hydrodynamics + THERMINATOR 2 with additional delay in kaon-emission time, $\Delta\tau = 0$.

The R_{out} and μ_{out} as the function of $<\beta_T>$ with the predictions from THERMINATOR 2 model with $\Delta\tau = 1$ fm/c in kaon emission are shown in Fig. 5.9. There is no distinct difference in the comparison of R_{out} with the predictions with $\Delta\tau = 0$ fm/c and $\Delta\tau = 1$ fm/c. However, it is observed that the predictions with $\Delta\tau = 1$ fm/c underestimates the μ_{out} more than the case with $\Delta\tau = 0$ fm/c.

In case of the k_T-integrated correlation functions, the average-transverse velocity of pion-kaon pairs is estimated to be within the range of $0.85<\beta_T<0.9$. In Fig. 5.10, the measured values of R_{out} and μ_{out} in the β_T bin: 0.85−0.9 with the predictions corresponding to $\Delta\tau = 0$ fm/c and $\Delta\tau = 1$ fm/c are shown for 0−5%, 20−30%, 40−50% and 70−80% centrality classes. In Fig. 5.2, it is observed that the measured values of μ_{out} lie between the lines corresponding to $\Delta\tau = 0$ fm/c and $\Delta\tau = 1$ fm/c, however, it is clear from Fig. 5.10 that the measured values

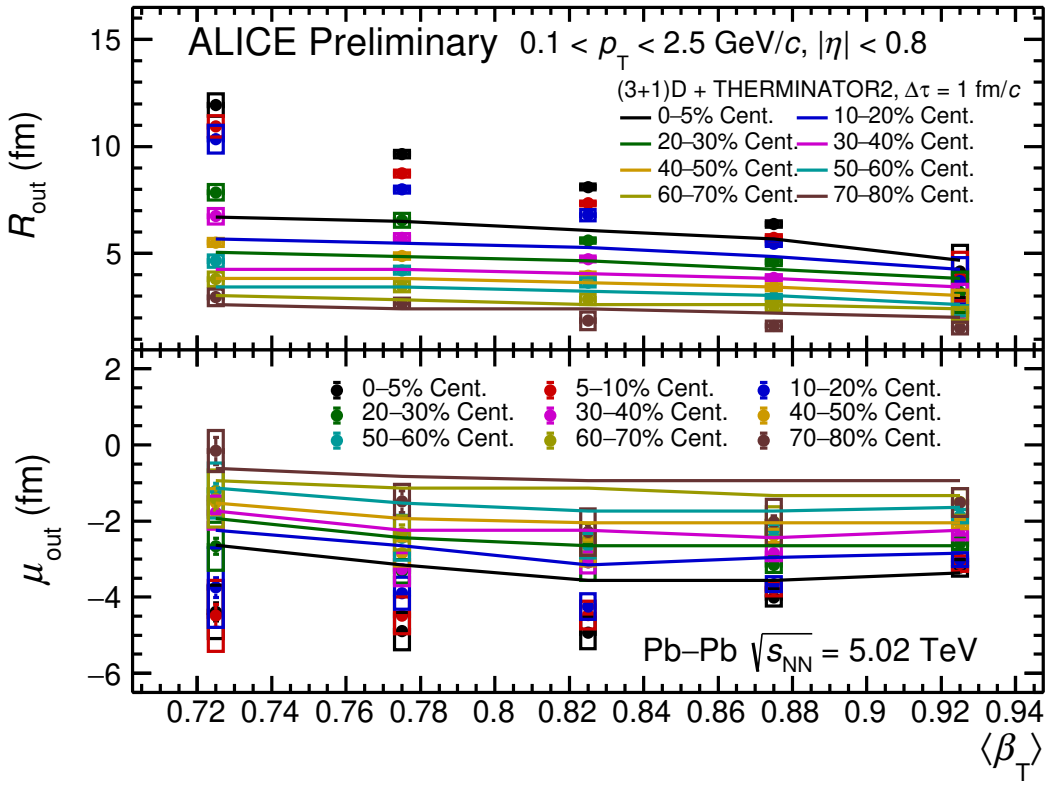

Figure 5.9: The R_{out} (upper plot) and μ_{out} (bottom plot) as the function of β_T in different centrality classes of Pb–Pb collisions at $\sqrt{s_{NN}}$ = 5.02 TeV in ALICE with the predictions from (3 + 1)D viscous hydrodynamics + THERMINATOR 2 with additional delay in kaon-emission time, $\Delta\tau$ = 1 fm/c.

are more close to the predictions with $\Delta\tau$ = 0 fm/c than $\Delta\tau$ = 1 fm/c. The predictions for R_{out} does not vary much with $\Delta\tau$ difference and underestimates the measured values in the high multiplicity events.

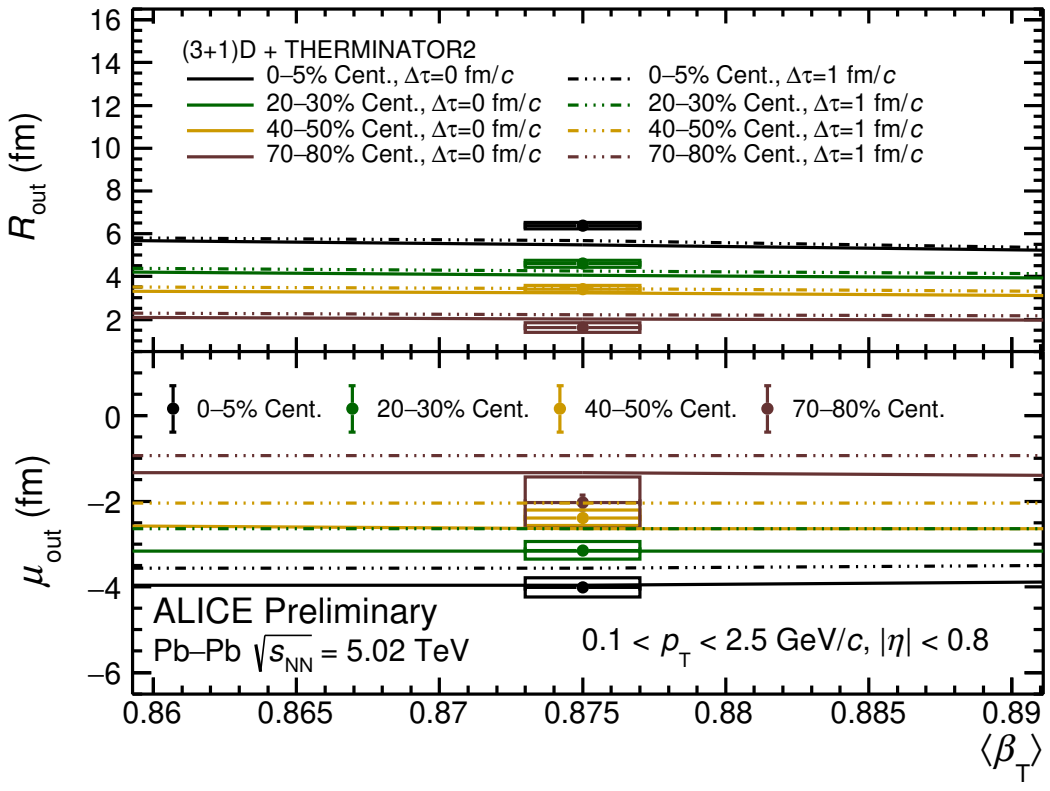

Figure 5.10: The R_{out} (upper plot) and μ_{out} (bottom plot) in the β_T bin: 0.85−0.9 in different centrality classes in Pb–Pb collisions at $\sqrt{s_{NN}}$ = 5.02 TeV in ALICE with the predictions from (3 + 1)D viscous hydrodynamics + THERMINATOR 2 with additional delay in kaon-emission time, $\Delta\tau$ = 0 and $\Delta\tau$=1 fm/s.

Chapter 6

Long-range near-side ridge correlations in high multiplicity p–p collisions

6.1 Introduction

The two-particle azimuthal correlation functions can describe the underlying physics phenomena related to the production of particles in the hadronic and heavy-ion collisions. The structures appearing in the two-dimensional $\Delta\eta - \Delta\phi$ distributions of charged-particle pairs produced in p–p collisions at $\sqrt{s}$ = 13 TeV in CMS experiment (Fig. 6.1), represent various physics mechanisms. An enhanced structure is observed in the region $(\Delta\eta, \Delta\phi) \sim (0, 0)$ [98, 99] which includes the contributions from Bose-Einstein correlations, jet fragmentation, resonance decays etc. A ridge-like structure is observed around $\Delta\phi = \pi$ spanning a longer region in $\Delta\eta$ due to the back-to-back jet correlations. The momentum conservation can also affect the overall shape of the two-particle correlation function. However, a long-range ridge-like structure is observed for the first time in the near side ($\Delta\phi = 0$) of $\Delta\eta - \Delta\phi$ distribution of the charged-particle pairs in the high multiplicity p–p collisions at $\sqrt{s}$ = 7 and 13 TeV in CMS experiment [98, 99] at LHC. This structure was not observed earlier in minimum bias p–p events.

In the heavy-ion collisions at RHIC experiment at BNL [100] and CMS experiment in the LHC at CERN (shown in Fig. 6.2) [101], a similar ridge-like structure was observed in the near-side region of $\Delta\eta - \Delta\phi$ correlations of the charged-particle pairs, extending up to large $\Delta\eta$

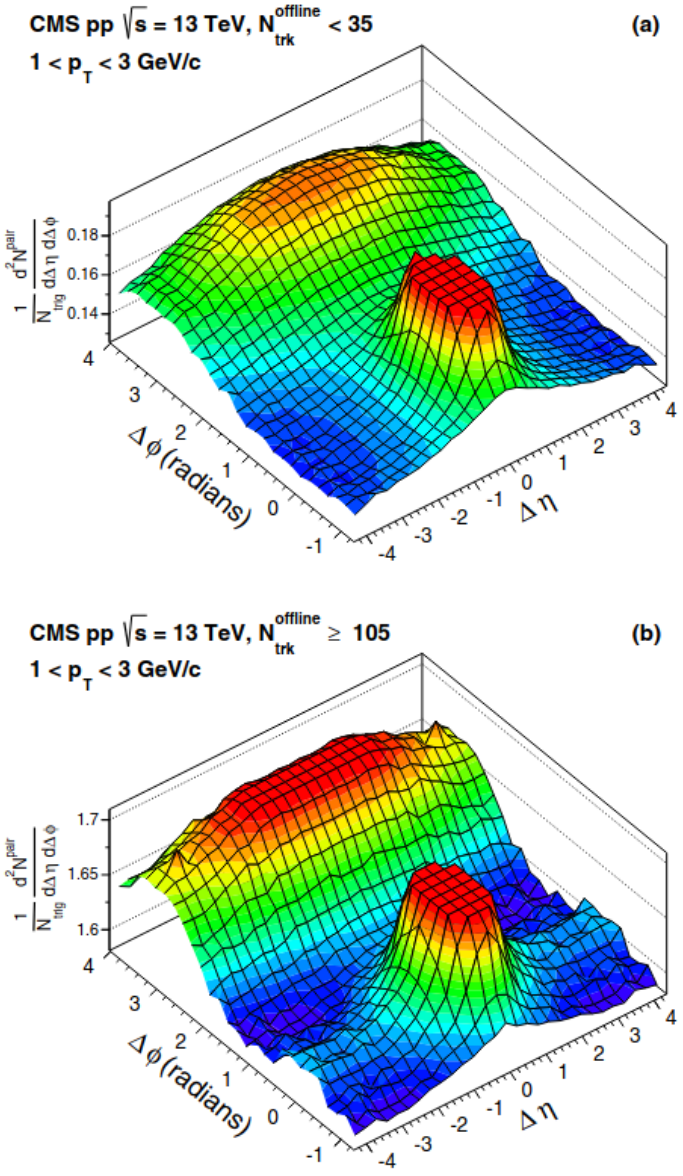

Figure 6.1: The $\Delta\eta - \Delta\phi$ correlation function of charged-hadron pairs within 1.0 $<p_{\mathrm{T}}$(GeV/c) <3.0 in p–p collisions at $\sqrt{s}$ = 13 TeV, measured by CMS experiment for the (a) low-multiplicity events and (b) high-multiplicity events. [99]

regions. The formation of this ridge-like structure was attributed to the presence of strong collectivity in the medium created in the heavy-ion collisions [102]. However, the system produced in p–p collisions is of very small size and short life time, compared to the heavy-ion collisions and hence, no QGP-like effect such as collectivity of the system is expected to be observed. Therefore, the observation of long-range ridge-like structure in the two-particle $\Delta\eta - \Delta\phi$ correlation function in p–p collisions has generated a lot of interest in the high energy community.

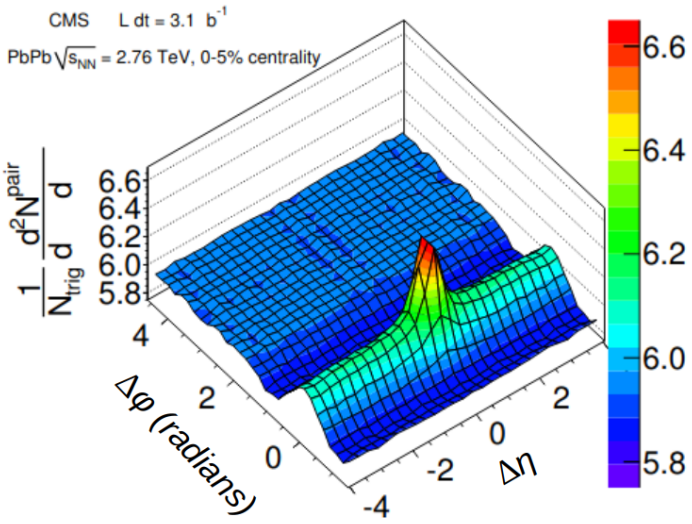

Figure 6.2: The $\Delta\eta - \Delta\phi$ correlation function of charged-hadron pairs in Pb–Pb collisions at $\sqrt{s_{\rm NN}}$ = 2.76 TeV, measured by CMS experiment. [101]

A ridge in the near side of $\Delta\eta - \Delta\phi$ correlation function, spanning over a long region in $\Delta\eta$ has also been observed for the charged particles in the high multiplicity p–Pb collisions at $\sqrt{s_{\rm NN}}$ = 5.02 TeV in CMS [103], as shown in Fig. 6.3. However, its amplitude was five times higher than the one found in p–p events. There are various hypotheses, based on the color glass condensate [104, 105] and onset of hydrodynamic[106] that can describe the formation of ridge in p–p collisions. A study that inspected the emission of correlated clusters in the azimuthal space (the correlated cluster model) established a common framework describing the ridge formation in various collision systems [107, 108]. Besides, the string-percolation process [109, 110] also describes the ridge formation in the near-side region. A qualitative description of the development of long-range ridge in p–p events is obtained from an analysis involving the DIPSY generator [111] which includes the rope hadronisation framework with string shoving mechanism.

This analysis reports the effect of color reconnection and rope-hadronisation mechanism on the two-particle $\Delta\eta - \Delta\phi$ correlation function for charged-hadron pairs in p–p events at $\sqrt{s}$ = 7 and 13 TeV, generated using PYTHIA 8.2 event generator.

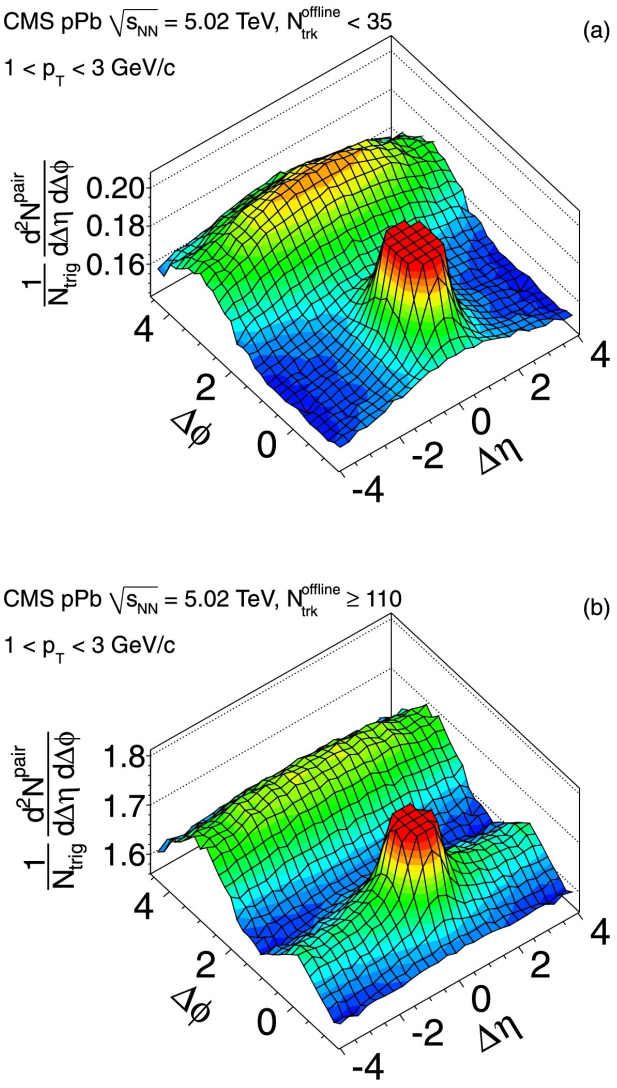

Figure 6.3: The $\Delta\eta - \Delta\phi$ correlation function of charged-hadron pairs within 1.0 $< p_{\mathrm{T}}$(GeV/c) <3.0 in p–Pb collisions at $\sqrt{s_{\mathrm{NN}}}$ = 5.02 TeV in CMS for the (a) low-multiplicity events and (b) high-multiplicity events [103]

6.2 PYTHIA 8.2

PYTHIA 8.2 is a Monte Carlo event generator that simulates the high-energy collisions between elementary particles (e^+e^-, $\mu^+\mu^-$) and hadrons (p–p). It consists of the following physics models: hard scattering of partons, partonic showers, matching and merging methods between hard processes and parton showers, beam remnants, multi-partonic interactions (MPI), hadronisation of final state partons and particle decays. This package is written in C++ using both the theoretical calculations and phenomenological models, developed from the experimental data.

PYTHIA 8.2 has been used substantially to understand the physical processes in LHC energies. More information on PYTHIA 8.2 can be found in [112].

The particle production in high-energy p–p collisions can be broadly visualised as:

- the initial hard scattering of partons,
- the underlying events, corresponding to any phenomenon other than the hard interactions,
- the hadronisation of the final-state partons.

The initial hard scattering of partons can be described by the perturbative QCD processes. Various models are proposed to explain the hadronisation process. The most successful one among them is Lund String Fragmentation, which has been used in PYTHIA 8.2. In this model, two partons are assumed to be bound by a color string and as the separation between these partons increase, the potential energy of the color string increases, which eventually breaks and creates more quark-antiquark pairs. The underlying events (UE) consist of the soft processes, e.g. initial- and final-state partonic showers, soft MPI, beam remnants etc. The perturbative QCD cannot describe the soft interactions of partons. Several phenomenological models are incorporated in PYTHIA 8.2 to explain the UE, however, various parameters, related to these models are needed to be optimised according to the experimental data.

Two very interesting mechanisms during the MPI that can affect the particle production substantially, are color reconnection and rope hadronisation (described below).

6.2.1 Color reconnection

The color-reconnection (CR) mechanism corresponds to the color rearrangement between the partonic strings prior to the stage when strings are hadronised. There are possibilities of the MPI in a single hadron-hadron collision and it is enhanced in the high multiplicity events. In this mechanism, the resultant string with the smallest total length is chosen as the final one [113, 114]. Different processes reassign the color flow in the beam remnant of the p–p event, which corresponds to various modes of CR mechanism. The three CR modes are following:

CR0 (based on MPI)

In this mode, the partons that belong to the MPI systems having lower p_{T} are fused with the ones from higher p_{T} systems ensuring the total length of the string is minimised.

CR1 (based on QCD)

Along with the string-length minimisation, this mode is based on the QCD color rules and considers the whole QCD multiplets scenario. It can also generate the structures with three color indices, known as junctions, which eventually causes enhancement in baryon number.

CR2 (based on gluon-move scheme)

This model chooses only gluons for the rearrangement with all the MPI systems to ensure the minimisation of total string length. In this model, there is no constraint on the p_{T} of the MPI systems while choosing the gluons from them for reconnections, unlike CR0 and CR1. This may influence the color flow from the hard interaction compared to CR0 mode.

6.2.2 Rope hadronisation (RH)

When the color strings produced in the high multiplicity events overlap with each other, they make a color rope, which eventually hadronises with relatively higher string tension [115, 116]. The higher energy density of the overlapping zone produces a dynamic pressure gradient which forces the strings to move outward with higher p_{T}. The excess energy and pressure gradient are slowly reduced as the strings move outward and rest of the strings are associated with less p_{T} and eventually, there will be no overlap. Thus, the strings grab more boost in the transverse direction by shoving each other and hence, the mean p_{T} of the heavier hadrons are enhanced. This mechanism mimics the collectivity, which is observed in heavy-ion collisions.

6.3 Analysis method

The correlation functions of the charged-particle pairs are represented as the function of $\Delta\eta$ and $\Delta\phi$. The events are catagorised into various multiplicity classes, each multiplicity class corresponds to the number of charged particles having $p_{\mathrm{T}} > 0.4$ GeV/c in the pseudorapidity range of $|\eta| < 2.4$. The trigger particles in a multiplicity class are chosen within a given p_{T} range and each trigger particle is combined with the rest of the charge particles ("associated particles") to form pairs in the given p_{T} range.

If η_1, ϕ_1 and η_2, ϕ_2 are the pseudorapidity and azimuthal angles of particle 1 and 2, respectively, then the yield of particle-pair per trigger particle from the same event ("signal") can be represented using Eq. (6.1).

$$S(\Delta\eta, \Delta\phi) = \frac{1}{N_{\mathrm{trig}}} \frac{d^2N^{\mathrm{same}}}{d\Delta\eta d\Delta\phi} \tag{6.1}$$

where, $\Delta\eta = \eta_1 - \eta_2$ and $\Delta\phi = \phi_1 - \phi_2$. The distribution of pairs from mixed events ("background") is formed by taking the trigger and associated particles from the mixed events as shown in Eq. (6.2).

$$B(\Delta\eta, \Delta\phi) = \frac{1}{N_{\mathrm{trig}}} \frac{d^2N^{\mathrm{mix}}}{d\Delta\eta d\Delta\phi}. \tag{6.2}$$

Using $S(\Delta\eta, \Delta\phi)$ and $B(\Delta\eta, \Delta\phi)$, the corrected associated yield, averaged over the number of events and trigger particle are calculated using Eq. (6.3).

$$\frac{1}{N_{\mathrm{trig}}} \frac{d^2N^{\mathrm{pair}}}{d\Delta\eta d\Delta\phi} = B(0,0) \frac{S(\Delta\eta, \Delta\phi)}{B(\Delta\eta, \Delta\phi)}. \tag{6.3}$$

In this study, a total of 100 and 80 million p–p events at $\sqrt{s} = 7$ TeV and 13 TeV, respectively, are simulated using PYTHIA 8.2 with the Monash 2013 tune [117]. The two-dimensional $\Delta\eta - \Delta\phi$ correlation functions of the charged-hadron pairs are constructed by selecting particles within p_{T} ranges 1-3 GeV/c and 0.5-3 GeV/c and three multiplicity classes: $0 < N < 20$, $80 < N < 100$ and $N > 100$, where N corresponds to the number of charged hadrons selected from the pseudorapidity range of $|\eta| < 0.5$. The three modes of color reconnection scheme i.e. CR0, CR1 and CR2 along with (and without) the rope-formation mechanism are studied to observe their effects on the two-particle correlations.

6.4 Two-dimensional $\Delta\eta - \Delta\phi$ correlation function

The two-dimensional $\Delta\eta - \Delta\phi$ correlation functions for the charged-hadron pairs, generated in two different multiplicity classes of p–p collisions at $\sqrt{s}$ = 7 TeV and 13 TeV are illustrated in Fig. 6.4 and Fig. 6.5, respectively. In both the figures, the combined effect of CR2 mode with RH=on and RH=off on the correlation functions are shown for multiplicity classes $0 < N < 20$ and $N > 100$. In both the low and high multiplicity classes, a peak in the region near $(\Delta\eta, \Delta\phi) = (0, 0)$, i.e. the near side is observed due to (mostly) the jet fragmentation. A structure similar to a ridge is observed in the away-side region ($\Delta\phi = \pi$) which covers a long $\Delta\eta$ region. This can be attributed to the correlations of back-to-back jets. Interestingly, a long-range ridge-like structure is observed in the near side of the correlation function for the events with multiplicity $N > 100$ and RH=on. This ridge-like structure covers both sides of the $\Delta\eta$ by almost three units and is not observed in the events with multiplicity $0 < N < 20$. Moreover, when rope formation is not taken into account, this ridge does not appear in the high multiplicity class. The near-side ridge is qualitatively alike with the ridge, observed in the $\Delta\eta - \Delta\phi$ correlations produced in the high multiplicity p–p collisions.

6.5 One-dimensional $\Delta\phi$ projection of the correlation function

To investigate the correlation functions in more details, the two-dimensional $\Delta\eta - \Delta\phi$ distributions are projected into one-dimensional distributions of $\Delta\phi$ in two different $\Delta\eta$ ranges: $|\Delta\eta|>$ 2.0 (long range) and $|\Delta\eta| <$1.0 (short range). To calculate the associated yield in both the short-range and long-range region for both energies, a standard zero-yield-at-minimum (ZYAM) method is used, where the one-dimensional $\Delta\phi$ distribution is fitted with a polynomial of second order within the range: $0.1 <|\Delta\phi| <2$ as shown in Fig. 6.6.

The minimum value of the fit function, C_{ZYAM} [119], is estimated which corresponds to the constant pedestal present in the $\Delta\phi$ distribution. By subtracting the pedestal from $\Delta\phi$ distribution, the minimum of the distribution is moved down to zero. The pedestal-subtracted correlated

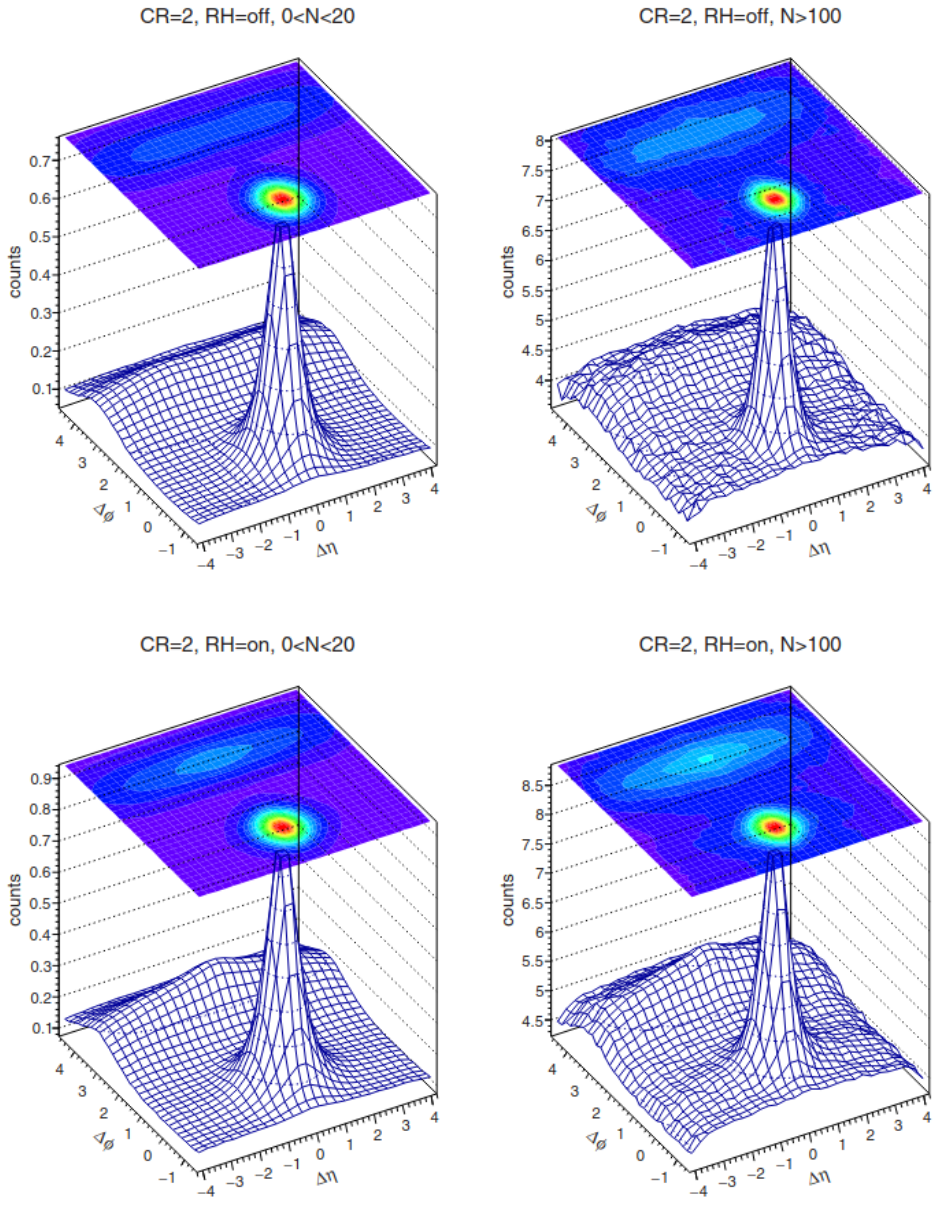

Figure 6.4: The $\Delta\eta - \Delta\phi$ correlation function for the charged-hadron pairs in p–p collisions at $\sqrt{s}$ = 7 TeV for the low and high multiplicity classes with CR2, RH=off (upper panels) and CR2, RH=on (bottom panels) configurations with 1.0 <$p_{\mathrm{T}}(Asso)$, $p_{\mathrm{T}}^{\mathrm{Trigg}}$(GeV/c) <3.0. [118]

$\Delta\phi$ distributions for multiplicity classes $0 < N < 20$, $80 < N < 100$ and $N > 100$ with the color reconnection schemes, CR1, CR2 and CR3 along with (and without) rope hadronisation are illustrated in Fig. 6.7 and Fig. 6.8 for p–p events at $\sqrt{s}$ = 7 TeV and 13 TeV, respectively. The upper panels of Fig. 6.7 and Fig. 6.8 correspond to the $\Delta\phi$ distributions in the long-range region. The broad peaks observed in the away side for the three multiplicity classes relate to the correlations of back-to-back jets. Moreover, an associated-yield peak is also observed for the

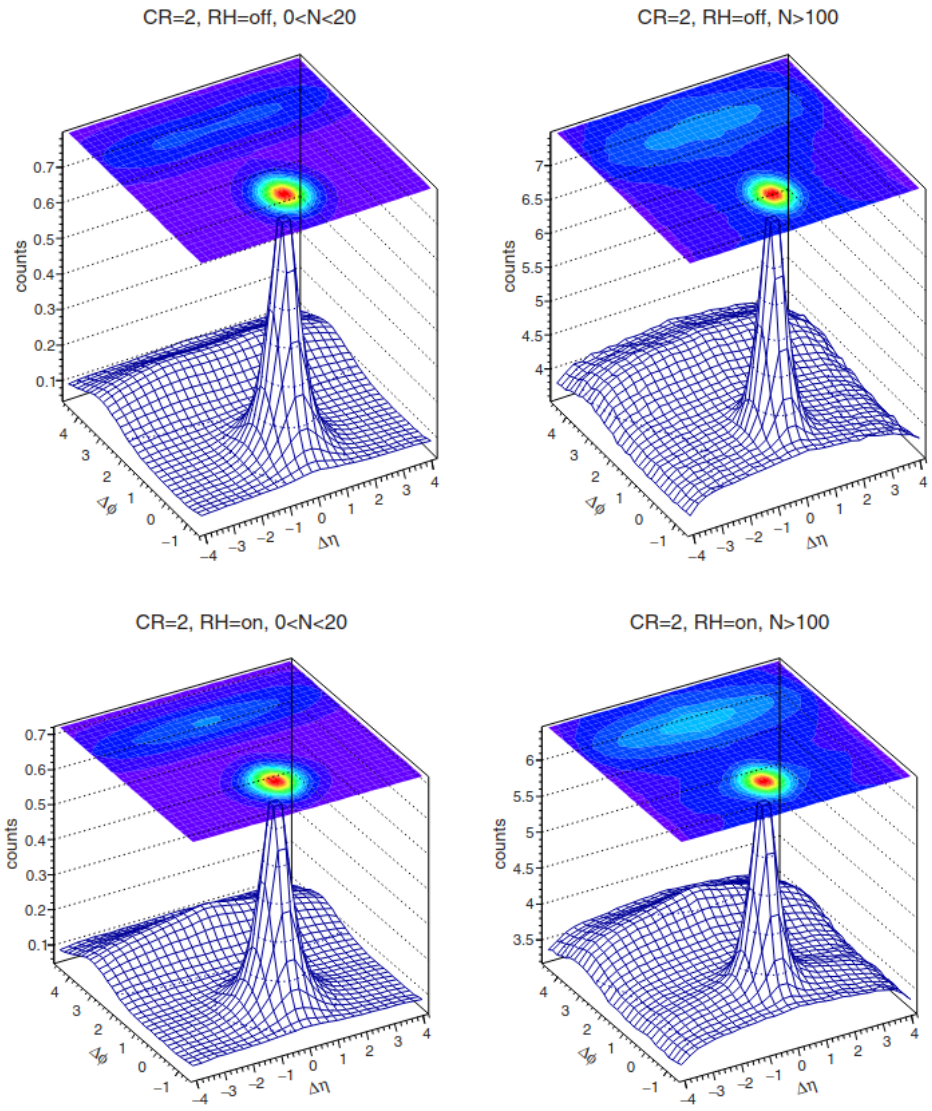

Figure 6.5: The $\Delta\eta - \Delta\phi$ correlation function for the charged-hadron pairs in p–p collisions at $\sqrt{s}$ = 13 TeV for the low and high multiplicity classes with CR2, RH=off (upper panels) and CR2, RH=on (bottom panels) configurations with 1.0 <$p_{\mathrm{T}}(Asso)$, $p_{\mathrm{T}}^{\mathrm{Trigg}}$(GeV/c) <3.0 [118] [118]

high multiplicity classes in the near-side region when the rope formation is considered. This indicates that the color reconnections in partonic level along with the overlapping of strings that leads to the rope-formation and eventual string-shoving and hadronization can produce a ridge in the near-side in the high multiplicity p–p events.

In the short-range region (the bottom panels of Fig. 6.7) and Fig. 6.8), the peaks are observed at the near side due to the jet correlations, while the ridge-like structures appear at the

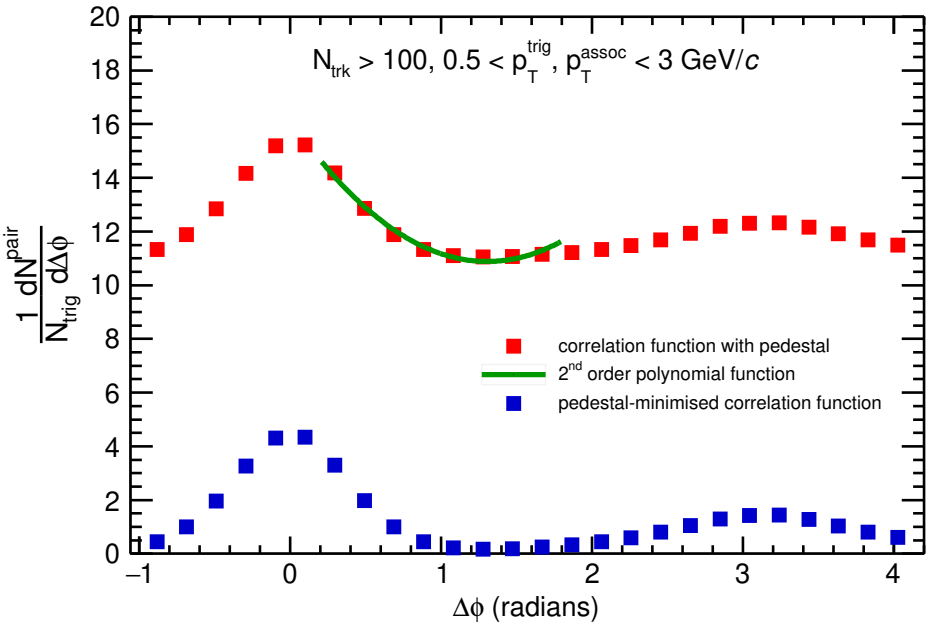

Figure 6.6: The $\Delta\phi$ projection of correlation function for the charged-hadron pairs before and after minimising the pedestals using the ZYAM technique in p–p collisions at $\sqrt{s}$ = 13 TeV for $N > 100$.

away side due to the momentum conservation and back-to-back jet correlations. It is observed that the strength of correlation function with CR0 configuration is lower compared to CR1 and CR2. The reason behind it might be the additional reconnections in CR1 and CR2 due to the junction formation and shifting of gluons as a result of the string-length minimisation. The magnitudes of both the away-side and near-side peaks are observed to be dependent on the beam energy.

Hence, the study indicates that a ridge-like structure might appear in the near-side region of two-particle $\Delta\eta - \Delta\phi$ correlation function of charged hadrons in the high multiplicity p–p events because of the microscopic processes of color reconnection along with the rope hadronisation. The interplay of these two processes can imitate the features of collectivity without considering the production of a hot-dense thermalized medium.

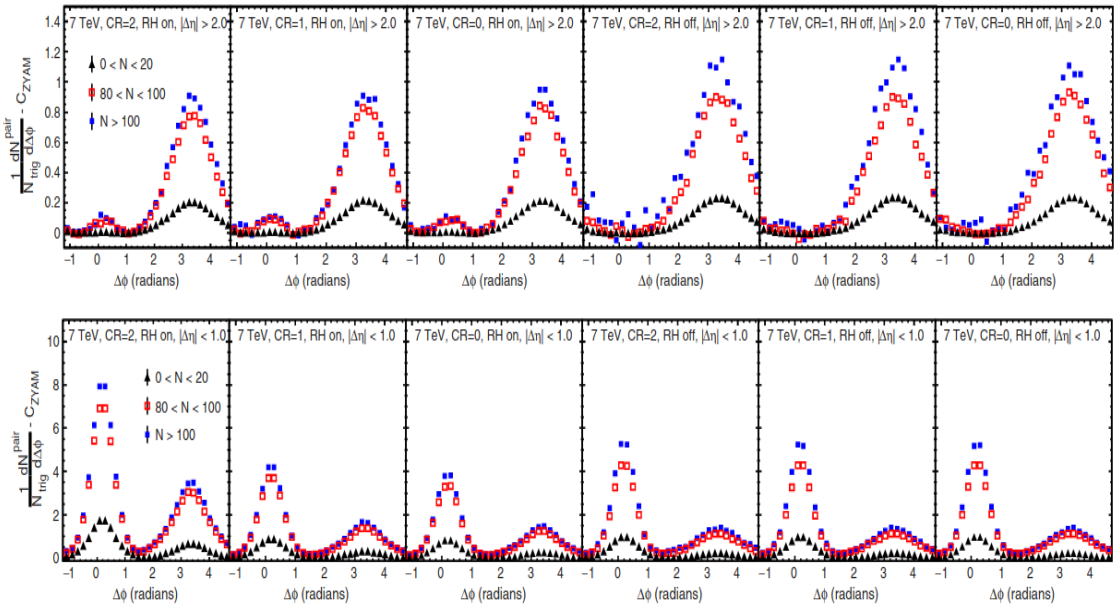

Figure 6.7: The $\Delta\phi$ projection of correlation function for the charged-hadron pairs in the long (upper panels) and short range (bottom panels) for three multiplicity classes in p–p collisions at $\sqrt{s}$ = 7 TeV. [118]

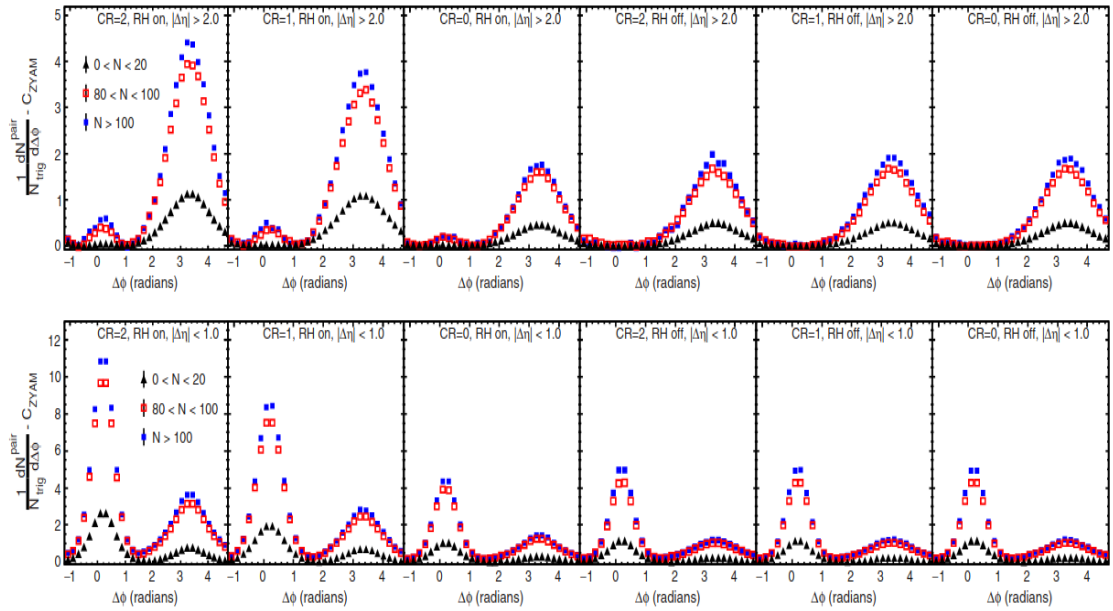

Figure 6.8: The $\Delta\phi$ projection of correlation function for the charged-hadron pairs in the long (upper panels) and short range (bottom panels) for three multiplicity classes in p–p collisions at $\sqrt{s}$ = 13 TeV. [118]

Chapter 7

Summary and outlook

In this thesis, the femtoscopic analysis of charged pion-kaon pairs, produced in Pb–Pb collisions at $\sqrt{s_{\mathrm{NN}}}$ = 5.02 TeV was discussed. The measurement was done with the help of ALICE detector at LHC. The dimensions, or more specifically, the region of homogeneity of the particle emitting source created in heavy-ion collisions as well as the emission asymmetry between the pion and kaon in a pair were estimated using the spherical harmonic representation of the pion-kaon correlation functions. The analysis was carried out in 0−5%, 5−10%, 10−20%, 20−30%, 30−40%, 40−50%, 50−60%, 60−70% and 70−80% centrality classes. The charged pions and kaons were identified using the TPC and TOF detectors.

The centrality dependence of the femtoscopic parameters was studied and it was observed that the size of the particle emitting source increased with the multiplicity as the number of participants increased. The pair-emission asymmetry was always negative, implying that pions were always emitted closer to the center of the source than kaons. The magnitude of the pair-emission asymmetry also decreased with decreasing multiplicity as the size of system decreased. By comparing the results with the predictions from THERMINATOR 2 model, it was found that the hadronic rescattering phase might be present in the system along with the collective flow. Moreover, no beam-energy dependence of the femtoscopic parameters was found upon comparing the results with previously performed pion-kaon femtoscopic analysis in Pb–Pb events at $\sqrt{s_{\mathrm{NN}}}$ = 2.76 TeV.

The results from the pair-transverse momentum (k_{T})-dependent femtoscopic analysis showed that the source size decreased with increasing k_{T} because the high-k_{T} pairs are formed mostly with the particles with high pair-transverse momentum (p_{T}) that are emitted in the vicinity of each other. The pair-emission asymmetry decreased in the higher k_{T} region as the contribution from collectivity surpassed the random thermal velocities.

This thesis also reported the first ever measurement of the pion-kaon femtoscopic parameters as a function of pair-transverse velocity (β_{T}). This measurement directly probed the femtoscopic parameters with the collectivity of the system. The source size decreased with increasing β_{T} of the pair, suggesting that the region of homogeneity decreases with increasing p_{T} of the particles, as discussed in the previous paragraph. The predictions from (3 + 1)D + THERMINATOR 2 model calculations with different values of additional kaon-emission delay underestimated the source size in the higher multiplicity events but agreed with the same in the lower multiplicity events. The magnitude of pair-emission asymmetry decreased with increasing β_{T} in the higher multiplicity events as the contribution from collectivity surpassed the random thermal velocities. However, in the lower multiplicity classes, its magnitude increased up to certain value of $<\beta_{\mathrm{T}}>$ and then gradually decreased. The predictions from model calculations showed similar trend with the results. However, it underestimated the measured values of pair-emission asymmetry in the lower β_{T} region. This observation might open up the scope to check for the resonance contribution in the lower β_{T} region in THERMINATOR 2 model calculations. The values of pair-emission asymmetry were more closer to the predictions with no additional delay in kaon emission, compared to an additional delay of 1 fm/c.

This thesis also included the study of two-dimensional $\Delta\eta-\Delta\phi$ correlations of the charged-particle pairs in p–p collisions at $\sqrt{s}$ = 7 and 13 TeV using PYTHIA 8.2 Monte Carlo event generator with color reconnection and rope hadronisation mechanisms. The analysis was performed in three multiplicity classes. It was observed that a ridge-like structure appeared in the near side of the $\Delta\eta - \Delta\phi$ correlation function for the high multiplicity events, when both the color reconnection and rope hadronisation were considered. In case of heavy-ion collisions, the observation of ridge was attributed to the presence of collectivity in the system. However,

the possibility of forming a system with finite size in p–p collisions is highly unlikely. Hence, the observation of ridge in the high multiplicity p–p events suggests that the color reconnection along with the rope hadronisation mechanism can mimic the collectivity without considering the formation of a thermalised medium.

7.1 Future outlook

The pion-kaon source size is the convolution of the sizes of pion and kaon systems as given by Eq. 7.1.

$$R_{\rm out}^{\pi K} = \sqrt{(R_{\rm out}^{\pi})^2 + (R_{\rm out}^{K})^2}. \tag{7.1}$$

It will be interesting to compute the pion-kaon source size from the individually measured source sizes of pion and kaon systems in Pb–Pb collisions at $\sqrt{s_{\rm NN}}$ = 5.02 TeV and compare them with the measured pion-kaon source size in the respective $k_{\rm T}$ range. Conversely, the individual sizes of pion, kaon and proton systems can be estimated from the source radii measured in pion-kaon, pion-proton and kaon-proton femtoscopy as given in Eq. 7.2-7.4 [60].

$$R_{\rm out}^{\pi} = \sqrt{((R_{\rm out}^{\pi K})^2 + (R_{\rm out}^{\pi p})^2 - (R_{\rm out}^{K p})^2)/2}, \tag{7.2}$$

$$R_{\rm out}^{K} = \sqrt{((R_{\rm out}^{\pi K})^2 + (R_{\rm out}^{K p})^2 - (R_{\rm out}^{\pi p})^2)/2}, \tag{7.3}$$

$$R_{\rm out}^{p} = \sqrt{((R_{\rm out}^{\pi p})^2 + (R_{\rm out}^{K p})^2 - (R_{\rm out}^{\pi K})^2)/2}. \tag{7.4}$$

Similarly, the emission asymmetry between kaon-proton and pion-proton pairs can also be measured from femtoscopic analysis of the respective pairs and verify Eq. 7.5.

$$\mu_{\rm out}^{\pi p} = (\mu_{\rm out}^{\pi K}) + (\mu_{\rm out}^{K p}). \tag{7.5}$$

Moreover, it will also be interesting to analyse the femtoscopic correlations of charged pairs in the high multiplicity p–p collisions as the multi-partonic interactions can mimic the features of collectivity.

Appendix A

Barlow test

In Fig. A.1-A.4, the Δ/σ as a function of k^* are shown for the variations in $z_{\rm vtx}$, DCA and η for four charged-pair combinations. The Δ/σ for the DCA variations are shown in 1^{st} and 2^{nd} column, the η variations are shown in 3^{rd} and 4^{th} column and the $z_{\rm vtx}$ variations are shown in 5^{th} and 6^{th} column. The variations in Δ/σ in different centralities are shown in the rows. The values of Δ/σ for C_0^0 and ReC_1^1 for DCA and η variations are showing a distinct trend and going beyond/on the border of statistical limit. Hence, they contribute to the systematic uncertainties of the correlation functions. In case of $z_{\rm vtx}$, the values are randomly scattered. Hence, it does not contribute to the systematic uncertainties.

In Fig. A.5-A.8, the Barlow plots are shown for the variations in minimum number of TPC clusters (TPC ncls) (1^{st} and 2^{nd} column), $\Delta\eta_{max}$ (3^{rd} and 4^{th} column), number of events for mixing (5^{th} column) and magnetic polarity (6^{th} column). In case of the variations in TPC ncls and magnetic polarity, the values of Δ/σ are observed to go beyond the statistical uncertainties and the trend is very distinct. Hence, they contribute to the systematic uncertainties. The Δ/σ for variations in the $\Delta\eta_{max}$ and number of events for mixing are randomly scattered. Hence, they do not contribute to the systematic uncertainties.

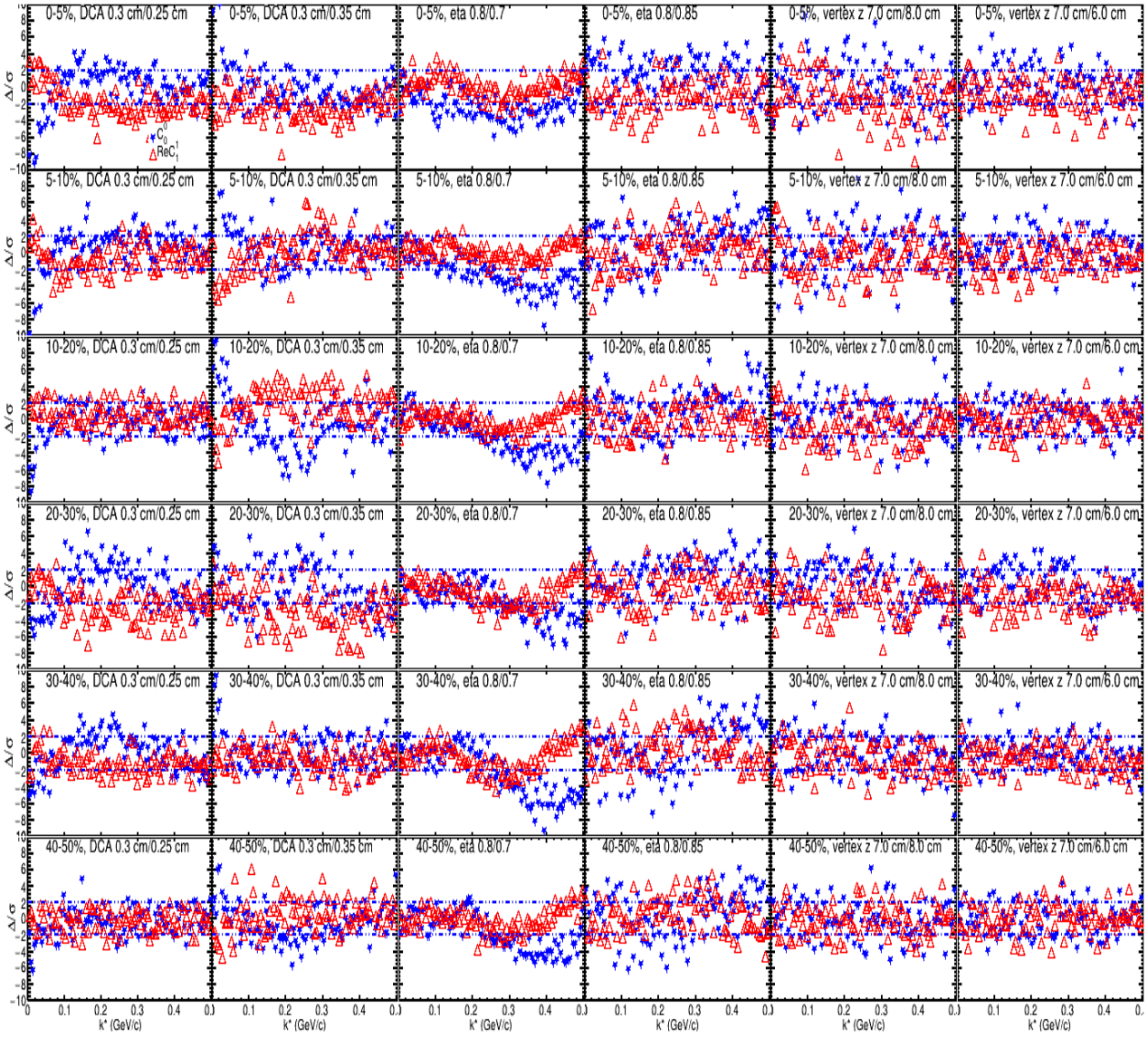

Figure A.1: The Δ/σ as a function of k^* for π^+K^+, 1^{st} column: DCA 0.3 cm and 0.25 cm, 2^{nd} column: DCA 0.3 cm and 0.35 cm, 3^{rd} column: η 0.8 and 0.9, 4^{th} column: η 0.8 and 0.7, 5^{th} column: z_{vtx} 7.0 cm and 8.0 cm, 6^{th} column: z_{vtx} 7.0 cm and 6.0 cm for Pb−Pb collisions at $\sqrt{s_{\mathrm{NN}}}$ = 5.02 TeV in ALICE.

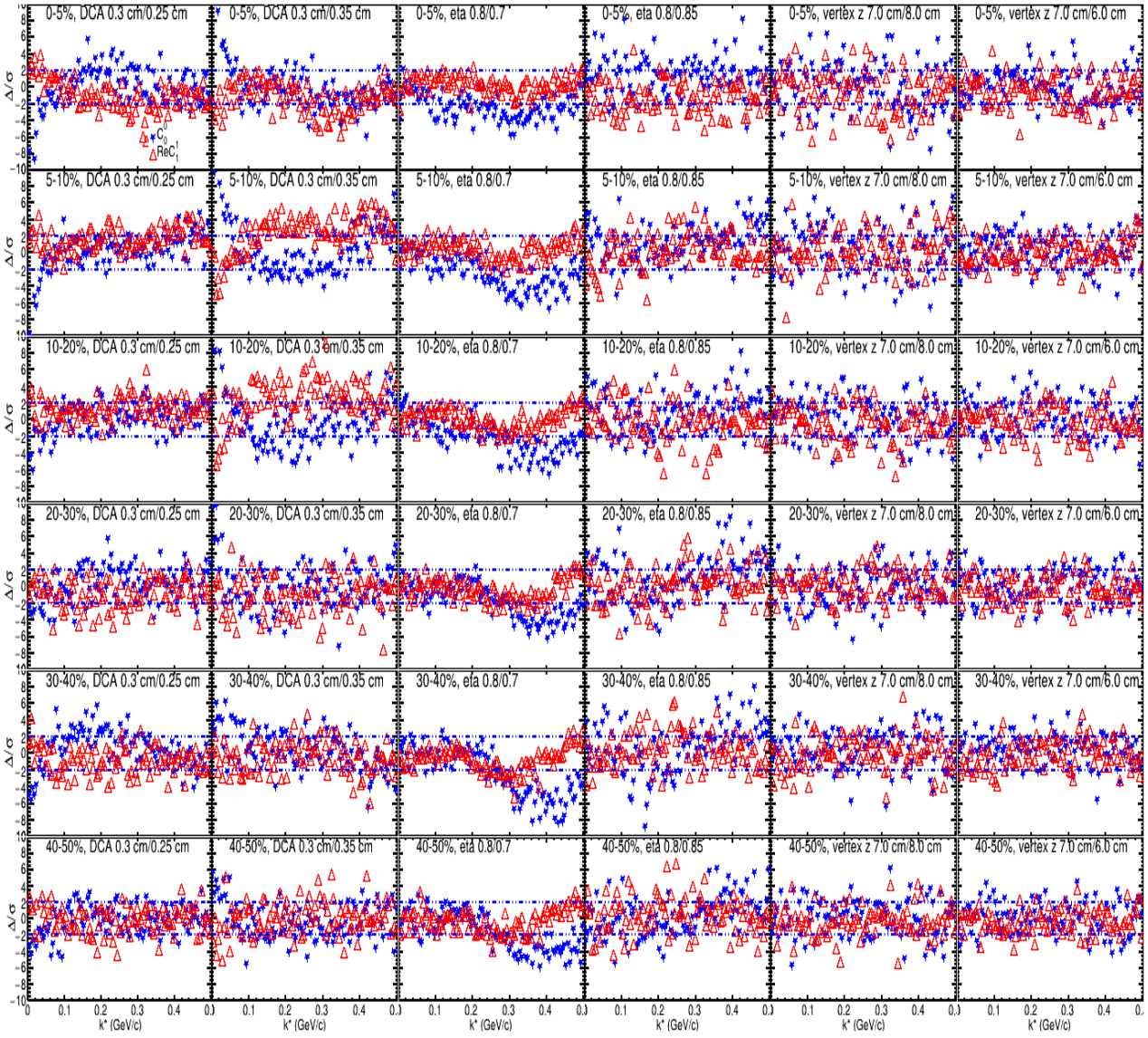

Figure A.2: The Δ/σ as a function of k^* for $\pi^- K^-$, 1^{st} column: DCA 0.3 cm and 0.25 cm, 2^{nd} column: DCA 0.3 cm and 0.35 cm, 3^{rd} column: η 0.8 and 0.9, 4^{th} column: η 0.8 and 0.7, 5^{th} column: z_{vtx} 7.0 cm and 8.0 cm, 6^{th} column: z_{vtx} 7.0 cm and 6.0 cm for Pb−Pb collisions at $\sqrt{s_{\mathrm{NN}}}$ = 5.02 TeV in ALICE.

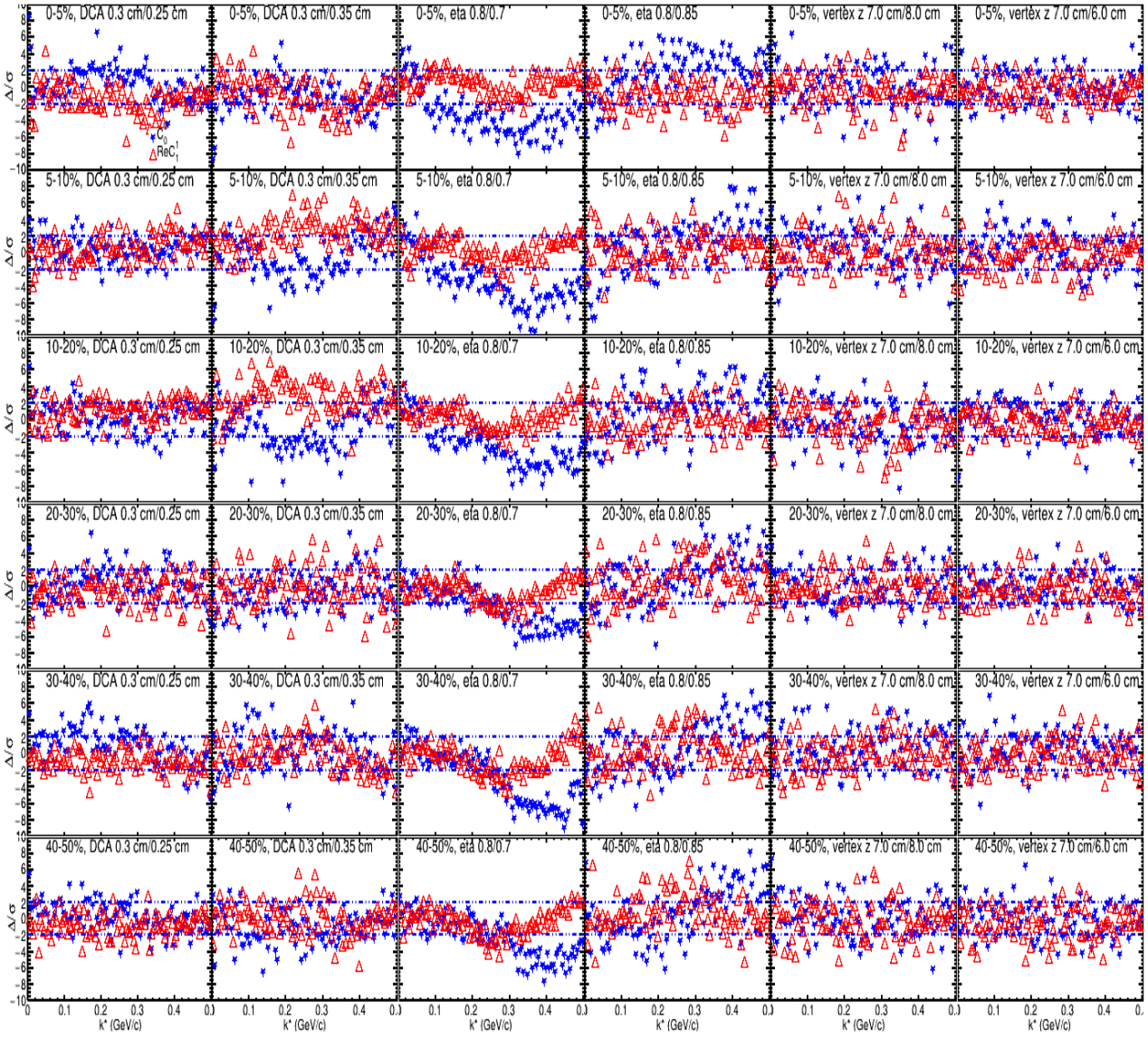

Figure A.3: The Δ/σ as a function of k^* for π^+K^-, 1^{st} column: DCA 0.3 cm and 0.25 cm, 2^{nd} column: DCA 0.3 cm and 0.35 cm, 3^{rd} column: η 0.8 and 0.9, 4^{th} column: η 0.8 and 0.7, 5^{th} column: z_{vtx} 7.0 cm and 8.0 cm, 6^{th} column: z_{vtx} 7.0 cm and 6.0 cm for Pb−Pb collisions at $\sqrt{s_{\mathrm{NN}}}$ = 5.02 TeV in ALICE.

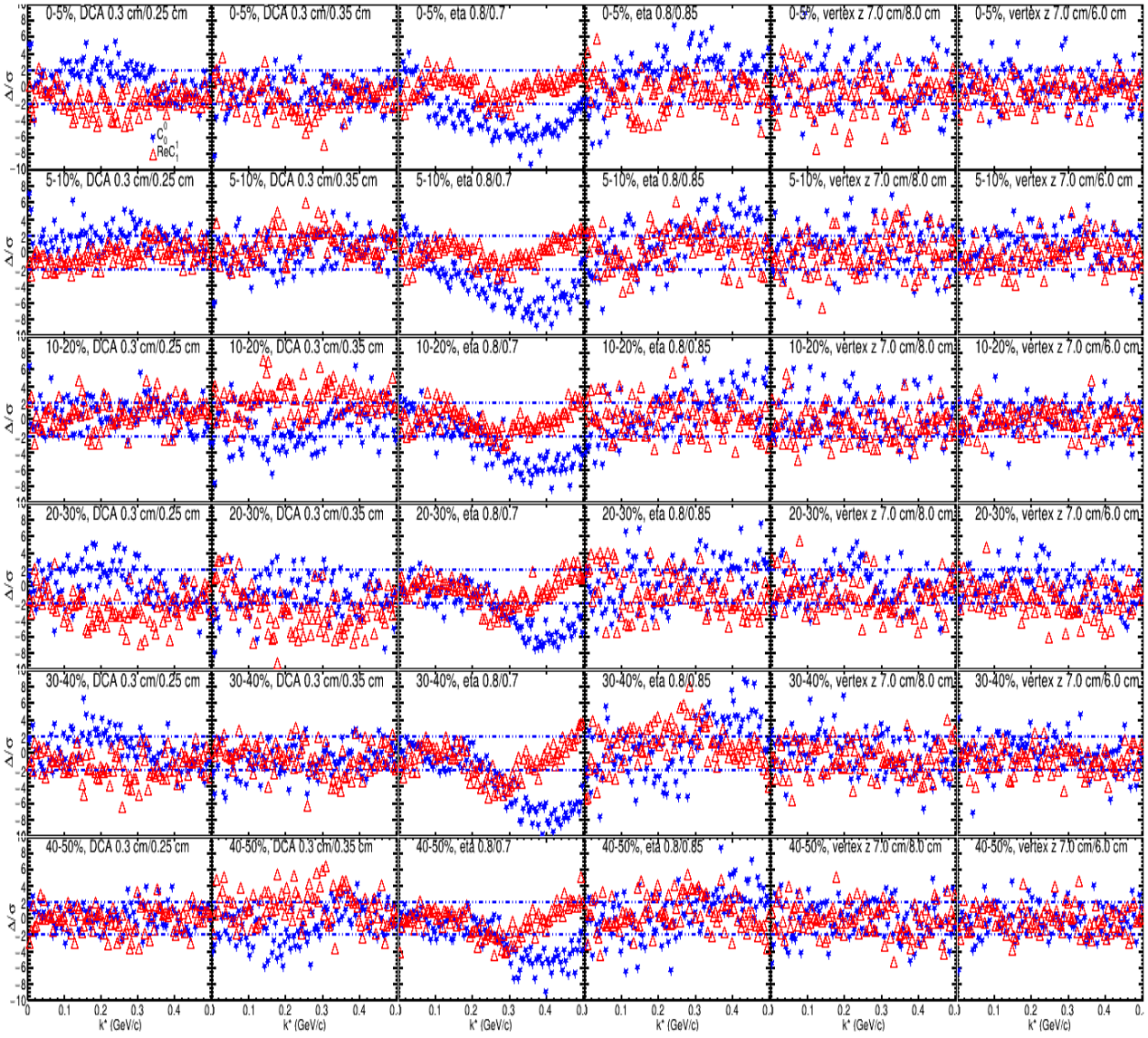

Figure A.4: The Δ/σ as a function of k^* for $\pi^- K^+$, 1^{st} column: DCA 0.3 cm and 0.25 cm, 2^{nd} column: DCA 0.3 cm and 0.35 cm, 3^{rd} column: η 0.8 and 0.9, 4^{th} column: η 0.8 and 0.7, 5^{th} column: z_{vtx} 7.0 cm and 8.0 cm, 6^{th} column: z_{vtx} 7.0 cm and 6.0 cm for Pb−Pb collisions at $\sqrt{s_{\mathrm{NN}}}$ = 5.02 TeV in ALICE.

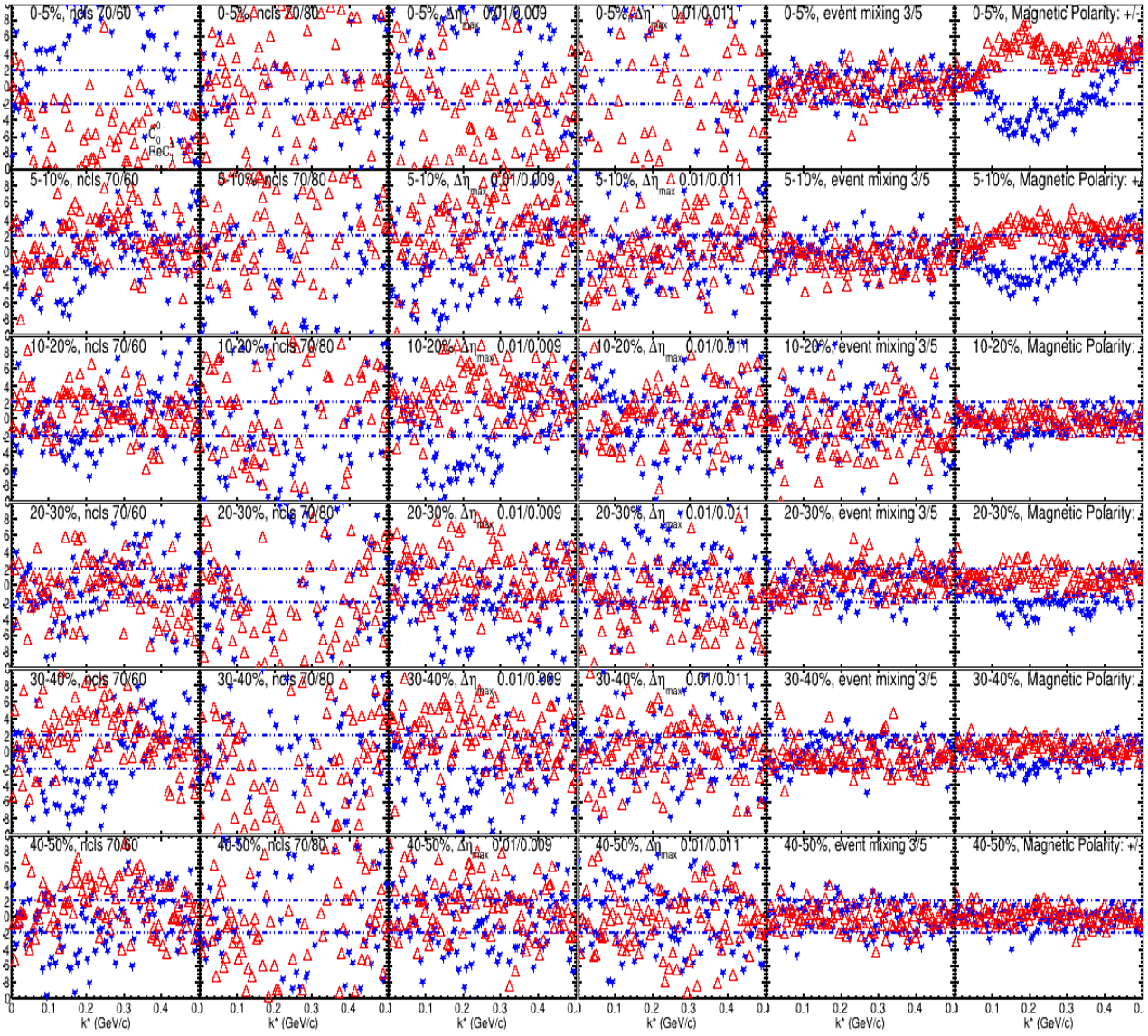

Figure A.5: The Δ/σ as a function of k^* for π^+K^+, 1^{st} column: TPC ncls 70 and 50, 2^{nd} column: TPC ncls 70 and 80, 3^{rd} column: $\Delta\eta_{max}$ 0.01 and 0.009, 4^{th} column: $\Delta\eta_{max}$ 0.01 and 0.011, 5^{th} column: no. of events for mixing 3 and 5, 6^{th} column: polarity of magnetic field ++ and −− for Pb−Pb collisions at $\sqrt{s_{\rm NN}}$ = 5.02 TeV in ALICE.

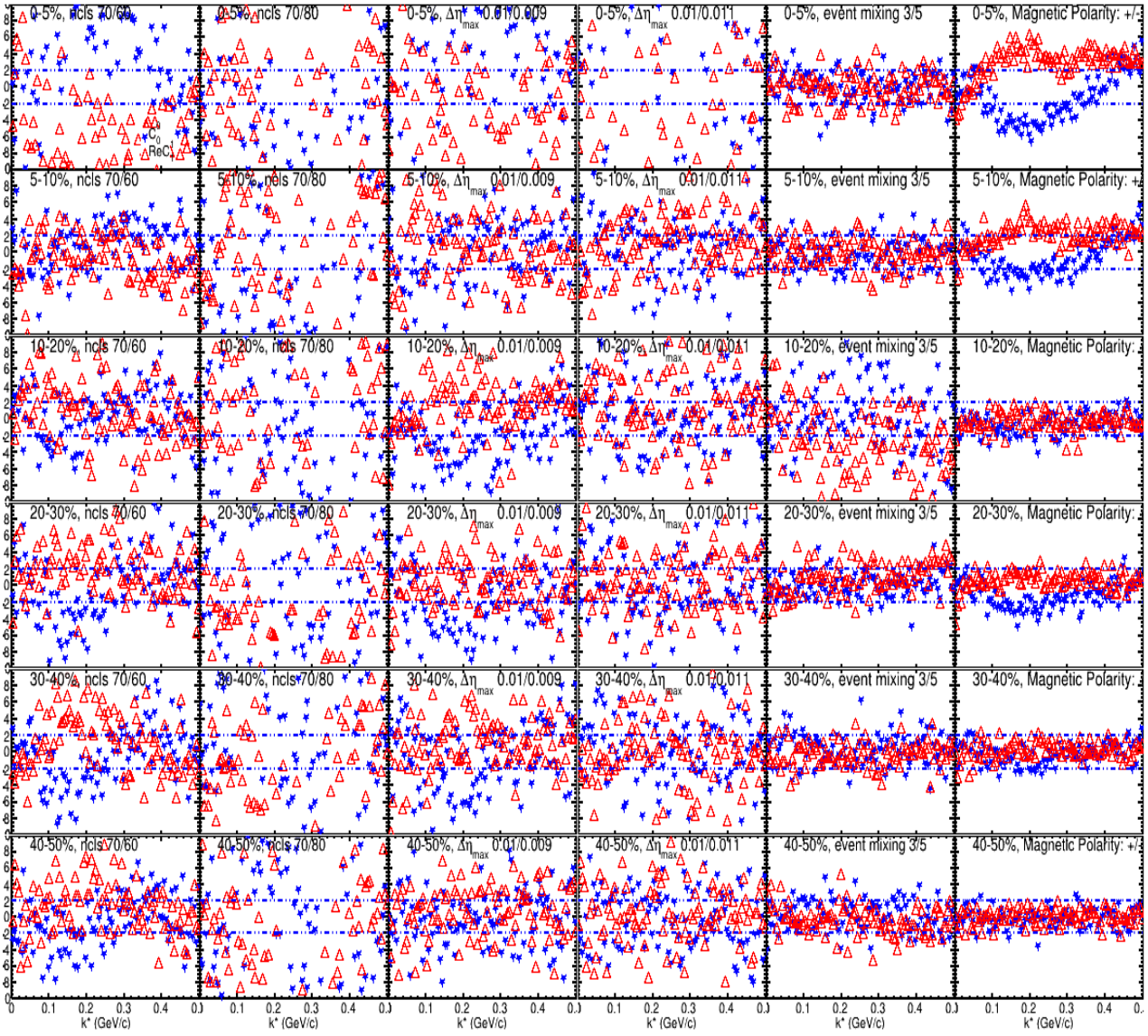

Figure A.6: The Δ/σ as a function of k^* for $\pi^- K^-$, 1^{st} column: TPC ncls 70 and 50, 2^{nd} column: TPC ncls 70 and 80, 3^{rd} column: $\Delta\eta_{max}$ 0.01 and 0.009, 4^{th} column: $\Delta\eta_{max}$ 0.01 and 0.011, 5^{th} column: no. of events for mixing 3 and 5, 6^{th} column: polarity of magnetic field ++ and −− for Pb−Pb collisions at $\sqrt{s_{\rm NN}}$ = 5.02 TeV in ALICE.

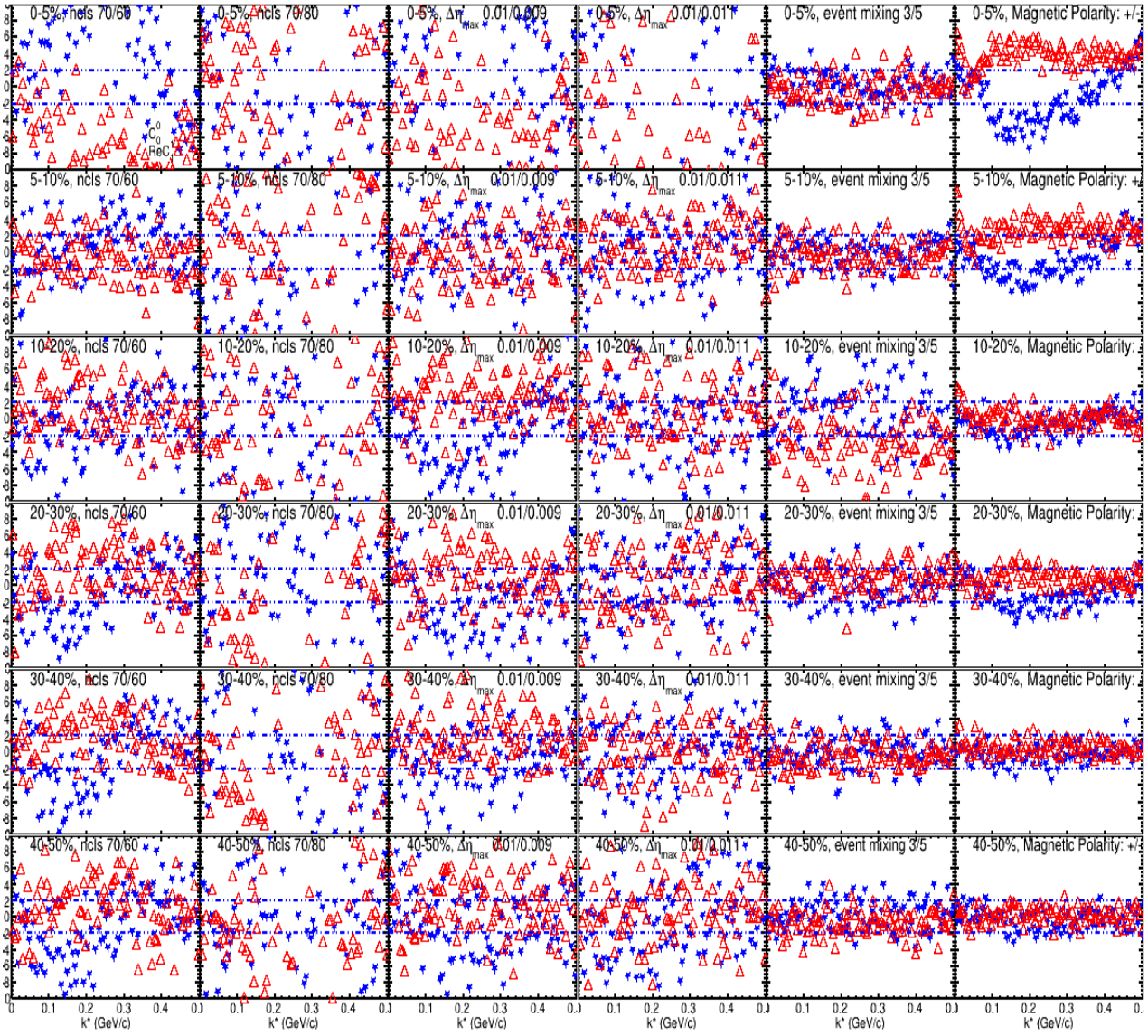

Figure A.7: The Δ/σ as a function of k^* for π^+K^-, 1^{st} column: TPC ncls 70 and 50, 2^{nd} column: TPC ncls 70 and 80, 3^{rd} column: $\Delta\eta_{max}$ 0.01 and 0.009, 4^{th} column: $\Delta\eta_{max}$ 0.01 and 0.011, 5^{th} column: no. of events for mixing 3 and 5, 6^{th} column: polarity of magnetic field ++ and −− for Pb−Pb collisions at $\sqrt{s_{\rm NN}}$ = 5.02 TeV in ALICE.

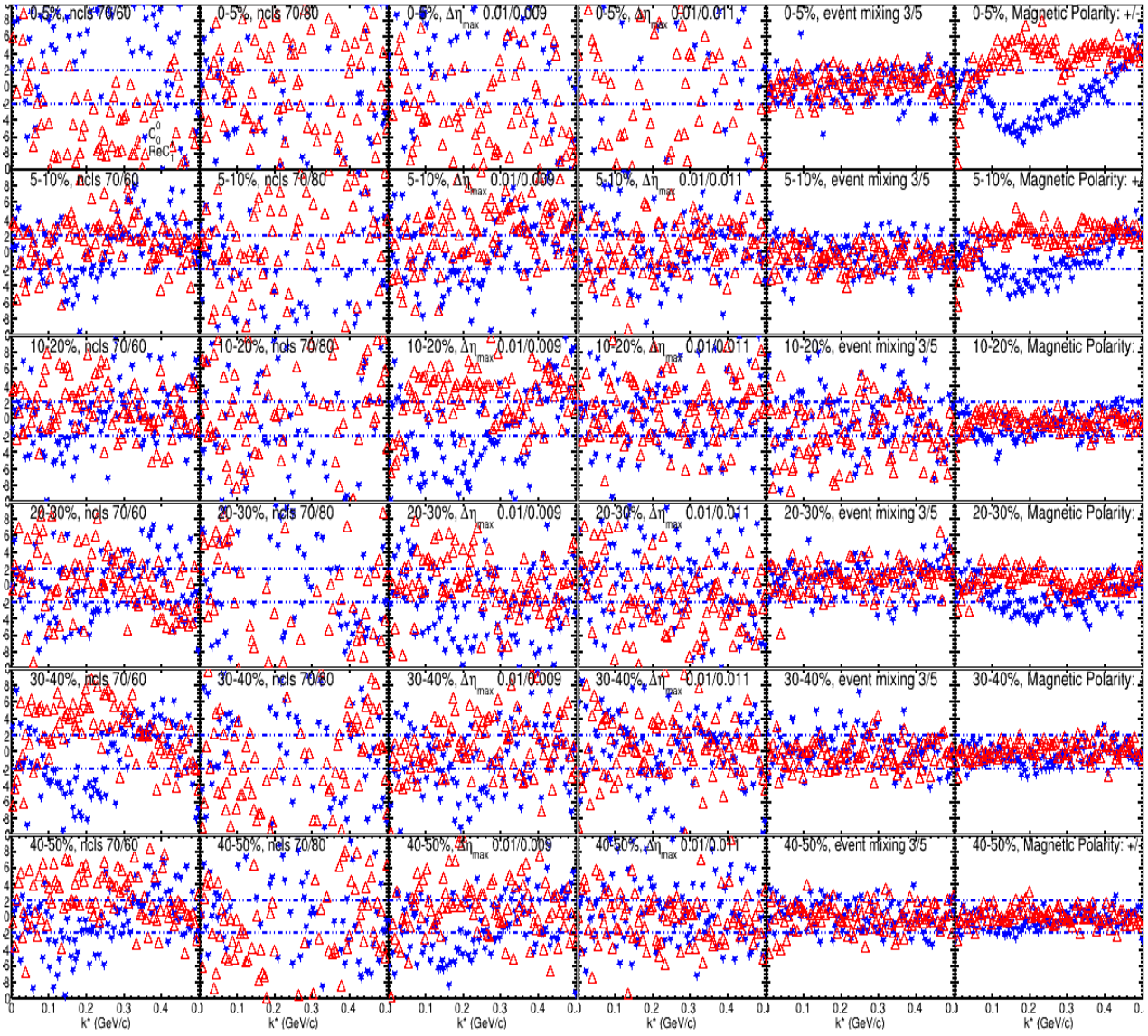

Figure A.8: The Δ/σ as a function of k^* for $\pi^- K^+$, 1^{st} column: TPC ncls 70 and 50, 2^{nd} column: TPC ncls 70 and 80, 3^{rd} column: $\Delta\eta_{max}$ 0.01 and 0.009, 4^{th} column: $\Delta\eta_{max}$ 0.01 and 0.011, 5^{th} column: no. of events for mixing 3 and 5, 6^{th} column: polarity of magnetic field ++ and −− for Pb−Pb collisions at $\sqrt{s_{\rm NN}}$ = 5.02 TeV in ALICE.

References

[1] Wikipedia, 2019, "Standard Model of Elementary Particles," https://en.wikipedia.org/wiki/File:Standard_Model_of_Elementary_Particles.svg

[2] G. Aad *et al.* [ATLAS Collaboration], 2012, "Observation of a new particle in the search for the Standard Model Higgs boson with the ATLAS detector at the LHC," *Physics Letters B* **716**, 1–29.

[3] S. Chatrchyan *et al.* [CMS Collaboration], 2012, "Observation of a new boson at a mass of 125 GeV with the CMS experiment at the LHC," *Physics Letters B* **716**, 30–61.

[4] M. T. *et al.* (Particle Data Group), 2018 Aug, "Review of particle physics," *Phys. Rev. D* **98**, 030001.

[5] B. Sahoo, 2022, "Measurement of $R_2(\Delta\eta, \Delta\varphi)$ and $P_2(\Delta\eta, \Delta\varphi)$ correlation functions in pp collisions at $\sqrt{s}$ = 13 TeV with ALICE at the LHC," presented 16-08-2022.

[6] P. A. Zyla *et al.* [Particle Data Group] (Particle Data Group), 2020, "Review of Particle Physics," *Progress of Theoretical and Experimental Physics* **2020**, 083C01. 2093 p.

[7] D. J. Gross and F. Wilczek, 1973 Jun, "Ultraviolet Behavior of Non-Abelian Gauge Theories," *Phys. Rev. Lett.* **30**, 1343–1346.

[8] H. D. Politzer, 1973 Jun, "Reliable Perturbative Results for Strong Interactions?." *Phys. Rev. Lett.* **30**, 1346–1349.

[9] F. Karsch, 2001, "Lattice qcd at high temperature and density," doi:\bibinfo{doi}{10.48550/ARXIV.HEP-LAT/0106019}

[10] L. C. P. Van Hove, 1987, “Theoretical prediction of a new state of matter, the "quark-gluon plasma" (also called "quark matter"),”

[11] K. Yagi, T. Hatsuda and Y. Miake, 2005, *Quark-gluon plasma: From big bang to little bang*, Vol. 23

[12] H. Satz, 1981, *Statistical Mechanics of Quarks and Hadrons: Proceedings of an International Symposium Held at the University of Bielefeld, F.R.G., August 24-31, 1980* (North-Holland). ISBN 9780444862273

[13] B. Naik, 2020 Nov, “Measurement of azimuthal correlations of D^0 mesons with charged particles in pp collisions at $\sqrt{s}$ = 5 TeV and 13 TeV with ALICE at the LHC,” presented 23 Feb 2021.

[14] A. Andronic and P. Braun-Munzinger, 2004, “Ultrarelativistic nucleus–nucleus collisions and the quark–gluon plasma,” in *The Hispalensis Lectures on Nuclear Physics Vol. 2*, edited by Arias, J. M. and Lozano, M. (Springer Berlin Heidelberg, Berlin, Heidelberg). ISBN 978-3-540-44504-3, pp. 35–67.

[15] H. H. Dalsgaard, 2011, “Pseudorapidity Densities in p+p and Pb+Pb collisions at LHC measured with the ALICE experiment,” presented 2011.

[16] F. Karsch, 2002, “Lattice results on QCD thermodynamics,” *Nuclear Physics A* **698**, 199–208.

[17] T. K. Nayak, 2020 Aug, “Probing the QCD phase structure using event-by-event fluctuations,” *J. Phys.: Conf. Ser.* **1602**, 012003. 11 p.

[18] J. D. Bjorken, 1983 Jan, “Highly relativistic nucleus-nucleus collisions: The central rapidity region,” *Phys. Rev. D* **27**, 140–151.

[19] Mattia, 2016, “Evolution of collisions and QGP,”

[20] B. B. Abelev *et al.* [ALICE Collaboration], 2014, "Transverse momentum dependence of inclusive primary charged-particle production in p–Pb collisions $\sqrt{s_{\mathrm{NN}}}$ = 5.02 TeV," *The European Physical Journal C* **74**, 3054.

[21] K. Aamodt *et al.* [ALICE Collaboration], 2011, "Suppression of charged particle production at large transverse momentum in central Pb−Pb collisions at $\sqrt{s_{\mathrm{NN}}}$ = 2.76 TeV," *Physics Letters B* **696**, 30–39.

[22] S. Chatrchyan *et al.* [CMS Collaboration], 2012, "Study of high-pT charged particle suppression in PbPb compared to pp collisions at $\sqrt{s_{\mathrm{NN}}}$ = 2.76 TeV," *The European Physical Journal C* **72**, 1945.

[23] J. Adams *et al*. [STAR Collaboration], 2003 Aug, "Evidence from d + Au Measurements for Final-State Suppression of High-p_T Hadrons in Au + Au Collisions at RHIC," *Phys. Rev. Lett.* **91**, 072304.

[24] Manceau, Loïc, 2013, "Quarkonium measurements in Pb-Pb and p-Pb collisions with ALICE at the LHC," *EPJ Web of Conferences* **60**, 13002.

[25] M. Wilde, 2013, "Measurement of Direct Photons in pp and Pb–Pb Collisions with ALICE," *Nuclear Physics A* **904-905**, 573c–576c.

[26] A. M. Poskanzer and S. A. Voloshin, 1998 Sep, "Methods for analyzing anisotropic flow in relativistic nuclear collisions," *Phys. Rev. C* **58**, 1671–1678.

[27] B. B. Abelev *et al.* [ALICE Collaboration], 2015, "Elliptic flow of identified hadrons in Pb-Pb collisions at $\sqrt{s_{\mathrm{NN}}}$ = 2.76 TeV," *Journal of High Energy Physics* **2015**, 190.

[28] J. Buxton, 2019, "ΛK and $\Xi^{-}\mathrm{K}^{\pm}$ Femtoscopy in Pb-Pb Collisions at from the LHC ALICE Collaboration," presented in 2019.

[29] J. Rafelski and R. Hagedorn, 1980, "From Hadron Gas to Quark Matter. 2," *International Symposium on Statistical Mechanics of Quarks and Hadrons*

[30] P. Koch and J. Rafelski, 1985, "Time evolution of strange-particle densities in hot hadronic matter," *Nuclear Physics A* **444**, 678–691.

[31] J. Rafelski, 1984, "Strangeness production in the quark gluon plasma," *Nuclear Physics A* **418**, 215–235.

[32] B. Abelev *et al*. [ALICE Collaboration], 2014, "Multi-strange baryon production at mid-rapidity in Pb–Pb collisions at $\sqrt{s_{\rm NN}}$ =2.76 TeV," *Physics Letters B* **728**, 216–227.

[33] J. Adams *et al*. [ALICE Collaboration], 2015 Nov, "One-dimensional pion, kaon, and proton femtoscopy in Pb-Pb collisions at $\sqrt{s_{NN}}$ = 2.76 TeV," *Phys. Rev. C* **92**, 054908.

[34] N. Cabibbo and G. Parisi, 1975, "Exponential hadronic spectrum and quark liberation," *Physics Letters B* **59**, 67–69.

[35] J. Adams *et al.* [STAR Collaboration], 2005, "Experimental and theoretical challenges in the search for the quark–gluon plasma: The STAR Collaboration's critical assessment of the evidence from RHIC collisions," *Nuclear Physics A* **757**, 102–183.

[36] B. B. Back *et al.* [PHOBOS Collaboration], 2005, "The PHOBOS perspective on discoveries at RHIC," *Nuclear Physics A* **757**, 28–101.

[37] K. Adcox *et al.* [PHENIX Collaboration], 2005, "Formation of dense partonic matter in relativistic nucleus–nucleus collisions at RHIC: Experimental evaluation by the PHENIX Collaboration," *Nuclear Physics A* **757**, 184–283.

[38] K. Aamodt *et al.* [ALICE Collaboration], 2010 Dec, "Elliptic Flow of Charged Particles in Pb-Pb Collisions at $\sqrt{s_{NN}}$ = 2.76 TeV," *Phys. Rev. Lett.* **105**, 252302.

[39] J. Adam *et al.* [ALICE Collaboration], 2015, "Measurement of jet suppression in central Pb–Pb collisions at $\sqrt{s_{NN}}$ = 2.76 TeV," *Physics Letters B* **746**, 1–14.

[40] G. I. Kopylov, and M. I. Podgoretsky, "Correlations of identical particles emitted by highly excited nuclei," *Sov. J. Nucl. Phys.* **15**, 219.

[41] G. I. Kopylov, V. L. Lyuboshits, and M. I. Podgoretsky, "Correlations Between the Particles Which Have Small Relative Momenta," *Sov. J. Nucl. Phys.* **18**, 336.

[42] G. Goldhaber, S. Goldhaber, W. Lee, and A. Pais, 1960 Oct, "Influence of Bose-Einstein Statistics on the Antiproton-Proton Annihilation Process," *Phys. Rev.* **120**, 300–312.

[43] HANBURY BROWN, R., TWISS, R., 1956, "A Test of a New Type of Stellar Interferometer on Sirius," *Nature* **178**, 1046–1048.

[44] Yu. M. Sinyukov and S. V. Akkelin and Iurii Karpenko and Yogiro Hama, 2009 Apr., "Kinetics vs hydrodynamics: generalization of Landau/Cooper-Frye prescription for freeze-out," *Acta Physica Polonica B* **40**, 1025.

[45] W. Broniowski, M. Chojnacki, W. Florkowski, and A. Kisiel, 2008 Jul, "Uniform Description of Soft Observables in Heavy-Ion Collisions at $\sqrt{s_{NN}} = 200$ GeV," *Phys. Rev. Lett.* **101**, 022301.

[46] J. Vredevoogd and S. Pratt, 2009, "Universal Flow in the First fm/c at RHIC," *Nuclear Physics A* **830**, 515c–518c.

[47] I. G. Bearden *et al.* (NA44 Collaboration), 2001 Aug, "Two-Kaon Correlations in Central *Pb* + *Pb* Collisions at 158AGeV/c," *Phys. Rev. Lett.* **87**, 112301.

[48] S. V. Afanasiev *et al.* (NA49 Collaboration), 2003, "Bose–Einstein correlations of charged kaons in central Pb+Pb collisions at Ebeam=158 GeV per nucleon," *Physics Letters B* **557**, 157–166.

[49] I. G. Bearden *et al.* (NA44 Collaboration), 2000, "Space-time evolution of the hadronic source in peripheral to central Pb+Pb collisions," *The European Physical Journal C - Particles and Fields* **18**, 317–325.

[50] M. A. Lisa, S. Pratt, R. Soltz, and U. Wiedemann, 2005, "FEMTOSCOPY IN RELATIVISTIC HEAVY ION COLLISIONS: Two Decades of Progress," *Annual Review of Nuclear and Particle Science* **55**, 357–402.

[51] J. Adams *et al.* (STAR Collaboration), 2004 Mar, "Identified Particle Distributions in pp and Au + Au Collisions at $\sqrt{s_{NN}}$ = 200 GeV," *Phys. Rev. Lett.* **92**, 112301.

[52] B. I. Abelev *et al.* (STAR Collaboration), 2006 Nov, "Neutral kaon interferometry in Au+Au collisions at $\sqrt{s_{NN}}$ = 200 GeV ," *Phys. Rev. C* **74**, 054902.

[53] L. Adamczyk *et al.* (STAR Collaboration), 2013 Sep, "Freeze-out dynamics via charged kaon femtoscopy in $\sqrt{s_{NN}}$ = 200 GeV central Au + Au collisions," *Phys. Rev. C* **88**, 034906.

[54] K. Aamodt *et al.* (ALICE Collaboration), 2011, "Two-pion Bose–Einstein correlations in central Pb–Pb collisions at $\sqrt{s_{NN}}$ = 2.76 TeV," *Physics Letters B* **696**, 328–337.

[55] J. Adam *et al.* (ALICE Collaboration), 2016 Feb, "Centrality dependence of pion freeze-out radii in Pb-Pb collisions at $\sqrt{s_{NN}}$ = 2.76 TeV," *Phys. Rev. C* **93**, 024905.

[56] S. Acharya *et al.* (ALICE Collaboration), 2017 Dec, "Kaon femtoscopy in Pb-Pb collisions at $\sqrt{s_{NN}}$ = 2.76 TeV," *Phys. Rev. C* **96**, 064613.

[57] B. Batyunya, L. Malinina, K. Mikhaylov, E. Rogochaya, G. Romanenko and K. Werner, 2020 dec, "Identical pion and kaon femtoscopy in EPOS 3 with and without the hadronic afterburner UrQMD ," *Journal of Physics: Conference Series* **1690**, 012102.

[58] Y. Sinyukov, V. Shapoval and V. Naboka, 2016, "On mT dependence of femtoscopy scales for meson and baryon pairs," *Nuclear Physics A* **946**, 227–239.

[59] J. Adam *et al.* (STAR Collaboration), 2003 Dec, "Pion-Kaon correlations in central Au+Au collisions at $\sqrt{s_{NN}}$ = 130 GeV," *Phys. Rev. Lett.* **91(26)**, 262302(6).

[60] A. Kisiel, 2010, "Non-identical particle femtoscopy at $\sqrt{s_{\rm NN}}$ = 200 AGeV in hydrodynamics with statistical hadronization," *Phys. Rev. C* **81**, 064906.

[61] H. Sorge, 1995 Dec, "Flavor production in Pb(160A GeV) on Pb collisions: Effect of color ropes and hadronic rescattering," *Phys. Rev. C* **52**, 3291–3314.

[62] S. Acharya *et al.*. [ALICE Collaboration], 2021, "Pion-kaon femtoscopy and the lifetime of the hadronic phase in Pb−Pb collisions at $\sqrt{s_{\mathrm{NN}}}$ = 2.76 TeV," *Physics Letters B* **813**, 136030.

[63] A. Kisiel, 2018 Oct, "Pion-kaon femtoscopy in Pb-Pb collisions at $\sqrt{s_{NN}}$ = 2.76 TeV modeled in (3+1)D hydrodynamics coupled to the Therminator 2 code, and the effect of delayed kaon emission," *Phys. Rev. C* **98**, 044909.

[64] R. Lednický, 2009, "Finite-size effect on two-particle production in continuous and discrete spectrum," *Physics of Particles and Nuclei* **40**, 307–352.

[65] S. E. Koonin, 1977, "Proton pictures of high-energy nuclear collisions," *Physics Letters B* **70**, 43–47.

[66] S. Pratt, T. Csorgo and J. Zimányi, 1990 Dec, "Detailed predictions for two-pion correlations in ultrarelativistic heavy-ion collisions," *Phys. Rev. C* **42**, 2646–2652.

[67] A. Kisiel, M. Gałażyn and P. Bożek, 2014 Dec, "Pion, kaon, and proton femtoscopy in Pb-Pb collisions at $\sqrt{s_{NN}}$ = 2.76 TeV modeled in (3+1)D hydrodynamics," *Phys. Rev. C* **90**, 064914.

[68] S. Acharya *et al.* (ALICE Collaboration), 2021, "Kaon–proton strong interaction at low relative momentum via femtoscopy in Pb–Pb collisions at the LHC," *Physics Letters B* **822**, 136708.

[69] A. Kisiel and D. A. Brown, 2009 Dec, "Efficient and robust calculation of femtoscopic correlation functions in spherical harmonics directly from the raw pairs measured in heavy-ion collisions," *Phys. Rev. C* **80**, 064911.

[70] A. Kisiel, 2007, "Non-identical particle femtoscopy in models with single freeze-out," *Braz. J. Phys.* **37**, 917–924.

[71] "LHC Guide," *CERN-Brochure-2017-002-Eng*, (2017).

[72] L. Evans and P. Bryant, "LHC Machine," *Journal of Instrumentation* **3**, S08001.

[73] E. Lopienska, "The CERN accelerator complex, layout in 2022,"

[74] L. Y. Abramova *et al*. [ALICE Collaboration], 1995, *ALICE: Technical proposal for a Large Ion collider Experiment at the CERN LHC*, LHC technical proposal (1995) (CERN, Geneva).

[75] K. Aamodt *et al*. [ALICE Collaboration], 2008, "The ALICE experiment at the CERN LHC," *Journal of Instrumentation* **3**, S08002.

[76] B. B. Abelev *et al*. [ALICE Collaboration], 2014, "Performance of the ALICE experiment at the CERN LHC," *International Journal of Modern Physics A* **29**, 1430044.

[77] K. Aamodt *et al*. [ALICE Collaboration], 2010, "Alignment of the ALICE Inner Tracking System with cosmic-ray tracks," *Journal of Instrumentation* **5**, P03003.

[78] J. Alme *et al*. [ALICE Collaboration], 2010, "The ALICE TPC, a large 3-dimensional tracking device with fast readout for ultra-high multiplicity events," *Nuclear Instruments and Methods in Physics Research Section A: Accelerators, Spectrometers, Detectors and Associated Equipment* **622**, 316–367.

[79] W. Blum, W. Riegler, and L. Rolandi, 2008, *Particle detection with drift chambers; 2nd ed.* (Springer, Berlin).

[80] F. Carnesecchi. [ALICE Collaboration], 2019, "Performance of the ALICE Time-Of-Flight detector at the LHC," *Journal of Instrumentation* **14**, C06023.

[81] G. Volpe. [ALICE Collaboration], 2017, "The High Momentum Particle IDentification (HMPID) detector PID performance and its contribution to the ALICE physics program," *Nuclear Instruments and Methods in Physics Research Section A: Accelerators, Spectrometers, Detectors and Associated Equipment* **876**, 133–136.

[82] The ALICE collaboration, 2013, "Performance of the ALICE VZERO system," *Journal of Instrumentation* **8**, P10016.

[83] J. Adam *et al*. [ALICE Collaboration], 2016, "Study of cosmic ray events with high muon multiplicity using the ALICE detector at the CERN Large Hadron Collider," *Journal of Cosmology and Astroparticle Physics* **2016**, 032.

[84] R. Frühwirth, 1987, "Application of Kalman filtering to track and vertex fitting," *Nuclear Instruments and Methods in Physics Research Section A: Accelerators, Spectrometers, Detectors and Associated Equipment* **262**, 444–450.

[85] B. B. Abelev *et al* [ALICE Collaboration], 2013 Oct, "Centrality determination of Pb-Pb collisions at $\sqrt{s_{NN}}$ = 2.76 TeV with ALICE," *Phys. Rev. C* **88**, 044909.

[86] "Analysis note, pK femtoscopy in Pb−Pb collisions with ALICE at LHC,"

[87] "Analysis note, Pion-kaon femtoscopy in Pb−Pb collisions at $\sqrt{s_{NN}}$ = 2.76 TeV with ALICE at LHC,"

[88] A. Kisiel, 2017, "Non-identical particle correlation analysis in the presence of non-femtoscopic correlations," *Acta Phys. Polon. B* **48**, 717.

[89] B. Zhang, C. M. Ko, B. A. Li and Z. Lin, 2000 May, "Multiphase transport model for relativistic nuclear collisions," *Phys. Rev. C* **61**, 067901.

[90] R. Barlow, 2002, "Systematic Errors: facts and fictions,"

[91] S. K. D. *et al.*, 2022, "Dynamics of Hot QCD Matter – Current status and developments,"

[92] A. Kisiel, 2004, "CorrFit − a program to fit arbitrary two-particle correlation functions," *NUKLEONIKA* **49(Supplement 2)**, S81–S83.

[93] J. Adam *et al.* (STAR Collaboration), 2005 Apr, "Pion interferometry in Au+Au collisions at $\sqrt{s_{NN}}$ = 200 GeV," *Phys. Rev. C* **71**, 044906.

[94] S. S. Adler *et al.* (PHENIX Collaboration), 2004 Oct, "Bose-Einstein Correlations of Charged Pion Pairs in Au + Au Collisions at $\sqrt{s_{NN}}$ = 200 GeV," *Phys. Rev. Lett.* **93**, 152302.

[95] M. Chojnacki, A. Kisiel, W. Florkowski, W. Broniowski, 2012, "THERMINATOR 2: THERMal heavy IoN generATOR 2," *Computer Physics Communications* **183**, 746–773.

[96] J. Adam *et al.* (ALICE Collaboration), 2016 Feb, "Centrality dependence of pion freeze-out radii in Pb-Pb collisions at $\sqrt{s_{NN}} = 2.76$ TeV," *Phys. Rev. C* **93**, 024905.

[97] R. Lednický, 2008 oct, "Finite-size effect on two-particle production," *Journal of Physics G: Nuclear and Particle Physics* **35**, 125109.

[98] V. Khachatryan *et al.* [CMS Collaboration], 2010, "Observation of long-range, near-side angular correlations in proton-proton collisions at the LHC," *Journal of High Energy Physics* **091**, (2010).

[99] V. Khachatryan *et al.* [CMS Collaboration], 2016 Apr, "Measurement of Long-Range Near-Side Two-Particle Angular Correlations in pp Collisions at $\sqrt{s} = 13$ TeV," *Phys. Rev. Lett.* **116**, 172302.

[100] J. Adams *et al.* [STAR Collaboration], 2005 Oct, "Distributions of Charged Hadrons Associated with High Transverse Momentum Particles in pp and Au + Au Collisions at $\sqrt{s_{NN}} = 200$ GeV," *Phys. Rev. Lett.* **95**, 152301.

[101] S. Chatrchyan *et al.* [CMS Collaboration], 2011, "Long-range and short-range dihadron angular correlations in central PbPb collisions at $\sqrt{s_{NN}} = 2.76$ TeV ," *Journal of High Energy Physics* **076**, (2011).

[102] B. H. Alver, C. Gombeaud, M. Luzum and J. Y. Ollitrault, 2010 Sep, "Triangular flow in hydrodynamics and transport theory," *Phys. Rev. C* **82**, 034913.

[103] S. Chatrchyan *et al.* [CMS Collaboration], 2013, "Observation of long-range, near-side angular correlations in pPb collisions at the LHC," *Physics Letters B* **718**, 795–814.

[104] K. Dusling and R. Venugopalan, 2012 Jun, "Azimuthal Collimation of Long Range Rapidity Correlations by Strong Color Fields in High Multiplicity Hadron-Hadron Collisions," *Phys. Rev. Lett.* **108**, 262001.

[105] Adrian Dumitru *et al.*, 2011, "The ridge in proton–proton collisions at the LHC," *Physics Letters B* **697**, 21–25.

[106] K. Werner, I. Karpenko and T. Pierog, 2011 Mar, " "Ridge" in Proton-Proton Scattering at 7 TeV," *Phys. Rev. Lett.* **106**, 122004.

[107] M.-A. Sanchis-Lozano and E. Sarkisyan-Grinbaum, 2017, "A correlated-cluster model and the ridge phenomenon in hadron–hadron collisions," *Physics Letters B* **766**, 170–176.

[108] M. A. S. Lozano and E. S. Grinbaum, 2017 Oct, "Ridge effect and three-particle correlations," *Phys. Rev. D* **96**, 074012.

[109] C. Andrés, A. Moscoso and C. Pajares, 2014 Nov, "Onset of the ridge structure in *AA*, *pA*, and *pp* collisions," *Phys. Rev. C* **90**, 054902.

[110] M. A. Braun, C. Pajares, and V. V. Vechernin, 2015, "Ridge from strings," *The European Physical Journal A* **51**, 44.

[111] C. Flensburg, G. Gustafson, and L. Lönnblad, 2011, "Inclusive and exclusive observables from dipoles in high energy collisions," *Journal of High Energy Physics* **103**, (2011).

[112] T. Sjöstrand, S. Ask, J. R. Christiansen, R. Corke, N. Desai, P. Ilten, S. Mrenna, S. Prestel, C. O. Rasmussen, and P. Z. Skands , 2015, "An introduction to PYTHIA 8.2," *Computer Physics Communications* **191**, 159–177.

[113] C. Bierlich and J. R. Christiansen, 2015 Nov, "Effects of color reconnection on hadron flavor observables," *Phys. Rev. D* **92**, 094010.

[114] J. R. Christiansen and P. Z. Skands, 2015, "String formation beyond leading colour," *Journal of High Energy Physics* **3**, (2015).

[115] T. S. Biro, H. B. Nielsen and J. Knoll, 1984, "Colour rope model for extreme relativistic heavy ion collisions," *Nuclear Physics B* **245**, 449–468.

[116] C. Bierlich *et al.* , 2015, "Effects of overlapping strings in pp collisions," *Journal of High Energy Physics* **148**, (2015).

[117] P. Skands, S. Carrazza, and J. Rojo , 2014, "Tuning PYTHIA 8.1: the Monash 2013 tune," *The European Physical Journal C volume* **74**, 3024.

[118] P. Chakraborty, and S. Dash, 2020 Nov, "Understanding long-range near-side ridge correlations in $p-p$ collisions using rope hadronization at energies available at the CERN Large Hadron Collider," *Phys. Rev. C* **102**, 055202.

[119] N. N. Ajitanand *et al.* , 2005 Jul, "Decomposition of harmonic and jet contributions to particle-pair correlations at ultrarelativistic energies," *Phys. Rev. C* **72**, 011902.

List of Publications

Journal publications

1. **Pritam Chakraborty**, Tulika Tripathy, Subhadip Pal and Sadhana Dash, "Multiplicity dependence of strange and multi-strange hadrons in p–p, p–Pb and Pb–Pb collisions at LHC energies using Tsallis-Weibull formalism", *The European Physical Journal A* **56**, 103 (2020)

2. **Pritam Chakraborty** and Sadhana Dash, "Understanding long-range near-side ridge correlations in p–p collisions using rope hadronization at energies available at the CERN Large Hadron Collider", *Phys. Rev. C* **102**, 055202 (2020)

3. **Pritam Chakraborty**, Ashutosh Kumar Pandey and Sadhana Dash, "Identical-particle (pion and kaon) femtoscopy in Pb–Pb collisions at $\sqrt{s_{\rm NN}}$ = 5.02 TeV with Therminator 2 modeled with (3+1)D viscous hydrodynamics", *The European Physical Journal A* **57**, 338 (2021)

Conferences proceedings

1. **Pritam Chakraborty** and Sadhana Dash, "Understanding long-range near-side ridge correlations in p–p collisions using rope hadronization at energies available at the CERN Large Hadron Collider", *Proceedings of the XXIV DAE-BRNS High Energy Physics Symposium, Jatni, India. Springer Proceedings in Physics, vol 277. Springer, Singapore, 2022*

2. **Pritam Chakraborty** (for the ALICE Collaboration), "Non-identical particle femtoscopy in Pb–Pb collisions at $\sqrt{s_{\rm NN}}$ = 5.02 TeV with ALICE",*Proceedings of the Dynamics of Hot QCD Matter – Current Status and Developments, Goa, India, 2022* arXiv:2208.13440, accepted in International Journal of Modern Physics E

3. **Pritam Chakraborty** (for the ALICE Collaboration), "Non-identical particle femtoscopy in PbPb collisions at 5.02 TeV with ALICE", *Proceedings of the 41st International Conference on High Energy physics (ICHEP2022), Bologna, Italy, 2022, Proceedings of science, volume 414, pages 463, 2022*.

Analysis Notes in ALICE

1. Non-identical particle femtoscopy in Pb–Pb collisions at 5.02 TeV with ALICE. `https://alice-notes.web.cern.ch/node/970`

Contribution to other conferences

1. "Non-identical particle femtoscopy in Pb–Pb collisions at 5.02 TeV with ALICE", Poster presentation at Quark Matter 2022 conference, Krakow, Poland.

2. Non-identical particle femtoscopy in Pb–Pb collisions at 5.02 TeV with ALICE, Poster presentation at 20$^{\rm th}$ International Conference on Strangeness in Quark Matter (SQM 2022), Busan, Republic of Korea.

3. "Identical-particle (pion and kaon) femtoscopy in Pb–Pb collisions at $\sqrt{s_{\rm NN}}$ = 5.02 TeV with Therminator2 modeled with (3+1)D viscous hydrodynamics", Poster presentation at 10$^{\rm th}$ Edition of the Large Hadron Collider Physics Conference (online), 2022.

4. "Identical-particle (pion and kaon) femtoscopy in Pb–Pb collisions at $\sqrt{s_{\rm NN}}$ = 5.02 TeV with Therminator2 modeled with (3+1)D viscous hydrodynamics", Poster presentation at International Conferences on High Energy Physics 2022, Bologna, Italy.

Acknowledgements

The completion of this thesis would not have been possible without the support and guidance of many individuals and institutions.

First of all, I would like to express my deepest gratitude to my PhD supervisor, Prof. Sadhana Dash for her invaluable guidance, continuous support, and patience during my PhD study. Her immense knowledge and plentiful experience have encouraged me in all the time of my academic research and daily life. Whenever I was stuck in my analyses, her out-of-the-box thinking always got me back on track. She has always inspired me to push the limits, perform multitasking and stay organized throughout the research process. I am deeply grateful for her mentor-ship and unwavering support. Thank you madam for believing in me and providing me with the opportunity to pursue my research goals.

I would also like to extend my thanks to Prof. Basanta Kumar Nandi for his encouragement, support and invaluable advice in pursuing my research. His expertise in the field of particle physics has been a great source of inspiration for me. Every physics discussion we had, enriched my understanding of the subject and helped me to clarify my thoughts on various topics.

I would like to extend my deepest gratitude to Dr. Georgy Kornakov for our endless discussions on femtoscopy and THERMINATOR. I cannot forget his contributions towards providing a solid basis for this thesis. Thank you Georgy for the support and also, for the barbeque party we had at your place during our visit at CERN.

I am extremely thankful to Prof. Asmita Mukherjee for evaluating my research each year and providing valuable suggestions.

I would like to express my regards to all the members of PAG-FEMTOSCOPY and PWG-CF group of ALICE, especially Lukasz Kamil Graczykowski, Malgorzata Anna Janik, Laura Fabbietti, Ludmila Malinina, Mesut Arslandok, Igor Altsybeev, Valentina Mantovani Sarti, Elena Rogochaya for the extensive discussions we had during the weekly PAG meetings that helped the analysis to move forward. I would like thank Oton Vazquez Doce, Andreas Michael Mathis and Dimitar Lubomirov Mihaylov for the detailed review of my analysis note.

I would like to express my deepest gratitude to Marian I Ivanov who was the supervisor of my service task. His dedication towards the job is inspiring. He helped me a lot to learn about the shell scripting, C++, Python, Jupyter Notebook as well as various technicality of the ALICE detector. It was a privilege to work with him.

I would like to express my deepest gratitude to my teacher during by bachelor studies, Dr. Bijoy Sidhanta who motivated me to pursue the quest for knowledge and cheered for me even for my tiniest achievements. His passion towards understanding the physical laws of nature is truly inspiring.

I had a great experience working at the EHEP lab of IIT Bombay because of the wonderful lab-mates. Thank you Dr. Ashutosh Kumar Pandey, Dr. Pragati Sahoo, Dr. Ranjit Kumar Nayak, Dr. Bharati Naik, Dr. Ankita Goswami, Dr. Himani Bhatt, Dr. Baidyanath Sahoo, Dr. Akash Pandey, Subhadeep Roy, Deependra Sharma, Sonali Padhan, Dr. Shubhalaxmi Rath, Santosh Kumar, Ayush Yadav for the encouragement and valuable discussions.

I would like to extend my heartfelt thanks to my friends, Kashimul Hossain, Dibakar Bauri, Mohammad Monish, Sucharita Giri, Tulika Tripathy, Urvashi Bothra, Manisha Meena, Supriti Ghorui, Gopa Sardar, Bhawna and also, Dr. Poulab Chakrabarti and Bikash Chandra Barik for making my PhD-life so colourful.

Finally, I would like to express my deepest gratitude to my father and mother for their love and support through out my academic career. I would like to extend my heartfelt thanks to my father-in-law and mother-in-law for believing in me. Lastly, I would like to thank my wife Sayantani Acharya Chakraborty for her unwavering love and support throughout my PhD

journey. Without her patience, understanding, and sacrifices, it would not be possible to focus on my research work and achieve my goals.

Pritam Chakraborty

IIT Bombay

20 March 2023